TECHNISCHE UNIVERSITÄT DRESDEN

Fakultät Maschinenwesen

Institut für Luft- und Raumfahrttechnik

DISSERTATION

Experimental Investigations of the Mach-effect for Breakthrough Space Propulsion

Vorgelegt von: M.Sc. Maxime Monette

Zum Erlangen des akademischen Grades *Doktor-Ingenieur*.

Gutachter: Prof. Dr. techn. Martin Tajmar

Prof. Dr. Thomas Krause

Tag der Verteidigung: 31.08.2023

Acknowledgements

It is with the help of Prof. Dr. techn. Martin Tajmar, the German Aerospace Center, the Gouvernement du Québec, a team of excellent colleagues and of course, a supporting environment that I was able to start and pursue this quest to the stars. For an international graduate student looking around the world for opportunities to keep exploring the universe, Prof. Tajmar was and still is the reference with whom to pursue academic studies with a concentration in space propulsion, and one of the rare ones in the world to do rigorous scientific work on breakthrough propulsion. Having built an expertise on electric propulsion and sensitive thrust measurements in vacuum over the years, Prof. Tajmar has the knowledge, the creativity, the equipment and the drive required to lead such experiments. My arrival at the TU Dresden luckily coincided with the start of the SpaceDrive project funded by the DLR, without which we would never have had as much freedom to carry all the promising experiments. The project was the first of its kind and size in Germany and one of the few in the world, with the sole purpose of testing theories that promise super-fast, propellantless travel in space. My participation to this project would not have been possible without the generous three-year scholarship from the Fonds de Recherche du Québec that first brought me from Canada to Germany, and an opportunity given by Prof. Tajmar after a meeting in Seoul, Korea, during my master studies at KAIST.

The complex thrust balance experiments would not have been possible without the extraordinary engineering sense and friendly collaboration of my colleagues: Dipl.-Ing. Christian Drobny and Dipl.-Ing. Jan-Philipp Wulfkühler, for their patience and experience with vacuum chambers, Dipl.-Ing. Jörg Heisig, for his electrotechnical genius and philosophical inputs, Dipl.-Ing. Matthias Kößling for his torsion balance, extreme helpfulness and his programming and modeling talents, Dipl.-Ing. Oliver Neunzig, for his double-pendulum balance, his inspiring discipline and scientific work, Dr.-Ing. Marcel Weikert for his deep space knowledge and creativity, Dr.-Ing. Tino Schmiel for the friendly support and thought-provoking discussions, and Dipl.-Ing. Willy Stark for his centrifugal balance and his encouragement. I also had the incredible opportunity to collaborate with Prof. Woodward and Prof. Hal Fearn, the original instigators of the theory and experiments behind the Mach-effect propulsion, as well as Marc Millis, group lead of the legendary Breakthrough Propulsion Physics Program funded by NASA a few years back, and I thank them for their passion, creativity and inspiring drive to publish professional and scientific work on breakthrough propulsion. I am also sincerely grateful to my critical draft reviewers, Dr. Robin Schäfer, Dr.-Ing. Konstantin Kojucharow, Dipl.-Ing. Matthias Kößling and Dipl.-Ing. Alrik Dargel.

Of course, none of my work would have come to life without the support of my nurturing environment next to the Elbe in beautiful Dresden and of my parents and siblings abroad in Quebec. I will be forever grateful for the support of my Korean, German and Canadian families. In Dresden, a healthy work-life balance was made possible by my badminton and sailplane clubs. Finally, I was fortunate to count on my furry home-office companion Giovanni, and my lovely Isa for her encouragement, wisdom and perfectionism.

Abstract

This research was conducted within the framework of the SpaceDrive project funded by the German Aerospace Center to develop propellantless propulsion for interstellar travel. The experiments attempted to measure mass fluctuations predicted by the Mach-effect theory derived from General Relativity and observed through torsion balance measurements by Woodward (2012). The combination of such mass fluctuations with synchronized actuation promises propellantless thrust with a significantly better thrust-to-power ratio than photon sails. Thus, experiments using different electromechanical devices including the piezoelectric Mach-effect thruster as tested by Woodward et al. (2012) were pursued on sensitive thrust balances. The tests were automated, performed in vacuum and included proper electromagnetic shielding, calibrations, and different dummy tests. To obtain appropriate driving conditions for maximum thrust, characterization of the experimental devices involved spectrometry, vibrometry, finite element analysis, and circuit modeling. Driving modes consisted of sweeps, resonance tracking, fixed frequency, and mixed signals. The driving voltage, frequency, stack pre-tension, mounting, and thruster orientation were also varied. Lastly, different amplifier electronics were tested as well, including Woodward's original equipment.

Experiments on the double-pendulum and torsion balances with a resolution of under 10 nN and an accuracy of 88.1 % revealed the presence of force peaks with a maximum amplitude of 100 nN and a drift of up to 500 nN. The forces mainly consisted of switching transients whose signs depended on the device's orientation. These force transients were also observed in the zero-thrust configurations. No additional thrust was observed above the balance drift, regardless of the driving conditions or devices tested. In addition, finite element and vibrometry analysis revealed that the vibration from the actuator was transmitted to the balance beam. Moreover, simulations using a simple spring-mass model showed that the slower transient effects observed can be reproduced using small amplitude, high-frequency vibrations. Hence, the forces observed can be explained by vibrational artifacts rather than the predicted Mach-effect thrust.

Then, centrifugal balance experiments measured the mass of a device subjected to rotation and energy fluctuations, with a precision of up to 10 µg and a high time resolution. The measurements relied on piezoelectric- and strain gauges. Their calibration methods presented limitations in the frequency range of interest, resulting in discrepancies of up to 500 %. However, the tests conducted with capacitive and inductive test devices yielded experimental artifacts about three orders of magnitude below the mass fluctuations of several milligrams predicted by the Mach-effect theory. Although the piezoelectric devices presented more artifacts due to nonlinearity and electromagnetic interaction, all rotation experiments did not show the expected dependence on the rotation frequency.

In summary, the search for low thrust and small mass fluctuations consisted of challenging experiments that led to the development of innovative and sensitive instruments, while requiring a careful consideration of experimental artifacts. The results analysis led to the rejection of mass fluctuations and thrusts claimed by Woodward's Mach-effect theory and experiments. The quest for breakthrough space propulsion must thus continue a different theoretical or experimental path.

Abstrakt

Die Arbeit wurde im Rahmen des vom Deutschen Zentrum für Luft- und Raumfahrt finanzierten SpaceDrive-Projekts zur Entwicklung eines treibstofflosen Antriebs für interstellare Reisen durchgeführt. Bei den Experimenten wurde versucht, Massenschwankungen nachzuweisen, die in der von Woodward (2012) abgeleiteten Mach-Effekt-Theorie vorhergesagt und mit Schubmesswaagen beobachtet wurden. Die Kombination synchronisierter elektromechanischer Ansteuerung und solcher Massenfluktuationen solle treibstofflosen Schub mit einem deutlich besseren Schub-Leistungs-Verhältnis als Photonensegel ermöglichen. Daher wurden Experimente mit verschiedenen elektromechanischen Vorrichtungen, einschließlich des von Woodward et al. (2012) getesteten piezoelektrischen Mach-Effekt-Triebwerks, an empfindlichen Schubmesswaagen durchgeführt. Die Tests waren automatisiert, wurden im Vakuum durchgeführt und beinhalteten Kalibrierungen und verschiedene Dummy-Tests. Um geeignete Antriebsbedingungen für maximalen Schub zu erhalten umfasste die Charakterisierung der Versuchsgeräte Spektrometrie, Vibrometrie, Finite-Elemente-Analyse und Schaltkreismodellierung. Die Ansteuerungsmodi bestanden aus Sweeps, Resonanzverfolgung, Festfrequenz und gemischten Signalen. Auch die Ansteuerungsspannung, die Frequenz, die Vorspannung, die Verstärkerelektroniken, die Halterung und die Ausrichtung des Triebwerks wurden variiert.

Bei den Experimenten an den Doppelpendel- und Torsionswaagen mit einer Auflösung von unter 10 nN und einer Genauigkeit von 88,1 % traten Kraftspitzen mit einer maximalen Amplitude von 100 nN und einem Drift von bis zu 500 nN auf. Die Kräfte bestanden hauptsächlich aus Schalttransienten, deren Vorzeichen von der Ausrichtung des Geräts abhingen. Diese Krafttransienten wurden auch in den schubfreien Konfigurationen beobachtet. Unabhängig von den Antriebsbedingungen und den getesteten Geräten wurde kein zusätzlicher Schub über dem Drift hinaus beobachtet. Darüber hinaus ergaben Finite-Elemente- und Vibrometrie-Analysen, dass die Schwingungen des Antriebs auf den Waagebalken übertragen wurden. Darüber hinaus zeigten Simulationen unter Verwendung eines einfachen Feder-Masse-Modells, dass langsamere transiente Effekte durch hochfrequente Schwingungen mit kleiner Amplitude reproduziert werden können. Daher können die beobachteten Kräfte auf Vibrationsartefakte anstatt den vorhergesagten Mach-Effekt zurückgeführt werden.

Anschließend wurde in Zentrifugalwaagenexperimenten die Masse einer Vorrichtung, welche Rotations- und Energieschwankungen ausgesetzt ist, mit einer Genauigkeit von bis zu 10 µg und einer hohen zeitlichen Auflösung gemessen. Die Messungen stützten sich auf piezoelektrische Sensoren und Dehnungsmessstreifen. Deren Kalibrierungsmethoden wiesen in dem relevanten Frequenzbereich Grenzen auf, was zu Abweichungen von bis zu 500 % führte. Die mit kapazitiven und induktiven Testgeräten durchgeführten Versuchen ergaben jedoch experimentelle Artefakte, die etwa drei Größenordnungen unter den nach der Mach-Effekt-Theorie vorhergesagten Massenschwankungen von mehreren Milligramm lagen. Trotz größerer Artefakte aufgrund von Nichtlinearität und elektromagnetischer Wechselwirkung in den piezoelektrischen Vorrichtungen, zeigten die Messungen nicht die erwartete Abhängigkeit von der Rotationsfrequenz.

Die Suche nach geringem Schub und kleinen Massenschwankungen bestand aus anspruchsvollen Experimenten, die zur Entwicklung empfindlicher Instrumente führten und gleichzeitig eine sorgfältige Berücksichtigung experimenteller Artefakte erforderten. Die Analyse der Ergebnisse führte zur Ablehnung der von Woodwards Mach-Effekt-Theorie und -Experimenten behaupteten Massenschwankungen und Schübe. Die Suche nach einem bahnbrechenden Raumfahrtantrieb muss daher auf einem anderen theoretischen oder experimentellen Weg fortgesetzt werden.

Table of Contents

List of Figures

List of Tables

List of Abbreviations

AC	Alternating Current
CAD	Computer Aided Design
CB	Centrifugal Balance
CD	Centrifugal Device
COM	Communication
CSUF	California State University, Fullerton
DC	Direct Current
DFT	Discrete Fourier Transform
DLR	German Aerospace Center
DOF	Degree of Freedom
DP	Double-Pendulum
DUT	Device Under Test
EM	Electromagnetic
EMI	Electromagnetic Interaction
FEM	Finite Element Method
FEEP	Field Emission Electric Propulsion
GEO	Geostationary Earth Orbit
GND	Ground
IR	Infrared
LC	Large Chamber
LHS	Left-Hand Side
LEO	Low Earth Orbit
MEGA	Mach-effect Gravity Assist
MET	Mach-effect Thruster
MFP	Mean Free Path
NGND	Not Grounded
OLC	Overly Large Chamber
PC	Personal Computer
PZT	Lead-Zirconium-Titanate
QCM	Quartz Crystal Microbalance
RHS	Right-Hand Side
RLC	Resistor Inductor Capacitor
S&M	Steiner & Martin
SNR	Signal to Noise Ratio
TB	Torsion Balance
TC	Thermal Correction
TEOM	Tapered Element Oscillating Microbalance
TRAFO	Transformer
TUD	Technical University Dresden
VC	Voice Coil
WMAP	Wilkinson Microwave Anisotrope Probe

List of Variables and Symbols

Constant	Unit	Description	Value
c	m/s	Speed of Light	299.792.458
g_0	N/kg	Earth's Gravitational Acceleration	9.807
G	Nm^2/kg^2	Gravitational Constant	6.6743015E-11
ε_0	s^4A^2/m^3kg	Electric Permittivity of Free Space	8.85418782E-12
μ_0	H/m	Magnetic Permittivity of Free Space	4π E-7
j	-	Imaginary Number	$\sqrt{-1}$

Variable	Unit	Description
f, F	N	Force
m, M	kg	Mass
v_e	m/s	Exit Velocity
$\dot{m}$	kg/s	Mass Flow Rate
I_{sp}	s	Specific Impulse
$\ddot{x}, a$	m/s^2	Acceleration
$\dot{x}, v$	m/s	Velocity
x	m	Displacement
η_{pr}	-	Propulsive Efficiency
P	W	Power
Ø	-	Gravitational Potential
m_0	kg	Rest Mass
Δv	m/s	Delta-v
t, τ	s	Time

LIST OF VARIABLES AND SYMBOLS

Variable	**Unit**	**Description**
ρ_0	kg/m^3	Rest Density
E_0	J	Rest Energy
E	V/m	Electric Field
C	F	Capacitance
V	V	Voltage
A	m^2	Cross-sectional Area
δm	kg	Mass Fluctuation
ω	rad/s	Angular Frequency
L	H	Inductance
I	A	Current
N	-	Number of Turns
ε_r	s^4A^2/m^3kg	Relative Dielectric Permittivity
μ_r	H/m	Relative Magnetic Permittivity
d_{33}	pC/N	Piezoelectric Coupling Constant
Q	-	Quality Factor
η	-	Clamping Efficiency
k_A	N/m	Actuator Spring Constant
T	N/m^2	Mechanical Stress
S	-	Mechanical Strain
E	V/m^2	External Electric Field
g	V/N	Piezoelectric Voltage Constant
k	-	Electromechanical Coupling
s	m/N	Mechanical Compliance
$tan\ \delta_m$	-	Mechanical Loss Coefficient

Variable	**Unit**	**Description**
D	C/m^2	Electric Displacement
Y	N/m^2	Young’s Modulus
λ_i	m	Wavelength
c	m/s	Sound Speed
μ	m	Elongation
R	Ω	Resistance
M	V^2/m^2	Electrostrictive Coefficient
J	kg/m^2	Rotational Inertia
ζ	-	Damping Coefficient
Ψ	Nm	Torque
K	V/N	Conversion Factor
Z	Ω	Impedance
r	m	Radius
n	-	Number of Elements
α	N/m^2kg	Mechanical Nonlinear Coefficient
β	N/V^2	Dielectric Nonlinear Coefficient
γ	N/mV	Piezoelectric Nonlinear Coefficient
t_B	m	Thickness
L_T	m	Length

1. Introduction

1.1 Research Motivation

Humans have looked up to the stars for orientation, for answers on the origin of the universe, or in search of other life-harboring systems, however, despite improving observation techniques their reach still seems to elude us. The main reason is that even the closest stars are simply too far away. For a rendezvous mission to the nearest star within a human lifetime using current propulsion technology would take an amount of propellant significantly greater than the mass of the entire visible universe [1]. The conventional method of propulsion relies on ejecting fuel and using its 'lost' momentum to move forward according to Tsiolkovsky's [2] equation, derived from Newton's[3]action-reaction principle. The efficiency of different propellants can be characterized by their exit velocity or specific impulse [4]. Whereas jet fuel engines used in launchers such as the Saturn V have a theoretical limit of 500 seconds in specific impulse, ion thrusters using electrostatic propulsion are limited to about 10,000 seconds [5]. Only with a concept employing the products of fusion or anti-matter reactions can the specific impulse reach around 60,000 seconds, resulting in the propellant requirement amounting to the mass of the Earth in order to reach Proxima Centauri [6].

Solar propulsion and laser beam propulsion are propellantless methods that could be interesting candidates for interstellar propulsion. However, both methods are characterized by a very low thrust-to-power ratio, equal to at most two over the speed of light [7]. Also, the thrust being proportional to the sail area, a significant acceleration or payload capacity would only be achieved with sails reaching astronomical proportions. Furthermore, beamed propulsion presents many challenges that remain to be solved in terms of thermal management, pointing accuracy, enormous Earth- or orbit-based laser installations, and critical material strength and durability for sails [8]. Solar propulsion presents the additional disadvantage of depending on photon energy density, making it efficient only in the vicinity of large stars. These weaknesses strongly indicate the need for a paradigm shift for interstellar ventures, and the need for a breakthrough in space propulsion. This thesis is the result of an experimental journey to discover that.

While different concepts of propellantless propulsion have been brought forward by physicists over the past few decades, all depend on exotic physics that has not been supported by experimental evidence. Alcubierre's warp drive is an example of a means of propulsion that relies on negative energy to create a bubble around the passengers that modifies the metric of spacetime to provide forward motion [9]. Forward's theoretical concept of propulsion relies on negative mass to provide acceleration [10]. Some scientists are convinced of a method of exploiting the quantum vacuum to generate propulsion by amplifying the dynamic Casimir force [11]. These ideas and several more have been investigated by experimental programs in the United Kingdom, under the Greenglow Project [12], and in the United States, through the Breakthrough Propulsion Program in the '90s [13]. While offering different insights and improving measurement methods, the projects were not successful at developing any readiness level for the technologies investigated. Among them, were Shawyer's EmDrive [14], Millis' Diametric Drive [13], Podkletnov's Superconducting Beam [15] and Woodward's Mach-effect Thruster (MET) [16]. The SpaceDrive Project [17] at the Technical University of Dresden

(TUD) funded by the German Aerospace Center (DLR) was Germany's first project of a kind, active from 2017 to 2021, which aimed at pushing the investigation of the MET, EmDrive, and other breakthrough propulsion ideas a step further.

1.2 Objectives

The phenomena that still cannot be explained by known physics hint at undiscovered physics and include the rotation rate of spiral galaxies, the origin of inertia, the existence of dark energy and dark matter, the nature of vacuum, the graviton, and disparities between General Relativity and quantum field theory [18]. Despite the presence of alternative theories, fundamental experiments often require vast quantities of energy that cannot be obtained in a laboratory on Earth. One of the testable propulsion concepts, described in Woodward's book [16], proposes to use of a version of Mach's Principle in generating a mass fluctuation and combining it with a simultaneous actuation to provide forward motion. This concept is embodied in a table-top experiment that predicts measurable thrust [19]. The so-called Mach-effect has been an unsolved mystery that explains the origin of inertia as being the connection of local matter to the distant matter in the universe; it relies on a universal inertial frame that would be explained by Einstein's cosmological constant [20].

This thesis examines the Mach-effect concept, mass fluctuation measurement, and the possibility of generating thrust using a combination of mass fluctuation and an oscillating actuator. First, by performing multiple experiments with Woodward's devices using sensitive thrust balances in vacuum, different electromechanical artifacts will be investigated. Then, the mass of test devices undergoing energy fluctuations will be monitored using piezoelectric sensors on a centrifugal force balance. Thus, although the main objective is to examine the claim of thrust coming from the Mach-effect, improving measurement accuracy and deepening the understanding of the phenomena appearing in low force measurements are also key. The work serves in supporting the quest for breakthrough propulsion with solid testing and analysis, and contribute to improving the force measurement techniques for space propulsion. The objectives of this research were in line with the SpaceDrive project initiated by Prof. Tajmar, having for goal the testing of different fringe theories for space propulsion and developing precise measuring instruments for forces.

1.3 Content Overview

Chapter 2 lays the theoretical foundation for the experimental investigation. A summary of the literature demonstrates the limits of current space propulsion and exposes the current understanding of the Mach-effect and transient mass propulsion. The theory behind the Woodward thruster is summarized, followed by a critical assessment of the experimental work performed with similar devices. Finally, an overview of force and mass measurement in the literature sets the stage for the balance experiments to discover mass fluctuation effects.

Chapter 3 constitutes a complete electromechanical characterization of all parts of the experimental setup ranging from the vacuum chamber to the piezoelectric sensors and the thrust balances. Most test devices are based on a piezoelectric ultrasonic actuator; thus, the concept is examined from its basic constituents and relevant piezoelectric properties. The bulk of the characterization then consists of impedance spectra, finite element method (FEM), circuit modeling, vibration measurements, and voice coil tests. Non-linear effects are examined in detail as well. The chapter also leads to concrete predictions of the effect to be measured according to Woodward's theory.

Chapter 4 contains key results from thrust balance experiments including dummy, magnetostrictor, and MET tests. The results show force, applied voltage and temperature curves, and beam vibrations for different driving parameters. Each subsection includes a discussion that focuses on the experimental artifacts and the sources of error.

Chapter 5 then focuses on the experiments with the centrifugal balance, in an attempt to directly measure the mass fluctuations. The design of the test devices, the sensor calibration methods, and the sources of error are also described in that chapter.

The findings are summarized in Chapter 6, where the intimate connection of the different units in an electromechanical system and their influence on the system resonances and experimental artifacts is shown. Realizations from the characterization tests, thrust balance, and centrifugal balance experiment results are combined to reach the conclusion.

1.4 Team Work

The SpaceDrive project kicked-off on April 1st, 2017, and was negotiated between DLR and Prof. Tajmar, who supported and led the research efforts described in [17]. The project (50RS1704) was funded by the German Federal Ministry for Economic Affairs and Energy. The other team members were Dipl.-Ing. Jörg Heisig, Dipl.-Ing. Matthias Kößling, Dipl.-Ing. Oliver Neunzig, Dipl.-Ing. Willy Stark and Dipl.-Ing. Marcel Weikert, as well as a few master students. Matthias Kößling was responsible for the design, assembly, testing, calibration, and fine-tuning of the torsion balances (TB), on which we conducted most of the MET experiments. The joint effort led to several conference publications [17,21,22] and journal publications [23,24]. Oliver Neunzig was responsible for the design, assembly, calibration, and testing of a double-pendulum thrust balance as well as a levitating rotation thrust balance. The double-pendulum balance was used mostly for the EmDrive and laser resonator experiments conducted by Marcel Weikert, which also led to several publications [25–27]. The author conducted a few tests with the MET on the double-pendulum balance as well, leading to a conference publication [28]. Willy Stark designed, assembled, calibrated, and tested the centrifugal balance, and the joint effort with the rotating Mach-effect investigations has led to a recently submitted publication [29]. Prof. Tajmar also took care of the LabVIEW software logistic behind the experiments, enabling communication with all laboratory devices and automation of the vacuum chamber experiments. Jörg Heisig, the group's electrotechnician and systems administrator, assisted the experiments by assembling, testing, and repairing the electrical devices used, such as filters, amplifiers, computers, and diverse communication devices. The author was in charge of all Mach-effect investigations involving torsion, double-pendulum, and centrifugal balance tests, vibrometry, FEM, spectrometry, and the design of test devices. These experiments, however, would not have been possible without the collaboration of the engineers mentioned above. Additionally, computational resources were made available by the High-Performance Computing and Storage Complex of the TUD for the numerical analysis using ANSYS. Further characterization tests of the piezoelectric devices were also made possible by the Fraunhofer IKTS in Dresden, allowing the author's use of an impedance spectroscope, as well as an electrodynamic testing machine from the Institute of Building Construction (TUD) for the dynamic calibration of sensors.

Last but not least, the SpaceDrive research team had the invaluable opportunity to collaborate with Prof. James F. Woodward, the initiator of the Mach-effect experiments, and his collaborator Prof. Hal Fearn of the California State University, Fullerton (CSUF). The collaboration involved the team's participation in two Advanced Propulsion Workshops in California [30,31], the exchange of equipment and ideas, a visit to the CSUF laboratory, as well as Hal Fearn's visit to the TUD laboratory and supervision of experiments.

2. Literature Review

2.1 Fundamentals of Space Propulsion

Propulsion in space represents a great challenge due to the lack of a medium to push off from. Unlike cars that push off the road to drive forward or submarines and airplanes that propel themselves forward using their turbine blades to push off the surrounding water or air, spacecraft cannot push off the surrounding vacuum. Well below the Karman line, the highest altitude records for non-rocket-powered airplanes were set at around 37 km due to the inability to generate enough lift using their engines [32]. At an altitude of 100 km, the surrounding atmosphere already drops to a pressure of $3 \cdot 10^{-4}$ mbar ($3 \cdot 10^{-2}$ Pa) where the average mean-free-path of an atom (MFP), defined as the mean distance traveled by an atom before its next statistically possible collision with another atom, is greater than 10 cm compared to the mere 70 nm at ground level. In interstellar space, far enough from the solar system, the atmospheric pressure figuratively drops below 10^{-12} mbar (10^{-10} Pa) with an MFP greater than 10,000 km. Thus, pushing against atoms in interstellar space seems out of the question. What else is there in interstellar space? An overview of the constituents, number and energy densities is sketched in Table 1. Interstellar space consists of different regions containing galaxies, clusters and clouds, but in the mean interstellar medium, most of the particles are gas particles at 99%, and dust at 1% by mass; by number, 91% of the atoms are hydrogen mainly in molecular form, 8.9 % helium, and 0.1% heavier atoms [33]. Depending on the regions of the interstellar medium, like molecular clouds, warm neutral, or warm ionized medium, the density and state of the hydrogen atoms may vary. Propulsion using interstellar atoms has been the subject of a futuristic propulsion concept, the Bussard Ramjet, which represents many engineering challenges [13,34]. Neutrinos are interesting since some of them contain a large energy density – the most numerous as observed from Earth, for example, come from the sun with an energy of 10 MeV [35] – however, they do not participate in any electromagnetic or strong nuclear force reactions and only interact through the weak force interaction. Vacuum energy can be thought of as quantum vacuum fluctuations or as the creation and annihilation of any number of virtual particle pairs, however, whether these can be used for propulsion, and what the exact energy density is, remain a mystery [11,13].

Constituent	Number Density [ppcm^3]	Energy Density [eV/cm^3]
Hydrogen Atoms [33]	$10^{-4} - 10^{6}$	$10^{5} - 10^{15}$
Neutrinos [35,36]	$10^{-5} - 10^{2}$	$4 \cdot 10^{-4} - 10^{12}$
Cosmic Radiation [37] **Background/Photons**	$4.1 \cdot 10^{2}$	$2.6 \cdot 10^{-1}$
Vacuum Energy [13] **/Virtual Particles**	$10^{-\infty} - 10^{+\infty}$	$4 \cdot 10^{3}\ or\ 10^{-\infty} - 6 \cdot 10^{125}$

Table 1 – Constituents of Interstellar Space

The extremely low number density of the interstellar medium constituents useful for propulsion compared to the 10^{19} particles per cubic centimeter at ambient pressure on Earth should explain why conventional spacecraft have to bring their propellant on board and expel it to provide forward momentum. Below is a derivation of Tsiolkovsky's [2] rocket equation which explains how the forward momentum arises from expelling fuel to the back. The existence of a forward force depends on the conservation of momentum.

Equation (1) shows the momentum conservation for a closed system, with mass m and velocity $\boldsymbol{v}$, where an external force $\boldsymbol{F}$ results in a change in momentum over a time step dt:

$$\vec{\boldsymbol{F}} = \frac{d}{dt}(m\vec{\boldsymbol{v}}) \quad . \tag{1}$$

The rocket equation is derived from the conservation of mass and momentum, by considering the system that includes the rocket of mass M and velocity v and its propellant of mass dm and exhaust velocity v_e, a moment of dt seconds after ejection. For this derivation, external influences like drag or gravity are neglected. The closed system is shown in Fig. 1.

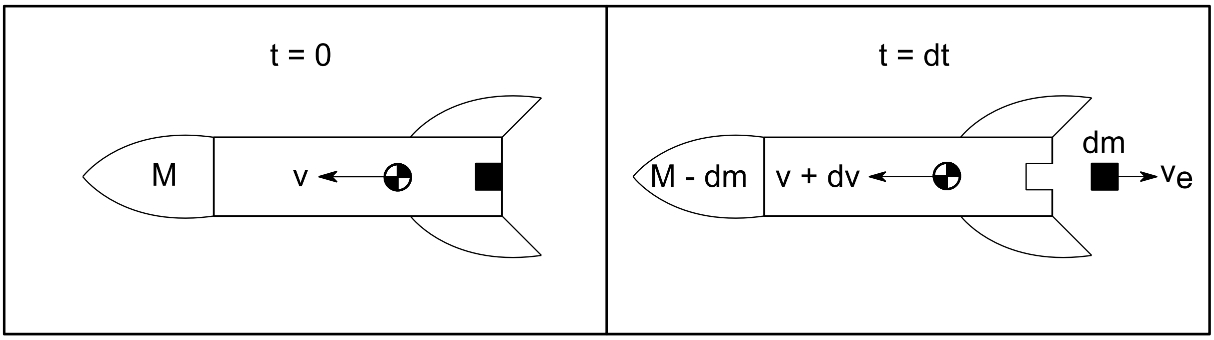

Fig. 1 – Rocket Equation Diagram

The following equality results from the conservation of momentum by considering all parts of the system above in the absence of external forces acting on it, thus, $F = 0$ and

$$0 = (M - dm)(\mathrm{v} + dv) + dm(\mathrm{v} - v_e) - Mv \quad , \tag{2}$$

$$Mdv = -v_e dm \quad . \tag{3}$$

The small, higher-order term $dmdv$ was neglected. The conservation of mass leads to: $dm = -dM$, and the integration of both sides, assuming $v_i = 0$ since the inertial frame is traveling with the rocket, is performed as follows:

$$\int_0^{\Delta\mathrm{v}} \frac{1}{v_e} dv = \int_{M_i}^{M_f} \frac{1}{M} dM \quad . \tag{4}$$

The drag and gravity-free rocket equation is obtained below:

$$\Delta\mathrm{v} = v_e \ln\left(\frac{M_f}{M_i}\right) \quad , \tag{5}$$

whereas the formula for thrust is obtained by considering the momentum conservation of either the vehicle being emptied, or in this case, the ejected propellant separately:

$$\vec{\boldsymbol{F}}dt = v_e dm \quad , \tag{6}$$

$$\vec{\boldsymbol{F}} = v_e \dot{m} \quad . \tag{7}$$

The delta-v (Δv) budgets for different space missions can then be examined to provide a reference for the exceptional requirements for interstellar space missions in terms of energy demand. Typical values have been summarized in Table 2.

Mission	**Δv Budget [m/s]**
East-West Station-Keeping Maneuver	5
Atmospheric Drag Offset	1,200
Orbit Transfer LEO – GEO	3,900
Earth-Mars Transfer	5,594
Slow Interstellar Trip to Proxima Centauri	30,000,000

Table 2 – Typical Delta-V Budgets [5]

Finally, the amount of fuel carried for a typical Earth-Mars transfer mission is obtained for different types of engines using Equation (5) and the exit velocity or specific impulse of these engines. The specific impulse of air-breathing machines is compared to other types of propulsion in Table 3, given in seconds as per Equation (8) below. It is a good indication of the engine's efficiency in terms of the thrust produced per fuel consumption:

$$I_{sp} = \frac{F}{\dot{m}\, g_0} = \frac{V_e}{g_0} \quad . \tag{8}$$

Time requirements in space missions also place a lower limit on the necessary level of thrust, which is dependent again on the mass of the spaceship including the propellant tanks [6]. Table 3 also shows the amount of fuel mass needed for a fictional 1000 metric ton spacecraft to accomplish a one-way rendez-vous mission to Alpha-Centauri in about 40 years, amounting to 30,000 km/s in Δv [1]. The calculations do not take into account relativistic effects, any thrust limitations to provide the required acceleration despite high start masses, or the general engineering feasibility of the propulsion system that includes thermal load management, tank structure, power supply requirements, canalization of the exhaust products, and many more challenges [38].

Engine Type	**Specific Impulse [s]**	**Thrust [N]**	**Exit Velocity [km/s]**	**Fuel Mass [t]**
Air-breathing [4]	1,000–8,000	$<1.6 \cdot 10^5$	0.6	N/A
Chemical Rocket [5]	300–450	$<1.3 \cdot 10^7$	4.4	10^{2914}
FEEP Thruster [5]	8,000–12,000	$10^{-3} - 10^{-6}$	100	10^{133}
Antimatter Rocket [5]	60,000	$\sim 10^2$	600	$5 \cdot 10^{24}$

Table 3 – Specific Impulse and Fuel Consumption for a Slow Interstellar Trip

Thus, an idea to circumvent this type of propulsion regroups solar sails and magnetic sails [39], which use radiation coming from the sun, or beamed propulsion [40], which uses concentrated radiative energy from man-made lasers**.** These propulsion methods also entail certain disadvantages and limitations, such as low thrust efficiency, the need for absurdly large areas of heat-resistant material for the sails to provide significant thrust, and the requirement of proximity to a star or a powerful laser (TW) with great pointing accuracy on Earth [41]**.** Other possibilities for propulsion including warp drives, warp bubbles, and diametric drives might be realizable theoretically, however, the concepts rely on large negative energy densities without the means to generate them [9,13]. Negative energy density and effective mass have been used to explain phenomena such as the Casimir effect [42], however, Forward's idea [10] relies on negative mass that has never been measured directly [43].

Another possibility to provide forward momentum using Newtonian mechanics without having to carry propellant would be to use oscillations in mass. This idea is investigated while examining the conservation of momentum for a device undergoing mass oscillations floating in free space like in Fig. 2. In this figure, two masses m_1 and m_2 are connected by an electromechanical actuator with spring constant k, but it could also be an electromagnetic link.

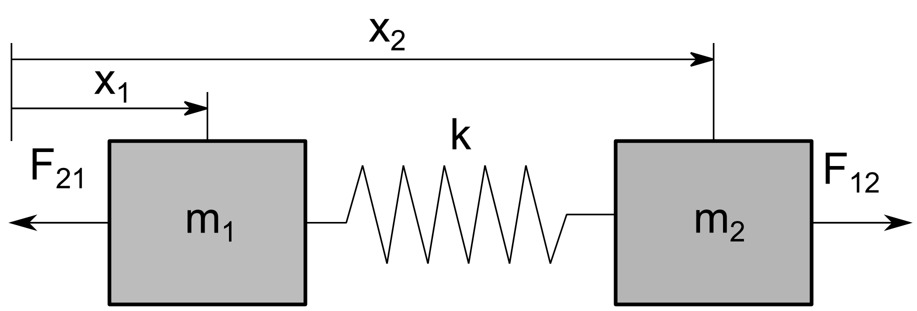

Fig. 2 – Two-Body Interaction [44]

If a force F_{21} is imparted to the actuator to push both masses apart, considering the conservation of momentum used in Equation (1), Newton's action-reaction law results in any case in the following:

$$m_1 \ddot{x}_1 = -m_2 \ddot{x}_2 \quad . \tag{9}$$

If both masses stay constant, the conservation of momentum equation for the system of two masses and a spring without external force yields a trivial solution: the system of masses oscillates about a reference point, but no absolute motion is gained and the momentum is conserved, as shown in Equation (10):

$$\frac{d}{dt}(m\vec{\boldsymbol{v}}) = m_1\ddot{x}_1 + m_2\ddot{x}_2 = 0 \quad . \tag{10}$$

However, if mass m_2 undergoes a transient mass variation by some mechanism, Wanser [44] suggests that the formulation of the conservation of momentum above does not apply to that system. Instead, the more general second law of Newton needs to be considered. Equation (10) becomes:

$$\frac{d}{dt}(m\vec{\boldsymbol{v}}) = \dot{m}_2\dot{x}_2 + m_1\ddot{x}_1 + m_2\ddot{x}_2 \quad , \tag{11}$$

and using Equation (9), Equation (11) becomes:

$$\frac{d}{dt}(m\vec{\boldsymbol{v}}) = \dot{m}_2\dot{x}_2 \quad . \tag{12}$$

Thus, the momentum for the system of the two masses is not conserved. Instead, one must consider that the system of variable masses includes mass transfer in and out of the system, in other words, the two-body problem is not a closed system. Next, the acceleration of the center of mass of such a system is examined, assuming that mass m_2 undergoes a mass fluctuation and $x_2 = 0$, $\dot{m}_1 = 0$ and $\ddot{m}_1 = 0$. The equation for the center of mass is:

$$x_{cm} = \frac{m_1 x_1}{m_1 + m_2} \quad . \tag{13}$$

Differentiating twice with respect to time, and making good use of Equation (9):

$$\ddot{x}_{cm} = \frac{2\dot{m}_2\dot{x}_2}{m_1 + m_2} - \frac{m_1\ddot{m}_2 x_1 - 2\dot{m}_2(m_1\dot{x}_1 + m_2\dot{x}_2)}{(m_1 + m_2)^2} + \frac{2m_1x_1\dot{m}_2^2}{(m_1 + m_2)^3} \quad , \tag{14}$$

Assuming $m_1 \gg m_2$, the equation can be simplified to:

$$\ddot{x}_{cm} = \frac{2\dot{m}_2\dot{x}_2 - \ddot{m}_2 x_1}{m_1} - \frac{\dot{m}_2(m_1\dot{x}_1 + m_2\dot{x}_2 + 2\dot{m}_2 x_1)}{m_1^2} \quad . \tag{15}$$

The derivation shows that if mass oscillations were made possible, a forward acceleration of the whole system is possible. In theory, the specific impulse is infinite, since it depends on a different physical mechanism than the propulsion governed by Tsiolkovsky's equation [2]. The generation of force solely depends on the amount of energy available and the thrust-to-power ratio η_T shown by Equation (16):

$$\eta_T = \frac{F}{P} \quad . \tag{16}$$

The additional requirement for efficient interstellar travel is then to have a thrust-to-power ratio greater than solar or beamed propulsion, which is true only if mass fluctuations can be generated more efficiently than using Einstein's mass-energy relationship $E = mc^2$. This has been promised by Woodward, claiming an observed thrust to power ratio of the order of 0.1 to 10 mN/kW [16] compared to the photon rocket's 3.3 μN/kW. On one hand, Higgins [45] has demonstrated using relativistic considerations that any propellantless space drive with a thrust-to-power ratio greater than a photon rocket would lead to a perpetual motion machine thus, violating the known laws of thermodynamics. On the other hand, Sedwick and White [46] have shown several possibilities for spacedrives to exist without violating energy conservation.

Lastly, the derivation above is only possible if Equation (11) can be used for this variable mass system. However, it is not always the case. In the event of an isotropic mass loss, for instance, the contribution to the forward momentum is known to be zero [47]. Similarly, if the system's mass is lost perpendicularly to the motion, the velocity is not influenced. An example to illustrate this point is by considering a cart full of sand that is traveling on tracks while losing sand through a crack in the cart; its velocity along the tracks is not modified by the falling sand, even though the weight of the cart is gradually reduced. An oscillation in mass, however, could introduce new possibilities and open a path for new theories of physics.

2.2 Mach's Principle

"You are standing in a field looking at the stars. Your arms are resting freely at your side, and you see that the distant stars are not moving. Now start spinning. The stars are whirling around you and your arms are pulled away from your body. Why should your arms be pulled away when the stars are whirling? Why should they be dangling freely when the stars don't move?"

- Steven Weinberg [48]

Mach's Principle is an idea attributed to Ernst Mach that is widely known to have influenced Einstein's development of his General Relativity Theory (GRT), a theory that can be summarized by Equation (17), and the most successful theory in predicting behavior of phenomena on the astronomical scale [49]. The equation shows how the spacetime geometry of the universe, expressed by the Einstein tensor $G_{\mu v}$ on the left-hand side, is shaped by matter as expressed by the stress tensor on the right-hand side $T_{\mu v}$, where G is the universal gravitational constant, c the speed of light, Λ the cosmological constant, $R_{\mu v}$ the Ricci curvature tensor, R the Ricci scalar and $g_{\mu v}$, the metric tensor:

$$G_{\mu v} = R_{\mu v} + \left(\Lambda - \frac{1}{2}R\right) g_{\mu v} = \frac{8\pi G}{c^4} T_{\mu v} \quad . \tag{17}$$

In 1918, Einstein stated his principles of GRT [49]:

"1. The principle of relativity as expressed by general covariance.

2. The principle of equivalence.

3. Mach's principle: … that the $g_{\mu v}$ are completely determined by the mass of bodies, more generally by $T_{\mu v}$".

The first statement requires that the physical laws take the same mathematical form in all coordinate systems. The second statement requires that the gravitational and inertial masses are the same. The third statement involves Mach's Principle and has several definitions and interpretations. One broad statement on Mach's principle from Stephen Hawking [50] is: "local physical laws are determined by the large-scale structure of the universe", whereas Albert Einstein's interpretation of Mach's principle was summarized by "inertia originates in a kind of interaction between bodies", which manifested itself in the Lense-Thirring or frame-dragging effect predicted by Einstein in 1912 [51] and experimentally observed with an uncertainty of 19% by the space experiment Gravity Probe B in 2005 [52]. A list of different interpretations of Mach's Principle was summarized by Bondi et al. based on the literature on General Relativity and is shown in Table 4, giving the reader an appreciation of how inspiring the original thought was and still is [53].

Mach 0	The universe, as represented by the average motion of distant galaxies, does not appear to rotate relative to local inertial frames.
Mach 1	Newton's gravitational constant G is a dynamic field.
Mach 2	An isolated body in otherwise empty space has no inertia.
Mach 3	Local inertial frames are affected by the cosmic motion and distribution of matter.
Mach 4	The universe is spatially closed.
Mach 5	The total energy, angular and linear momentum of the universe are zero.
Mach 6	Inertial mass is affected by the global distribution of matter.
Mach 7	If you take away all matter, there is no more space.
Mach 8	The theory contains no absolute elements.
Mach 9	Overall rigid rotations and translations of a system are unobservable.

Table 4 – Definitions of Mach's Principle [53]

An embodiment of Mach's Principle was provided by Sciama [20], who was puzzled that Einstein's field equations included inertial properties for a single particle in an empty universe, and he showed that local inertia arose from the interaction with distant matter using an electrodynamic analogy to the gravitational field. However, Sciama's theory [54] did not end up passing the test of local invariance. Other theories of gravity have involved a stricter consideration of Mach's Principle, such as the Brans-Dicke theory [55], and the Hoyle-Narlikar [56] theory of gravity, both did not end up being as successful as GRT in predicting astronomical phenomena. The Brans-Dicke's [55] scalar-tensor theory of gravity suggested that the universal gravitational constant actually depended on the distribution of mass in the universe about the point where it is measured. Föppl [57] was also inspired by Mach's Principle and believed that the existence of inertial frames of reference would have observable effects on gyroscopes; his experiments, however, did not demonstrate that effect. Hofmann's [57] ideas also point to a relationship between a rotating body and the surrounding masses to be at the origin of the centrifugal force. Nordtvedt [58] is another physicist claiming that the gravitomagnetic effects observed in nature in the form of orbital motions are a result of Mach's

Principle. Fearn [59] and Rodal [60] recently revisited Hoyle-Narlikar's [61] conformal theory and obtained an expression for inertial induction, or an action-at-a-distance being responsible for the resistance to acceleration. Ultimately, Woodward's[62] derivation is a modern interpretation of Mach's Principle, specifically supported by Sciama's [20] result and the work of others stated above, that provides hope for measurable experimental evidence of mass fluctuations for the use in promising space propulsion. The derivation is examined in the next section.

2.3 Woodward's Mach-effect Theory

"[…] the origin of inertia is and remains the most obscure subject in the theory of particles and fields."

- Abram Pais [49]

2.3.1 Derivation of the Mass Fluctuation Equation

Inspired by Sciama's [20] derivation of the origin of inertia in his paper from 1952, Woodward [62] went on to apply the same principle using a linearized version of Einstein's theory of gravity. His derivation [16] is revisited in full detail below with a few extra steps to lead to the final equation available in the reference material, along with a list of assumptions that are discussed further**.**

1. Consider the acceleration of a small test object with rest mass m_0 by an external force $\vec{F}_{ext}$ in a universe of constant and homogeneous matter density. Newton's laws are applied and the change in momentum $d\overrightarrow{P}$ over time $d\tau$ is obtained:

$$\vec{F} = -m_0\vec{a} = -\vec{F}_{ext} = -\frac{d\overrightarrow{P}}{d\tau} \quad . \tag{18}$$

2. Lorentz invariance is imposed using 4-dimensional vectors (space, time) to ensure correct time-dependence. This is consistent with GRT and the momentum is defined as the four-vector below:

$$\vec{P} = (\gamma m_0 c, \vec{p}) \quad , \tag{19}$$

$$\gamma = \frac{1}{\sqrt{1-\frac{v^2}{c^2}}} \quad . \tag{20}$$

3. Consider the instantaneous rest frame of the object: then $\tau = t$, and $\gamma = 1$, since the velocity v is zero. The change in momentum or four-vector of the inertial force is then:

$$\vec{F} = -\frac{d\overrightarrow{P}}{d\tau} = -\left(c\frac{\partial m_0}{\partial t}, \frac{d\vec{p}}{dt}\right) = -\left(c\frac{\partial m_0}{\partial t}, \vec{f}\right) \quad . \tag{21}$$

4. As the electric field is obtained by dividing the Coulomb force by the charge, the inertial reaction force field $\vec{F}_m$ could be obtained by analogy by dividing the inertial reaction force by the rest mass:

$$\vec{F}_m = \frac{\vec{F}}{m_0} = -\left(\frac{c}{m_0}\frac{\partial m_0}{\partial t}, \vec{f}\right) \quad . \tag{22}$$

5. The denominator and numerator are divided by the volume of the object. The known definition of proper energy density is used from Special Relativity, $E_0 = \rho_0 c^2$.

$$\vec{F}_m = -\left(\frac{c}{\rho_0}\frac{\partial \rho_0}{\partial t}, \vec{f}\right) = -\left(\frac{1}{\rho_0 c}\frac{\partial E_0}{\partial t}, \vec{f}\right) \quad . \tag{23}$$

6. Take the four-divergence of the four-vector inertial reaction force field, and equate it to the local source mass density, as an analogy to the source charge density.

$$\nabla \cdot \vec{F}_m = 4\pi G \rho_0 \quad . \tag{24}$$

Hence follows,

$$\frac{1}{c^2}\frac{\partial}{\partial t}\left(\frac{1}{\rho_0}\frac{\partial E_0}{\partial t}\right) - \nabla \cdot \vec{f} = 4\pi G \rho_0 \quad , \tag{25}$$

$$-\frac{1}{\rho_0 c^2}\frac{\partial^2 E_0}{\partial t^2} + \frac{1}{\rho_0^2 c^2}\frac{\partial \rho_0}{\partial t}\frac{\partial E_0}{\partial t} - \nabla \cdot \vec{f} = 4\pi G \rho_0 \quad . \tag{26}$$

7. $E_0 = \rho_0 c^2$ is used to get time-derivatives of the energy density.

$$-\frac{1}{\rho_0 c^2}\frac{\partial^2 E_0}{\partial t^2} + \left(\frac{1}{\rho_0 c^2}\right)^2 \left(\frac{\partial E_0}{\partial t}\right)^2 - \nabla \cdot \vec{f} = 4\pi G \rho_0 \quad . \tag{27}$$

8. $\vec{f} = -\nabla\emptyset$ is used because $\nabla \times \vec{f} = 0$ for a translational force and acceleration. The negative sign comes from the sign convention of the gravitational potential (force is attractive, and the direction is opposite the gradient of the scalar potential).

$$\nabla^2\emptyset - \frac{1}{\rho_0 c^2}\frac{\partial^2 E_0}{\partial t^2} + \left(\frac{1}{\rho_0 c^2}\right)^2 \left(\frac{\partial E_0}{\partial t}\right)^2 = 4\pi G \rho_0 \quad . \tag{28}$$

9. From Sciama's [20] derivation of the gravitational potential of the universe at a point particle using vector potentials, assuming a smooth, isotropic universe, Minkowskian space, and connection of the particle with the rest of the universe: $c^2 = \emptyset$, is always true where $\emptyset$ is the local gravitational potential, thus $E_0 = \rho_0 c^2 = \rho_0 \emptyset$ [20]. The second term of the LHS of Equation (28) is expanded:

$$-\frac{1}{\rho_0 c^2}\frac{\partial^2 E_0}{\partial t^2} = -\frac{1}{\rho_0 c^2}\frac{\partial}{\partial t}\left(\rho_0\frac{\partial \emptyset}{\partial t} + \emptyset\frac{\partial \rho_0}{\partial t}\right) = \frac{1}{c^2}\frac{\partial^2 \emptyset}{\partial t^2} - \frac{2}{\rho_0 c^2}\frac{\partial \emptyset}{\partial t}\frac{\partial \rho_0}{\partial t} - \frac{\emptyset}{\rho_0 c^2}\frac{\partial^2 \rho_0}{\partial t^2} \quad . \tag{29}$$

10. The third term of the LHS is also expanded:

$$\left(\frac{1}{\rho_0 c^2}\right)^2 \left(\frac{\partial E_0}{\partial t}\right)^2 = \left(\frac{1}{\rho_0 c^2}\right)^2 \left(\rho_0 \frac{\partial \emptyset}{\partial t} + \emptyset \frac{\partial \rho_0}{\partial t}\right)^2$$
$$= \frac{1}{c^4}\left(\frac{\partial \emptyset}{\partial t}\right)^2 + \frac{2\emptyset}{\rho_0 c^4}\frac{\partial \emptyset}{\partial t}\frac{\partial \rho_0}{\partial t} - \left(\frac{\emptyset}{\rho_0 c^2}\right)^2 \left(\frac{\partial \rho_0}{\partial t}\right)^2 \quad . \tag{30}$$

11. Equations 26 and 27 are added together, $\emptyset = c^2$ is used once more; note the two terms that cancel each other and substitute back in Equation (28). A classical wave equation with source terms is obtained:

$$\nabla^2\emptyset - \frac{1}{c^2}\frac{\partial^2\emptyset}{\partial t^2} = 4\pi G\rho_0 + \frac{\emptyset}{\rho_0 c^2}\frac{\partial^2 \rho_0}{\partial t^2} - \left(\frac{\emptyset}{\rho_0 c^2}\right)^2\left(\frac{\partial \rho_0}{\partial t}\right)^2 - \frac{1}{c^4}\left(\frac{\partial \emptyset}{\partial t}\right)^2 \quad . \tag{31}$$

12. Assuming the following form for the wave equation relating mass to its scalar potential,

$$\nabla^2\emptyset - \frac{1}{c^2}\frac{\partial^2\emptyset}{\partial t^2} = 4\pi G\rho_0\big(\rho_0 + \delta\rho_0(t)\big) \quad . \tag{32}$$

13. Neglecting the last term in Equation (31), the expression for the object's mass density fluctuation is obtained. If E_0 is the object's internal energy density, then P_0 is its power density.

$$\delta\rho_0(t) = \frac{1}{4\pi G\rho_0}\frac{\partial^2\rho_0}{\partial t^2} - \frac{1}{4\pi G\rho_0^2}\left(\frac{\partial \rho_0}{\partial t}\right)^2 \quad , \tag{33}$$

$$\delta\rho_0(t) = \frac{1}{4\pi G}\left[\frac{1}{\rho_0 c^2}\frac{\partial^2 E_0}{\partial t^2} - \frac{1}{\rho_0^2 c^4}\left(\frac{\partial E_0}{\partial t}\right)^2\right] \quad , \tag{34}$$

$$\delta\rho_0(t) \approx \frac{1}{4\pi\rho_0 G c^2}\frac{\partial P_0}{\partial t} \quad . \tag{35}$$

Equation (35) is the final Mach-effect equation obtained by Woodward, which was then used to predict mass fluctuations in laboratory experiments. It shows how an object's density can oscillate in time due to the rate of power transfer. The effect also depends on the object's density.

Here are a few assumptions that can be discussed:

a. Newton's laws are applicable, and Newton's universal gravitational constant is defined and valid in this context.

The possibility that Newton's universal gravitational constant is not constant everywhere has been suggested before [55,63,64]. However, Woodward's derivation only requires that the universal constant is locally invariable.

b. Lorentz's invariance is necessary.

This is consistent with GRT since Einstein's principle of covariance requires it.

c. The gravitational field is analogous to the electromagnetic field.

Although this concept was not fully explained by Sciama [20], it has been widely used in the literature and criticized by Williams and Inan [65] as being the opposite of a systematic approach.

d. The inertial reaction force is the action of the gravitational field of the distant matter in the universe on the test particle. Thus, the scalar potential is the gravitational potential at the particle due to the distant matter [20].

This is a very interesting explanation of the nature of inertia and the essence of Sciama's argument [20]. However, he failed in obtaining a tensor solution compatible with Einstein's GRT to support his argument in the subsequent paper [54].

e. The relation $c^2 = \emptyset$ is true for the local gravitational potential.

This equality was derived by Sciama [20] for an asymptotically flat universe. Indeed, it was observed by WMAP [66] that the universe is flat up to a 0.4% margin of error. The meaning of the local gravitational potential has also been discussed recently between Woodward [67] and Rodal [60], and Woodward's explanation seems compatible with Brans' spectator-matter argument [68].

f. E_0 is the object's internal energy density.

According to classical thermodynamics, internal energy is defined as the energy required to bring the internal state of a closed system to a different state [69]. This is an important point, since Woodward also excludes the gravitational potential and kinetic energy of the system as a whole as contributions to mass fluctuations [16].

g. The wave equation was chosen to apply to Equation (32).

Most importantly, Woodward's derivation starts with the assumption that a system is being accelerated, or acted upon by an external force, and it leads to a real, measurable effect. Hence, even if the connection between the mass fluctuation and the accelerating force is not shown explicitly, it is a given (p. 74) [16].

Even if Woodward's derivation presents several weaknesses, there are also alternative derivations for possible mass fluctuations. Tajmar [70] obtained a mass fluctuation from GRT as well, and Fearn [59] obtained a similar result using a theory from Hoyle-Narlikar's conformal gravitation theory. The different derivations all lead to dependencies on the driving frequency. Hence, the experiments examine the existence of any relationship between the effect and the driving frequency.

2.3.2 Design of a Mass Fluctuation Thruster

When considering the simplest form of a device with fluctuating energy, several examples come to mind: a capacitor, a solenoid, a piezoelectric crystal, a microwave oscillator, and many more. The simplest way to measure this effect would be with a balance. However, this balance should be able to measure weight change rates in the order of a few kilohertz, and have an accuracy of a few milligrams to detect the predictions that follow. Furthermore, the balance should be insensitive to vibration, thermal and electromagnetic interaction to eliminate any spurious signal that could be mistaken for a weight change. The energy input to a few common devices is obtained below, to calculate the predicted mass fluctuation.

For a *capacitor*, its electrostatic potential energy is given by the following;

$$E_0 = \frac{CV^2}{2} \quad , \tag{36}$$

where the voltage V is taken to be a sinusoidal function of the form $V_0 \sin(\omega t)$, and C is the capacitance of a plate capacitor. Thus, according to Woodward's formula, expressed with the internal energy E_0,

$$\delta m(t) = \frac{1}{4\pi G c^2 \rho_0} \frac{\partial^2 E_0}{\partial t^2} \quad , \tag{37}$$

the mass fluctuation is given for a capacitor by the expression below:

$$\delta m(t) = \frac{1}{4\pi G c^2 \rho_0} \frac{\partial^2 \left(\frac{C V_0^2 \sin^2 \omega t}{2} \right)}{\partial t^2} \quad , \tag{38}$$

after differentiation, it results in:

$$\delta m(t) = \frac{C \omega^2 V_0^2 \cos(2\omega t)}{4\pi G c^2 \rho_0} \quad . \tag{39}$$

For a *solenoid*, its electrical energy is given by the following:

$$E_0 = \frac{LI^2}{2} \quad , \tag{40}$$

where the current I is taken to be a sinusoidal function of the form $I_0 \cos(\omega t)$ and the inductance of a toroid, for example, given by:

$$L = \frac{\mu_0 \mu_r A N^2}{2\pi r_m} \quad . \tag{41}$$

Thus, according to Woodward's formula (37), the mass fluctuation is given for an inductor by the expression below:

$$\delta m(t) = \frac{1}{4\pi G c^2 \rho_0} \frac{\partial^2 \left(\frac{L I_0^2 \, cos^2 \, \omega t}{2} \right)}{\partial t^2} \quad , \tag{42}$$

after differentiation, results in:

$$\delta m(t) = \frac{-L \omega^2 I_0^2 \sin(2\omega t)}{4\pi G c^2 \rho_0} \quad . \tag{43}$$

For a *piezoelectric stack*, its mechanical energy can be estimated using different approaches. The first approach uses the standard idea of mechanical work:

$$P_0 = Fv \quad , \tag{44}$$

where the velocity is given by the first derivative of the deflection of the piezoelectric actuator due to the induced voltage, $V(t) = V_0 \sin(\omega t)$:

$$x(t) = d_{33} Q \eta V(t) \quad . \tag{45}$$

Note that the deflection amplitude is increased by a factor Q at resonance, which is determined experimentally. Furthermore, this derivation assumes that the head mass is fixed and only considers the displacement of the tail mass. The coupling constant d_{33} was also determined experimentally, and was close to the standard value for the material. The factor η is a clamping factor [71] which reduces the expected displacement because of the counterforce exerted by the load (i.e., the stainless-steel screws connected to the aluminum end caps):

$$\eta = \frac{k_A}{k_A + k_L} \quad , \tag{46}$$

where k_A is the actuator's spring stiffness and considers the piezo-disks, electrodes, and epoxy layers in series to result in 1.2 GN/m, and $k_L$is the load's spring stiffness that consists of the M3 screws, and the aluminum end caps. The stiffness of the load amounts to 0.26 GN/m, which is lower than the actuator's stiffness. Thus,

$$v(\mathrm{t}) = d_{33} \omega Q \eta V_0 \cos(\omega t) \quad , \tag{47}$$

while the force is:

$$F(t) = k_A x(t) \quad , \tag{48}$$

where k_A is the spring constant that includes the screws, epoxy and copper layers, and the end parts. This gives the following mechanical power to the actuator:

$$P_0(t) = \frac{k_A \eta^2 d_{33}^2 \omega Q^2 V_0^2}{2} \sin(2\omega t) \quad , \tag{49}$$

and the following formula for the mass fluctuation:

$$\delta m(t) = \frac{1}{4\pi G c^2 \rho_0} \frac{\partial P_0}{\partial t} \quad , \tag{50}$$

$$\delta m(t) = \frac{k_A \eta^2 d_{33}^2 \omega^2 Q^2 V_0^2 \cos(2\omega t)}{4\pi G c^2 \rho_0} \quad . \tag{51}$$

To transform the mass fluctuation into a thrust force that can be used for space propulsion, Woodward's concept uses an actuator to exploit the mass fluctuation, represented by K in Fig. 3. Furthermore, to produce a non-zero net force, the actuating force needs to act synchronously with the mass fluctuation, with a frequency of 2ω as shown in Equations (39), (43), and (51).

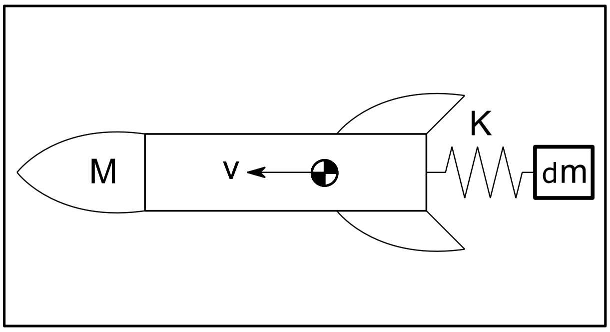

Fig. 3 – Mass Fluctuation Thruster Concept

The actuator selected is a piezoelectric actuator and its actuation is given by the application of voltage V_p:

$$x(t) = d_{33} Q \eta V_p(t) \quad . \tag{52}$$

In combination with a mass fluctuation, using Newton's first law $F = mdv/dt$, considering a variable mass, where averaging over one cycle leaves one term remaining if the actuation and the mass fluctuation operate at the same frequency:

$$F_{avg} = \frac{\omega}{2\pi} \int_0^{\frac{2\pi}{\omega}} \delta m(t) \ddot{x}(t) dt \quad . \tag{53}$$

Averaging over one cycle results in a static force. Thus, in combination with a capacitor, a solenoid, or a piezoelectric device, the thrust force is given by:

$$F_{cap} = \frac{\omega^4 C V_0^2 V_p \eta Q d_{33}}{2\pi G \rho_0 c^2} \cos\varphi \quad , \tag{54}$$

$$F_{ind} = \frac{-\omega^4 L I_0^2 V_p \eta Q d_{33}}{2\pi G \rho_0 c^2} \cos\varphi \quad , \tag{55}$$

$$F_{pzt} = \frac{\omega^4 k_A V_p^3 \eta^3 Q^3 d_{33}^3}{2\pi G \rho_0 c^2} \cos\varphi \quad . \tag{56}$$

where φ is the phase difference between the acceleration and the mass fluctuation at a frequency 2ω. Thus, the maximum force is obtained for a zero-phase difference between the actuation and the mass fluctuation. In Equation (56), the same piezoelectric stack was used for both the mass fluctuation and actuation.

These derivations show how the Mach-Effect theory can lead to measurable forces. As derived by Wanser [44], and shown in Equation (15), this kind of device would theoretically work if the system was free-floating in space, assuming that the mass fluctuations predicted are real. However, do thrust balance experiments reveal the actual force? The next section shows how the forces were measured.

2.4 Woodward-type Experiments

This section is a brief overview of the experiments surrounding the MET experiments, setups and their research parameters, in order to highlight the ambiguities. The first embodiment of the Woodward experiments differed slightly from the modern thruster concept that was analyzed in Section 2.3; it consisted in weighing capacitors as precisely as possible using a force transducer [16]. In the first set of experiments in 1990, different capacitors were weighed as they were charged and discharged to attempt a direct measurement of the mass fluctuation. The concept is shown in Fig. 4, where an AC signal was transmitted at the resonance of the force transducer to amplify the weight signal. The weight change observed was in the order of 30 mg, as shown in Fig. 4, but appeared to be a spurious signal [72]. The beat pattern in the result was most likely produced by driving the power frequency near the mechanical resonance frequency of the transducer and causing vibrations. The effects could also be a consequence of the vibration of the capacitors or electromagnetic interaction (EMI) with the force transducer. The transducer consisted in a diaphragm spring coupled with two Hall-effect probes as position sensors from Unimeasure (U-80), that was encased in a Faraday cage from mu-metal and aluminum.

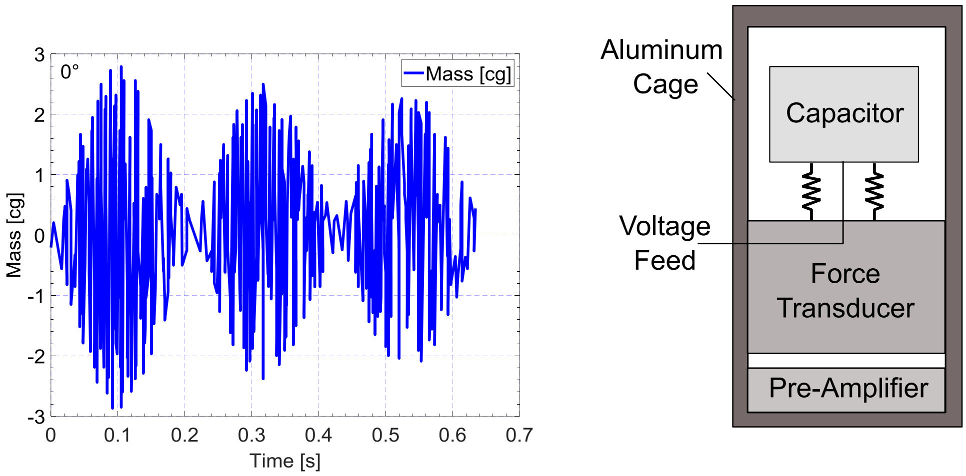

Fig. 4 – Woodward's First Experiments [71]

left: mass measurement vs time | right: sketch of the experimental setup

The next set of experiments combined the mass fluctuation of the capacitors to a multi-layered piezo-ceramic (PZT) actuator as shown conceptually in Fig. 5 to transform the transient mass fluctuation into a stationary force. Again, the device was weighed using the force transducer U-80 [73]. In that setup, phase-dependent interference effects were expected, as well as inductive pickup between the capacitor array and force generator circuits. The new experimental setup is a result of Woodward's theoretical realization that a transient mass shift only occurs in an accelerated system, as explained in Section 2.3.1.

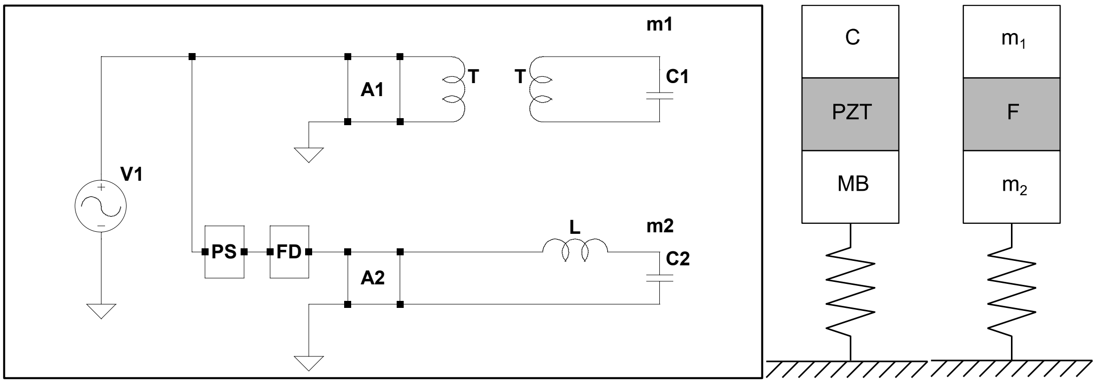

Fig. 5 – Woodward's Second Experiments Setup [74]
left: circuit diagram of the experiment | right: sketches of the experimental concept

The experiments led to the patent design of 1994 [74], where two methods are introduced to produce a mass fluctuation. In Method 1, a weighing mechanism ascertains weight changes by applying an alternating voltage to an array of capacitors (C) while at the same time applying a synchronous pulsed force on the mass block (MB) with a piezoelectric force generator (PZT). In Method 2, a periodic mass fluctuation is generated in a capacitor using an inductive-capacitive (LC) circuit shown in Fig. 5 and a power amplifier. The actuator is driven by a phase shifter (PS) and frequency doubler (FD) that links the signal generator from the LC circuit to the actuator. This way, the actuation can act at the same frequency as the mass fluctuation (2ω). High efficiencies can be obtained in the LC circuit at radio frequencies, the thrust must be pulsed with directed microwave radiation. Experiments were pursued along those lines and the results with Method 1 described in the patent were presented in 1996 [75]. The capacitors have detectable first and second-order electromechanical responses. The relative phase between the PZT actuator and capacitor voltage was varied from 0° to 180°, 90°, and 270° to investigate its relationship with the observed effect. The device was weighed using the same force transducer as in previous experiments. Fig. 6 shows the result of subtracting the different mass measurements when comparing opposite phase shifts.

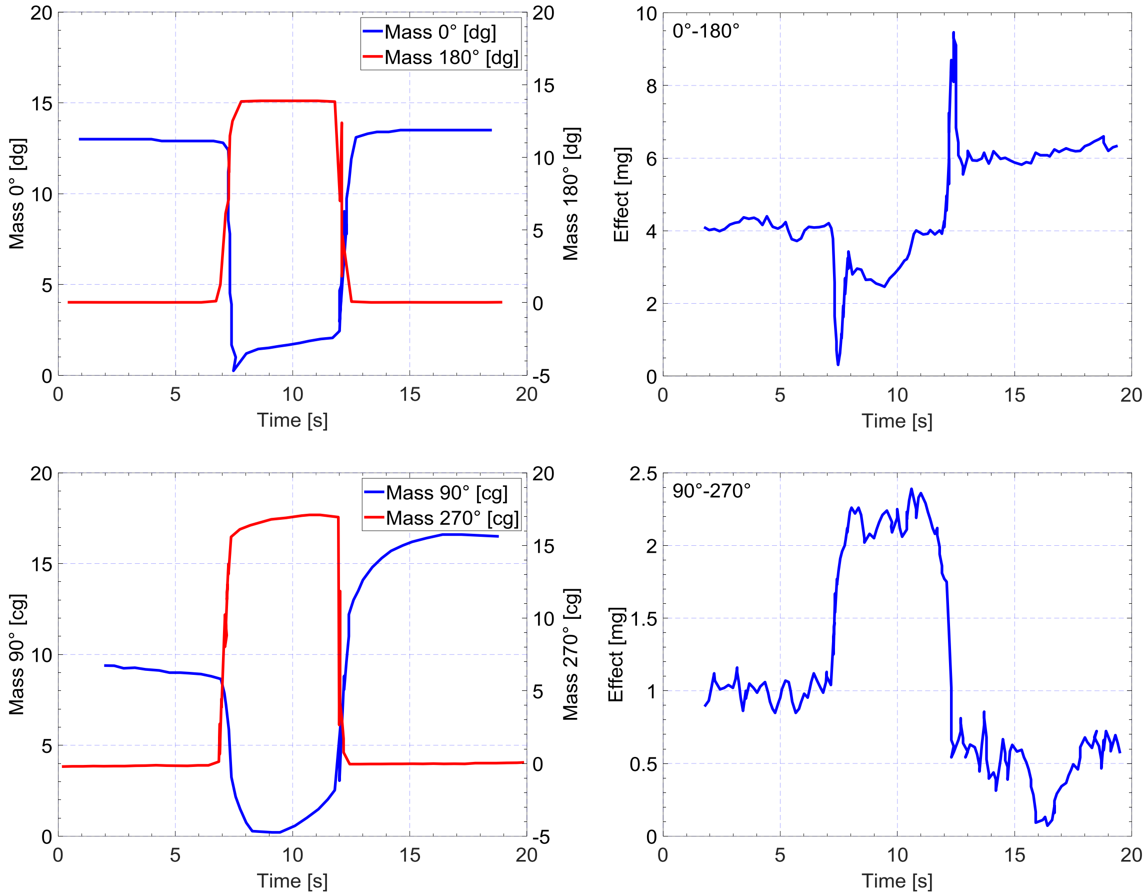

Fig. 6 – Woodward's Second Experiment Results [75]

top left: mass measurements 0° and 180° configurations | top right: net curve

bottom left: mass measurements 90° and 270° configurations | bottom right: net curve

The net curves obtained from the subtraction of two opposite configurations show an effect that is two orders of magnitude lower than the actual weight measurement. The results show the need for a better measurement resolution, since the effect sought is hidden within a larger, nonlinear signal. Moreover, these investigations only evaluated the change in electrostatic energy using capacitors. Efforts using this sort of device were later abandoned in favor of another idea using an inductor and a capacitor wired in series.

The new devices were introduced by Woodward [62] as Mach-Lorentz thrusters and the concept, shown in Fig. 7, uses the Lorentz force produced by the interaction of the capacitor's electric field with the coil's magnetic field to act on the oscillating ions in the capacitor undergoing the mass fluctuation**.** The relative phase between the magnetic and the electric fields could also be varied by having separate circuits for the capacitor and inductor.

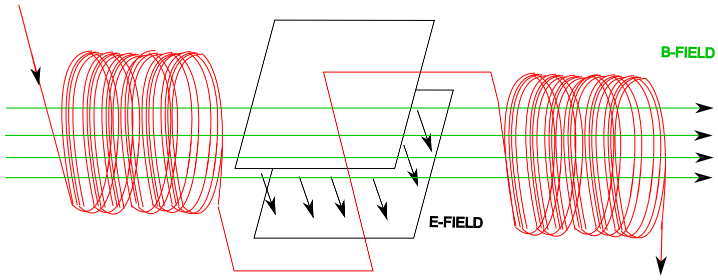

Fig. 7 – Woodward's Mach-Lorenz Thruster Concept [62]

The devices were weighed using the force transducer U-80 once again and a Faraday cage was used to remove the possibility of EMI. However, the signal-to-noise ratio (SNR) shown from the results pictured in Fig. 8 remained very low, contradicting the optimistic conclusion from the paper [62].

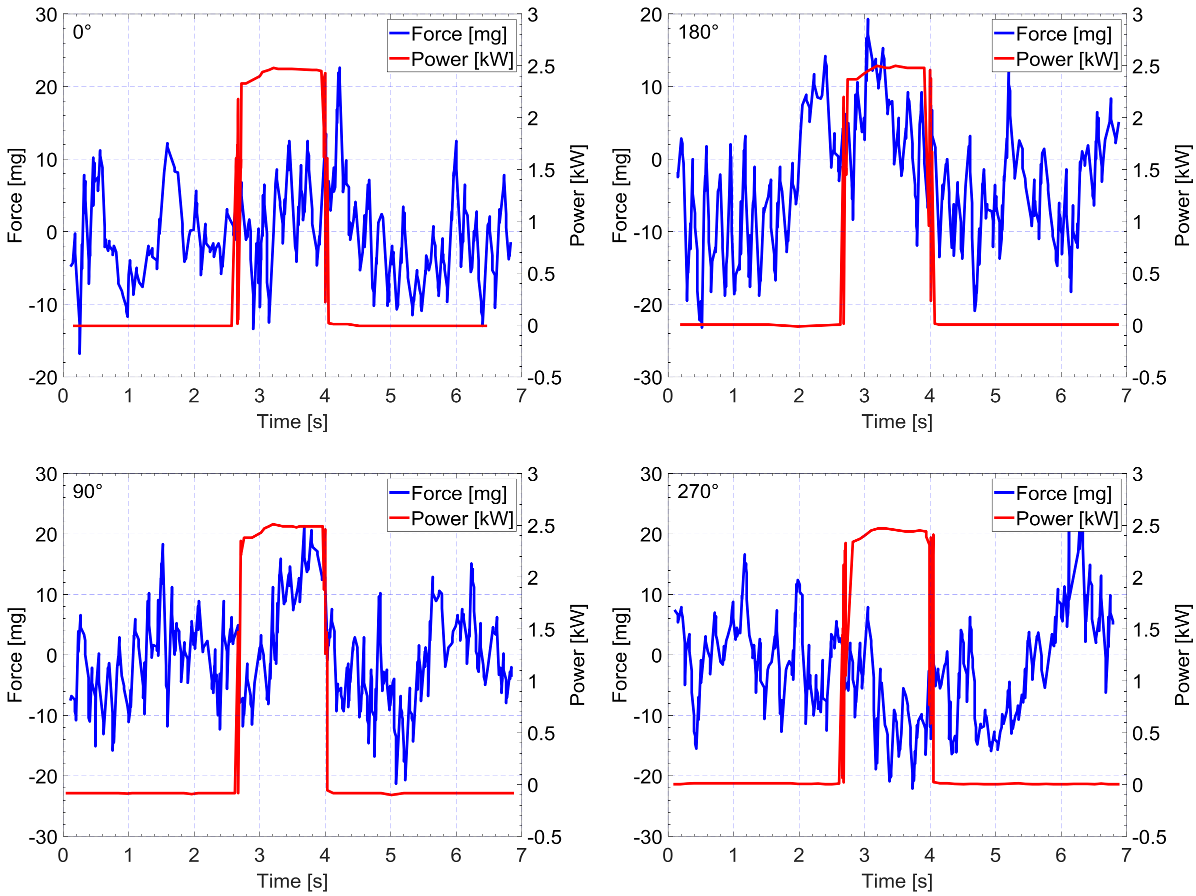

Fig. 8 – Woodward's Mach-Lorentz Experiment Results [62]
top left: 0° configuration force diagram | *top right: 180° configuration force diagram*
bottom left: 90° configuration force diagram | *bottom right: 270° configuration force diagram*

Finally, the publication of 2012 [19] showcased the full torsion balance (TB) setup in a vacuum chamber with clear Plexiglas walls, and the first mention of the MET or Mach-Effect-Assist-Drive (MEGA), marked a significant change with the statement:

"[..] in light of the calculation based on explicit acceleration dependence, it would appear that this other method of calculating Mach effects (using the electrical properties of the system being considered without regards to the details of the accelerations present in the system) is fundamentally flawed and should be avoided".

This demonstrates that the older devices were rejected, and the measurable mass fluctuation should only come from piezoelectric effects. The new device-under-test (DUT) is a multi-layered, pre-stressed piezoelectric actuator sandwiched between two masses. The design is shown in detail in Fig. 9. The thrust balance is a torsion-type balance with a high resolution and low friction as used in the field of electric propulsion [76], relying on low-stiffness C-flex bearings [77]. The TB concept is shown in Fig. 10. Subsequent experiments have all been performed with the same balance and devices of roughly the same design as this one, with a few deviations. The dimensions for the different MET devices are shown later, in Table 7.

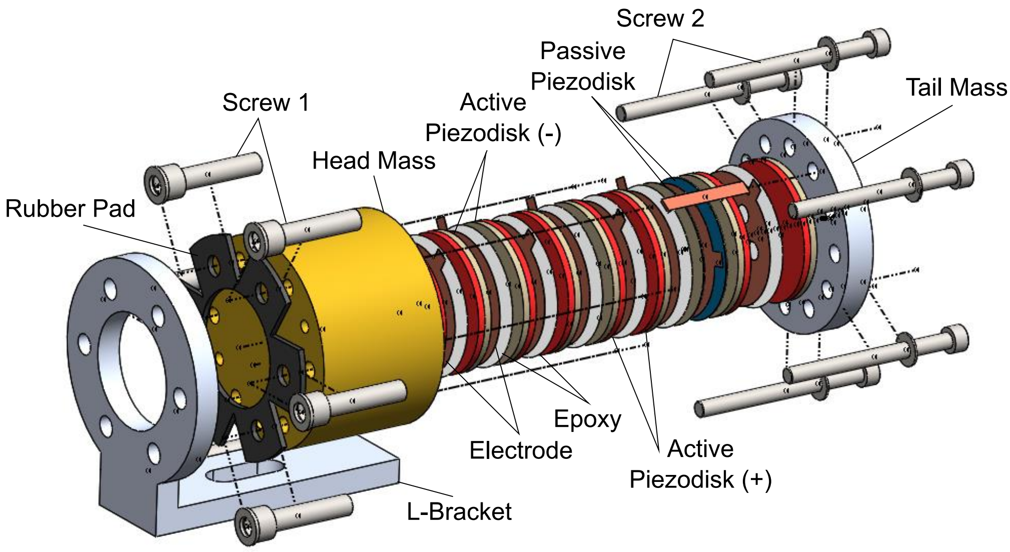

Fig. 9 – Exploded View of the MET

The DUT is placed in a metal box, forming a Faraday cage, which is then connected to a mounting yoke attached to the balance. Cables are run from power amplifiers to the device through the balance pivot using Galinstan contacts to allow free rotation. The DUT is mounted on a "vibration-isolating" yoke that purportedly decouples the device vibration from the balance, the concepts are shown in Fig. 10. A sinusoidal voltage is applied to the piezo-disks that are connected electrically in parallel and mechanically in series using a thin epoxy layer. Copper or brass electrodes between each disk pair provide the perfect electrical connection. A pair of thin, passive piezo-disks is embedded in the stack to provide information about resonances and nonlinearity. The stack is pre-stressed by a set of screws between the head mass (brass) and tail mass (aluminum). The L-bracket serves as the connection to the yoke and experiment box. A rubber pad is placed between the L-bracket and head mass to dampen the vibration transmission. The head mass and bracket are at the same electric potential as one side of the piezo-disks, which are placed in pairs of two with the proper orientation; positive poles are connected together.

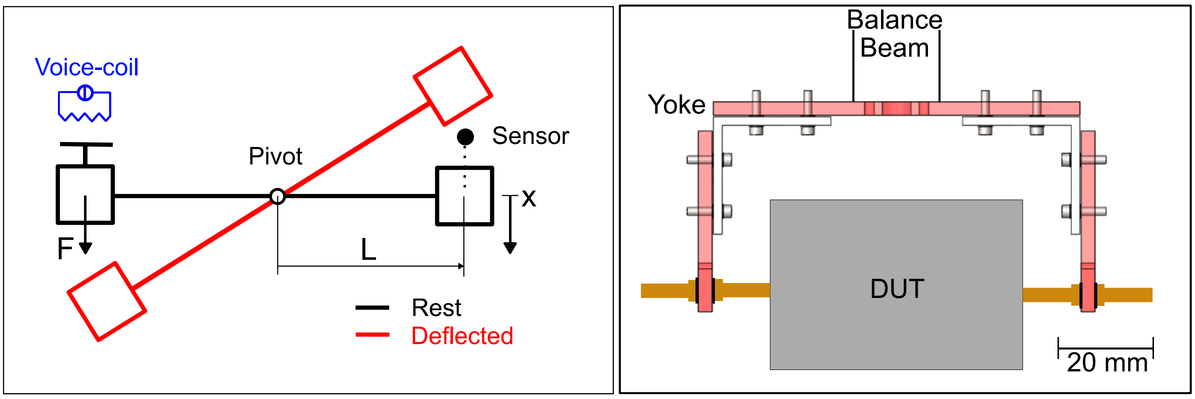

Fig. 10 – Woodward's Experimental Setup [16]
left: Woodward's torsion balance | right: Woodward's mounting yoke

The driving frequency is held constant and chosen to amplify the stationary effect sought. Key results from Woodward's MET experiments are shown in Fig. 11 for different device orientations with respect to the balance, since the yoke can be rotated. The forward orientation is associated with the head mass of the device being on the right when looking from the device to the balance's pivot axis. The thruster's longitudinal axis is perpendicular to the torsion beam and within the torsion plane. The reverse configuration has the thruster being flipped by 180° within the torsion plane. The results were then superposed and subtracted to produce a net curve with visible switching transients and a steady pulse of 2 μN.

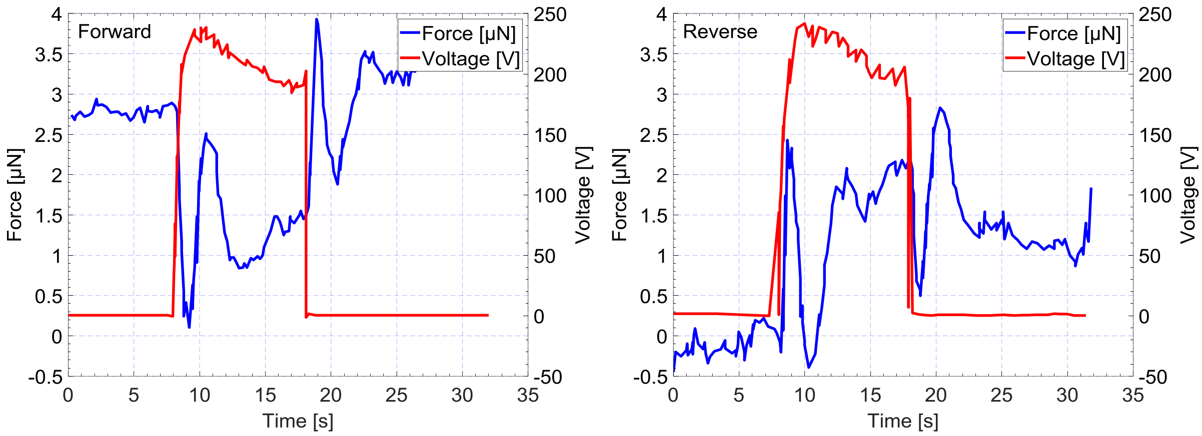

Fig. 11 – Woodward's MET Experiment Results I [19]
left: forward configuration force diagram | right: reverse configuration force diagram

The forces claimed in Woodward's experiments are 10 to 20 μN but no calibration plot is offered [16]. In the new device, lead-zirconium-titanate (PZT) disks act as capacitors by storing energy in their dielectric core as they are polarized, and the variation of energy occurs as the ions in the crystal lattice are accelerated by the changing external field.

The same experiment was repeated with a different amplifier and the net force measured was around 400 nN for the 46 kHz pulse in 2019 [78], shown in Fig. 12. This time, the results of the 90° and 270° configuration were also shown, where the thruster's axis is perpendicular to the torsion plane. The transformers were allegedly critical for the operation of the device.

However, no theory explains the use of the rubber pad and L-bracket shown in Fig. 9, or the transformer used in the electronics. The average of runs was obtained for around 5 runs per graph, as in previous experiments. There is a significant variation in the power input, and the thrust-to-power ratio is around 15 nN/W, compared to the lower limit of 7 nN/W for photon thrusters.

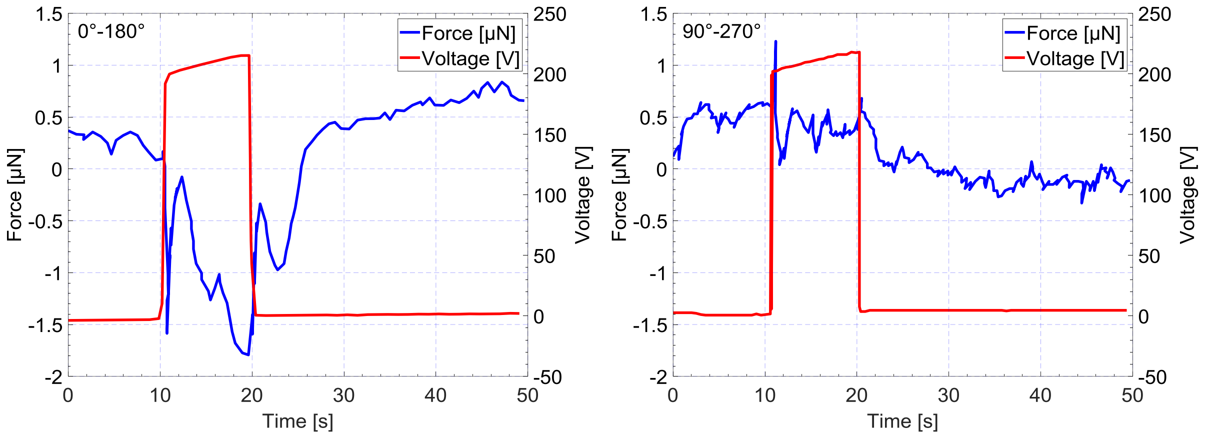

Fig. 12 – Woodward's MET Experiment Results II [78]
left: net force measurement 0°-180° | right: net force measurement 90°-270°

Woodward [16] revealed important conditions that are consistent with the derivation obtained in Section 2.3.1 for the success of the experiment. The thrust comes about by applying a periodic force at the frequency of the mass fluctuations, thus, relying on the piezoelectric device's natural electrostriction. The force and the mass fluctuations need to be in phase to deliver maximum thrust, and if these terms are out of phase, then no thrust would be expected.

Fearn and Woodward [79] also responded to the criticism of their experiments involving vibrational artifacts using the following statement : "the effect cannot be caused by Dean drive vibrations since these could be caused by friction in the bearings of the balance, they would not reverse upon reversing the device, hence they would average to zero and show no net thrust".

The experiments have since been replicated by other researchers. In 2006, Buldrini et al. [80] repeated the Mach-Lorentz experiments on a TB in a vacuum chamber at the Austrian Research Center. With a resolution of about 0.5 μN, thermal artifacts were observed using two different devices with proper electromagnetic shielding, as shown in Fig. 13. With one of the devices, EMI between the balance structure and the twisted cable pair exiting from the outgassing slit appeared to cause a force. Since the same thrust signature was obtained when driving the capacitor in combination with the coil as well as without operating the coil, the thrust was dismissed as an experimental artifact due to inadequate electromagnetic shielding.

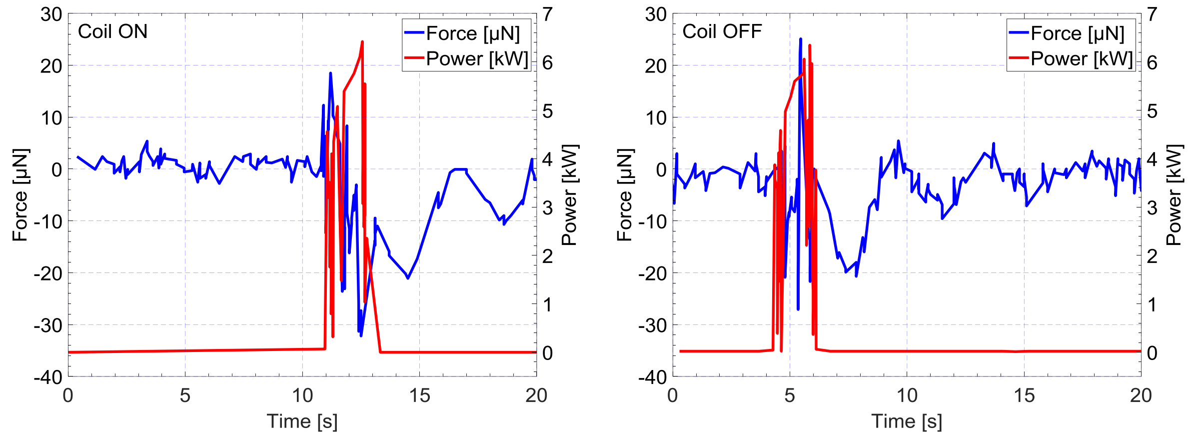

Fig. 13 – Buldrini's Mach-Lorenz Experiment Results [80]

left: force measurement with the active coil | right: force measurement with deactivated coil

Perhaps the strongest evidence for thrust, outside of Woodward, appeared in the experiment from Buldrini [81] at FOTEC, Austria in 2017. In that case, a thrust balance with a much higher resolution than the previous one, about 50 nN, was used to test a MET device from Woodward. The chosen operating frequency of 40 kHz corresponded to the maximum thrust production after having tested the device at different frequency values. In Fig. 14, one sees a clear force profile with three distinct cycles and a maximum steady-force magnitude of 150 nN. Both the amplifier and the step-up transformer had the same specification as the ones used by Woodward. The device had been sent by Woodward in 2014, two years before publication.

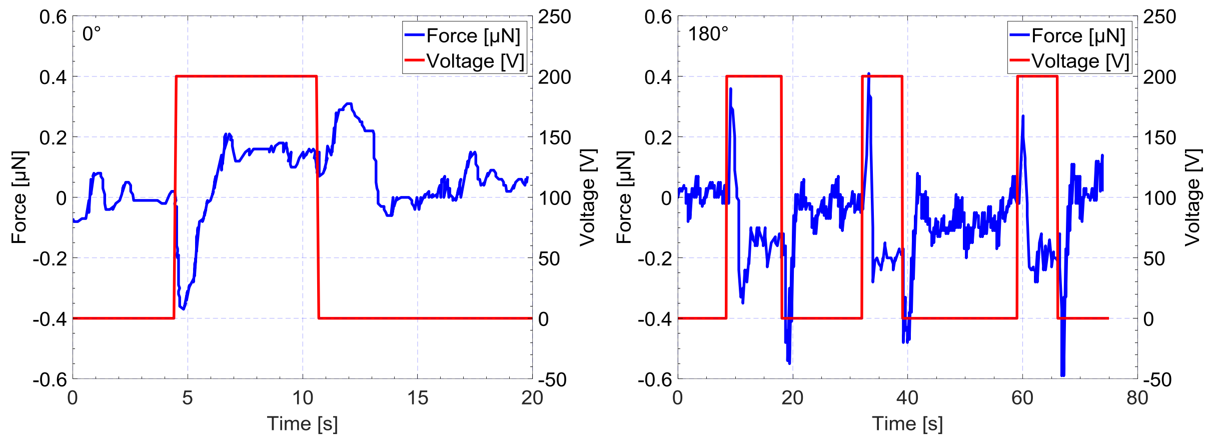

Fig. 14 – Buldrini's MET Experiment Results [81]

left: single pulse 0° configuration | right: multi-pulse 180° configuration

The measurements show repeatable results, with switching transients in the opposite direction when turning the device on and off, as well as a small stationary component. The direction of the force depends on the device's orientation. There are no experiments that show the generation of a stationary force for more than 16 seconds using the MET. Furthermore, the publication does not show the results of tests with the device oriented at 90° to confirm the absence of experimental artifacts. Other researchers[21–23]have attempted these experiments and came up with similar conclusions.

The MET experiments from Woodward's research group [82] have since then continuously been pursued and modified, being financially supported by a NASA Innovative Advanced Concepts Phase II grant, and eventually moved on from the TB experiments to an air sledge, and then to a pendulum tested in the standard atmosphere. The measurements with the pendulum promise hundreds of μN in thrust force with a MET device equipped with a different supporting structure than the L-bracket. However, the investigation of experimental artifacts due to vibration, or the larger thermal, ionization and convective effects at atmospheric pressure with the new pendulum has not yet been as thorough as with the TB experiments.

2.5 Force and Transient Mass Measurements

Precisely measuring mass variations during a process is important for many applications including monitoring chemical reactions, examining surface interactions in material, in experimental and fundamental physics, and, most recently, in space propulsion with the idea of utilizing hypothetical mass fluctuations [83–85]. There exist multiple scale or balance mechanisms that display unique characteristics appropriate to specific weight and force ranges sought; the traditional balance concept consists of the long-arm fulcrum and two weighing pans, but there exist many other types. Today, most laboratory scales [86] used for measuring weight are analytical balances that employ a magnetic voice coil (VC) to counteract the measured mass, shown in Fig. 15, and these offer ultra-precise measurements with a readability as low as 0.1 μg for a maximal load capacity of 2 g, or 0.1 g readability for the high capacity of 70 kg. The current input to the VC is then output as a digital mass readout. For larger forces or pressure measurements, load cells are very versatile as they include hydraulic, pneumatic, piezoelectric, piezoresistive, and strain gauge load cells. Piezoelectric load cells [87,88] depend on the piezoelectric effect and typically have 0.25% in Full-Scale accuracy for a maximum load range spanning 100 N to 10 kN, but for a wide dynamic range, up to several hundred kHz.

In a strain gauge scale, the deflection of a beam on which the unknown mass is placed is measured using an electric conductor with measurable, strain-dependent electrical resistance. For specific force measuring applications like thrust stands for the aerospace sectors, electromechanical balances, typically of the torsion type shown in Fig. 10, are used so that they can be fine-tuned. The TB can have a resolution down to sub-micro-Newtons and have a response time of a few seconds [76,89–91]. The cantilever balance uses the known deflection of a cantilever beam to measure the mass suspended at the end of it. To measure very small masses, a nanocantilever uses a strip of silicon carbide to detect masses as small as one attogram; it uses the dependency of its vibrational frequency on the mass of particles resting on it [92]. A quartz crystal microbalance (QCM) also uses the properties of piezo-crystals, since the resonance frequency of a piezo-crystal highly depends on its mass [85]. Similarly, a tapered element oscillating microbalance (TEOM) can detect aerosol particle deposition by making use of a small vibrating glass tube whose oscillation frequency depends on the number of aerosol particles deposited on it [84]. Superconducting levitation balances allow a force measurement without friction over a 360° rotation with high resolution as well [27,93].

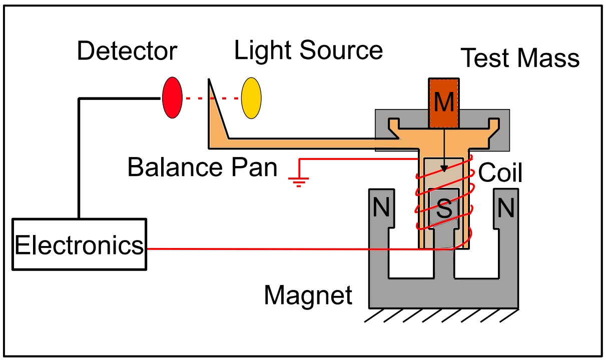

Fig. 15 – Analytical Balance Principle [94]

Table 5 shows an overview of different types of balances with their characteristics:

Balance	**Type**	**Resolution [g]**	**Max. Weight [g]**	**Reaction [s]**
MEMS Resonator [92]	Resonator	10^{-14}	10^{-11}	5
Torsion Thrust Balance [76]	Torsion	10^{-9}	$5 \cdot 10^{2}$	6
Ultra-Micro Lab Balance [86]	Analytical	10^{-7}	2.1	2
Liquid Engine Thrust Stand [89]	Torsion	1	$2 \cdot 10^{3}$	0.01
High Capacity Lab Balance [86]	Analytical	0.1	$7 \cdot 10^{4}$	2
Piezoelectric Load Cell [95]	Load Cell	20	$4.5 \cdot 10^{3}$	10^{-5}

Table 5 – Overview of Balance Types

Finally, a different approach to measuring mass, and one that was investigated during this project, is a centrifugal balance that utilizes rotation and its centrifugal acceleration on the object to determine its mass. It was first proposed by Woodward to measure nanogram mass fluctuations in the kHz range predicted by his Mach-effect theory [96]. Although the balance presents difficulties of calibration and spurious signals, it is possible to apply any desired gain, allowing it to simulate microgravity (<1g_0) to hypergravity (>1g_0), in the direction perpendicular to the rotation, depending on the rotation rate. To detect the mass change using such a setup, strain gauges or piezoelectric load cells can be used. Strain gauges are superior in accuracy, with a linearity of 0.01%, and are perfectly adapted for static forces [88,97]. Both types have a ringing or resonant frequency that limits the application bandwidth, however, piezo-gauges can have a higher resonant frequency because of their high stiffness [98]. Thus, this balance uses a combination of both types of sensors to offer both a high resolution and a large measurement bandwidth.

3. Electromechanical Characterization

3.1 Piezoelectric Actuators

This section examines the design of ultrasonic transducers and their properties. Knowledge of the design characteristics and piezoelectric properties is vital to the understanding of the Woodward devices and experiments.

The piezoelectric effect causes the generation of a voltage when applying pressure to certain crystals. Conversely, the mechanical deformation of those crystals under the application of an external electric field is known as the inverse piezoelectric effect. Both effects are used in many applications including force transducers, energy harvesting devices, high-voltage ignition, and many more [99]. Piezoelectric disks can also be stacked and sandwiched to provide precise displacement and high actuating force as actuators, or good acoustic power transmission as transducers.

3.1.1 Basic Properties

The material properties of polycrystalline piezoelectric crystals relevant to MET experiments are defined using a simple geometry: a solid disk with a coordinate system illustrated in Fig. 16. In this case, the disk is composed of a polycrystalline ceramic such as Lead-Zirconate-Titanate (PZT) and is polarized in the thickness direction (z-axis). The elastic and electric properties of the polarized disk are anisotropic; their values are different along the z-axis when compared to the x- and y-axes. This is due to the asymmetric crystal structure of PZT, the unique domain structure in polycrystalline materials and its orientation along the polarizing electric field [100].

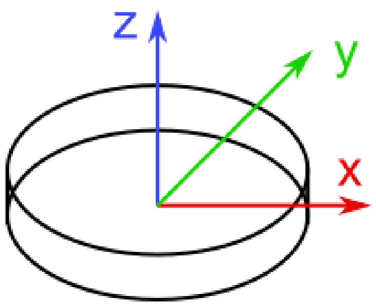

Fig. 16 – Piezoelectric Disk Geometry

The thickness direction is also used interchangeably with direction 3, the y-axis is number 2 and the x-axis is number 1 in the notation.

According to Uchino [100], if the generated stress and electric field are not too large, the mechanical stress T and the dielectric displacement D can be represented by the following linear equations in tensor form. The piezoelectric constitutive equations demonstrate the relation between the electric field E and the mechanical strain S through the piezoelectric coupling constant or matrix $d,$ the equations below use the tensor notation:

$$S_i = s_{ij}^E T_j + d_{mi} E_m \quad , \tag{57}$$

$$D_m = d_{mi} T_i + \varepsilon_{mk}^T E_k \quad . \tag{58}$$

In turn, the dielectric displacement is given by the piezoelectric coupling to the mechanical stress T and the product of the material's dielectric permittivity ε and the electric field. There are a few properties that can be derived from these linear piezoelectric equations.

The *piezoelectric strain constant* d is given by the ratio of the external electric field E to the induced strain and indicates the magnitude of the inverse piezoelectric effect, useful for actuator applications:

$$d = \frac{S}{E} \quad . \tag{59}$$

Conversely, the *piezoelectric voltage constant* g is given by the ratio of the induced electric field E to the external mechanical stress T, to indicate the magnitude of the direct piezoelectric effect. This figure of merit is useful for transducer applications and is also given in relation to the piezoelectric strain constant, using the material's dielectric permittivity ε:

$$g = \frac{E}{T} = \frac{d}{\varepsilon} \quad . \tag{60}$$

The *electromechanical coupling* factor k is given as a ratio of the stored mechanical energy to the input electrical energy for actuators or as a ratio of the stored electrical energy to the input mechanical energy for transducers:

$$k = \sqrt{d^2/\varepsilon s} \quad . \tag{61}$$

The mechanical properties include the *stiffness* Y of the material and its *compliance* s, which relate the induced strain to the applied stress or vice-versa:

$$Y = \frac{1}{s} = \frac{T}{S} \quad . \tag{62}$$

When applying an external electric field to the piezoelectric specimen, its displacement response amplitude reaches maximum at resonance (or series resonance), and minimum amplitude at anti-resonance (or parallel resonance). The *resonance frequency* is determined by the specific vibration mode. For a solid disk, the simplest resonance modes consist of the first radial and longitudinal modes. The longitudinal, or thickness, resonance frequency is calculated using the following equation:

$$\omega_T = \frac{2\pi}{L}\sqrt{\frac{Y}{\rho}} \quad . \tag{63}$$

The resonance frequency can also be calculated using the frequency coefficient in the thickness- and radial modes, if the *frequency numbers* are known beforehand:

$$\omega_T = \frac{2\pi N_T}{t} \quad . \tag{64}$$

$$\omega_R = \frac{2\pi N_R}{D} \quad . \tag{65}$$

The *mechanical quality factor* or simply, *Q-factor*, characterizes the sharpness and intensity of an electromechanical resonance, for example in a power spectrum where a system's response to an input signal with constant amplitude over a broad frequency range is obtained. The *Q-factor* is calculated according to the equation below:

$$Q_M = \omega_0/2\Delta\omega \quad . \tag{66}$$

The frequency bandwidth $\Delta\omega$ is the half-power bandwidth measured using the 3-dB rule. The peaks of the power spectrum correspond to a resonance, and the sharpness of the peak indicates a higher Q-factor according to Equation (66). It also determines the strain amplification at resonance, since the maximum strain is the product of the strain under normal circumstances and the quality factor [100]. In Equation (67), the piezoelectric strain constant is the matrix element d_{33} for the coupling of strain and the electric field along the polarized, longitudinal direction, in this case d_{ZZ}:

$$S = Q_M d_{33} E \quad . \tag{67}$$

The inverse of the quality factor represents the tangent loss or damping, which is proportional to the amount of heat generated when the actuator is driven at resonance:

$$1/Q_M = tan\ \delta_m \quad . \tag{68}$$

Piezoelectric materials suffer energy loss in the form of heat during stress cycles in a process called hysteresis. This property is best described using a diagram or butterfly curve representing the relationship between strain S and induced electric field E. In Fig. 17, the path is explained as follows: point A is right after ceramic sintering where no mechanical stress is present, and mechanical strain can then be observed when applying an electric field until saturation at point B. Reducing the electric field to zero shows the remanent strain in the material. Reducing the electric field further until the coercive field E_c at point D would reverse the polarization of the material. The difference between the paths BD and GB or between the paths GE and ED is due to frictional losses and thus, the larger the area of the butterfly wings the greater the hysteresis in the material. There are three loss origins in piezoelectric materials: dielectric, elastic, and piezoelectric losses. Domain wall motions contribute to extensive losses. According to Uchino, heat generation at off-resonance is attributed mainly to intensive dielectric loss, while heat generation at resonance originates mainly from intensive mechanical loss [101]. Intensive parameters are T and E, induced mechanical stress, and induced electric field. Extensive parameters are S and D , resulting in mechanical strain and polarity displacement. Extensive losses are due to domain wall motions [100].

The *Curie temperature* is a material's phase transition temperature, above which its piezoelectric properties disappear. Thus, the piezoelectric material should not be heated to reach its Curie temperature during the operation.

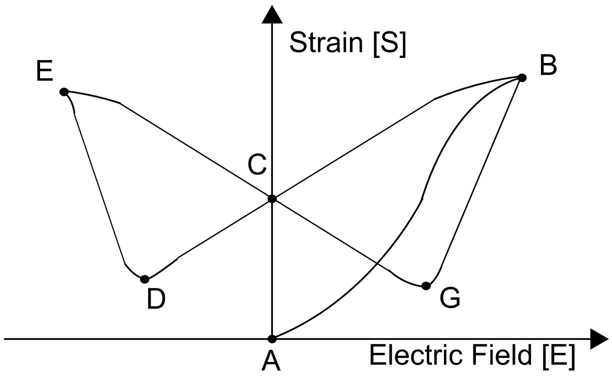

Fig. 17 – Butterfly Curve [101]

Referring to Fig. 17, since the path CD is shorter than the path CB, most actuator applications introduce a DC bias to use the full electric field range without approaching the coercive field. So far, most properties were obtained from the linear piezoelectric equations. However, there are several non-linear parameters as well. The constitutive piezoelectric equations around the pre-stressed static state were described by Guyomar et al. [102]. The equations derived from thermodynamic relations to reflect the experimental observations observed under high power driving conditions show that there can be nonlinearity in the mechanical, dielectric, and piezoelectric coupling coefficients, represented by $\alpha,\ \beta$ and γ respectively. Hence, second harmonic signals result from the quadratic relationship between the stress and polarity displacement to the induced fields:

$$T = T_0 + sS - eE + \frac{\alpha S^2}{2} + \frac{\beta E^2}{2} - \gamma SE \quad , \tag{69}$$

$$D = D_0 + eS + \varepsilon E + \frac{\gamma S^2}{2} + \frac{\delta E^2}{2} - \beta SE \quad . \tag{70}$$

Electrostriction is a secondary electromechanical coupling observed in all dielectrics and insulators that are not affected by hysteresis or aging [100]. In electrostriction, strain is generated in proportion to the square of the electric field. In the Lead-Zirconate-Titanate system, electrostriction only corresponds to a very small fraction of the nonlinearity [103]. Table 6 lists the different properties mentioned for various piezo-materials. It is important to note that electrostriction is very small in comparison to the piezoelectric effect as well as other nonlinearity for most piezoelectric material. The values of the electrostriction coefficients were obtained from Li et al. [104] and converted to the appropriate units by using the respective electric permittivity values. Other nonlinear effects most likely result in greater distortions of the actuator's operation than the electrostriction [105]. These properties were used in the FEM and thrust force prediction.

Material	**PZT5H** [100]	**PZT4** [100]	**PIC155** [106]	**PIC255** [106]	**PIC181** [106]	**PMN-PT** [100]	**SM111** [107]	**SM211** [107]
Density [kg/cm³]	7.5	7.5	7.75	7.8	7.85	8.2	7.9	7.8
Curie Temperature [°C]	193	325	340	350	330	150	320	165
Dielectric Coefficient $[\varepsilon_{33}/\varepsilon_0]$	3400	1300	1550	1850	1100	6000	1400	5400
Dielectric loss, $\tan\delta$	2	0.4	0.25	0.2	0.05	0.01	0.4	3
Coupling constant, k_p	0.65	0.58	0.62	0.62	0.56	0.9	0.58	0.67
Piezoelectric constant, d_{33} $[10^{-12}\ m/V]$	593	285	360	400	265	2750	320	650
Voltage constant, g_{33} $[10^{-3}\ Vm/N]$	19.7	24.9	27	25	25	34.7	25	13.6
Elastic Compliance, s_{33}^E $[10^{-12}\ m^2/N]$	16.4	12.2	19.7	20.7	14.2	57.7	13.7	19.6
Mechanical Quality Factor, Q_M	65	500	80	80	2000	–	1800	60
Electrostrictive Coefficient [105] $[10^{-18}\ m^2/V^2]$	9	1.3	1.9	1.9	2.7	158	1.5	22.9

Table 6 – Piezoelectric Material Properties

3.1.2 Actuator Design

An overview of the main design parameters, operational limitations, and performance parameters is given here using the properties defined in Section 3.1.1. The typical geometry of the Langevin ultrasonic transducer, or a pre-stressed, multi-layer, piezoelectric stack actuator is shown in Fig. 18. The important elements include the central bolt or screw, the piezo disks, which are connected electrically in parallel and mechanically in series, and the head and tail masses. The stack actuator, with total length L, is placed under pre-load by the central bolt, with length L_b, screwed in the head mass to keep the ceramic disks, length L_c, under compression since their tensile strength is much lower than their compressive strength.

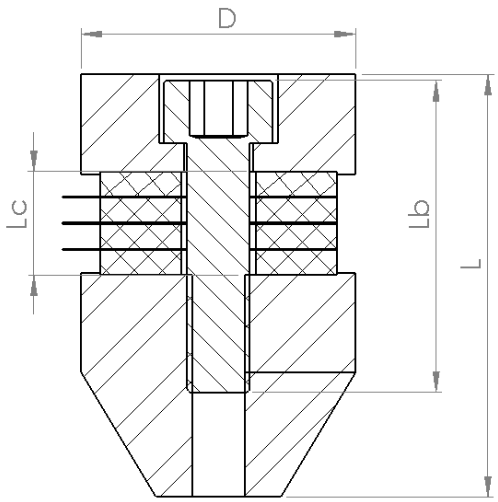

Fig. 18 – Langevin Transducer Geometry [108]

A few key points of the transducer design procedure from Abdullah et al. [108] are introduced here with consistent notation. First, the average acoustic power can be related to the oscillatory stress amplitude in the ceramic, $T_{c,0}$, where c_c is here the sound velocity in the material, μ_0 the vibration amplitude, ω the driving frequency, A_c the cross-sectional area:

$$P = \frac{1}{2\mathrm{Y_c}} T_0^2 c_c A_c \quad , \tag{71}$$

$$T_0 = Y_c \mu_0 \omega / c_c \quad . \tag{72}$$

The maximum fatigue stress limits in the ceramic and the bolt, $T_{f,c}$, $T_{f,b}$ set the rest of the material properties. Considering a safety factor β, the maximum allowable stresses are:

$$T_{c,max} \leq T_f/\beta \quad , \tag{73}$$

$$T_{b,max} = \frac{A_c T_{p,c}}{A_b} + 2T_{b,0} \leq T_{f,b}/\beta \quad , \tag{74}$$

where A_b is the cross-sectional area of the bolt, $T_{p,c}$ is the pre-load stress in the ceramic and $T_{b,0}$ is the oscillatory stress amplitude in the bolt.

The displacement amplitude is given below, where n is the number of ceramic disks:

$$\mu_0 = \frac{nd_{33}V_0}{2} Q_m \quad . \tag{75}$$

The resonance frequency ω_0 is selected to determine the total length L_T and the diameters of the individual parts, D_i, using certain criteria to avoid interfering with shear or lateral resonances by considering the sound wavelength in individual parts λ_i:

$$L_T = \lambda/2 = \mathrm{c}/2\pi\omega_0 \quad , \tag{76}$$

$$\frac{\lambda_i}{D_i} < 2 \quad . \tag{77}$$

The maximum stress in the PZT ceramic is determined using Equation (78):

$$T_{c,max} = nY_c \frac{\omega}{2c_c} Q_m d_{33} V_{max} \quad . \tag{78}$$

Using the same notation, but considering the actuator as a spring fixed at one end, the oscillation of the stack actuator can be described using Equation (79) in the quasi-static regime, and without pre-load, where k_A is the stiffness of the stack and F the vibration force:

$$\mu_0 = F/k_A \quad . \tag{79}$$

However, with a bolt pre-load with high stiffness k_L, the relation changes to Equation (80), in the quasi-static regime, meaning at low frequencies (<1 kHz):

$$\mu_1 = \mu_0 \left(\frac{k_A}{k_A + k_L}\right) \quad . \tag{80}$$

The relationships are illustrated in Fig. 19 [71,109]:

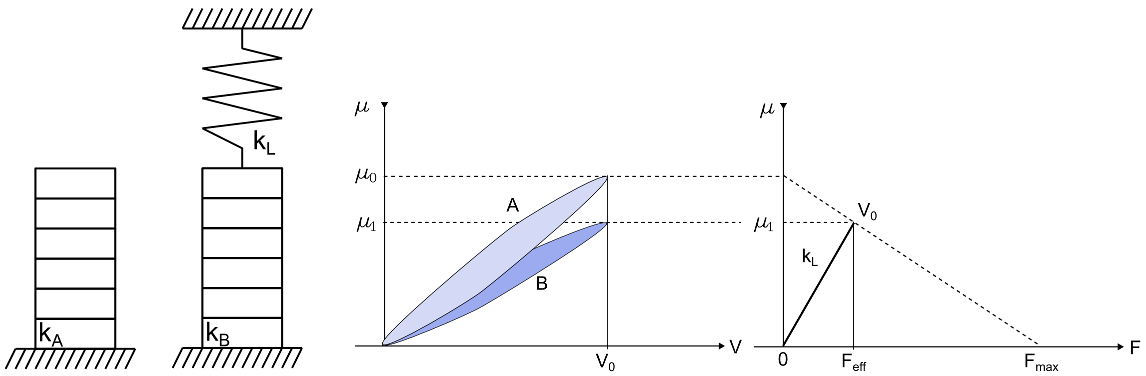

Fig. 19 – Comparison of Loaded and Unloaded Stacks [71]
left: sketch of unloaded and load stacks | middle: elongation vs voltage
right: elongation vs force

An improved design should also consider the length of the bolt and the length of the thread, to avoid parasitic resonances [110]. Furthermore, the appropriate selection of end cap materials is made by considering impedance matching to prevent acoustic power transmission loss [108]. These properties are used in the thrust force prediction and referred to in Section 3.1.9., they were also used in the design of CD05, introduced later for the centrifugal balance experiments in Section 5.1.2.

3.1.3 Mach-effect Thruster Devices

The MET design is based on the Langevin-type ultrasonic transducer. The individual devices all follow the same model and there are very few differences in the material selection and dimensions. The thickness of each part has an influence on the longitudinal resonance of the device and the aluminum L-bracket is related to a particular bending mode. More important is the fact that the PZT disks are subjected to a different number of stress cycles, and have been manufactured using a process that can result in up to 20% discrepancy [107] in the properties described in Table 6. This deviation can lead to great offsets in the resonance frequencies and electromechanical behavior.

The MET are described according to Fig. 20, and the dimensions for all the devices used are summarized in Table 7. Missing from the table is the presence of a pair of passive piezo-disks of SM211 material with 0.3 mm thickness in all devices, except MET04, towards the end of the stack. Woodward calls that pair of disks the “accelerometer”, which can be used as a transducer to provide qualitative information about the vibration in the stack [16]. Between each piezo-disk are 50 µm-thick brass electrodes and a thin layer of epoxy (≈50 µm), except MET04, which had 100 µm-thick copper electrodes. The stacks were coated in epoxy made from Epon 815C and Versamid 140, with the exception of MET04, which was coated with heat-insulating epoxy from Loctite. Pictures of the devices can be found in Appendix A.

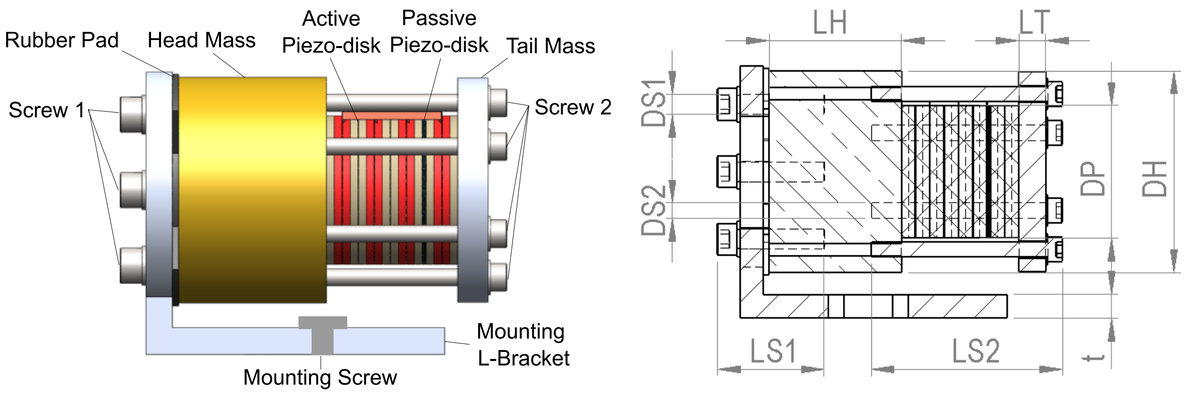

Fig. 20 – MET Schematic

left: MET CAD side view with annotation | right: CAD MET drawing cross-section

Device	PZT	L_H	D_H	L_T	D_P	L_{S1}	D_{S1}	L_{S2}	D_{S2}	t_B
MET01	SM111	9.5	28.7	4.3	19	40.5	2.8	–	–	1.7
MET02	SM111	19	28.3	3.9	19	18.5	2.8	39.5	2.2	3.2
MET03	SM111	19	28.3	3.9	19	18.5	2.8	39.5	2.2	3.2
MET04	PIC181	19	29.0	4.0	20	13.0	3.0	33.0	3.0	3.0
MET05	SM111	19	28.5	4.7	19	15.0	2.9	39.5	2.3	3.1
MET06	SM111	19	28.5	4.7	19	15.0	2.9	39.5	2.3	3.1

**dimensions in mm*

Table 7 – MET Properties

3.1.4 Magnetostrictive Actuator

CU18A is an actuator based on the magnetostrictive properties of Terfenol-D [111]. As for piezoelectric materials, where the material domains get reoriented by the application of an electric field, the magnetic material domains of a magnetostrictive material get reorganized under the application of a magnetic field. Using magnetostriction, high strains can be achieved with relatively low losses through hysteresis. Table 8 compares a few properties of magnetostrictive and piezoelectric materials.

Material	Effect	Coupling Constant	Hysteresis [%]	Elongation [%]	Energy [kJ/m^3]	Curie [°C] Temperature
PZT4 [100]	Piezoelectric	0.32 $[\mathrm{n}m/V]$	10	0.1	2.5	320
Terfenol-D [112]	Magnetostrictive	20 $[nm/A]$	2	0.2	0.02	650

Table 8 – Comparison of Magnetostriction Properties

Fig. 21 shows a picture of CU18A, purchased from Etrema [111]. The magnetic field is induced by a current applied to a coil wrapped around the Terfenol-D rod. A mass can be attached to the mounting guide and can be shaken by the magnetostrictive rod through a mechanical connection of Belleville springs. This type of spring was invented to provide high stiffness and fatigue resistance [113]**.** There are secondary and nonlinear processes occurring in magnetostrictive actuation as well, including electrostriction [114]. Thus, this model is very similar to the MET in the sense that a tail mass is excited using a sinusoidal function and a coupling between linear and nonlinear processes can be present. In this case, the power is greater, and the vibration amplitude is as well.

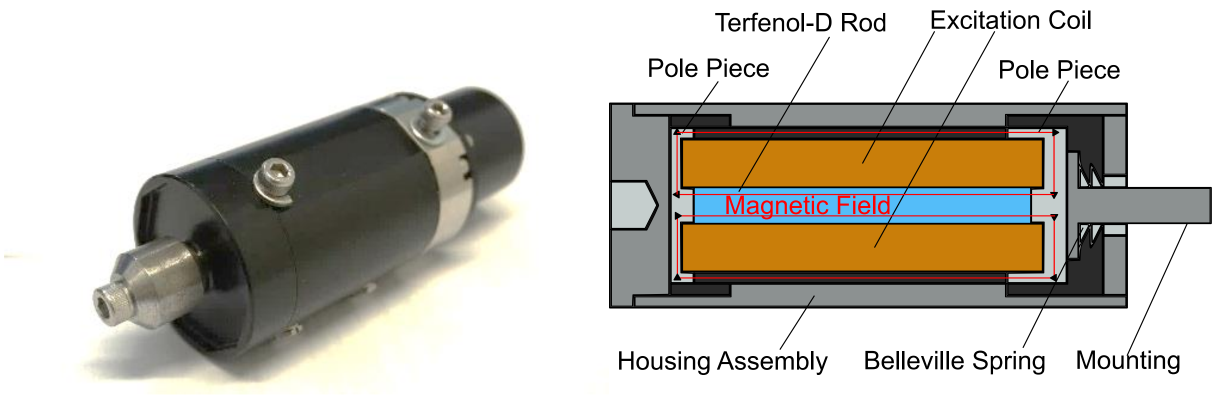

Fig. 21 – CU18A Picture and Magnetostrictive Actuator Design [115]
left: CU18A picture | right: magnetostrictive actuator design concept

3.1.5 Numerical Analysis of MET Behavior

This section describes the FEM performed with ANSYS Workbench and the Piezo-Mems 2021 extension for a qualitative analysis of the MET under the application of an oscillating electric field. The simulation includes the mechanical properties of the aluminum L-bracket, the stainless-steel screws, the aluminum and brass masses, and the rubber pad, as well as the electromechanical properties of the piezoelectric disks. The simplified geometry used in the model can be seen in Fig. 22.

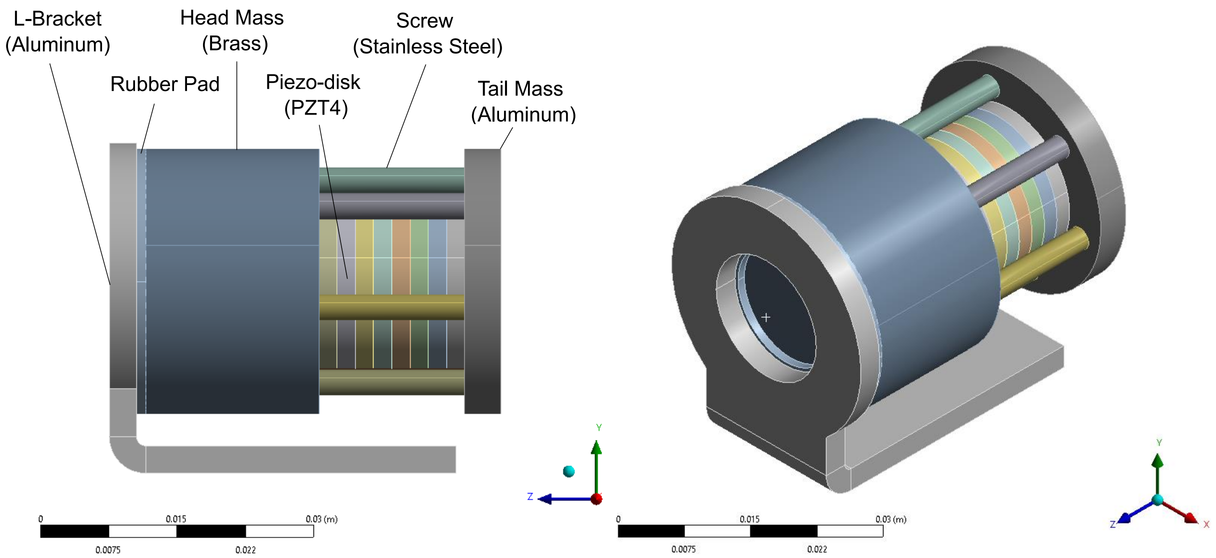

Fig. 22 – MET FEM Geometry

The analysis started with a 3D Computer-Aided-Design (CAD) model generated in Solidworks that could be directly implemented in ANSYS. Adapting the geometry included removing screw heads, holes, threads, and is recommended for easier meshing and more accurate calculations. Then, the material properties were defined using isotropic relations for metals and anisotropic elasticity matrices for the piezoelectric disks. The viscoelastic coefficients of the rubber pad were obtained from tensile tests performed at the Leibniz Institute for Polymer Research in Dresden. The experimental data took the form of loss tangents versus frequency and temperature. Next, using a good balance of coarse meshing for larger parts of the assembly and finer meshing for areas of importance such as the interface between screws and end caps could optimize the speed of conversion and accuracy. The boundary conditions included the fixed support, selected as the lower face of the L-bracket, the voltage on the electrodes in the stack applied to the positive poles of the disks. The contacts between the different parts were assumed to be fully bonded, instead of using threaded connections. The piezoelectric behavior of the disks was made possible using special solid elements that integrate the linear, piezoelectric constitutive equations in the PiezoMems extension. The solution parameters using the mechanical solver were selected to give the vibration modes and resonance displacements for a frequency range that is similar to the frequency sweep in the experiments. Finally, different solution methods were examined for comparison, and an iterative process was necessary to adapt the meshing and boundary conditions.

The density and isotropic elastic properties of aluminum, stainless steel and brass were taken from the material database available in ANSYS. However, the piezoelectric coupling, anisotropic compliance and anisotropic relative permittivity matrices had to be specified for the Z-poled PZT4 material [116]. Starting with Workbench 2022 the property matrices could be input in the IEEE format. The relative permittivity matrix was obtained for constant stress, and the compliance for constant electric field according to the strain-charge form.

The meshing was optimized after a few iterations and is shown in Fig. 23. the main meshing parameters are summarized in Table 9.

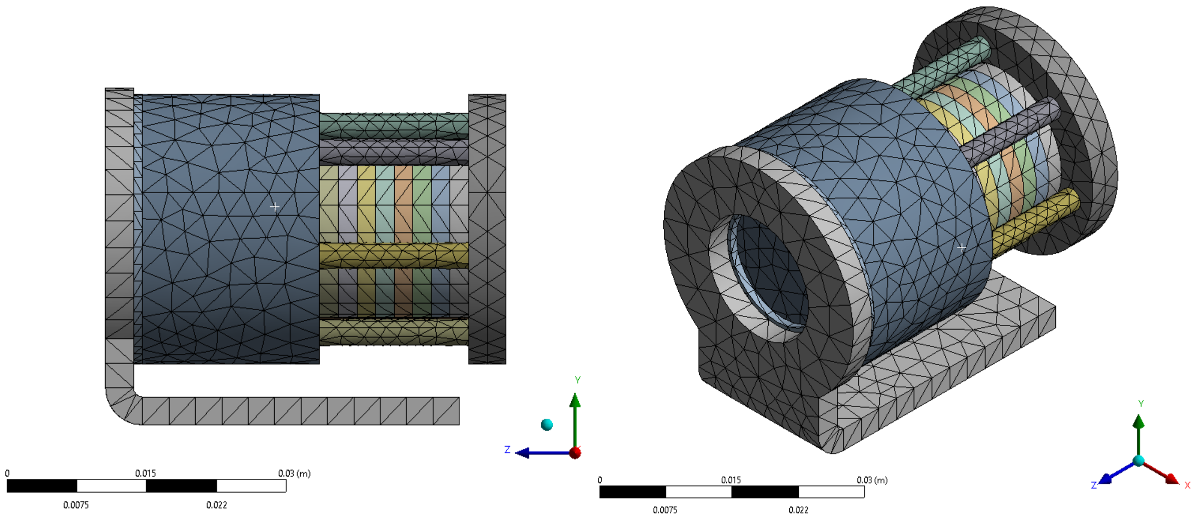

Fig. 23 – MET FE Geometry & Meshing

Meshing Quality	Element Type	Min. Element Size [mm]	Nodes	Elements
Middle	Tetrahedral	1.0	16,508	8,972

Table 9 – Meshing Parameters

The boundary conditions for the analysis consist in fixing the nodes of the bottom surface of the L-bracket, then applying a potential difference on the whole area of the electrodes between the piezoelectric disks, equivalent to 100 V. The modal and harmonic response analysis generate the solutions using the mechanical solver over a frequency range of 20 to 100 kHz. The modal, superposition mode, and full solutions were obtained for over 200 data sets. The solution is presented in Fig. 24 as absolute specific nodal displacements in the z-direction exclusively, over frequency for a fixed driving voltage. The observed displacements are the displacements of the nodes on the outer surface of the tail mass (aluminum), as well as the displacement of the head mass (brass). The phase diagram shows that the head and tail masses move opposite to each other over the entire frequency range with a few exceptions linked to some parasitic modes of the screws and numerical artifacts – shown by the many distortions at higher frequencies.

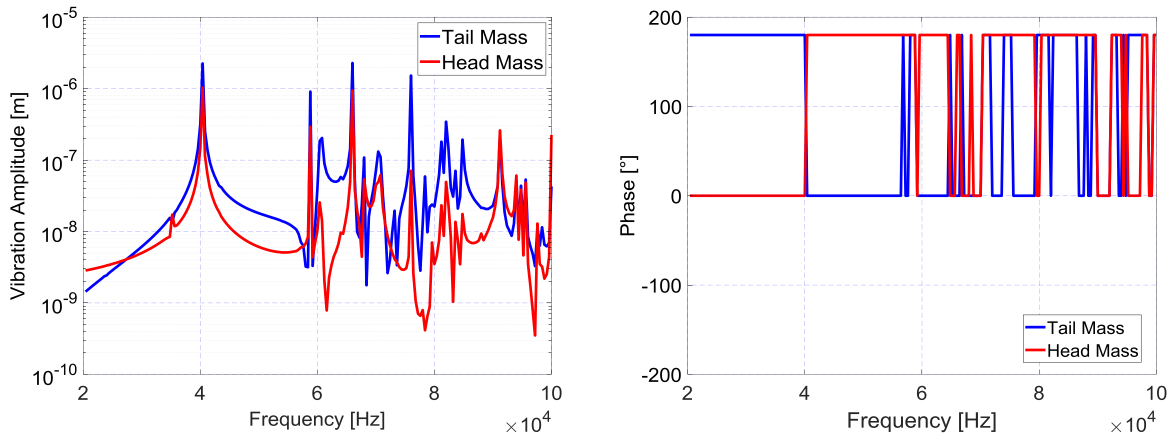

Fig. 24 – Numerical Analysis of Head and Tail Mass Z-Displacements

left: vibration amplitudes | right: displacement phase relationships

Furthermore, the post-processing allowed the visualization of deformation modes at some of the frequencies to investigate the nature of the vibration. The first mode in Fig. 25 shows the longitudinal displacement of the whole stack and masses along the z-axis. The second series of diagrams in Fig. 26, show a bending mode around 23 kHz and a parasitic screw vibration around 34 kHz, as was studied by DeAngelis et al. [110]. These modes were not observed in Fig. 24. The deformation gradient in the figures is only used for qualitative purposes. The most important conclusions from this analysis are the presence of one clear resonance peak between 20 and 55 kHz that is responsible for the longitudinal resonance of the stack, and that the aluminum and brass displacements should be similar in amplitude, and opposite in direction at resonance. The results also show that the rubber pad does not hinder the transmission of vibrations from the device to the supporting structure very much. Other modes including torsional, transverse and radial deformations were outside the experimental sweep range between 24 and 48 kHz, and therefore are not shown here.

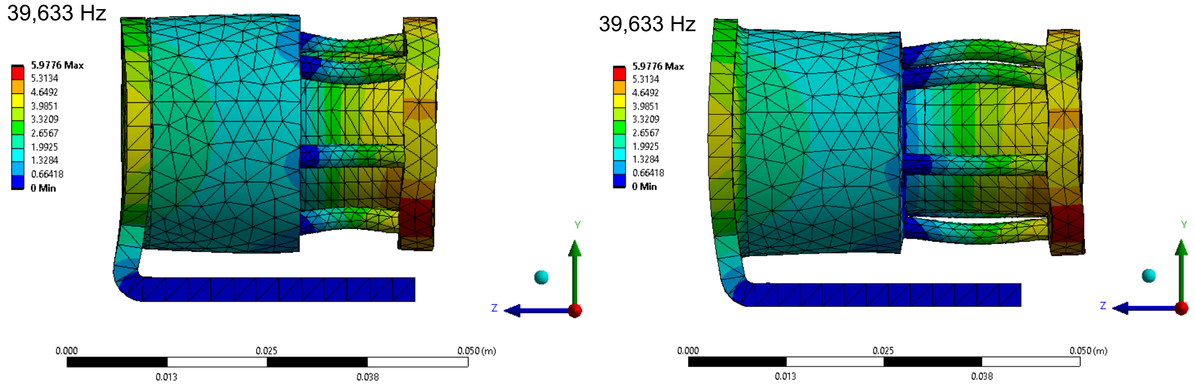

Fig. 25 – FEM Longitudinal Vibration Mode

left: minimum deformation at 39.6 kHz | right: maximum deformation at 39.6 kHz

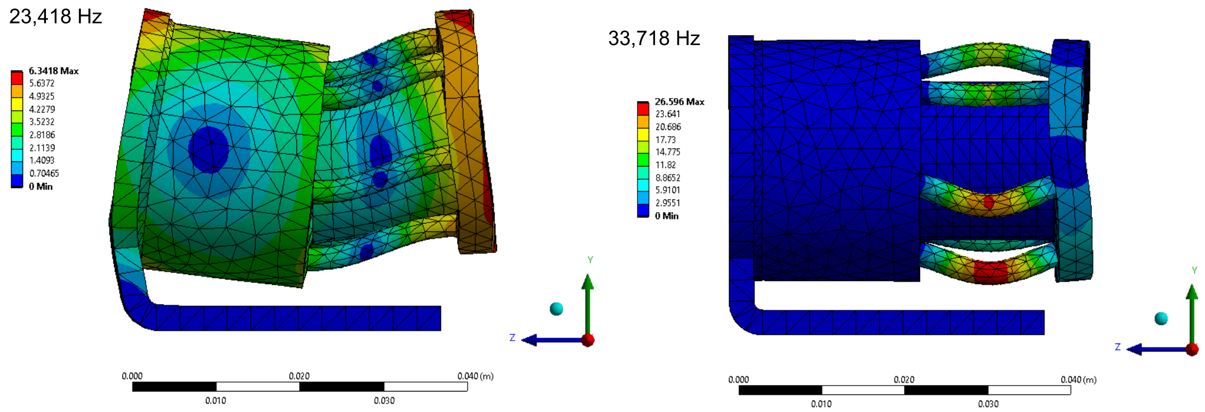

Fig. 26 – FEM Different Vibration Modes

left: bending deformation at 23.4 kHz | right: parasitic screw vibration at 33.7 kHz

3.1.6 Vibrometry Analysis

The goal of the experiment was to examine the mechanical resonance frequency of the device and to see the correspondence to the electric resonances observed using the impedance spectrometer. A reflective target was set up on both end masses of thrusters MET03 and MET04: in one test, the metal surface was polished until sufficient reflection, in another test, a round mirror with a 10 mm diameter was fixed on the target mass. Both methods yielded similar results. The interferometer, described in Section 3.3.1, is held in place using an optical mount to examine the velocity of the target. One target was examined at a time, while the driving frequency was swept over the frequency range of interest at a constant voltage using the amplifier electronics described in Section 3.2. The experimental setup can be seen in Fig. 27, where the device's L-bracket is fixed to an optical table via a stainless-steel mount.

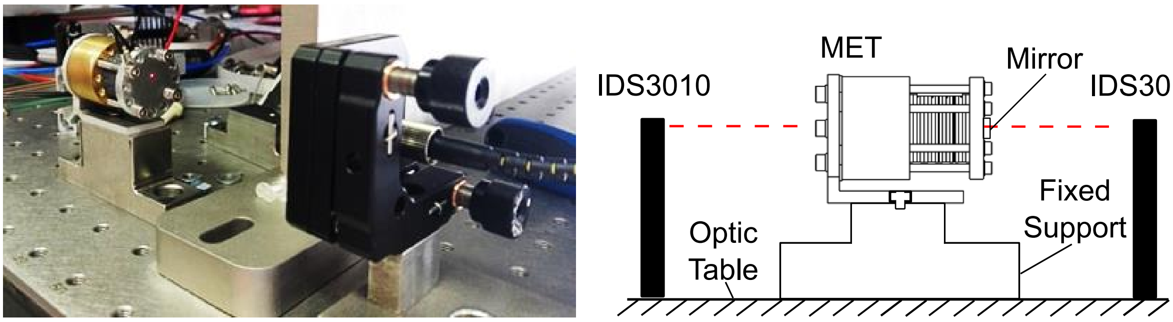

Fig. 27 – Vibrometry Setup

The results are compared to the impedance spectra in the next series of figures. As can be seen from Fig. 28, the vibration peaks are located around the lowest impedance. The impedance was calculated from the output voltage-to-current ratio (V_{OUT}/I_{OUT}), to maintain the same loading, voltage, and stress conditions for both experiments. The peaks are roughly at the same frequencies. Furthermore, the brass vibration amplitude is comparable to the aluminum mass' vibration amplitude at the resonance frequency. The driving voltage was 100 V. There seems to be a discrepancy between the vibration peak and the impedance minimum, which could be due to some latency in the processing program. The vibration amplitude of brass was obtained only between 24 and 48 kHz.

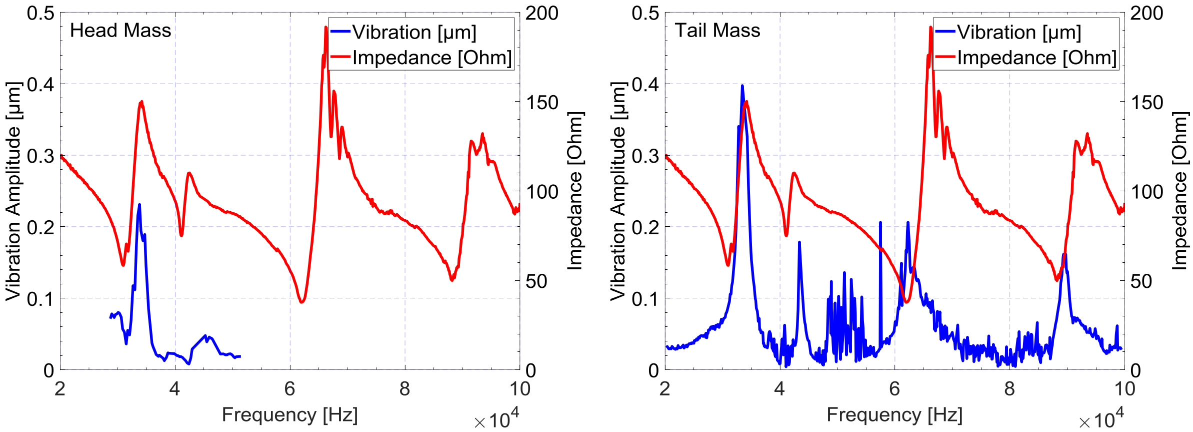

Fig. 28 – MET03 Head and Tail Mass Displacements

left: head (brass) mass displacement | right: tail (aluminum) mass displacement

The vibration of aluminum and brass masses for the MET04 device has been increased compared to the previous experiment, by increasing the driving voltage to 160 V. This also leads to smaller noise in Fig. 29. The peaks also occur around the impedance minima for this device as well. The brass amplitude is comparable to the aluminum amplitude and the mechanical resonance is at the same frequency as the resonances measured using the electric spectrum. However, the amplitude of the vibration cannot be inferred from the value of the impedance or the relative value of the impedance. In these diagrams, there is no discrepancy between the mechanical and electric resonance frequencies.

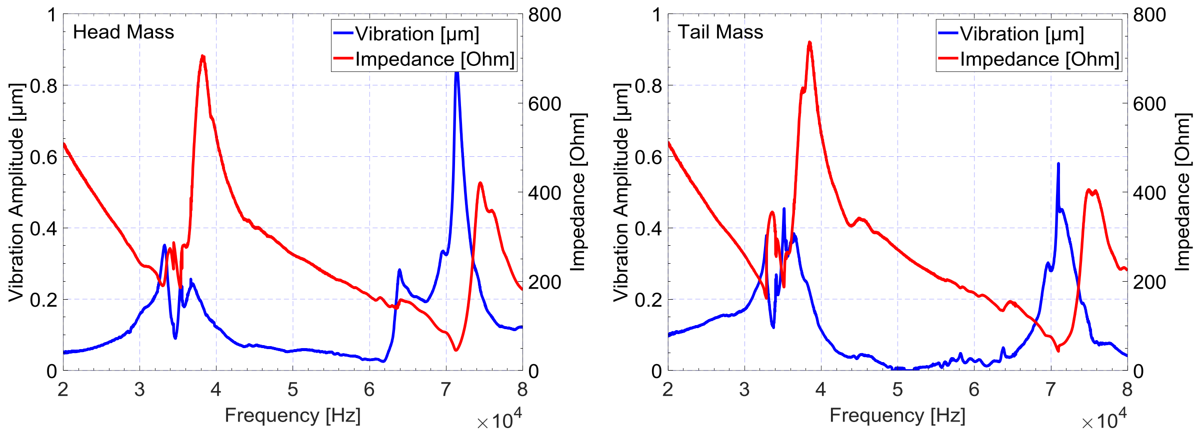

Fig. 29 – MET04 Head and Tail Mass Displacements

left: head (brass) mass displacement | right: tail (aluminum) mass displacement

3.1.7 Impedance Spectroscopy

Different tests can be used to characterize the piezoelectric devices and examine the effects of aging, humidity, pre-stress, or stress conditions. Their impedance or resonance spectra are also obtained using different methods and then compared. This section includes the characterization of the MET, how they compare to each other, and how they changed over time. The techniques used for characterization are vibrometry, impedance spectroscopy, and FEM. The pictures, geometry, physical properties, drawings, and circuits of the devices are included below. Table 10 shows the official model number used in the thesis in the first column, as well as the number of tests and runs for each one of them. The piezoelectric models used for balance experiments start with the notation MET, whereas the devices used in centrifugal balance experiments introduced in Section 5.1.2 start with the notation CD (Centrifugal Device). CU18A is the maker's model number for the magnetostrictor [111].

Device	Maker	Year Produced	No. Tests	No. Profiles	Resonance [kHz]
MET01	Woodward	<2013	9	240	38, 42, 56, 75
MET02	Woodward	<2017	37	5770	22, 42, 62, 75
MET03	Woodward	2018	49	6943	32, 43, 63, 90
MET04	Monette	2018	30	2810	36, 39, 73, 90
MET05	Woodward	2019	137	585	34, 46, 70
MET06	Woodward	2019	4	20	34, 46
CU18A	Etrema	2018	32	2948	9.5, 17.5

Table 10 – Overview of Test Devices

A few different methods were employed to examine the behavior of the devices in different driving conditions. In the first method, an impedance spectrometer (HP4294A, Agilent) was used to obtain the impedance spectra of the different devices. By the equivalence principle, the impedance of a piezoelectric device gives information about the mechanical behavior of the system. The test conditions include constant, and very low current of 50 mA and a frequency sweep from 1 mHz to 200 kHz. The instrument was first calibrated using the standard procedure with a short circuit, open connection, and 50 Ω resistor.

Fig. 30 shows the impedance spectrum of the different MET devices in Ohms. The impedance can also be given in dB in reference to the standard 50 Ω resistance. Where there's a dip in the impedance spectrum, there is also a resonance, where there's a peak there's also an anti-resonance. The phase also shows the different resonant modes; the phase should reach close to zero in the case of a resonance where most of the energy is converted to real work and the actuation is maximized. The spectra are shown between 20 and 60 kHz for all devices.

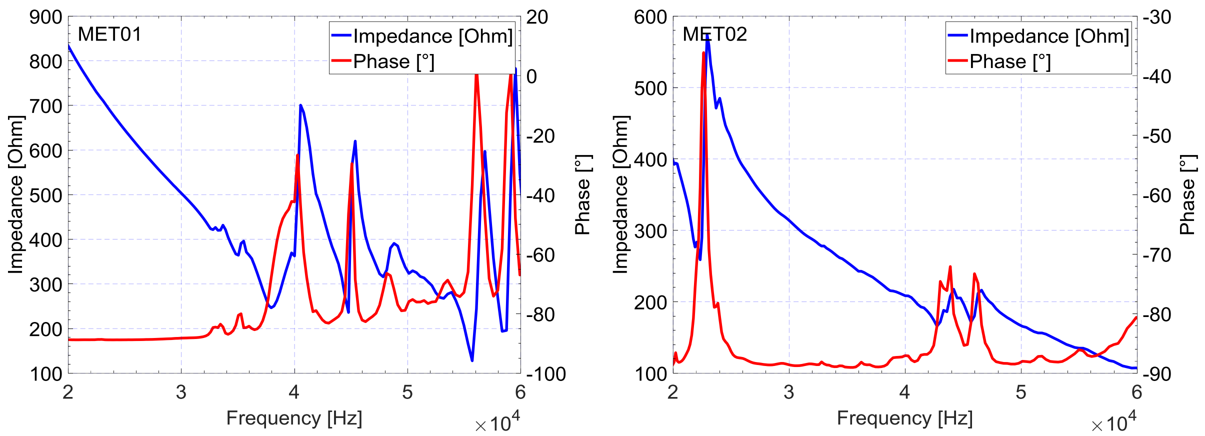

Fig. 30 – Impedance Spectra MET01 & MET02

left: MET01 spectrum | right: MET02 spectrum

The first curves show the impedance spectrum of MET01 and MET02, the two older devices are provided only as a reference. Generally, there are fewer resonances at the lower end of the spectrum, and the impedance generally decreases with frequency, similar to a capacitor. Then, the graphs show that there are more parasitic resonances for MET01 than for MET02, which may be due to ageing of the piezoelectric structure, since MET01 is significantly older than MET02. Both devices have a pretty clear resonance at 38 and 22 kHz, respectively, followed by a clear anti-resonance right after, at a slightly higher frequency. Furthermore, there seems to be a small resonance around 42 kHz in both devices. Overall, however, the resonances are not very clear and strong for both devices when compared to the next figures.

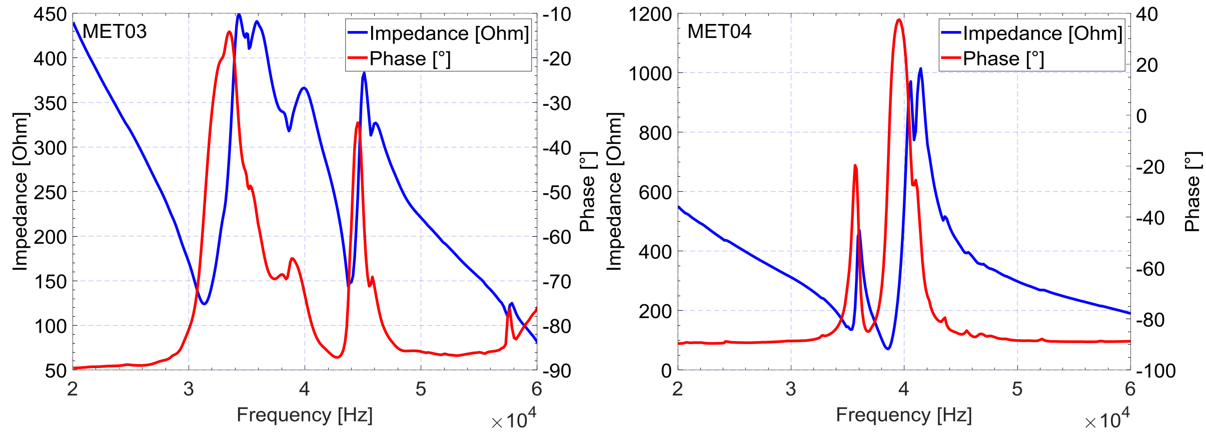

Fig. 31 – Impedance Spectra MET03 & MET04

left: MET03 spectrum | right: MET04 spectrum

In Fig. 31, the resonances of MET03 and MET04 are shown to be more significant in the frequency spectrum. MET03 has resonances at 32, 43, and 62 kHz. MET04 has resonances at 36, 39, and 74 kHz. It is not clear whether the resonance at 36 kHz for MET04 consists of a single resonance split due to bad coupling, or if these are two distinct resonances. One sees that there are much lower distortion and fewer parasitic modes, when compared to the spectra of MET01 and MET02. MET01, MET03 and MET04 suggest that the longitudinal resonance of interest lies somewhere between 32 and 39 kHz for the MET design.

The spectra of the last two devices were obtained in Fig. 32 by analyzing the strain gauge signal. This method consists in applying a fixed voltage across the piezoelectric device without an amplifier, sweeping the driving frequency from 10 to 100 kHz, and simultaneously monitoring the gauge signal using an oscilloscope. The voltage ratio of the gauge voltage V_{SG} to the commanded voltage V_{COM} is plotted on the y-axis. The method provides only a relative measure of the impedance and vibration strain, but it can also clearly show the resonances at the same frequencies as for the other impedance methods.

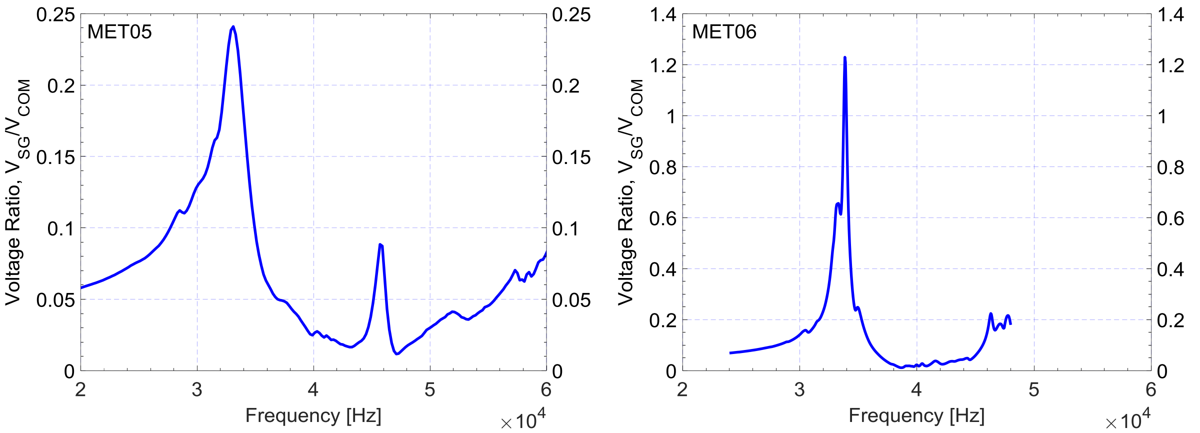

Fig. 32 – Resonance Spectra MET05 & MET06

left: MET05 spectrum | right: MET06 spectrum

Using this method, the resonances are characterized by peaks instead of valleys, where the vibration strain is the largest, and these can be found at 34 and 46 kHz for MET06 as well. The graphs show that the two devices MET05 and MET06 have almost identical behavior, which is expected, since they were built using the same procedure and materials. Fig. 33 shows the difference between using the impedance spectrometer, on the left, and obtaining the impedance amplitude from the output voltage and current across the device MET04 using an amplifier with low input voltage, on the right. All these methods equally provide a good visualization of the resonances, of their frequency and sharpness.

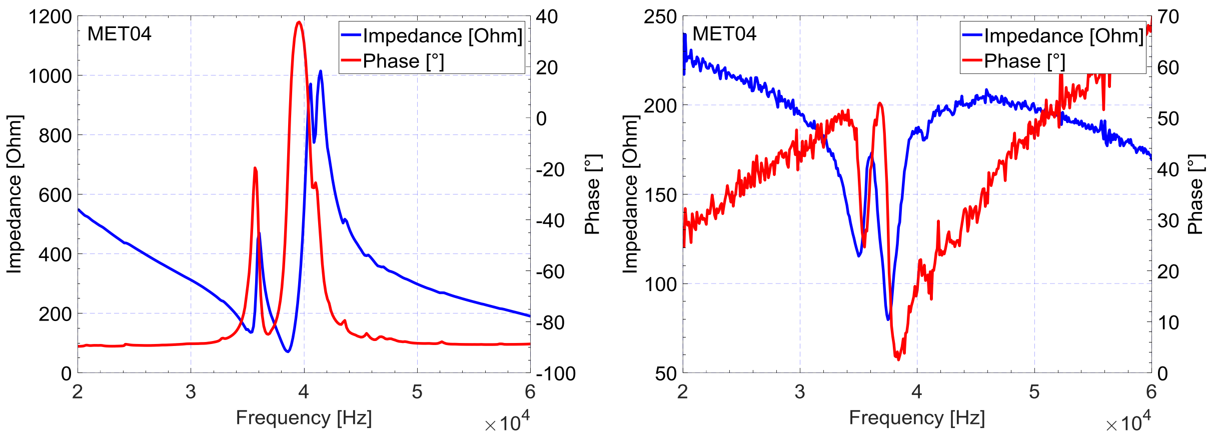

Fig. 33 – MET04 Spectrum Method Comparison

left: spectrum with impedance spectrometer | right: spectrum with amplifier and oscilloscope

Since the oscilloscope is not as precise as the impedance spectrometer, the very low impedance in the right-hand diagram cannot be read accurately, which is why the anti-resonances seem to disappear in a blur. However, due to the larger current at low impedances, the resonance frequencies can be distinguished clearly using this method. Using higher voltage leads to distortions in the impedance spectrum, due to the higher stresses on the ceramic, which is why the impedance spectrometer is preferred. However, since the tests are performed under high voltage and stress conditions, it also makes sense to examine the impedance under these conditions as well. Above all else, the instruments used in generating this type of impedance spectrum are readily available. The results show that the resonances can easily be obtained using different methods and correspond to the estimates seen in the simulation. To summarize, MET03 through MET06 all have the lone and main longitudinal resonance around 34 kHz, which is slightly lower than the FEM prediction of around 38 kHz but could be explained by slight deviations in the material parameters. MET01 has a higher longitudinal resonance frequency which can be explained by its shorter length. MET04 has a lower second resonance compared to the other devices and this could be explained by the bigger screws used in the construction. The lower resonance frequency of MET02 is more difficult to explain. Fig. 34 compares two impedance spectra of the device MET03 at different moments of the campaign. It is suspected that the device overheated during the tests in May 2018. The longitudinal vibration mode must have shifted to 24 kHz, just like in the case of the older MET02, due to the depolarization or fractures in the piezoelectric ceramic. The material may have become more compliant, thus shifting the resonance to a lower frequency.

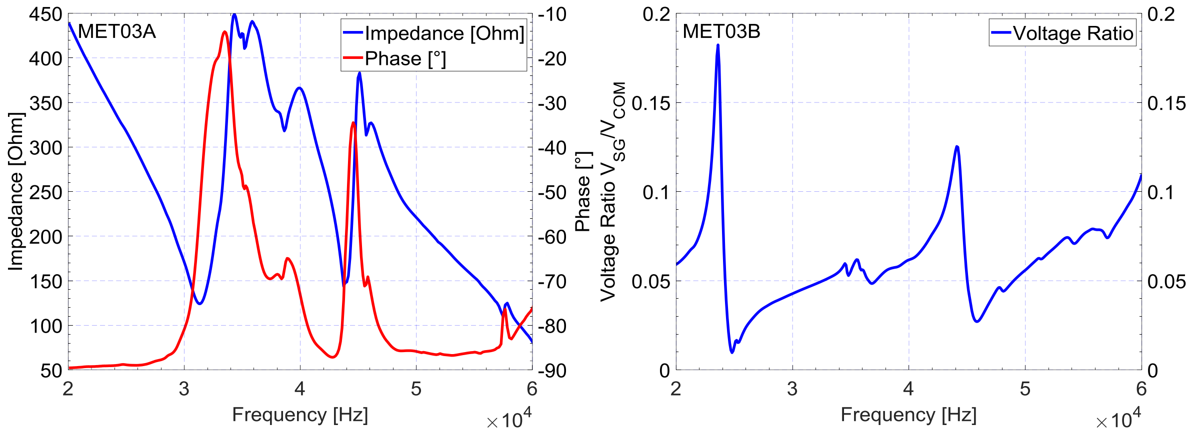

Fig. 34 – MET03 Spectrum Comparison Before-After Thermal Event

left: before the thermal event | right: after the thermal event

MET-04 was used to demonstrate the influence of stack pre-load or bolt pre-tension on the resonance spectrum. Fig. 35 shows impedance curves with different pre-load, controlled by a torque-wrench and incrementally adjusted to provide an approximate stack pre-load. Higher pre-loading seems to shift the main resonance frequency to the right, as the stiffness of the actuator increases. Parasitic resonances can appear where the coupling is not ideal. The behavior is repeated for both materials. The Q-factor also increases for the ideal pre-load and decreases if the pre-stress is too high for the material. It should be noted, that the pre-load is likely uneven because of the configuration using six smaller screws at the perimeter of the stack instead of a unique central screw [108]. The best mechanical quality factor is obtained for the higher pre-load of around 25 MPa, as shown in Fig. 35.

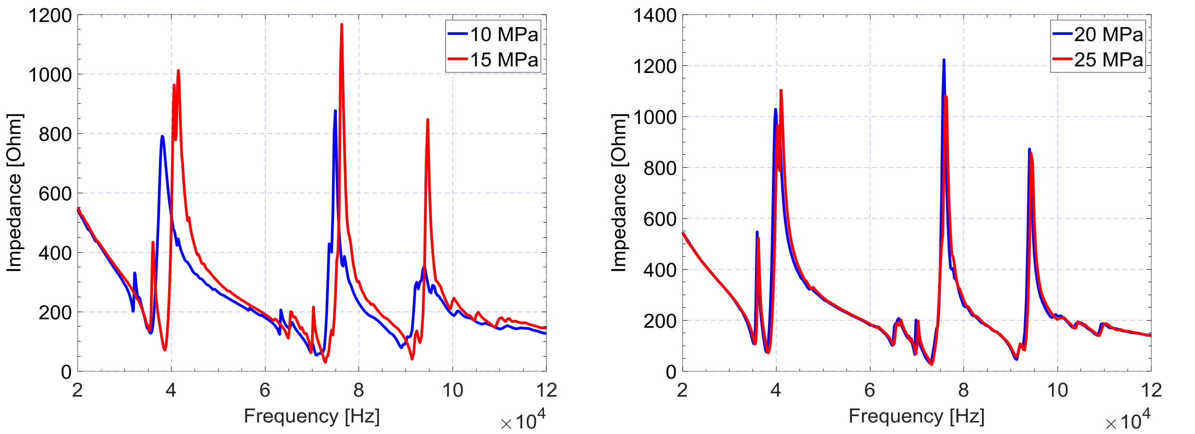

Fig. 35 – MET04 Impedance Spectra vs Pre-load

left: 10 and 15 MPa pre-load | right: 20 and 25 MPa pre-load

These graphs show that a specific amount of pre-load provides the best coupling between the piezoelectric and metal materials. This is recognized in the smooth spectrum with two distinct resonance peaks and the absence of many parasitic resonances. If the coupling is imperfect, several parasitic resonances can appear [110]. Moreover, the resonance frequencies can shift if the pre-load is varied. Thus, the main takeaways are the following:

- The presence of parasitic resonances depends on the coupling and the pre-load.
- The Q-factor of the resonance depends on the pre-load.
- The resonance frequency is shifted to the right when increasing the pre-load.

Next, Fig. 37 shows the influence of aging, humidity, and atmospheric pressure on the impedance spectrum and the physical characteristics of the devices. The test conditions are specified in the figure caption. One of the main causes for the discrepancies between the tests would be the loosening of the pre-tension. As seen earlier, pre-tension influences the location of the vibration peaks. Due to the mechanical mismatch between stainless-steel screws and the brass mass, there were several instances of brass powder found in the setup after the tests. Furthermore, the torque on all screws was adjusted on several occasions before and after the tests. Again, there were several instances where the screws were not at the required torque level of 0.45 Nm after a longer test or a series of tests.

The resonance spectrum shows that the various heating, outgassing, expansion, testing, and cooling processes have a direct influence on the device's response. Even if it the influence of each parameter is not exactly known, it is certain that the bolt-brass connection is subject to thermal expansion and vibration, and the material properties can vary with temperature and stress. Fig. 36 shows some evidence of brass powder deposit on the copper block after a few test runs, indicating the result of rubbing of the steel screws in the brass threads.

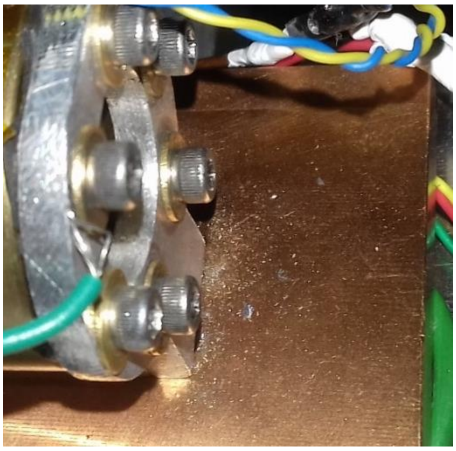

Fig. 36 – Evidence of Brass Powder Deposits

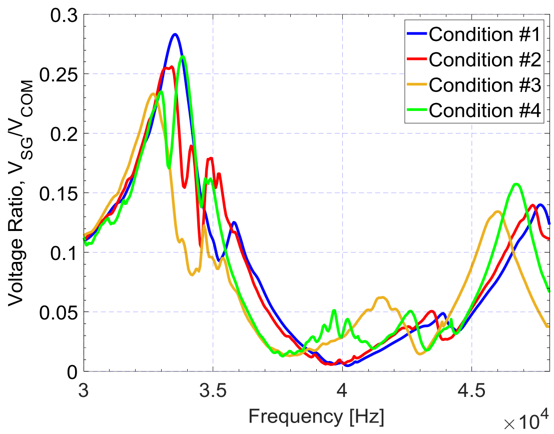

Fig. 37 – MET06 Dependency of Impedance on Environment

test condition #1: room temperature and atmosphere (date: 30.09.2020) | test condition #2: room temperature and vacuum (date: 01.10.2020) | test condition #3: after pulse series, 43°C and vacuum (date: 02.10.2020) | test condition #4: after cooldown, room temperature and vacuum (date: 04.10.2020)

Finally, Fig. 38 shows the impedance spectra of the magnetostrictive actuator using different masses. The figure shows how the resonance behavior of the magnetostrictor is influenced by the weight of the attached tail mass, as described in the manual. Furthermore, since this actuator is professionally designed with years of design optimization, the resonance is very clear, and there are no parasitic resonances.

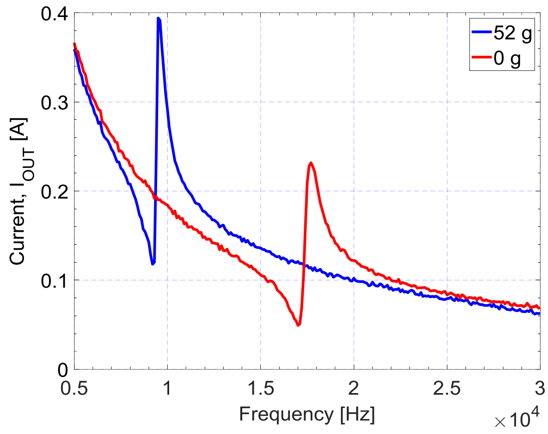

Fig. 38 – CU18A Current Spectrum vs Mass Loading

An explanation was given of phenomena such as the resonances, the anti-resonances, the effects of frequency shifting and pre-loading, as well as parasitic resonances. It is now possible to select reasonable driving frequencies for all the individual stacks. At the same time, the effects of vacuum, heating, and other test conditions on the behavior of the balance are better understood. These graphs have shown the following important points:

- One of the major resonance frequencies of this type of device is around 34 kHz.
- There are several parasitic frequencies next to the main resonances.
- The gauge spectrum is comparable to the impedance spectrum.
- There are a few distortions when comparing the high current vs low current impedance spectrum.
- The MET devices are not always similar.
- The presence of parasitic resonances depends on the coupling and the pre-load.
- The Q-factor of the resonance depends on the pre-load.
- The resonance frequency is shifted to higher frequencies when increasing the pre-load.
- The resonance spectrum can change after a series of tests due to thermal expansion, loosening of the screws, change in the coupling between the parts, and possibly a change in piezoelectric properties due to stress and fatigue.

3.1.8 Circuit Modeling

Modeling the piezoelectric transducer as a circuit element is a powerful tool that can help in optimizing the amplifier circuit and understanding some resonance phenomena. There are different circuits to model piezo-elements, and in the quasi-static regime, piezo-ceramics can be considered simply as capacitors. However, for higher driving frequencies approaching a vibration resonance, the impedance can change drastically and the typical equivalent circuit model used is the Van Dyke Model [117] consisting of an RLC series connected to a capacitor in parallel as shown in Fig. 39. The resistance represents the mechanical damping, the inductance the mass, the capacitance connected in series is the elastic compliance and the parallel capacitance is the electrostatic capacitance of the piezo-disk. The inconvenience with the Van Dyke model is that it does not include hysteresis, material losses and only features one resonance peak, while the different mechanical boundary conditions related to the mounting structure of the actuator can lead to additional resonances. Even though, the model makes it easy to calculate a unique series resonance, where the impedance is minimized in the lower branch of the circuit:

$$\omega_1 = \frac{1}{\sqrt{L_1 C_1}} \quad . \tag{81}$$

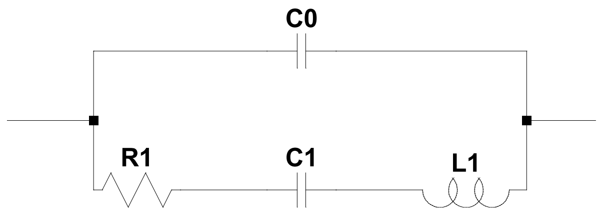

Fig. 39 – Van Dyke Equivalent Circuit Model [118]

The Sherrit model [118] showed that energy dissipation can be considered by introducing complex values to the electric components. Finally, the Van Dyke model can also be modified to include several resonances to represent different boundary conditions, by adding RLC branches connected in parallel. The most recent model that can accurately represent complex dynamic behavior for loaded and unloaded piezo-ceramics, was described by Kim [117]. Using a simple procedure, all resonances and anti-resonances can be accurately modeled, as shown in Fig. 40 and Fig. 43.

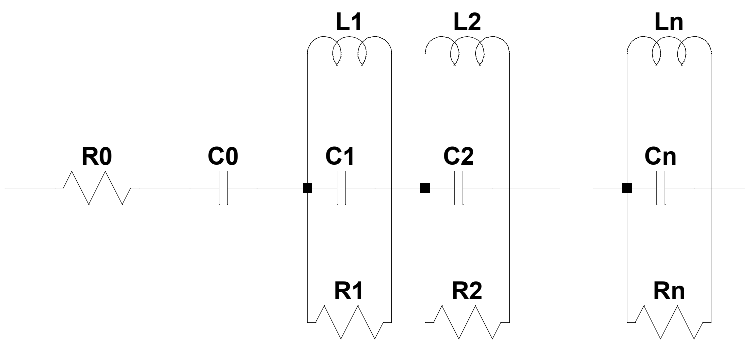

Fig. 40 – Extended Kim Model for Loaded Piezo [117]

By using an impedance spectroscope, one can obtain the resistance and reactance curves of the piezo-ceramic. The resistance value R_0 is determined from the resistance curve at very high driving frequency. The capacitance C_0 is then determined by taking the negative inverse of the reactance value at a very low frequency. The frequency at which the reactance is zero is taken to be the parallel resonance frequency ω_p. Then, the resistance of the unloaded PZT at the parallel resonant frequency is the value $R_{p,unl}$. The quality factor is calculated from the resistance curve using the 3-dB rule. Finally, the different elements can be calculated as follows:

$$R_1 = R_{p,unl} - R_0 \quad , \tag{82}$$

$$L_1 = R_1/\omega_p Q \quad , \tag{83}$$

$$C_1 = 1/L_1\omega_p^2 \quad . \tag{84}$$

This procedure can be repeated for all following resonances in the spectrum and is used to characterize the different devices. Having the equivalent circuit for the different piezoelectric actuators is a very powerful method to predict the current, phase, and power characteristics for a given voltage and frequency using a simulation tool such as LTspice.

Using the techniques described above, the different circuits matching the spectra of the different MET devices were obtained. Having the equivalent circuit models makes it possible to predict the current for a given voltage and frequency, and thus, to know from the current when some resonances have been shifted due to external conditions such as heating, higher voltage, or the presence of a transformer. Furthermore, the circuit model allows for predicting the influence of electronic components on the thruster behavior. As an example, the resistance and reactance curves of MET01 were obtained using an impedance spectrometer (Fig. 41) and were used to calculate the equivalent circuit (Fig. 42). A comparison between the experimental and modeled impedance curves for MET01 is shown in Fig. 43. The piezoelectric charge is modeled as a current source of 1 A in amplitude, to get the impedance directly from the voltage measurement. The graph shows that the anti-resonances are well portrayed, and the model can be improved if more parallel RLC branches are added.

In the right-handed figure, a comparison shows the effect of adding a transformer between the current source and the piezoelectric element. The transformer is taken with a 1:2 ratio, 150 µH for the first coil, an internal resistance of 2 Ω, and an ideal coupling. The graph shows clearly that the anti-resonance peaks have been slightly shifted and the peak values have also been modified. Thus, electronics can have a significant impact on the resonance spectrum of the electromechanical system.

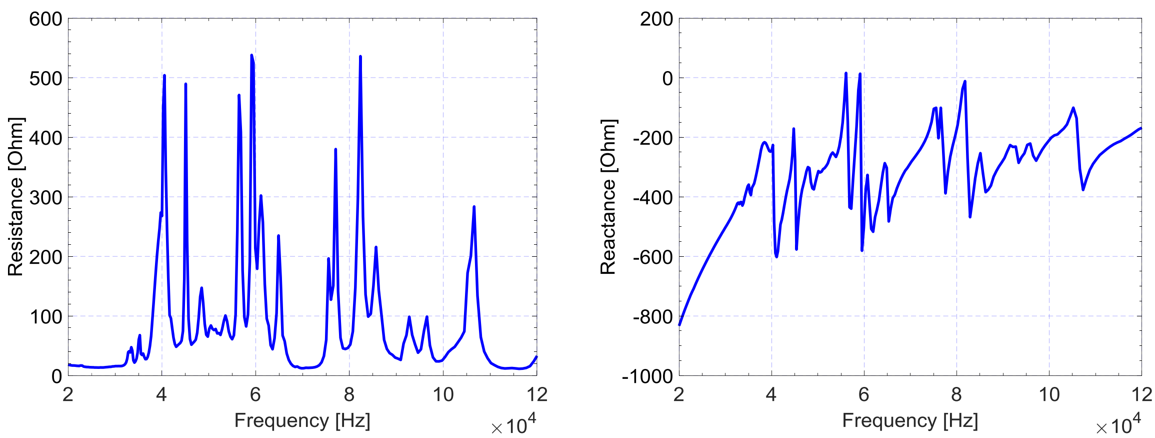

Fig. 41 – MET01 Resistance and Reactance Curves

left: resistance curve | right: reactance curve

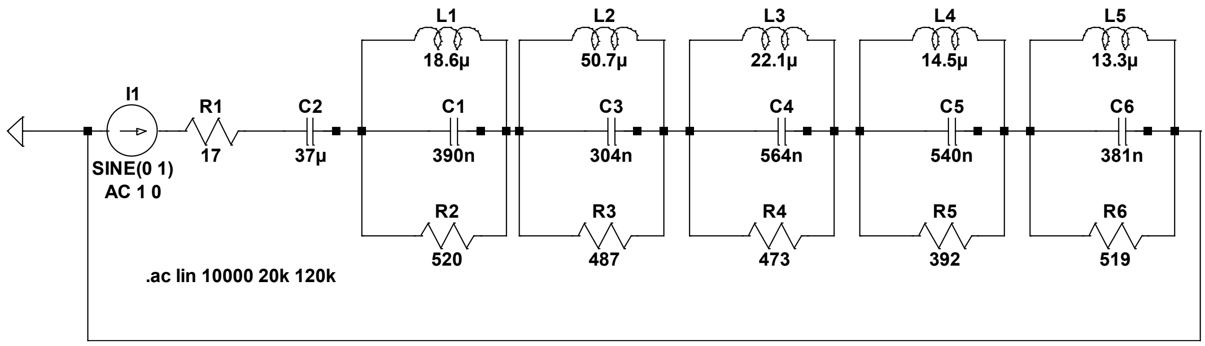

Fig. 42 – MET01 Equivalent Circuit

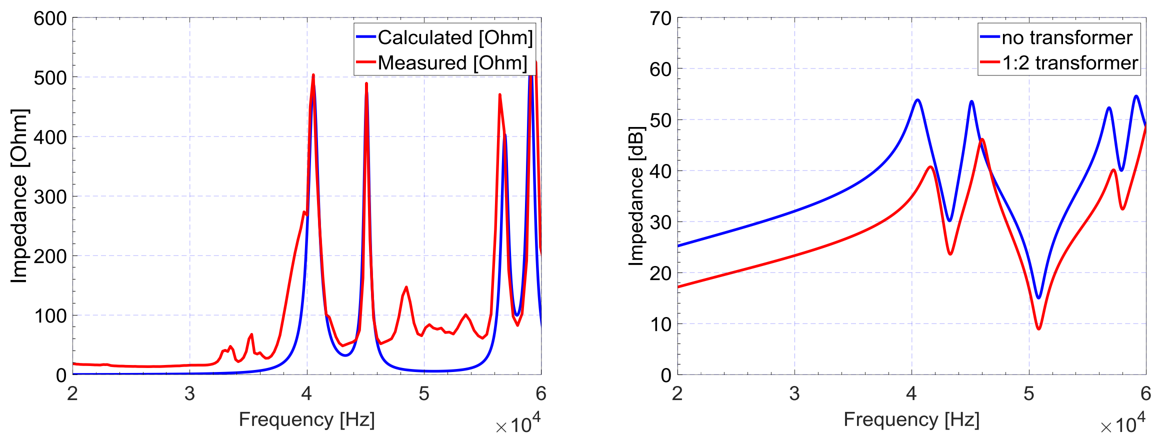

Fig. 43 – MET01 Spectrum Simulation

left: MET01 impedance spectrum comparison between calculated and measured data
right: simulation results with or without 1:2 transformer

3.1.9 Predictions

This section is completed by a summary table of the mass fluctuations and forces predicted for the different devices and various conditions (Table 11). MET05 is chosen as the model for all MET used, which should all yield very similar results.

Woodward's MET or MEGA Drive [59] design supposedly generates both the mass fluctuation and the actuation with a single voltage signal, relying on electrostriction within the device to provide the required, synchronous acceleration. As seen before, the mass fluctuation for the piezoelectric stack with an input signal $V(t) = V_0 \sin(\omega t)$ is given by Equation (51). Since the actuation of the mass fluctuation now depends on the nonlinearity of the piezoelectric stack, which can be represented by the nonlinear electrostriction parameter M_{33}, the displacement is first given by:

$$x(t) = \frac{M_{33} Q \eta}{\mathrm{L}} V(t)^2 \quad , \tag{85}$$

and after differentiation, the acceleration of the stack is given by:

$$\ddot{x}(t) = \frac{2M_{33}Q\eta V_0^2\omega^2}{L}\cos(2\omega t) \quad . \tag{86}$$

Thus, using the mass fluctuation for a piezoelectric stack given by equation (51) and combining it with the acceleration given in (86) and integrating according to equation (53), assuming the phase difference to be zero, the resulting thrust force F_{MET} amounts to:

$$F_{MET} = \frac{M_{33}d_{33}^2LQ^3\eta^3V_0^4\omega^4k_A}{2\pi Gc^2\rho_0 L} \tag{87}$$

This calculation represents a simplification of the dynamics of the device and is only valid for the longitudinal vibration modes. The calculation is simplified by assuming that the device is fixed at one end. In reality, the force should be dampened by the movement of the brass mass in the opposite direction to the tail mass movement, as seen from the FEM results. A more accurate prediction should consider the precise distribution of the mass fluctuation as well as the movement or acceleration of every element of the thruster [70]. Furthermore, the different piezoelectric, electrostrictive, elastic, and dielectric nonlinear parameters as well as the influence of the bolt pre-loading should be integrated into the FEM as well. Obtaining an exact solution is beyond the scope of the thesis, which focuses on experimental observations. The simplified calculation, however, gives a reasonable estimate of the order of magnitude expected, given the experimental parameters. It also underlines the influence of parameters such as the quality factor, driving frequency, and voltage, which can be used to increase thrust. A larger nonlinearity can also increase the predicted effect; however, the phase relationship between the nonlinear effects and the driving signal is difficult to predict.

The force can be further increased by applying a harmonic component to the driving signal. Indeed, if the voltage signal is represented by $V(t) = \frac{V_0}{2}\sin(\omega t) + \frac{V_0}{2}\sin(2\omega t + \emptyset)$, then, the acceleration can be provided by the larger piezoelectric effect, rather than relying on the smaller nonlinear acceleration:

$$\ddot{x}(t) = -2d_{33}\omega^2Q\eta V_0\sin(2\omega t + \emptyset) - \frac{d_{33}\omega^2Q\eta V_0}{2}\sin(\omega t) \quad . \tag{88}$$

Combining the mass fluctuation equation given by (51) with the acceleration from equation (88) and integrating over a period, the resulting force should even be flipped in sign, depending on the phase difference:

$$F_{MET} = -\frac{d_{33}^3Q^3\eta^3V_0^3\omega^4k_A}{2\pi Gc^2\rho_0}\cos\emptyset \quad . \tag{89}$$

The predictions for the thrust force with the magnetostrictor are approximate calculations using the displacement, resonance and impedance values obtained from the technical manual for different loads, assuming again that one end is fixed or oscillating at a very low frequency [111]. Furthermore, the nonlinearity in the magnetostrictor was neglected, as the current spectrum did not reveal significant second harmonics in its operation. Thus, in the absence of a synchronous acceleration of the mass fluctuation at 2ω, single-sine driving of the magnetostrictor should not produce any thrust. The mixed-mode driving, however, should produce a thrust according to the same procedure using equation (51), assuming the first voltage component to be at resonance producing the mass fluctuation, and the second component at double the driving frequency providing the acceleration. The mass fluctuation is obtained strictly from the kinetic energy of the moving load, resulting in a thrust force expressed in equation (90), having a dependence on frequency to the power of six, as derived before [70].

$$F_{MAG} = \frac{m\omega^6 x_1^2 x_2}{2\pi G c^2 \rho} \quad . \tag{90}$$

In the equation, m and ρ are the mass and density of the load, x_1 is the load's vibration amplitude at resonant driving frequency and x_2 is the amplitude for the second harmonic. The results are shown in Table 11, and set the values expected in the experiments.

Parameter	**MET05(1)**	**MET05(2)**	**MET05(3)**	**MET05(4)**	**CU18A(1)**	**CU18A(2)**
Condition	Resonance	Off Res.	Mixed-90°	Mixed-0°	Mixed - 0 g	Mixed - 52 g
Frequency [kHz]	36	60	36	36	18	9.6
Voltage [V]	180	180	90	90	60	60
Q-Factor	40	1	40	40	20	30
Energy [W]	180	36	180	180	18	76
Mass Fluct. Amplitude [g]	$4.4 \cdot 10^{-1}$	$7.7 \cdot 10^{-4}$	$1.1 \cdot 10^{-1}$	$1.1 \cdot 10^{-1}$	$2.2 \cdot 10^{-2}$	$5.7 \cdot 10^{-2}$
Thrust [N]	$4.5 \cdot 10^{-2}$	$5.4 \cdot 10^{-6}$	0	$1.2 \cdot 10^{1}$	$1.7 \cdot 10^{-2}$	0.125
Direction	$+$	$+$	N/A	$-$	$+$	$+$

Table 11 – Summary of Predictions

A simple analysis of the uncertainty propagation in the predictions considers a minimal variation of 10% in the stiffness and Q-factor properties of the thruster. This estimate was motivated by measurements of piezoelectric properties using a d_{33}-piezometer from Hantech, providing an averaged error of 2% for the piezoelectric coupling of the SM111 disks. Examining Equation (89), the total uncertainty in the MET thrust can be calculated as follows:

$$\frac{\Delta F}{F} = 3\frac{\Delta d_{33}}{d_{33}} + 3\frac{\Delta Q}{Q} + 3\frac{\Delta \eta}{\eta} + \frac{\Delta k_A}{k_A} \quad , \tag{91}$$

resulting in a total uncertainty of 76%. The same procedure using Equation (51) results in 54% for the mass fluctuation in a piezoelectric stack. The small uncertainty in the commanded frequency and driving voltage was neglected.

Regardless of these calculations, the minimum thrust predictions claimed by Woodward et al. [16,82] using similar equipment range from 1 to 200 µN.

3.2 Electronics

The amplifier electronics used in combination with the piezoelectric stacks have been shown to have an incredible impact on the impedance spectrum of the MET and resonance conditions. The electronics include the ones to drive the actuators such as the signal generator and amplifier, but also others to analyze the signal responses such as different oscilloscopes, instrumentation amplifiers, a lock-in amplifier, strain gauges, and voltage probes. The instruments also determine the measurement resolution and accuracy in the experiment, and so a summary of their capabilities is necessary.

3.2.1 Description

In Fig. 44, the electronics used in the MET experiment on thrust balances in vacuum according to the original TUD setup are illustrated in a block diagram. In this setup, the oscilloscope is also used as a frequency generator and its commanded voltage V_{COM} is monitored. The passive piezo-disk embedded in the stack is called a *strain gauge* for simplicity, and its voltage V_{SG} is measured using a differential probe connected to the oscilloscope. The voltage over the poles of the DUT is termed V_{OUT}. The individual components are described in Table 12 and the amplifiers are described in the next sub-section. The current I_{OUT} over the DUT was measured using a current transducer in the amplifier box and converted to a voltage.

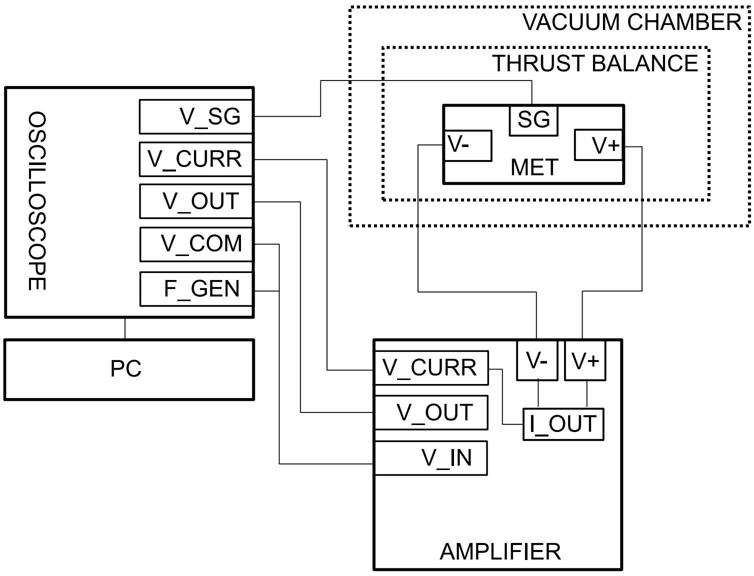

Fig. 44 – TUD Electronics Diagram

In Fig. 45, the block diagram shows the CSUF electronics as tested in Dresden. The setup is similar to Fig. 44 except the amplifier type and the 1:4 transformer used for impedance matching of the MET. This configuration is almost identical to Woodward's setup, valid between 2001-2018, except that a different frequency generator was used [16].

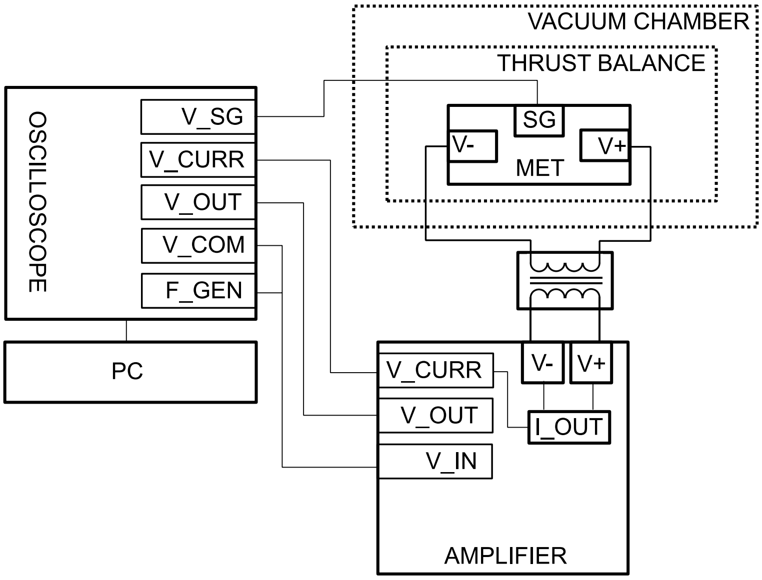

Fig. 45 – CSUF Electronics Diagram

Model	Type	Brand	Frequency Range [MHz]	Input/Output Impedance [$M\Omega/\Omega$]	Input Noise [μV]	Resolution [bit]
5442B	Oscilloscope	Picoscope	60	$1\ /50$	100	12
2445A	Oscilloscope	Picoscope	25	$1/\ 600$	150	8
MFLI	Lock-in Amplifier	Zurich Instruments	5	$10\ /50$	43*	16
PA04	Power Amplifier	APEX	0.1	$1 \cdot 10^5\ /\ 2$	10	50**
DCM1000	Audio Amplifier	Carvin	0.02	$0.02\ /\ 2$	10	50**

** noise density in $nV/\sqrt{Hz}$*
*** slew rate in V/μs*

Table 12 – Overview of Electronics

3.2.2 Characterization

A full characterization of the electronics was necessary to examine their influence on the driving of the piezoelectric and magnetostrictive devices, as well as on the measurement of impedance and current. Signal generation is the first step of the process, and the Picoscope and lock-in amplifier from Zurich Instruments can be compared as signal generators using a sinusoidal signal at constant voltage and frequency. The presence of noise, second harmonic, or nonlinear content in the signal generation can be examined in Fig. 46. For these measurements, the frequency generator output was simply connected to the input channel. A Discrete Fourier Transform (DFT) is used to transform the time-domain signal to the frequency-domain, using a sampling frequency of 4 MHz. The results show that the lock-in amplifier has a better frequency generator, as it includes less superharmonic content and is a more precise instrument to read sinusoidal voltage; however, it was only acquired at the end of the test campaign and was solely used for centrifugal experiments, shown in Chapter 5.

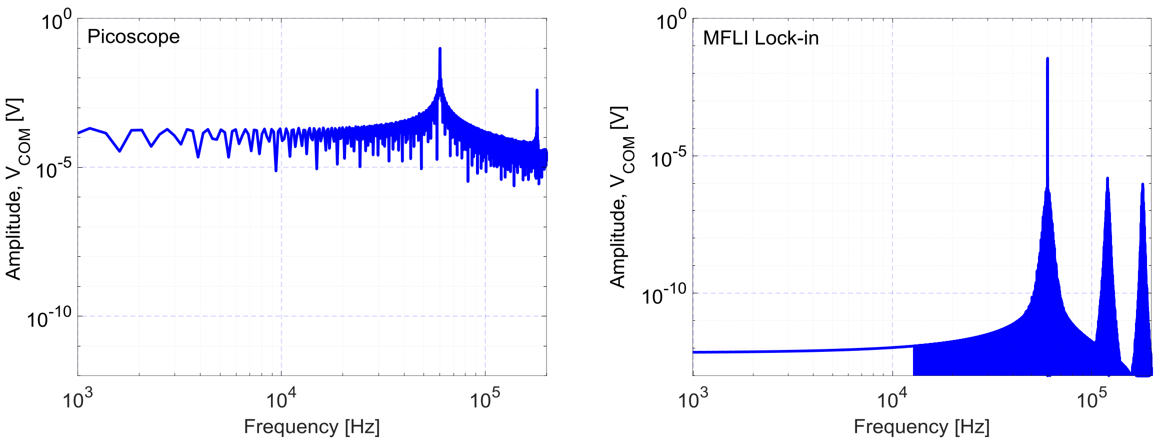

Fig. 46 – Frequency Generator Output Comparison DFT

left: Picoscope output | right: MFLI output

The Bode plots of the amplifiers in Fig. 47 were obtained from a DFT of the commanded and output voltages measured in open circuit, and only show the linear response. The Bode plots show the behavior of the amplifiers used across the relevant frequency range, more information can be obtained in the respective technical manuals [119]. The vertical axis shows the gain of the amplifier and the relative phase. The TUD amplifier was built by Dipl.-Ing. Jörg Heisig using the PA04 evaluation board, including a pre-amplifier and two PA04 high-voltage operational amplifiers from APEX. The current was measured using a current transducer, the LT6-NP from LEM. The plots show a constant voltage gain of 200 over the desired frequency range, as is expected from a dedicated power amplifier for driving piezoelectric devices. The Bode plot of the original audio amplifier used by Woodward also shows what is expected from the datasheet: this A/B class amplifier is not meant for driving frequencies above 25 kHz, which is shown by the variable voltage gain and the erratic phase behavior [119].

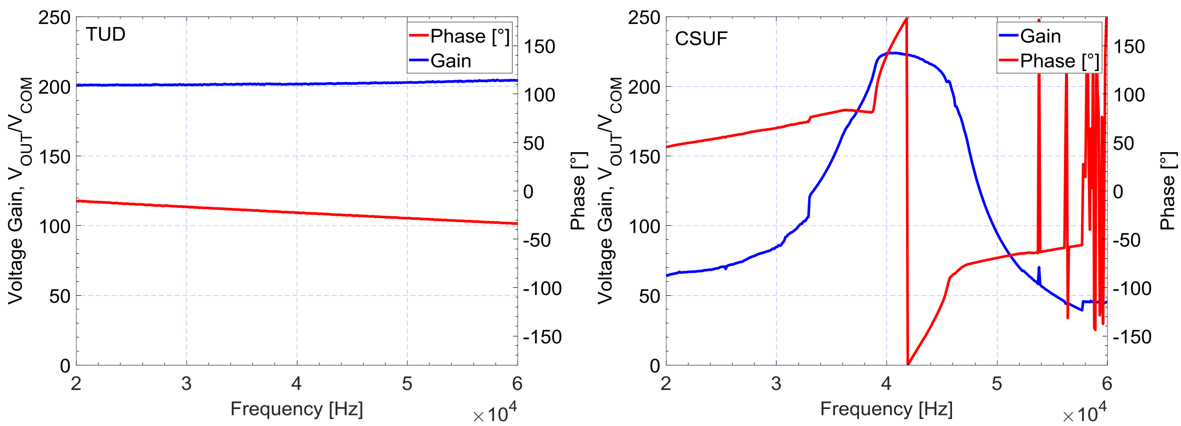

Fig. 47 – Amplifier Bode Plots

left : APEX PA04 Bridge-Mode | right : Carvin DCM1000

The next few plots show the noise and nonlinearity present in the amplification process when a piezoelectric device is connected to the amplifiers. Of course, the noise level depends on the impedance and the state of excitation of the device. Hence, DFT results are shown at different excitation frequencies for both amplifiers. The graphs represent the output current and the output voltage over MET05. Fig. 48 first shows the result of two different driving frequencies using the TUD electronics. The graphs show a few peaks in the current waveform, including a second harmonic peak, which is characteristic of the resonance mode since sub- and superharmonics are excited simultaneously. Further away from the resonance, there are fewer superharmonics excited, as shown in the left-hand diagram. In both cases, the output voltage of the amplifier, however, does not present the same nonlinearity as the current measurement, but rather a clear, distinct peak. The sampling rate used was 120 kHz.

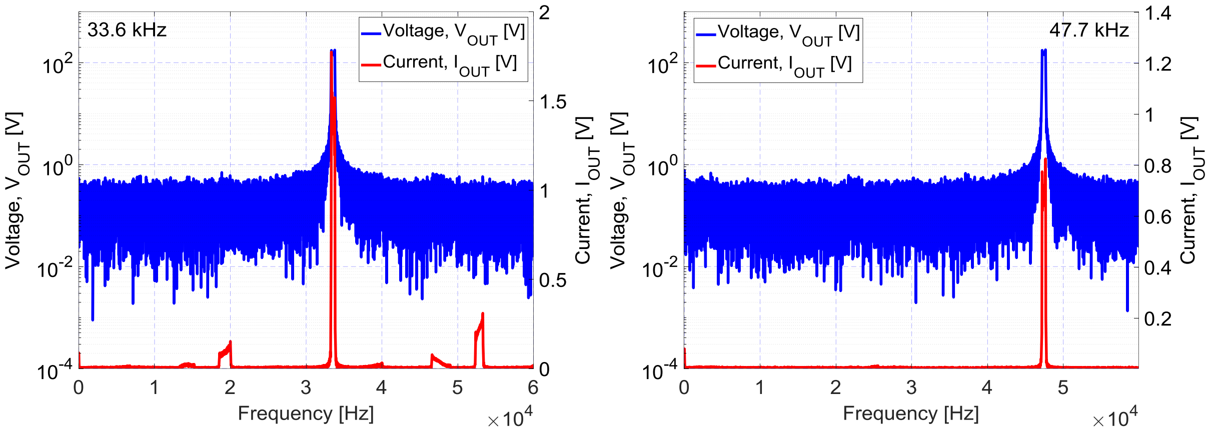

Fig. 48 – TUD Electronics Output DFT

left: waveform 1 at 33.6 kHz | right: waveform 2 at 47.7 kHz

In Fig. 49 are the current and output signals from the CSUF electronics connected with device MET05. In that case, the output voltage as well as the output current both present several peaks when the thruster is excited near a resonance. These results show more distortion, nonlinearity, and noise compared to the amplifier in the TUD electronics.

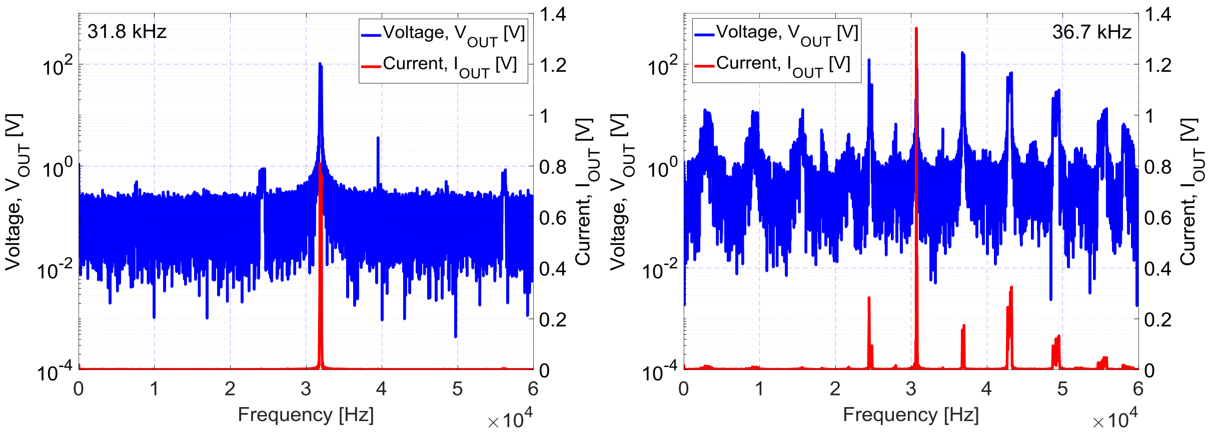

Fig. 49 – CSUF Electronics Output DFT

left: waveform 1 at 31.8 kHz | right: waveform 2 at 36.7 kHz

The next series of diagrams show the combination of MET05 with the different electronics and their effect on the output signals. In Fig. 50, the output current in a driving frequency sweep at constant input voltage between 24 and 48 kHz for MET05 connected to the different electronic setups is shown. The curves were obtained by extracting the amplitude of the first (1ω) and second harmonics (2ω) of the current signal through Fourier analysis. Both frequency components are plotted on the same x-axis, the excitation frequency. Thus, the 2ω component for an excitation frequency of 35 kHz, for instance, was observed at 70 kHz. All tests were performed with the same mechanical setup to compare the effect of electronics on the resonance spectrum of the thruster and examine the different nonlinearities. The gauge signal of the passive piezo-disk is not shown here, but was seen to follow the same nonlinear behavior as the current.

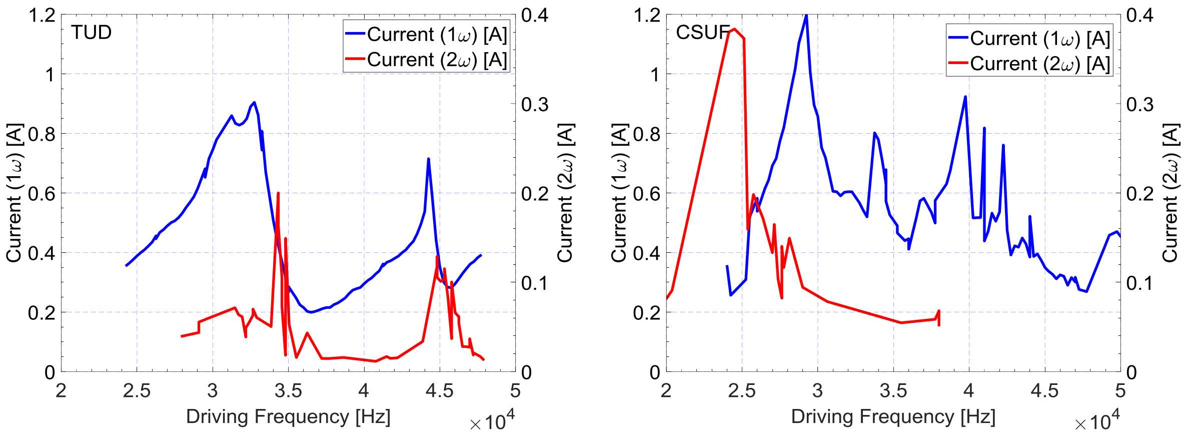

Fig. 50 – MET05 Electronics First and Second Harmonic Spectra

left: TUD electronics | right: CSUF electronics

The first graphs show the constant voltage amplification and the absence of nonlinearity in the output voltage over the frequency range. The resonances are visible in the current and gauge signal curves from the peaks at 31, 34, and 44 kHz. Furthermore, the nonlinearity in the current is also increased around the resonances. As expected, since the audio amplifier's performance depends on the load's impedance, the voltage is not constant despite the constant driving signal due to the fluctuating impedance of the piezoelectric load. There is increased noise between 37 and 42 kHz, which is shown by the irregular distribution of values in the left diagram, as well as the increased amplitude of the second harmonic signals in the right diagram. The resonance frequencies are 29, 33, and 38 kHz and have been shifted to the left when compared with the TUD electronics. Higher voltages can be reached, but there can be no higher vibration, as the remaining energy is converted to heat. This was also observed by Uchino [100] during the analysis of piezo-actuators under high-power driving conditions.

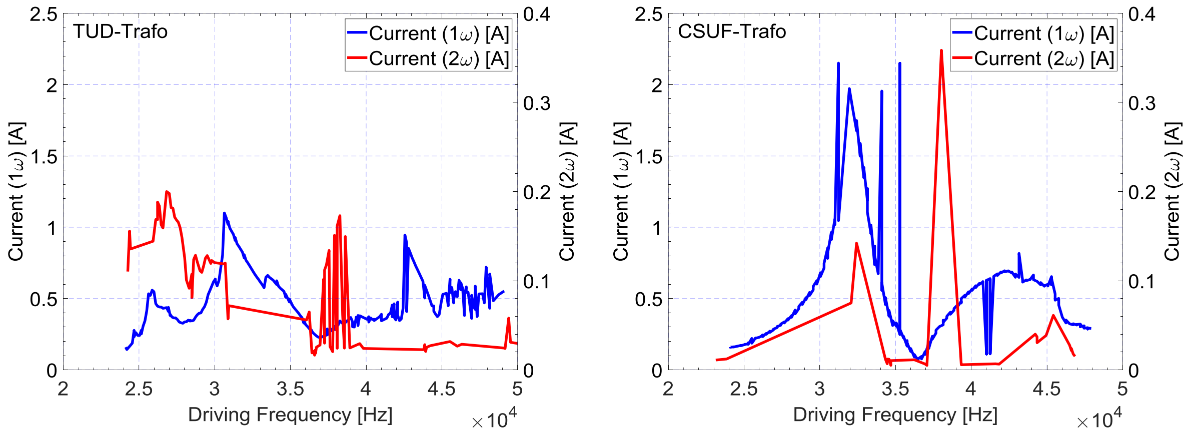

Fig. 51 – MET05 Spectra with Transformer (1:2)

left: TUD electronics with transformer | right: CSUF electronics with transformer

Adding a transformer between the device and the amplifier output results in changing the impedance spectrum. As a result of the added transformer, the resulting voltage output was not constant, even though the input voltage was, and it fluctuated by as much as 60% at certain frequencies. As observed in Fig. 51, a new resonance frequency was created at 26 kHz, and the peak current was at 31 kHz. The second harmonics spectrum shows nonlinearity in both current and voltage waveforms. The next tests were performed by switching the TUD electronics for the CSUF ones. Adding a transformer changed the spectrum more significantly, since the audio amplifier is more dependent on the load. The voltage was not constant over the frequency range, but the resulting output voltage and current were much cleaner, with a single resonance at 32 kHz, less distortion of the signal, and less nonlinearity compared to Fig. 50.

These observations are consistent with the investigation of the piezoelectric properties described in the previous section, and the simulation performed with LTspice, namely:

- The electronics should have a significant impact on the behavior of the device and affect the experiments on the thrust balances.
- The amplifier electronics and transformers have been shown to modify the electromechanical spectrum.
- There is a large nonlinearity present in the electromechanical spectrum, especially around the resonances.
- The behavior of the CSUF electronics presents more noise and nonlinearity than the TUD setup.

Additionally, one could match the load impedance with the output impedance of the amplifier by adding inductive and capacitive loads, as well as using transformers, to maximize energy transfer from the amplifier to the device. However, this was not performed in this research due to the only marginal potential gains, and also since the impedance of the devices changed constantly due to changing external and internal conditions such as heat, stress, and changing material properties.

3.3 Torsion Balances

This section describes the TBs and the mechanical aspect of the MET experiment setup. Torsion balances stem from the earliest type of balance used for the measurement of gravitational attraction, the Cavendish balance, and they rely only on one pivot axis representing only one degree of freedom. TB1 and TB2 were both developed and assembled by colleague Dipl.-Ing. Matthias Kößling [76] and are similar to the TB used by Woodward [16] and by Buldrini et al. [81,120] at the research center FOTEC in Austria as pictured in Fig. 10.

3.3.1 Description

To provide the most accurate force reading, the balance beam is allowed to rotate as freely as possible from mechanical interactions like friction or cable tension. The device-under-test (DUT) is placed in one of the boxes at one end of the balance beam, while a counterweight is placed on the other side of the beam to even out the moments on the beam support. A Fabry-Pérot type interferometer with 1 pm resolution from attocube (IDS3010), and 2 nm noise at ambient temperature, detects the displacement of the experiment box with great accuracy. The beam displacement can be converted to a force, with the knowledge of the balance's stiffness and beam length. In practice, the calibration of the balance is performed by imparting a force on the other end of the beam using a voice coil (VC) system to impart a known force; the copper coil is placed on the fixed structure next to the balance, and the permanent magnet is attached to the moving beam. Thus, the performance of the balance depends on the accuracy of the interferometer, the friction-free rotation of the central pivot point, and the linearity of the VC calibration.

The realization of the fifth iteration of the nano-newton TB is presented as a rendered CAD model in Fig. 52 on the left, and a picture with parts descriptions on the right. Both are isometric views of the balance. Liquid metal contacts are essential to providing power to the experiments on the balance without adding torsional forces on the beam. The low viscosity, good conductivity, and very low vapor pressure of Galinstan are especially useful for high-precision, frictionless vacuum experiments [121]. The experiment box can be rotated by a motor to test different thruster orientations without having to break vacuum. The calibration is performed by applying known forces with the VC using a precise current source and by measuring the resulting beam displacements. The different parts and the calibration process are described in more detail in a separate publication [22].

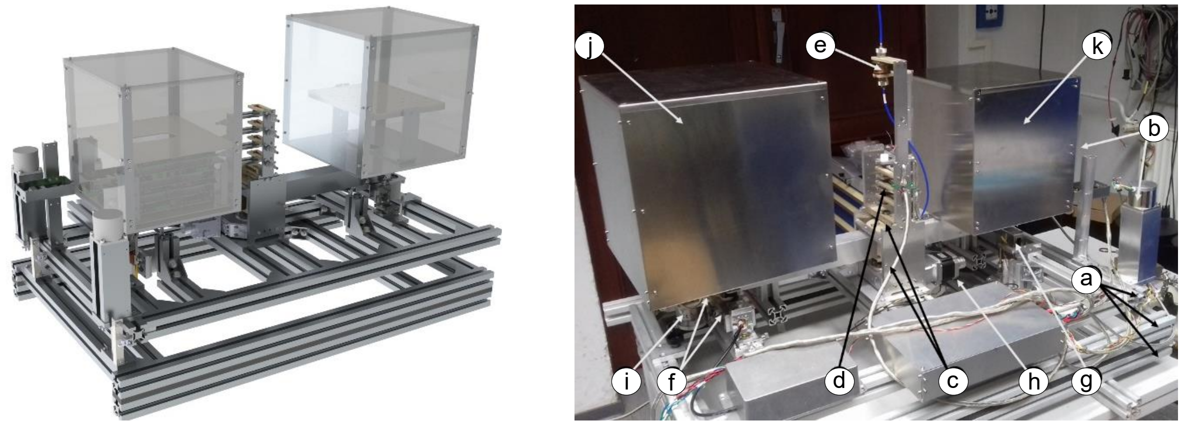

Fig. 52 – TB1 CAD and Picture

a) aluminum profile structure, b) tilt motor controls and shaft, c) torsion bearings from C-flex, d) liquid Galinstan power contacts, e) high-frequency feedthrough (not used), f) VC, g) adjustable eddy-current damping, h) central pivot rotation motor, i) experiment box rotation motor, j) experiment box with mu-metal shielding, k) electronics box with mu-metal shielding.

The next iteration, TB2, was made to accommodate smaller experiments to increase the measurement accuracy and the electromagnetic shielding. It is shown in Fig. 53 and described in more detail in a separate publication [76].

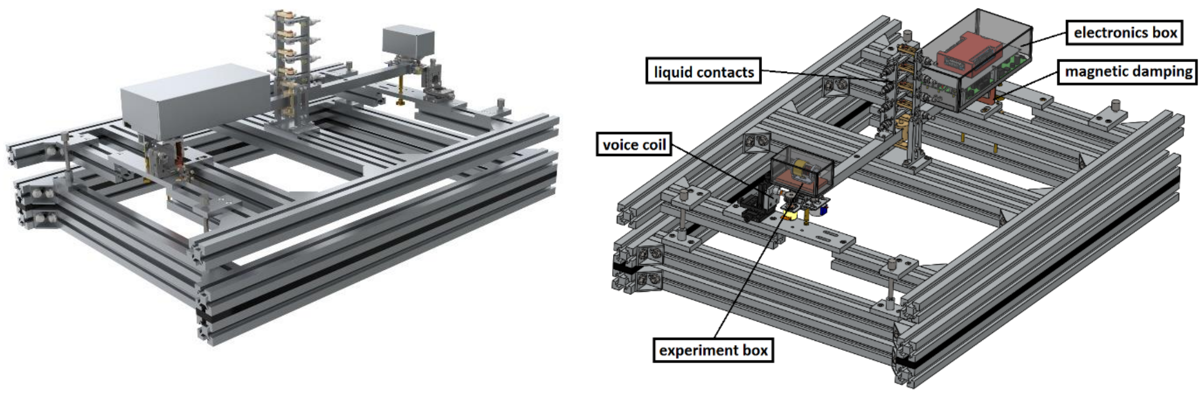

Fig. 53 – TB2 CAD

left: CAD isometric render | right: CAD isometric view with descriptions

Again, the important elements are the VC, the source-meter for calibration and precise command of the calibration force, the liquid contacts that offer force-free power transmission, the damping, the interferometer, and the overall geometrical features of the balance. Balance TB2 is nimbler than balance TB1 but it can also support less experimental load. Furthermore, TB2 integrates better electromagnetic shielding of the cables and experiments using mu-metal plates on the beam.

3.3.2 Characterization

The balances underwent different tests to characterize their time-response, and reaction to experimental artifacts and noise over different time periods. A thorough error analysis of the voice-coil calibration and behavior of TB2 already identified an absolute error of 6.4 % for a measured force of 1 µN and 11.9 % for a 10 nN force measurement [76]. The uncertainty for TB1 was estimated around 10 % for a 1 µN force measurement [23]. The tests shown in this section included a 3-axis calibration, pulses of different lengths, square and sinusoidal excitation with the VC, as well as noise evaluation in different conditions. This way, the damping and period of the balance were first investigated using the simple pulse response. By varying the position of the copper plate within the magnet, it was possible to vary the strength of the eddy-current damping. Fig. 54 shows the input VC pulse and the balance responses next to one another for both balances at a fixed damping ratio. These force diagrams show the calibrated force equivalent to the observed beam displacement, as well as the calibrated force equivalent to the commanded voice coil current. The pulses were also used for the regular balance calibration performed at least once a day, before and after each test series, where the steady-state force after a generous 10 s overshoot is selected as the average force for the calibration plots. The ideal damping was selected for a minimal overshoot, corresponding to a damping ratio of about 0.8 as suggested in the literature [122].

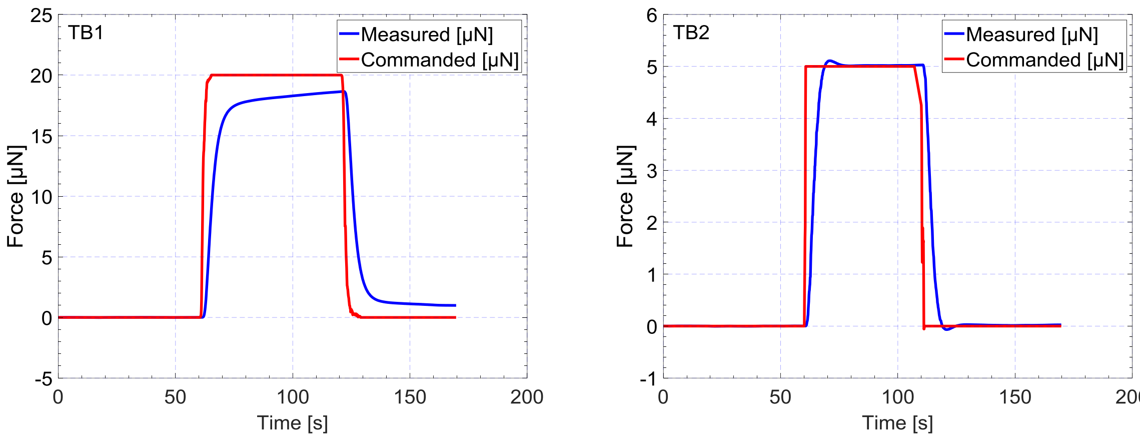

Fig. 54 – Voice Coil Pulse Responses

left: TB1 | right: TB2

Another important measurement is the noise experienced over different time intervals. The noise seen in an interval of around one minute is one that particularly affected the force measurements. Fig. 55 represents one balance response profile for each balance and shows the noise over a short-term period. It can be seen, that TB2 is subject to significantly less noise than TB1. Of course, several force response profiles can be averaged to reduce the overall noise in the force measurement. Note that the sampling frequency of the noise measurement for TB1 was around 10 Hz compared to 100 Hz for the TB2 measurement, which explains the fuzziness appearance of the right-hand diagram.

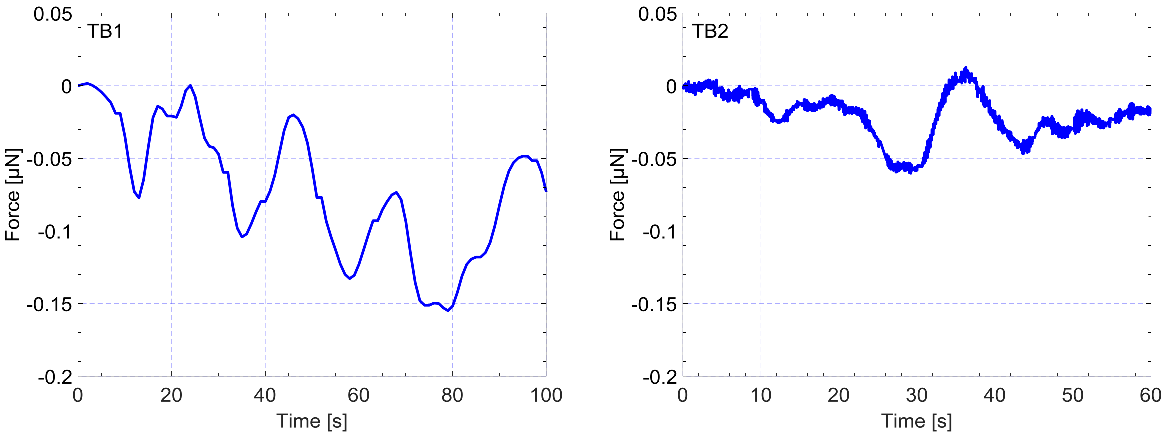

Fig. 55 – Short Term Noise in Vacuum

left: TB1 | right: TB2

Fig. 56 plots the balance drift over a longer time interval resulting in around 10 nN/min for TB2 and 8.3 nN/min for TB1, with the same sampling frequency of 10 Hz for both balances. The drift is most likely due to the small temperature change over the day-night cycle and the thermal expansion of the parts of the mechanical system. The difference between the two balances can be seen again in these longer-time samples. Since the force response line is finer for TB2, generally indicates less noise compared to TB1, as was seen in Fig. 55.

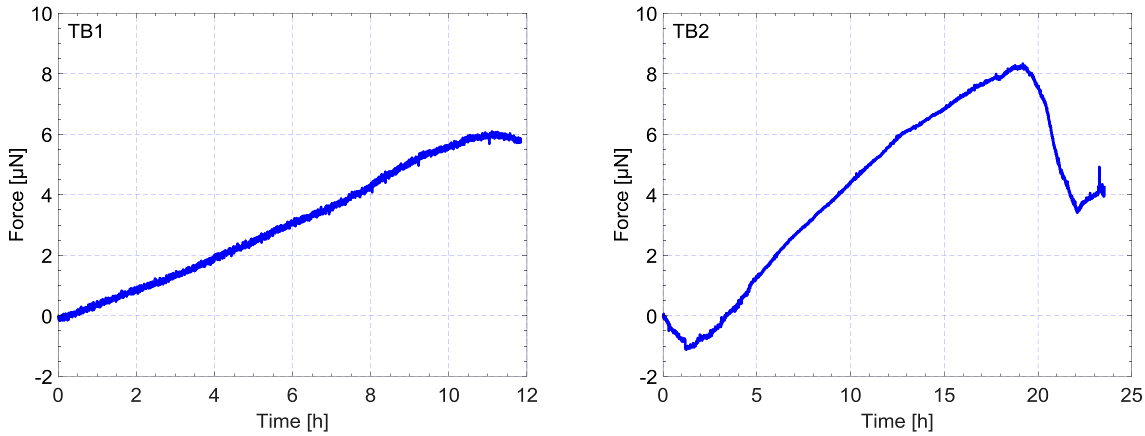

Fig. 56 – Long Term Noise in Vacuum

left: TB1, start time 00:00 | right: TB2, start time: 06:00 (March)

Then, reaction time tests were conducted with pulses of different lengths to examine the balance response over a broad frequency range. This test is relevant since the piezoelectric resonant conditions might only be active for a few milliseconds or a few seconds at a time. The tests show the maximum force reached depending on the length of the pulse. This behavior can also easily be simulated by a single degree-of-freedom (DOF) spring-mass system for shorter pulses, while the VC command is not adapted for repetition rates above 1 Hz. These measurements were only conducted with TB2 and are shown in Fig. 57, where the commanded pulse and the converted beam displacement are plotted for different pulse widths. The results show that the balance can react quickly to the 0.5 s pulse, albeit with only about 30% of the commanded force.

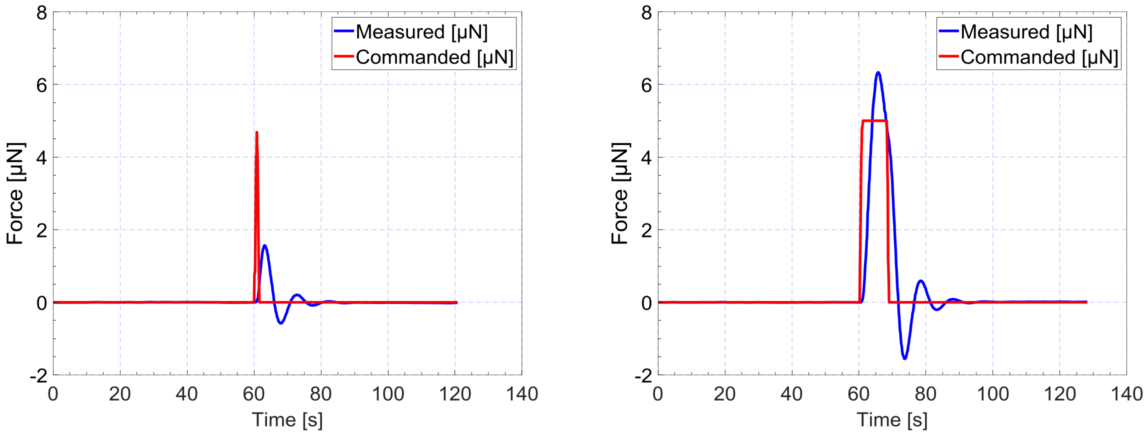

Fig. 57 – TB2 Reaction Time Tests

In another characteristic test, a sinusoidal forcing function with a driving frequency of 0.5 Hz and 1 μN amplitude was commanded with the VC to simulate the action of a vibrating device. The results are shown in Fig. 58. The typical switching transients can be observed, similar to what was observed by Woodward's MET experiment results shown in Fig. 11. The forcing function of 0.5 Hz can be seen in the balance response, and the switching transients assume a greater amplitude than the balance response at the driving frequency. The equipment, however, dictated an upper limit of less than 1 Hz for this experiment.

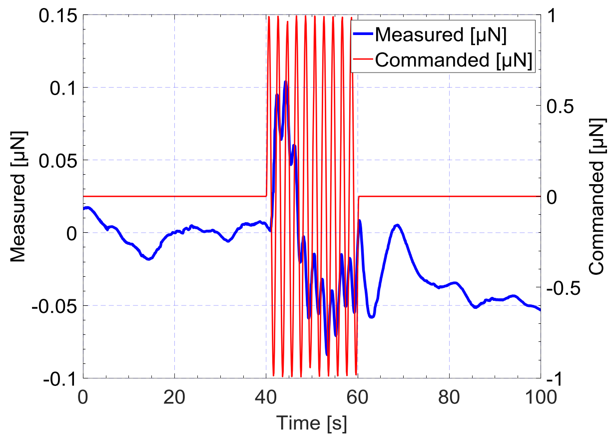

Fig. 58 – TB2 Sine Response

The different axes of the balance were also calibrated to determine the influence of forces in other directions on the balance response. A picture of the setup in Fig. 59 shows the two permanent magnets mounted on the balance beam and the supporting structures for the voice coils for the vertical and thrust test axes. The voice-coil in the parallel/aligned configuration is not shown in the picture.

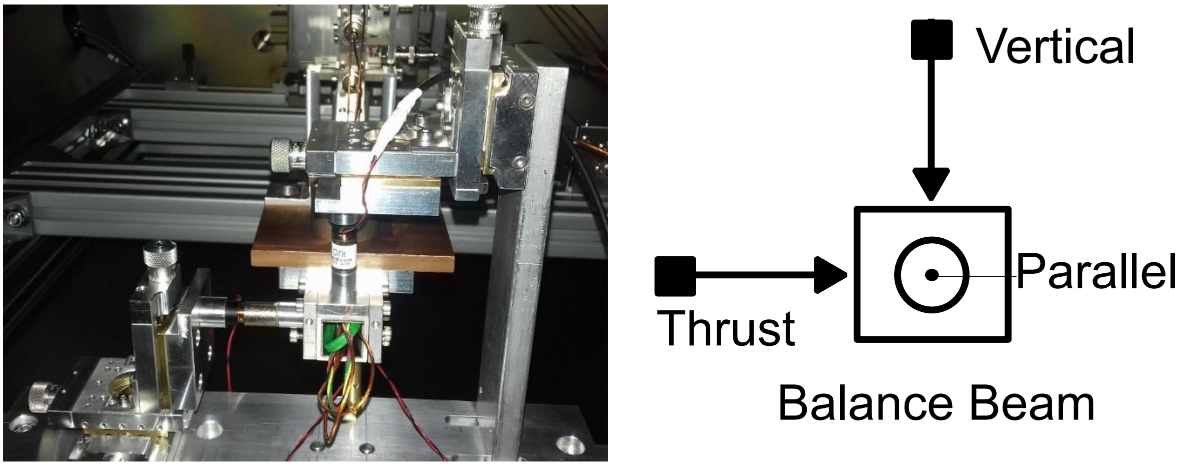

Fig. 59 – TB2 Vertical VC Test Setup

The vertical and aligned VC tests resulted in the force responses shown in Fig. 60, proving that the forces in these axes should not result in a significant force. The ratios of the transverse and parallel forces to the commanded voice coil force were only 0.4% and 0.2% respectively.

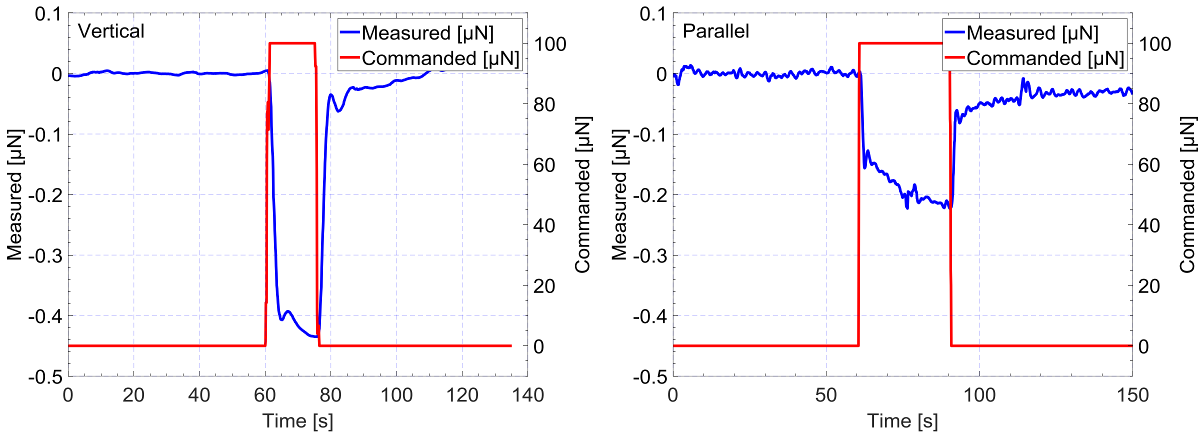

Fig. 60 – TB2 Vertical and Parallel VC Test Results

left: vertical voice-coil setup | right: parallel voice-coil setup

3.3.3 Simulation

Both TBs were simulated using a single DOF spring-mass model shown in Fig. 62. The model is useful to predict the balance's behavior for different types of forces, pulse lengths, and forcing functions. It also makes it easier to determine the deviation of the balance response from normal operation to identify experimental artifacts. Fig. 61 compares the 1D Matlab model with the balance response for TB2. First, the equation of motion is stated:

$$\frac{I\ddot{x}}{r^2} + 2\zeta\sqrt{\frac{I\omega_0}{r^2}}\dot{x} + \frac{J}{r^2}x = F \qquad , \tag{92}$$

where I is the rotational inertia of the balance beam, r is the rotation radius or half the beam length, ω_0 the natural frequency of the balance obtained through experiments, the damping ratio ζ was obtained through trial-and-error, and the rotational spring constant J is given by the supplier [77]. The mass, m, damping, c, and spring constant, k of the spring-mass system pictured in Fig. 62 were obtained using these quantities.

The boundary conditions are summarized below,

$$x(0) = 0, \qquad \dot{x}(0) = 0 \qquad . \tag{93}$$

The list of parameters for TB2 is contained in Table 13, and Fig. 61 shows that the model is very accurate and was used in Section 4.2.4 to analyze different possible artifacts.

Balance	**Rot. Inertia [kg·m²]**	**Radius [m]**	**Frequency [rad/s]**	**Damping Ratio**	**Rot. Stiffness [N·m/rad]**
TB2	0.2	0.35	0.34	0.8	0.0234

Table 13 – TB2 Balance Model Parameters

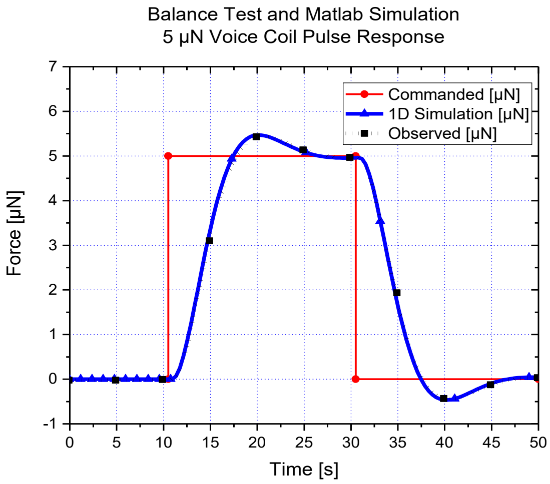

Fig. 61 – TB2 Response Simulation

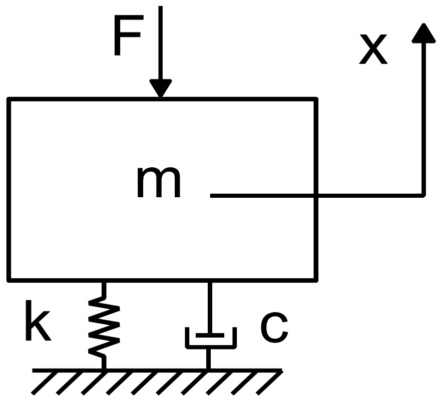

Fig. 62 – Single DOF Spring-Mass System

3.4 Double-pendulum Balance

This section describes the inverted double-pendulum balance and its characterization. DP1 is a different style of balance that relies on dynamic equilibrium and was created and assembled by colleague Dipl.-Ing. Oliver Neunzig. In contrast to TBs, which only rely on one pivot axis, the double-pendulum balance relies on nine pivots. The balance, its calibration, and all the individual parts are described in detail in a separate publication [26]; its accuracy was tested in the measurement of a photon thruster, which resulted in an error of only 15.9% in the measurement of a 2 nN force.

3.4.1 Description

To provide the most accurate force measurement, the platforms are allowed to rotate as freely as possible from mechanical interaction, exempt from friction or cable tension. The DUT is placed on the upper platform of the balance beam, while a counterweight is placed on the lower platform to balance the moments on the balance beams. The same Fabry-Pérot interferometer (IDS3010) from Attocube as used for the TB with 1 pm resolution, 2 nm at room temperature, detects the displacement of the experiment with great accuracy. Calibration of the balance is performed by imparting a force on the other end of the beam using a calibrated VC; the copper coil is placed on the fixed structure next to the balance, and the permanent magnet is attached to the moving platform. Thus, the performance of the balance depends on the accuracy of the interferometer, the friction-free rotation of all pivot points, and the linearity of the VC calibration. Below is a sketch of the concept. The main difference with this balance lies in the different supports for the experiment since each plane is connected to three flexural bearings, ensuring more twisting stability. The nine pivot bearings allow all three platforms to deflect according to the sketch below. The platforms allow better stability and resistance to undesired torques coming from the DUT, as opposed to the TB. The image of the CAD concept shows the fully built balance with the three beams, the aluminum profile structure, and the liquid metal contacts in the far corner are also using Galinstan. The VC calibration system is located on the lower platform, on the same side as the lens and laser interferometer. Fig. 63 shows the double-pendulum balance sketch, CAD, and the assembled instrument is shown in the large vacuum chamber (LC) in Fig. 64.

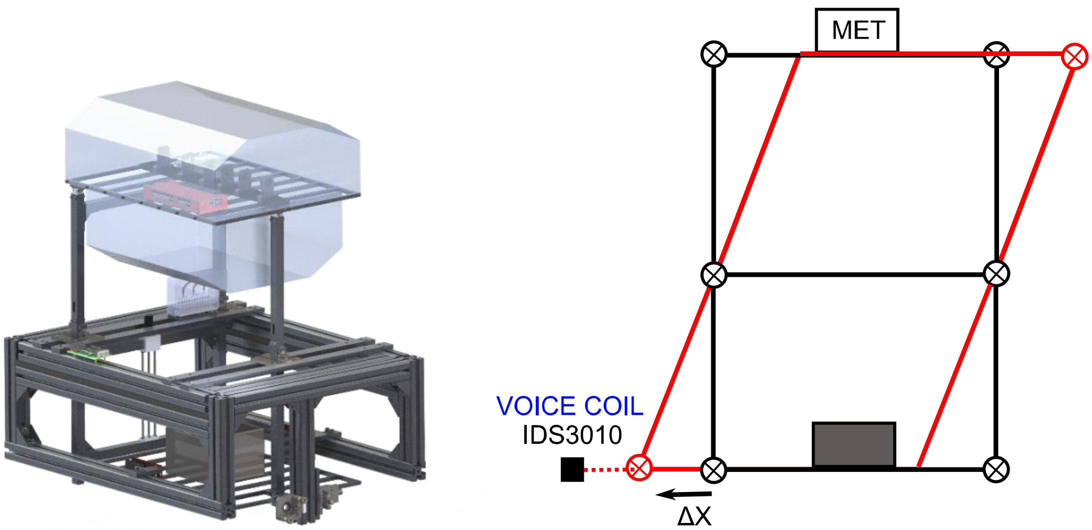

Fig. 63 – DP1 Sketch and CAD

left: CAD generated picture | right: concept diagram

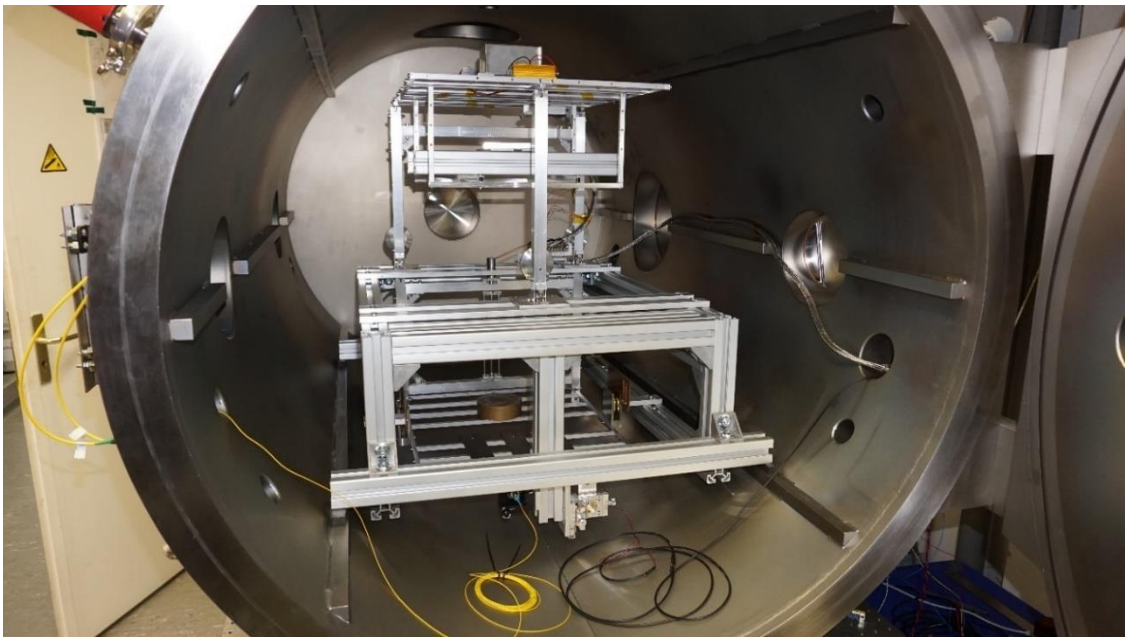

Fig. 64 – DP1 Picture

The force measurement capability of the DP1 is about the same as TB2. The differences to the TB are not numerous, but the test object is supported by a stable platform with three support points, rather than being placed on a single beam.

3.4.2 Characterization

The first tests performed in the framework of the calibration showed that the balance could be simulated using a 1 DOF mass-spring system as well. This behavior was precisely analyzed in a pulse response plotted in Fig. 65, which shows that the settling time of the balance is slightly shorter than 20 seconds after a slight overshoot.

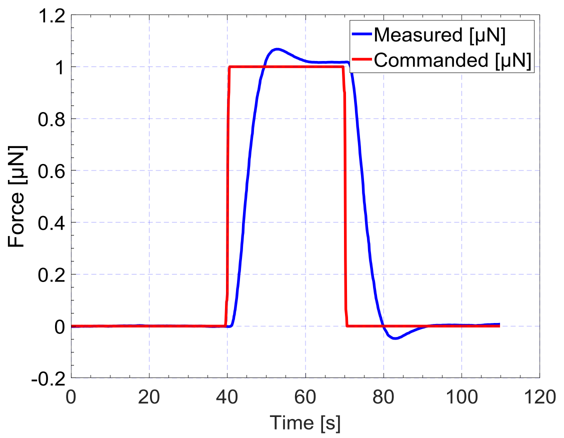

Fig. 65 – DP1 Voice Coil Pulse Response

The next set of characteristic tests consisted of a series of fast pulses using the VC and precise command of the current with the current source. An interesting result shown in Fig. 66

demonstrates that a forcing frequency above 1 Hz cannot be seen in the balance response, but a larger transient is detected nonetheless. The DC component of the force is only seen if a positive bias is added to the oscillation. When alternating the force pulse using a sinusoidal forcing function, the forcing frequency of 0.5 Hz could be seen and the switching transients were also observed just like in Woodward traces [16] and the results with TB2 [24].

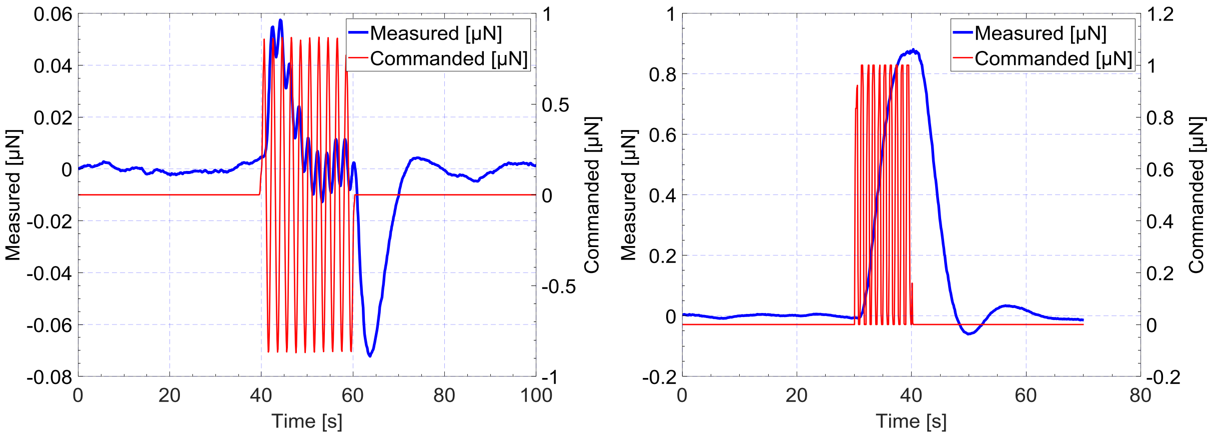

Fig. 66 – DP VC Pulse Tests

left: 0.5 Hz sinusoidal oscillation | right: 1 Hz square pulses

Fig. 67 shows the noise during a night log of the balance behavior in the vacuum chamber. The noise is shown over short- and long-time intervals. Sources of transient noise can include walking colleagues, vibrations from cars on the pavement near the building, oscillations of the rest atmosphere, or changes in the temperature of the mechanical parts. The long-term drift is calculated to be about 180 nN/min, one order of magnitude greater than the TB drift. This behavior can be explained by the increased complexity of the balance, the number of parts that can be affected by thermal expansion, and the increased surface area subject to the rest atmosphere. The short noise segment shows the absence of high-frequency vibration, most of the noise observed is due to the balance drift, which can be removed mathematically.

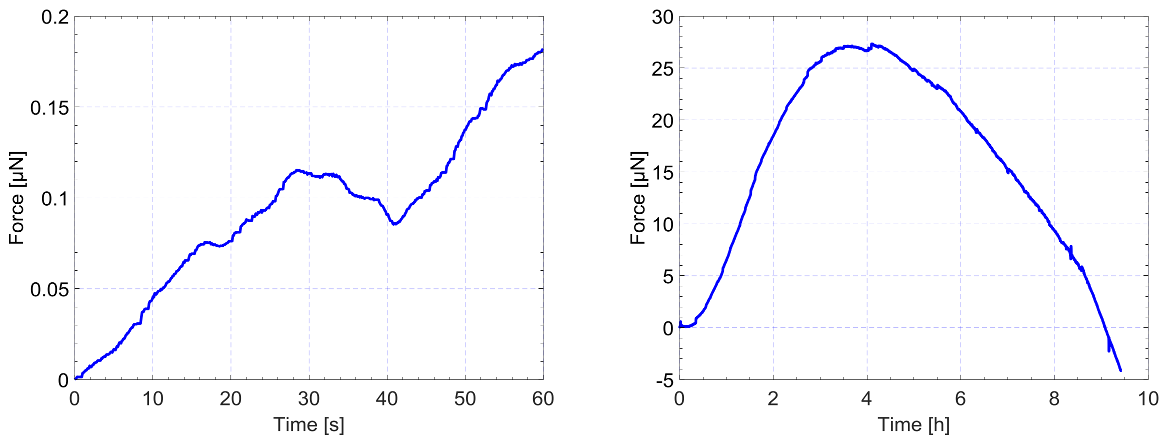

Fig. 67 – DP Noise Log

left: short-term noise | right: long-term noise, start time 01:00 (February)

There were no tests in the vertical and lateral directions like with TB2, so this balance is not as well characterized as the TB. However, since the platforms of the balance are more stable than the torsion beam in response to transverse forces, it can be assumed that the balance response to forces coming from other directions than the thrust direction are even lower than with TB2.

3.5 Laboratory Setup

Most experiments were performed in vacuum during the night and during the weekends to avoid noise and distortions coming from walking colleagues or cars circulating in the neighboring streets. Thus, the tests were largely automated. The description of the vacuum setup and automatization methods include the vacuum chambers, the measurement loop, the LabVIEW software, and the test structure.

3.5.1 Vacuum Chambers

Two vacuum chambers were available, although most experiments were performed in the LC, pictured on the left in Fig. 68. The Large Chamber (LC) is 1.45 m long and has a 0.88 m diameter, with a whole volume of 0.88 m^3. It is equipped with a pre-vacuum scroll pump and a high vacuum turbopump. The Overly Large Chamber (OLC), pictured on the right, is equipped with a pre-vacuum scroll pump and a very high vacuum cryopump. Its dimensions are 1.2 m by 1.5 m by 2.5 m with a total volume of 4.5 m^3. The pictures portray an isometric view of the respective chambers.

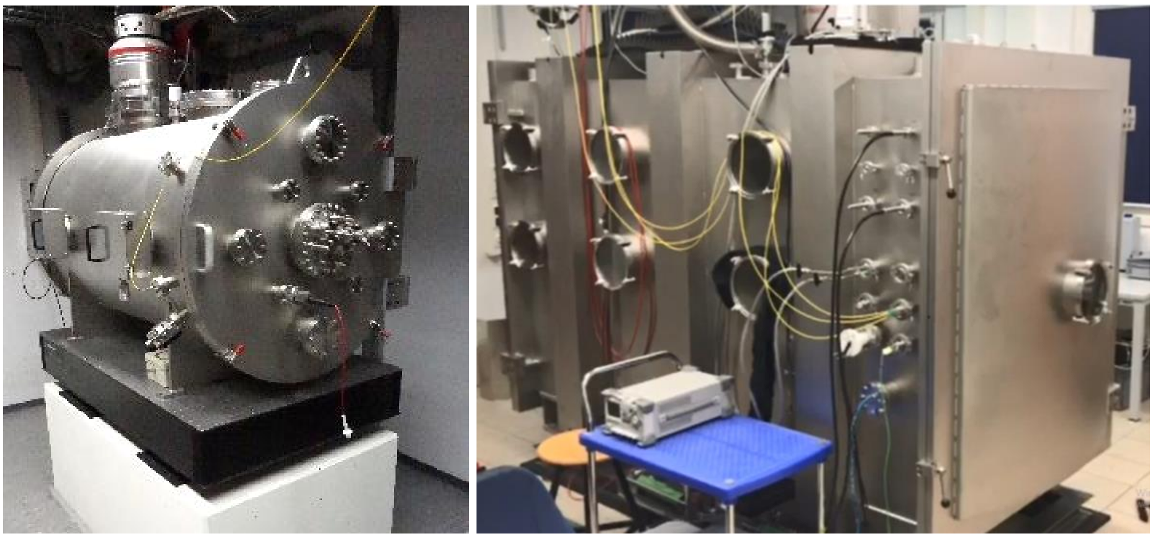

Fig. 68 – Overview of Vacuum Chambers
left: Large Chamber (LC) | right: Overly Large Chamber (OLC)

Table 14 summarizes the important parameters of these chambers and their pumps. Reaching a high vacuum was possible with both chambers, however, the end pressure was lower in the OLC because of the cryopump. Both the turbopump and the cryopump added a high-frequency vibration component that was detected by the balance, and thus had to be turned off during the measurement. The vibration of the scroll pumps was significantly lower and was not transmitted to the balances. The average mean-free-path (MFP) and Knudsen numbers are calculated using known formulas and can also be found in the table. According to the Knudsen number given by Equation (94) for a Boltzmann gas,

$$K_n = \frac{k_B T}{\sqrt{2}\pi d^2 p L} = \frac{\lambda}{L} \quad , \tag{94}$$

where the characteristic length is the diameter of the vacuum chamber, the flow can be characterized as such:

$K_n < 1$	Continuum flow
$0.01 < K_n < 1$	Slip flow
$0.1 < K_n < 10$	Transitional flow
$K_n > 10$	Free-molecular flow

The results show that the air flow in both chambers after using the pre-vacuum pump stays in the continuum regime. Using the cryopump results in a free-molecular flow with very rarefied air. The flow in the LC chamber is in the transitional regime. One of the test batches was performed in the OLC at very low pressure to provide a comparison and examine the influence of the flow regime in the chamber.

Pump	Chamber	Model	Brand	Suction Power [L/min]	Ultimate Pressure [mbar]	Average MFP [m]	Knudsen Number
Scroll	LC	XDS35i	Edwards	580	10^{-2}	$1.1 \cdot 10^{-3}$	0.001
Turbo	LC	HiPace 2300U	Pfeiffer	32	10^{-7}	$5.7 \cdot 10^{-1}$	0.648
Scroll	OLC	Ecodry 65 Plus	Leybold	920	10^{-2}	$1.9 \cdot 10^{-3}$	0.002
Cryo	OLC	Coolvac 10000 iCL	Leybold	167	10^{-9}	$5.7 \cdot 10^{4}$	47500

Table 14 – Vacuum Pump Features

The pressure curves for both types of vacuums can be seen in Fig. 69. The experiments were mostly performed in the medium vacuum from the scroll pump at a stable pressure of 0.03 ± 0.004 mbar. The scroll pump was always left on during the experiments and the chamber pressure was held constant. The pressure is not plotted along with the force measurements, since it was observed to stay at the pump’s end pressure without significant deviations.

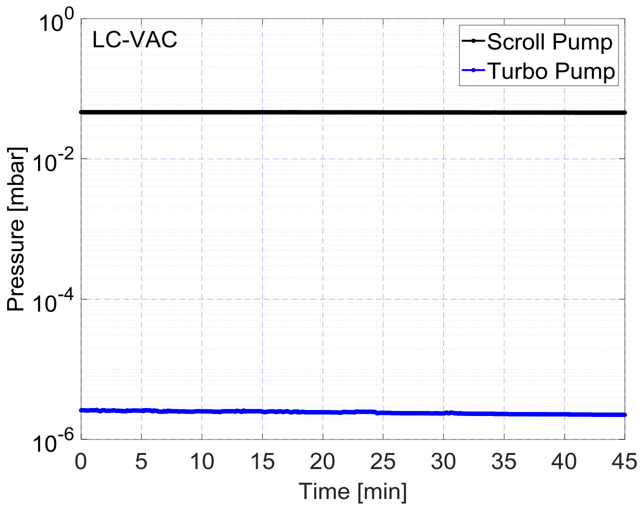

Fig. 69 – Vacuum Pressure Curves

3.5.2 Software and Test Setup

The test setup is described in Fig. 70 and it consists of the TB with the test device and electronics, as well as the vacuum chamber and the data acquisition system. To communicate to the balance and collect data, a vacuum chamber feedthrough is necessary. The box containing the DUT is the experiment box, and the other side is the electronics box. All electronic devices used in the tests such as the amplifiers (AMP), power supplies, sensors, gauges, motors, and communication devices are outside of the vacuum chamber and were implemented in LabVIEW by Prof. Tajmar to allow automated control. Signal sampling, processing, automation, script, and averaging of the data were also performed using LabVIEW. Fig. 70 shows the flow chart of the test setup, the vacuum chamber feedthrough, and the connection with the balance and electronics box.

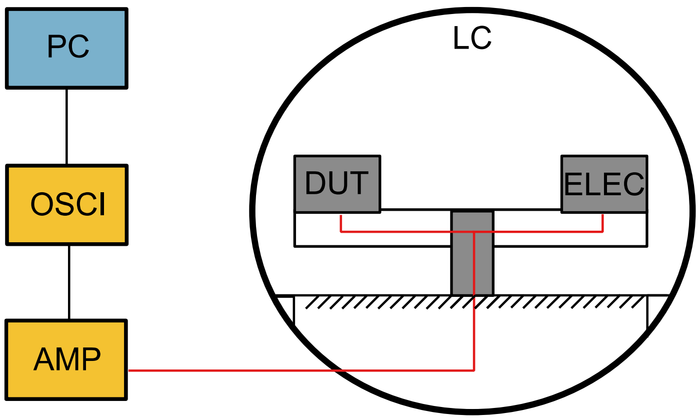

Fig. 70 – Balance Test Setup

The oscilloscope (OSCI) was connected to the PC and LabVIEW was used to coordinate the signal generator and power supplies. The devices were mostly connected through a MOXA card and a COM port allowing them a data transfer rate of 9600 bits per second. The experiment management software set a data sampling rate of 10 Hz, thus allowing enough time for the communication with all active devices. Some devices, such as the pressure gauge from Pfeiffer, sometimes needed longer than 0.1 seconds to communicate the pressure value, which resulted in the program copying the same value for multiple time entries in these occasions. In Table 15 is an overview of the devices that were connected to the LabVIEW Software and includes thermocouples, a Pfeiffer vacuum gauge, four oscilloscope channels, a frequency generator, power supplies, the interferometer, the stepper motor for rotating the experiment box, analog-to-digital input converters (Labjack) for temperature reading. For faster reading in the case of a higher sampling rate in the case of sweeps or other tests, a few devices were disconnected. An attempt is made in Table 15 to summarize the communication parameters between the devices and the PC using LabVIEW. The entries in Table 15 correspond to the maximum capacity of the devices.

Device	Model	Max Data Rate [Hz]	Data Size [bits]	Connection
ADC Toolkit	Labjack T7	~ 100	12	USB
Interferometer	Attocube IDS 3010	60	12^*	Ethernet
Oscilloscope	Picoscope 5442B	$4 \cdot 10^4$	12	USB/WIFI
Motors	OWIS DMT-100-D53	80	<120	USB
Pressure Gauge	Pfeiffer PKR361	40	240	Serial
Power Supply	EA-PS 5200	50	192	USB

**analog output*

Table 15 – Device Connections

The test profile structure is detailed in Fig. 71: Sector 1 is the first delay, Sector 2 is the ramp-up time, usually very short with 0.1 s, Sector 3 is the main pulse where the electric field is applied, Sector 4 is the ramp-down time, again very short with 0.1 s, and Sector 5 is the final delay, allowing the balance to settle down again. This profile structure is maintained throughout the entire test campaign.

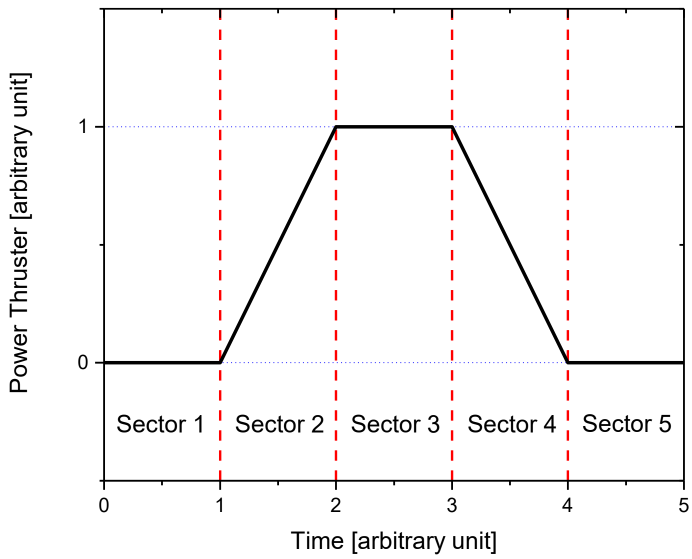

Fig. 71 – Profile Structure

The results can also be visualized, sorted, filtered, and adjusted in LabVIEW to remove all sorts of drifts and outliers, and to reduce the overall noise. The individual runs or an average of all the runs can be visualized as well as all the different parameters monitored such as current, voltage, temperature, pressure, etc. The tests were all automated and written using a script file along with the proper settings. The standard test run is composed of five sectors, portrayed in Fig. 71. This format allowed an automatic averaging of runs. Different drift removal techniques for data analysis can be implemented in one or more specific sectors.

Furthermore, the resonance tracker was programmed in LabVIEW specifically for the MET experiments. By commanding a constant voltage, measuring the current over the MET, and varying the driving frequency over the range of interest between 24 and 48 kHz, the resonances and their associated current peaks can be identified. After having performed a sweep and selecting the smaller frequency range in the area of the peak, the resonance tracker automatically varies the frequency back and forth to increase the output current and stay on resonance. The step size and time increment can be varied to optimize resonance tracking. The tracker was used in the TB1 experiments.

Lastly, another important LabVIEW feature that was programmed to simplify the data analysis is called drift removal or thermal correction and is explained in detail in a previous publication [23]. The feature is shown here again for completeness. In all diagrams shown in Chapters 4 and 5, the balance drift of Sector 1 has been removed, as it applies to all three sectors equally, and does not originate from the DUT. Furthermore, the thermal drift in sector 3 has not been removed unless specified by the mention “thermal correction (TC)”.

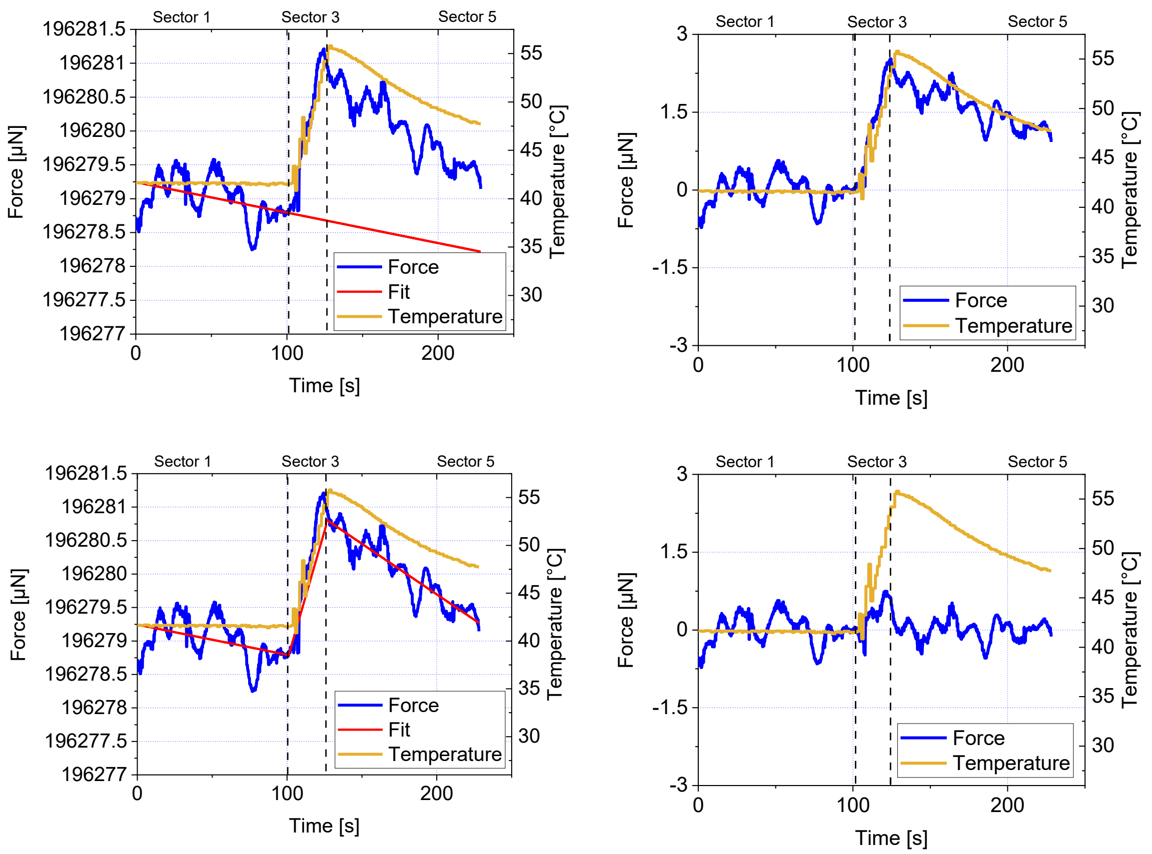

Fig. 72 – Drift Removal Process [23]

top left: raw data with sector 1 fit | top right: data with sector 1 drift correction

bottom left: raw data with thermal correction fit | bottom right: data with thermal drift correction

4. Thrust Balance Experiments

This chapter contains a summary, analysis, and discussion of the tests performed with TB1, TB2, and DP1. Each section gives an overview of the experiments performed on a single balance. The test results are grouped in sub-sections for each DUT, and each one includes pictures of the experimental setup, describes the test framework, and presents the force diagrams for key experiments. Each chapter is followed by a discussion of the lessons learned and the observations made. The results show the force measurements, or converted beam positions, as well as the voltage (V_{OUT}) or current (I_{OUT}) over the DUT during the experiments. The y-axis just represents force, voltage or current. Table 16 first regroups the capabilities of each thrust balance and compares them to Woodward's TB.

Balance	Bearing	Max. Load [kg]	Period [s]	Resolution [nN]	Noise [nN]	Beam Length [cm]
TB1	E-20 (2)	10	20	5	11	81
TB2	A-20 (2)	2	15	0.5	1	70
DP1	DD-10 (9)	10	12	0.5	1	30
WW [14]	E-10 (2)	5	5	100	200	44

Table 16 – Overview of Thrust Balance Properties

4.1 Torsion Balance I Test Results

4.1.1 Dummy Tests

The first tests consisted in examining electromagnetic and thermal interactions on the balance. Dummy tests help to detect experimental artifacts linked with the operation of electronic devices on the balance that can be mistaken for thrust. Knowing the cause of experimental artifacts enables one to reduce or eliminate the source of noise to obtain clearer thrust signals during experiments, or if the source of noise cannot be eliminated, to identify the level of distortion from experimental artifacts, as well as the balance's measurement limit. Once voltage is applied to resistors, for instance, current flow generates heat as well as a small magnetic field due to the inductive properties of nonideal resistors and cables leading to it. Since the resistors are not intended to produce thrust, any beam deflection represents an experimental artifact. The dummy tests included both DC and AC voltage experiments to examine their interaction with the balance, although, there are no DC components during MET experiments. The resistors had a total resistance of 26 or 33 Ω, chosen to approach the MET resistance around resonance. The resistors can be seen on the balance in Fig. 73. The experiment box was not rotated in different directions for this experiment. Table 17 summarizes the parameters and test conditions for all dummy experiments.

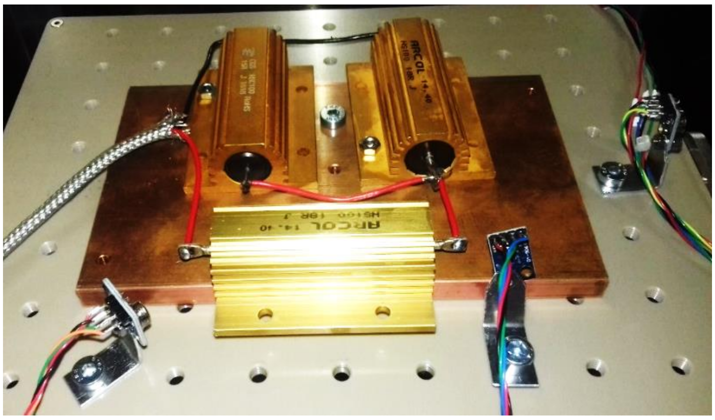

Fig. 73 – TB1 Resistor Dummy Test Setup

Resistor	No. Tests	No. Profiles	Voltage [V]	Pulse Time [s]	Signal Type
33 Ω	4	200	28	60	DC
33 Ω	1	200	28	60	AC
26 Ω	2	160	75	25	AC

Table 17 – TB1 Dummy Test Series

The plots seen in Fig. 74 show the results of DC voltage tests with the resistors. The force measurement shows noise with an amplitude of 0.1 μN at the sampling frequency of 10 Hz. The high-pass filter of the interferometer was set to 20 Hz. The TC graph on the right, shows how the thermal drift resulting from the current flow can simply be removed over the entire profile. Thermal correction also reveals a negative offset of around 0.2 μN in the force baseline during Sector 3, during which a voltage is applied. The offset most likely results from an electromagnetic interaction, since the temperature increase was below 0.1 °C.

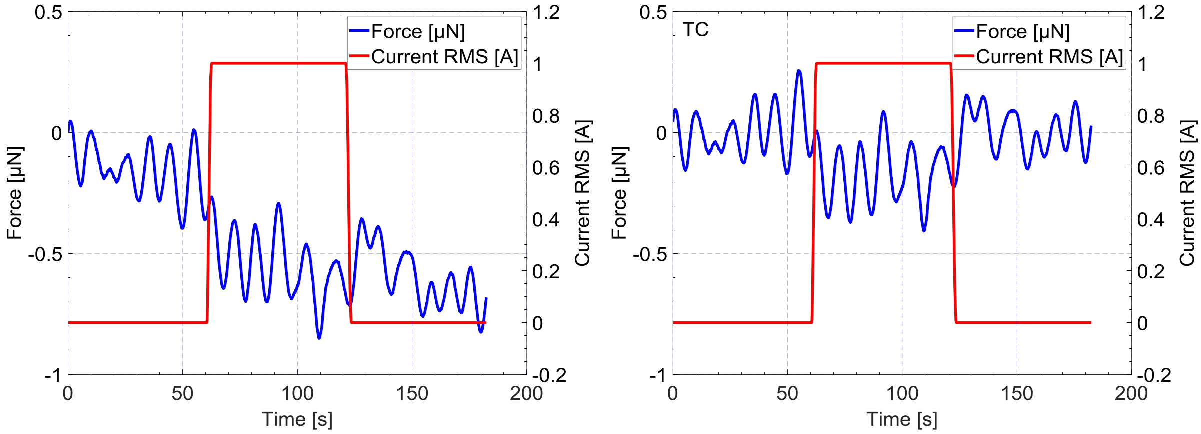

Fig. 74 – TB1 Resistor DC Test

left: no thermal correction | right: with thermal correction

AC voltage tests were conducted with a current of 3 A at a frequency of 9.6 kHz. The oscillation results in a stronger interaction with the balance, as seen by the stronger drift of 1.5 µN after applying the current, in Fig. 75. The behavior could be due to the thermal drift, since the current was higher than in the previous experiment, however, the increase in temperature as measured by the thermocouple on the copper block is below 0.5 °C. Moreover, after TC, the force trace shows a Woodward-type trace with small switching transients, as seen Fig. 12, with a steady-state component of around 0.25 µN. The effects seen in individual profiles are very close to the noise of the balance which is why the test runs are averaged over 200 profiles to increase the SNR. Thus, the dummy tests show the presence of thermal drift and possibly electromagnetic interaction (EMI). Fortunately, these effects are smaller than the predicted thrust levels.

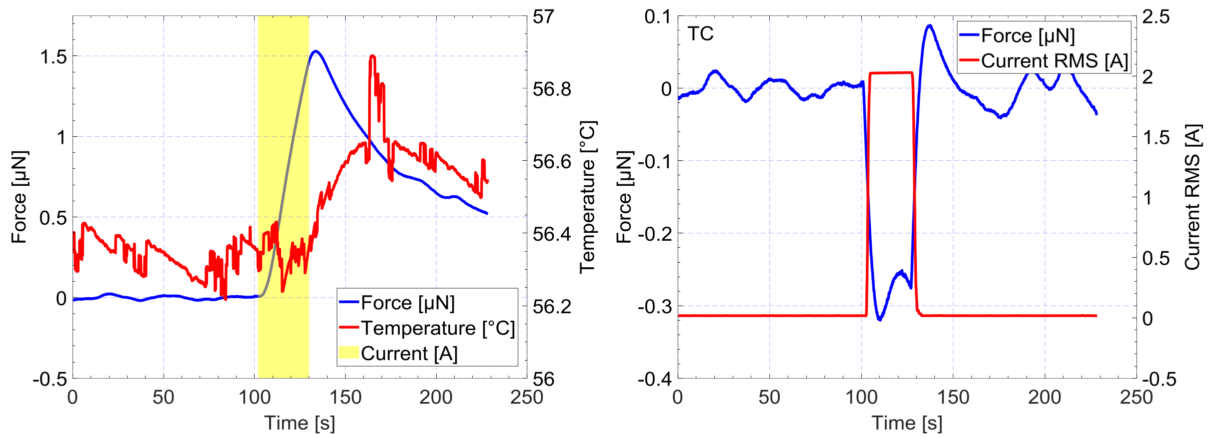

Fig. 75 – TB1 Resistor AC Test

left: no thermal correction | right: with thermal correction

4.1.2 CU18A

The magnetostrictor was introduced in Section 3.1.4 and was driven at different frequencies with a fixed voltage. During the tests, possible artifacts include the presence of EMI, thermal effects, and vibration. Heat generation is kept minimal, since the device has good thermal insulation and a copper plate was added to quickly dissipate the heat. The predicted Mach-effect thrust force for the magnetostrictor with an attached mass of 52 g is 0.125 N for the mixed-mode driving. In the absence of a significant nonlinear signal, the predicted thrust for the single-sine driving is close to null. As seen previously, the resonances should be around 17 kHz without tail mass and 9.6 kHz with it. In Fig. 76, the actuator is mounted on the PEEK plate inside the experiment box on TB1. The orientation seen in the figure on the left corresponds to orientation 0° with the mass located on the right and the actuator is in the balance's torsional plane, perpendicular to the balance beam. According to the balance configuration described in Chapter 3, a positive balance displacement or positive force entails that the thrust force is directed towards the end with a mass resulting in a clockwise rotation of the balance arm; thus, the actuator below would be moving to the left. 90° is the orientation shown on the right with the mass on the outside of the balance; the experiment box is simply rotated by 90° in the clockwise direction. Table 18 summarizes the tests performed with the magnetostrictor. The sensors that can be seen mounted to the side of the actuator are infra-red temperature sensors (MLX90614).

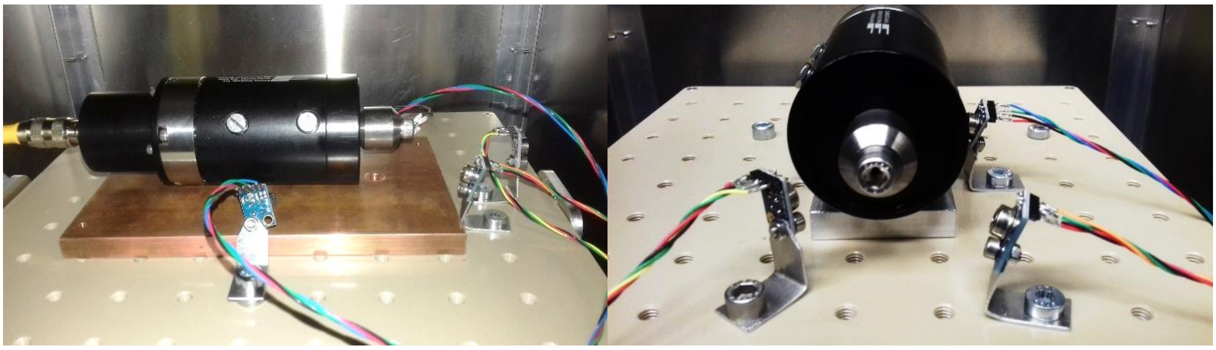

Fig. 76 – CU18A Magnetostrictor Test Setup
left: 0° configuration | right: 90° configuration

No. Tests	Mass [g]	No. Profiles	Voltage [V]	Pulse Time [s]	Signal Type	Particularity
10	0/52	200	75	20	Single	Tracker
15	0/52	160	37	60	Mix	No Tracker
2	0/52	160	75	25	Sweep	No Tracker

Table 18 – TB1 Magnetostrictor Test Series

The first tests were performed without a tail mass attached to the magnetostrictor and the results are shown in Fig. 77. Again, a comparison between graphs before and after TC for the 0° configuration shows how the balance drift can be removed. These tests also represent good dummy tests, since there is less thrust predicted for this configuration. The difference between 0 g at the tail mass and 52 g at the tail mass represents an increase from 36 W to 100 W in driving power. In this case, the 0°, 90°, and 180° orientations were tested, and are shown in the diagrams. The signals observed during active voltage are just above the noise in all cases, have the same shape as the noise peaks, and do not exceed 0.3 µN in magnitude. In all cases, the maximum power output by a single-chip amplifier PA04 was for a voltage of 75 V, corresponding to a current of 2 A. The resonance frequency of 15.4 kHz was set to reach maximum vibration amplitude without a mass. This frequency is lower than expected, and can be due to the higher driving voltage. A double-peak of 0.3 to 0.5 µN was detected, despite the high noise, with the force direction independent of the device's orientation. The results each represent an average of 200 profiles. The effect does not seem to represent unidirectional thrust, otherwise, the force would be reversed at 180°, and a different magnitude would be observed at 90°.

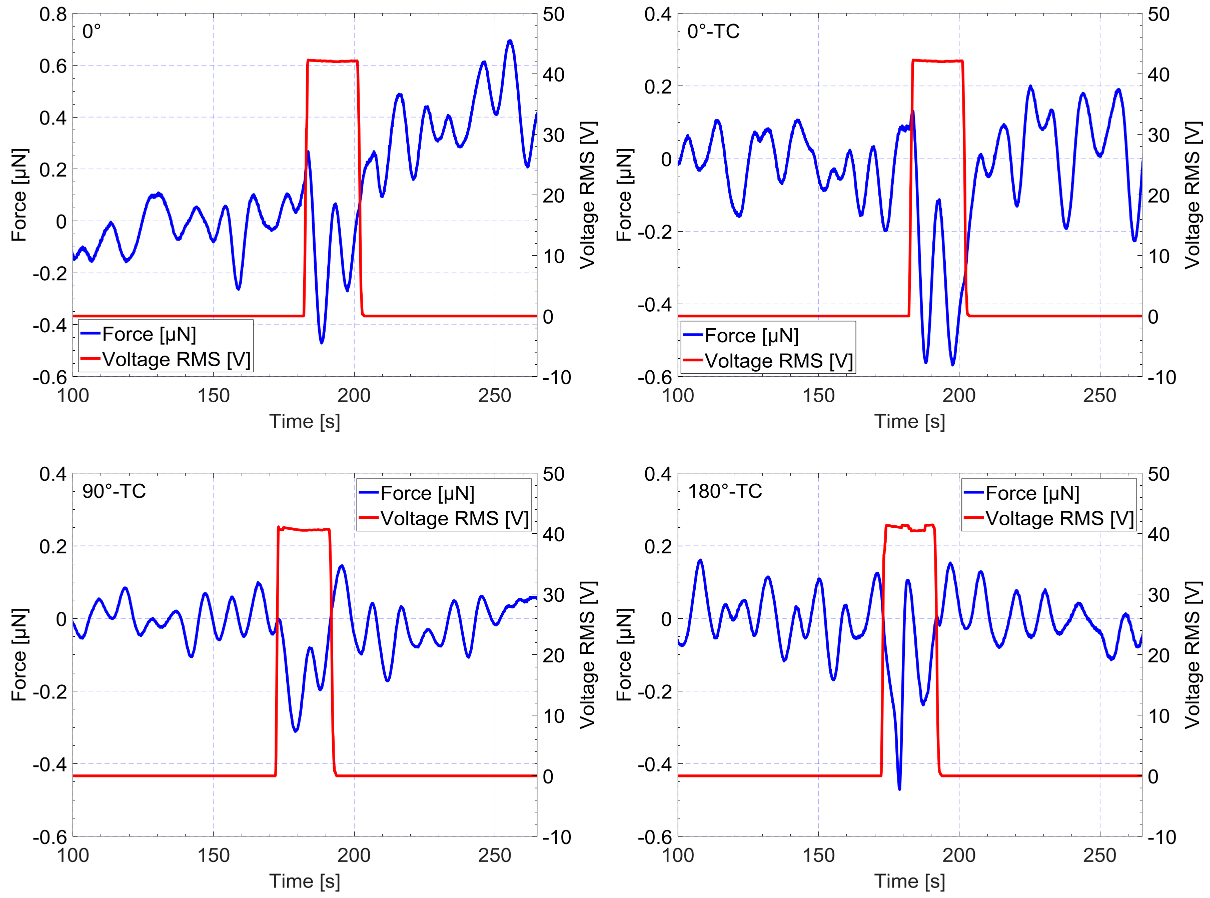

Fig. 77 – TB1 CU18A 0 g Tests

top left: no thermal correction 0° | top right: 0° with thermal correction

bottom left: 90° with thermal correction | bottom right: 180° with thermal correction

The next experiments were performed with a 52 g stainless-steel mass attached to the end of the actuator through a screwed connection. The maximum power output was selected for this configuration at the resonance of 9.6 kHz for a fixed voltage of 75 V. The preloading torque was 0.5 Nm on the screw. All three configurations were tested (0°, 90°, 180°). In Fig. 78, it can be seen that the tail mass has a great influence on the behavior. This time, the signal is greater than the noise. The graph without TC shows that the effect is almost immediate and that the force trace does not go back to the zero line after turn-off. Removing the thermal drift using a linear function has the effect of introducing switching transients, mostly due to the nonlinear nature of the effect. The same behavior can be seen when rotating the actuator to 90°, however, the force is inferior, with about 0.1 μN amplitude compared to 0.3 μN for 0°. Also, the force for both 0° and 180° configurations points to the same direction, which does not correspond to the concept of thrust. One graph also shows the current curve, which is seen to vary despite the constant voltage because of the changing driving frequency and impedance as a result of the tracking process. The programmed tracker modifies the commanded frequency as it tries to optimize the current. The optimal current is found towards the end of the pulsed time, but it does not result in a significant change in observed force. These results show how applying TC during data analysis can result in unexpected transients, when the drift is even slightly nonlinear. The temperature curve shows the temperature of the moving mass, the temperature of the actuator body did not increase significantly during the experiment.

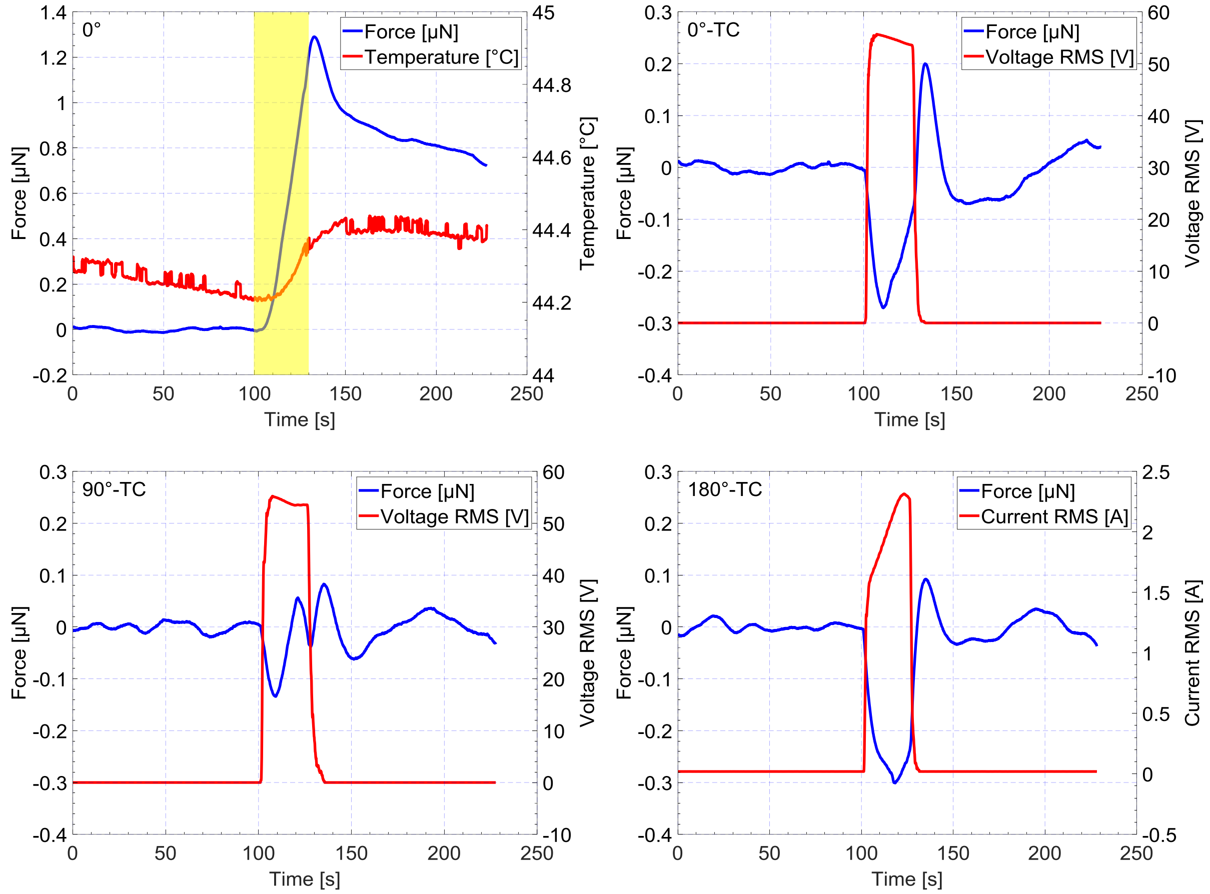

Fig. 78 – TB1 CU18A 52 g Tests

top left: no thermal correction 0° | top right: 0° with thermal correction

bottom left: 90° with thermal correction | bottom right: 180° with thermal correction

Lastly, tests were performed using a mixed-mode signal that allows two signals to be superposed. Using this method, the value of the second harmonic vibration can be increased, in order to generate the expected thrust according to the derivation in Section 3.1.9. Unfortunately, the voltage amplitude of the first harmonic to accommodate the signal superposition with the second harmonic. Nevertheless, the predicted force should be around 0.125 N for a phase difference of 0° between the two signals. In this test series, the mixed-mode signal was applied for 30 seconds with different relative phases between the two signals to cover all the possible phase relationships. Furthermore, the commanded frequency was maintained constant instead of using the tracker. The application of 37 V at 9.6 and 19.2 kHz is shown by the shaded area in the diagram.

Fig. 79 shows how all the different phase sweeps remain within the noise of the balance. The increased noise in comparison with the previous figures is due to the fewer number of profiles used for the average, each result being an average of only 5 profiles. Regardless of the phase, the measured force remains within the noise and is lower than 0.3 μN in amplitude.

This phase sweep test shows that any variation in phase between the mixed signals did not lead to an increase in the effect, despite the prediction. The results do not agree with the concept of thrust from the derived Mach-effect and the corresponding increase for the mixed-signal driving.

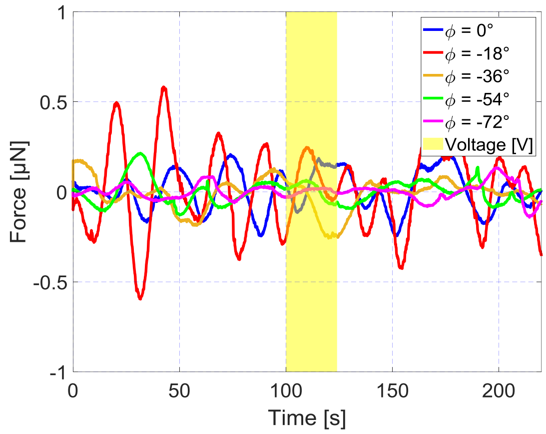

Fig. 79 – TB1 CU18A Phase Sweep

4.1.3 MET03

This sub-section describes the test results of the first Woodward-type device to be tested on TB1. MET03 was tested with amplifiers PA04(1) single-mode, PA04(2) bridge-mode, and PA04(1) single-mode with a transformer with a 1:4 coil ratio, but without Carvin amplifier from the CSUF electronics. The effect of the electronics was investigated. The device is placed in the 0° configuration since its longitudinal axis is in the torsional plane of the balance, or slightly above, and perpendicular to the balance beam. Also, its brass mass is on the left as shown in Fig. 80, meaning that a positive force or beam displacement are connected with a thrust force in the direction of the aluminum and the net displacement in the direction of the brass, or a clockwise rotation of the balance arm as seen from above. The device is mounted on a polyethylene (PE) piece connected with a stainless-steel screw to the experiment-box platform. In the first half of these experiments, the device was not placed in the middle of the box. The test parameters are summarized in Table 19.

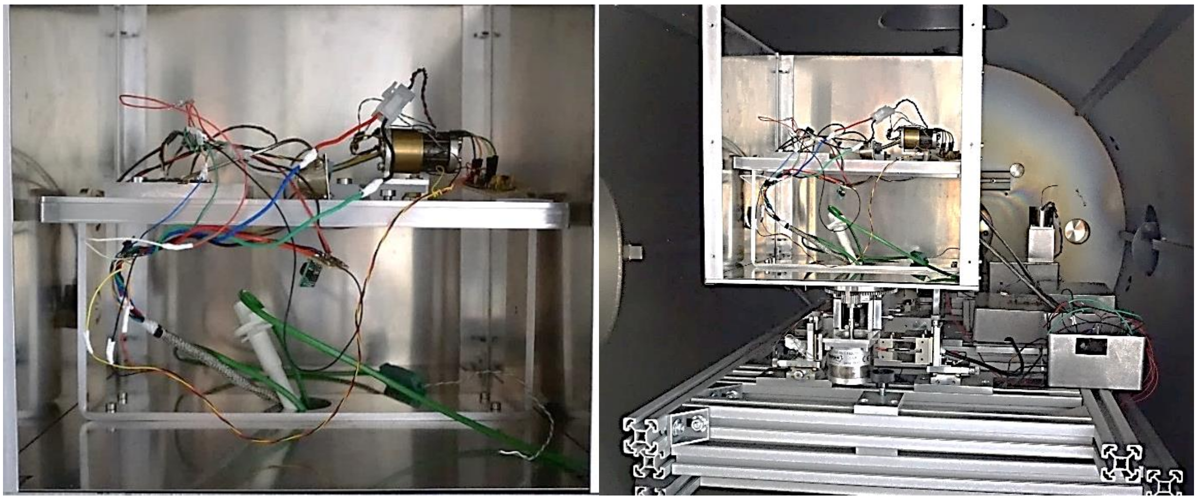

Fig. 80 – TB1 MET03 0° Configuration Setup

No. Tests	Orientations [°]	No. Profiles	Voltage [V]	Pulse Time [s]	Signal Type	Mounting	Electronics
24	0/90/180	200	90	20	Single/Mix	Offset	PA04(1)
6	0/90/180	200	160	20	Single	Middle	PA04-Trafo
4	0	200	180	20	Single	Middle	PA04(2)

Table 19 – TB1 MET03 Test Series

The whole experiment box is also rotated with a stepper motor to provide tests with different orientations (0°, 90°, 180°, -90°). The tests consist in driving a sinusoidal signal with constant voltage at the resonance frequency with the highest Q-factor, which is pin-pointed and tracked for the entire test duration. A test duration of 20 seconds was selected to limit the temperature increase, and based on similar test parameters to Woodward's experiments. The resonance frequencies that have been extracted from the analysis in Chapter 3 were around 32, 43, 63, and 90 kHz. The single-mode amplifier PA04(1) was used without a transformer, and the targeted frequencies were 31 and 62 kHz. The results after TC are shown in Fig. 81.

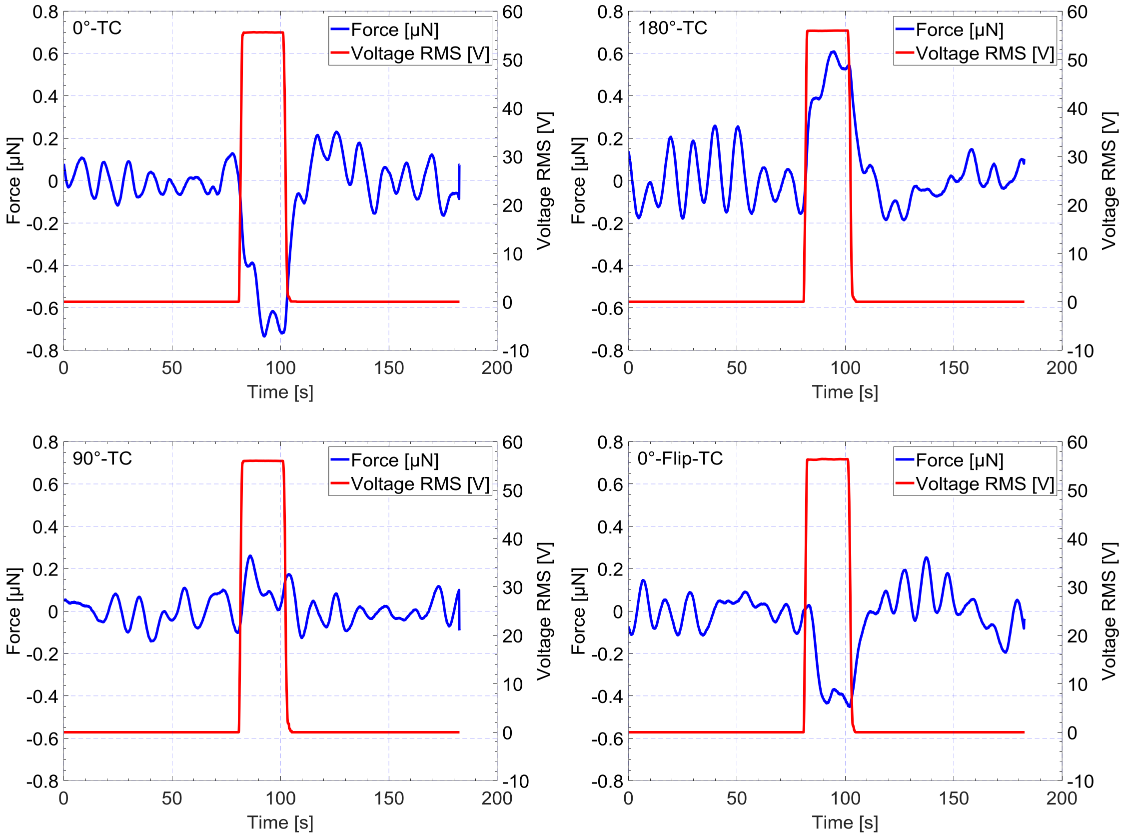

Fig. 81 – TB1 MET03 Fixed Frequency Tests [23]

top left: 0° with thermal correction | top right: 180° with thermal correction

bottom left: 90° with thermal correction | bottom right: 0° configuration and flipped device

The force traces shown in Fig. 81 do not look like the typical Woodward effect due to the absence of switching transients, but there is a clear force of about 0.5 µN that seems to depend on the thruster orientation. The sign of the force shows that the thrust is in the direction of the brass mass. The noise is still visible with an amplitude of around 0.15 µN after an averaging of 200 profiles, resulting in an SNR of approximately 3.8.

To investigate this, the MET was flipped by 180° inside the experiment box itself without rotating the box on the balance with the motor, keeping the cables and the offset on the balance beam identical to the 0° configuration. This had the result of showing a similar force to the original 0° configuration, demonstrating an experimental artifact related with the box orientation. These experiments showed that the force observed was independent of the device's orientation, disagreeing with the predicted thrust behavior.

In Fig. 82, the device was driven using mixed-mode signals using different phases between the first and second harmonics (31 and 62 kHz). The orientation of the MET is 0°, but three different relative phases between first and second harmonic signals were tested: 0°, 90°, and -90°. No thrust was expected for the last two measurements.

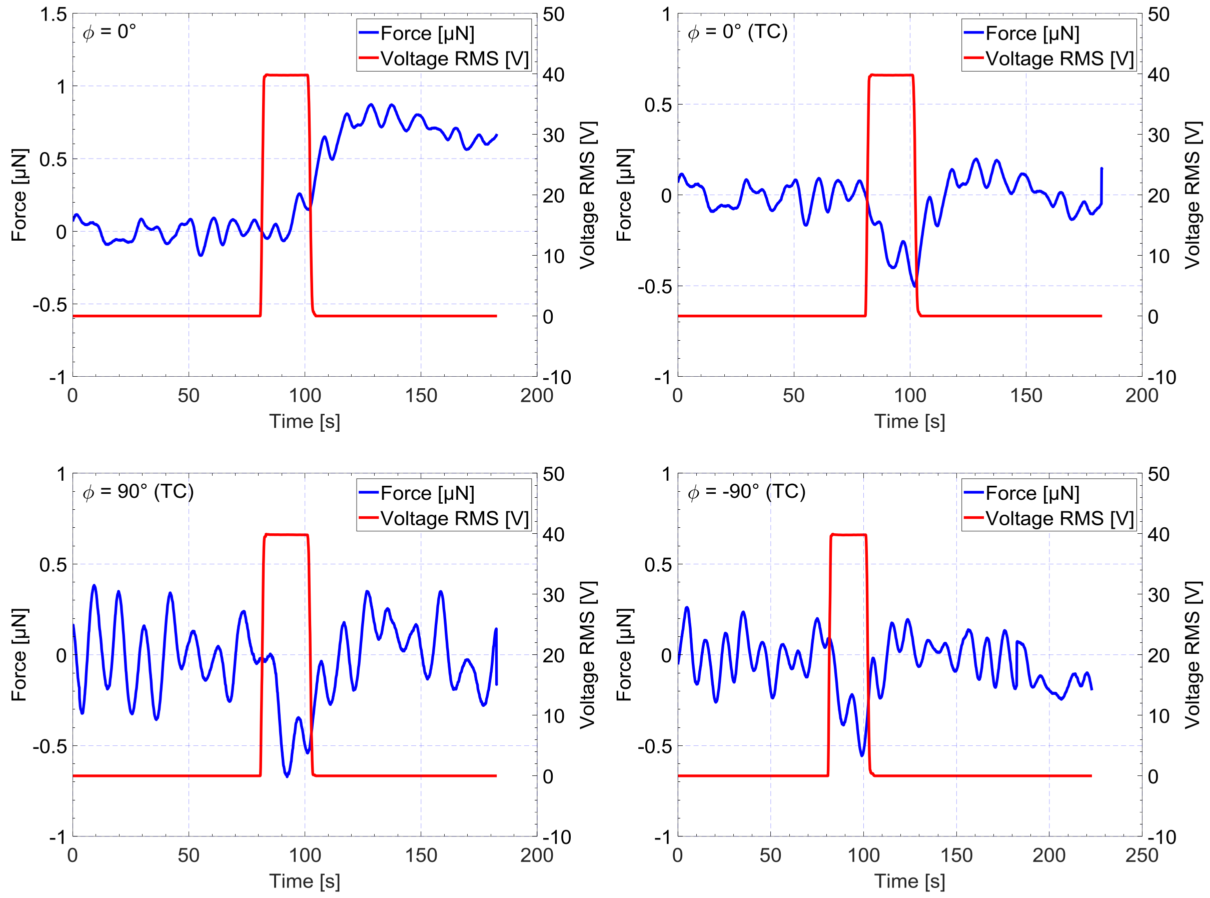

Fig. 82 – TB1 MET03 Mixed Frequency Tests [23]

top left: 0° relative phase | top right: 0° relative phase with TC

bottom left: 90° relative phase with TC | bottom right: -90° relative phase with TC

The results in Fig. 82 reveal again the presence of a drift and, after TC, a force peak of about 0.4 µN in a direction independent of the relative phase. Furthermore, the force observed was no bigger than in single-frequency tests, contradicting the derived formula for mixed driving, as with the magnetostrictor experiments. At this stage, the thruster was still placed slightly off the middle, connected to the PE piece.

The next tests included a transformer between electronics and MET, resulting in different driving voltages. The response without TC shows a strong drift starting after applying voltage, with the force trace not returning quickly to its baseline after turn-off. The direction of the drift does not depend on the orientation of the thruster. Even then, the drift is present in both 90° and 180° and does not resemble the force trace characteristic of a force or thrust pulse. Once the thermal drift from sector 3 is removed, the nonlinear drift gives rise to the effects seen in Fig. 83 and the appearance of a force. These tests led to larger effects with a force peak of 2 µN for the 0° configuration after TC. However, the Woodward-type trace with its switching transients was not observed. Furthermore, a large force of over 0.5 µN was still observable in the 90° orientation test, indicating the presence of artifacts. The 2 °C temperature increase is shown in the first graph, and the voltage is shown by a shaded area.

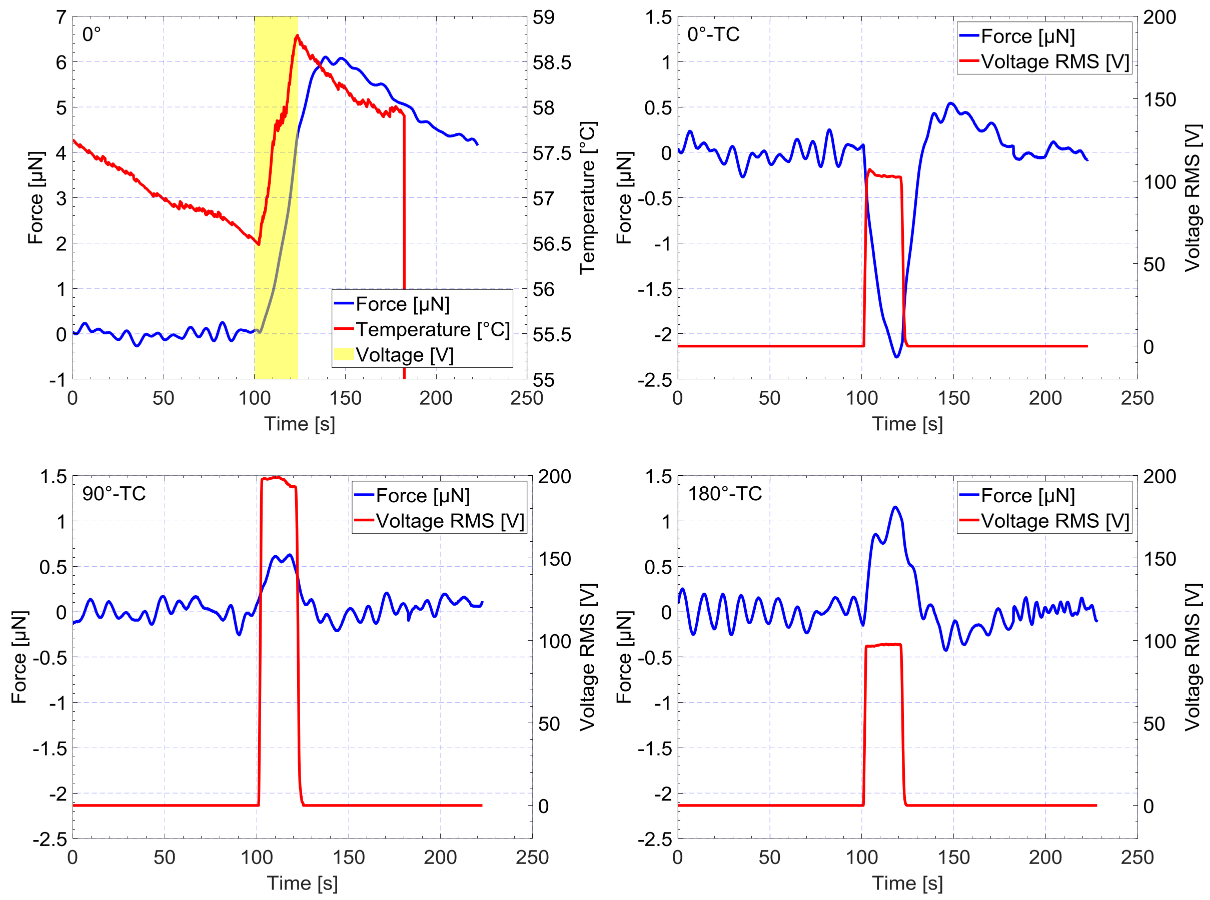

Fig. 83 – TB1 MET03 Tests with Transformer [23]
top left: no thermal correction 0° | top right: 0° with thermal correction
bottom left: 90° with thermal correction | bottom right: 180° with thermal correction

Finally, the tests with the bridge-mode PA04(2) amplifier were performed with the tracker, where twice as much power as the first amplifier was made available. However, the series of tests were interrupted when the PE mount melted due to the high heat and the full results are not shown. The tests have demonstrated that the resonance tracking method causes too much stress on the devices, hence, the tracker was not used in further tests.

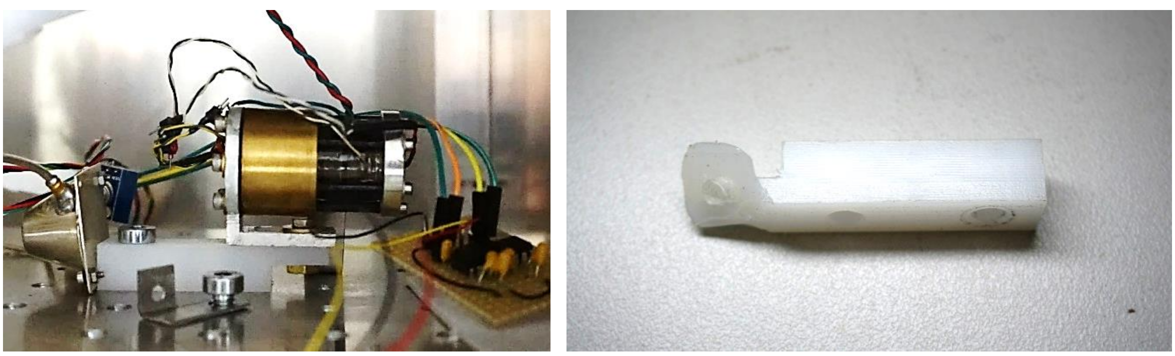

Fig. 84 – TB1 MET03 and Melted PE Mount
left: MET03 setup | right: melted polyethylene piece

4.1.4 MET04

This time, self-built device MET04 is placed in the middle of the box to reduce asymmetric effects and moments on the balance beam, and was mounted on a copper plate to dissipate the heat. The mounting is also more rigid than the PE connection. Fig. 85 shows the 0° configuration with the brass mass on the left. The same notation is used here as in the other experiments. This device is very similar to other devices, except that it was assembled with piezo-disks from a different manufacturer, the epoxy is slightly different (Scotchweld, 2216A) and there is no embedded passive piezo-disk. The resonance frequencies are at 36, 39, 73, and 90 kHz. Table 20 summarizes the tests performed with the device. The device is used to compare both TBs later, as it was used on TB1 and TB2. Furthermore, the experiment uses two types of amplifiers: the single-mode PA04(1) and the bridge-mode PA04(2).

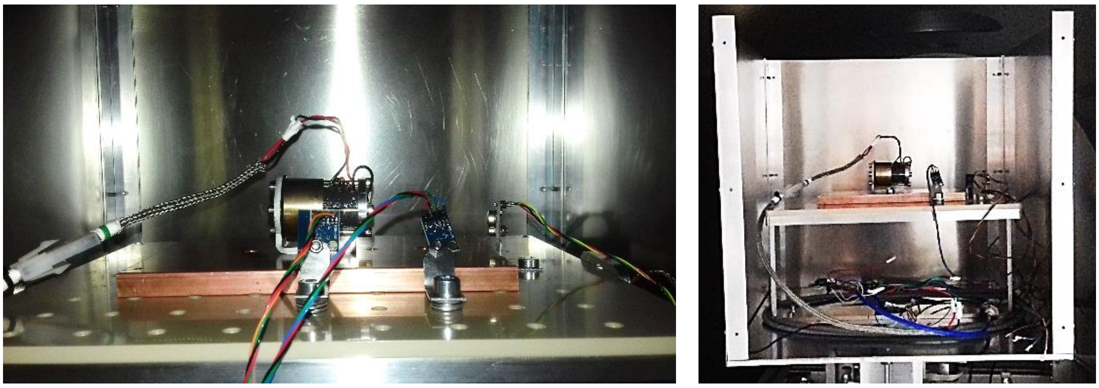

Fig. 85 – TB1 MET04 0° Configuration Setup with Copper Plate

No. Tests	Orientations [°]	No. Profiles	Voltage [V]	Pulse Time [s]	Signal Type	Particularity	Electronics
5	0	160	75	25	Single/ Mix	Middle	PA04(1)
6	0/180	160	180	25	Single	Middle	PA04(2)

Table 20 – TB1 MET04 Test Series

The MET was tested at two harmonic frequencies, using single-sine and mixed-signals, driven by single- and bridge-mode amplifiers, and mounted on a heat sink. The first tests compare the result of different levels of amplification. The current and voltage reached with the bridge-mode driving method are twice as great as with the single-mode amplifier. However, no effect can be seen in Fig. 86 when using a resonance frequency tracker around 37 kHz. The first diagram on the left shows the single-mode amplifier and on the right, the bridge-mode test results. In both cases, applying a sinusoidal voltage to the device did not result in any significant effect above the noise, which is around 50 nN in amplitude. These results indicate the need for an improved balance with less noise and better shielding from EMI.

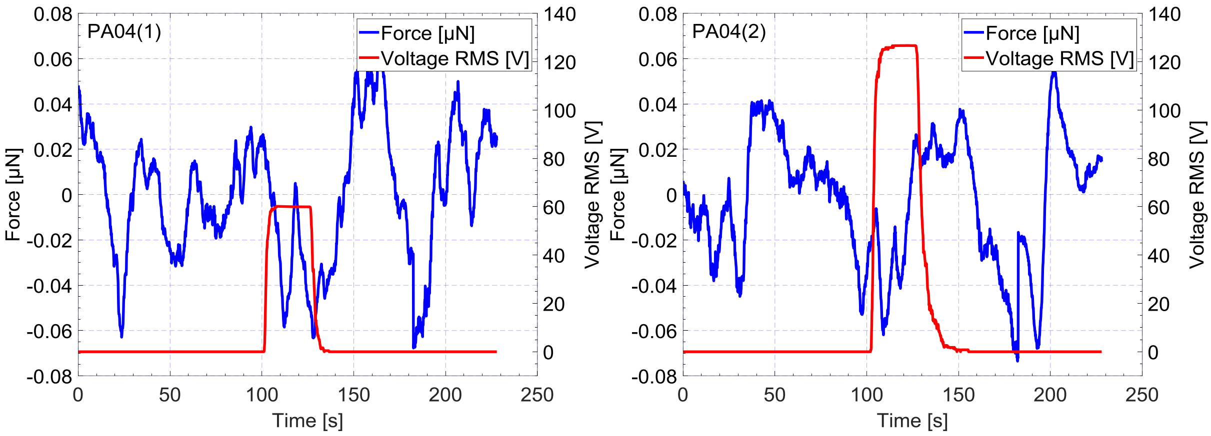

Fig. 86 – TB1 MET04 0° Single-Mode vs Bridge-Mode

left: single-mode amplifier driving | right: bridge-mode amplifier driving

This test also showed that changing the electronics can cause the impedance spectrum of the system to slightly shift, and the current was not higher despite the increased voltage.

In Fig. 87, the typical Woodward trace appears when driving the device at its second harmonic frequency. The first harmonic frequency test didn't show any significant force deflection, besides a 0.1 μN peak. The second harmonic test clearly shows switching transients and a small steady-force peak when applying a thermal correction. However, since the reversed effect was not observed in the 0° orientation, the results were first deemed inconclusive. The maximum effect was also only 0.15 μN in magnitude, which is much weaker than the predictions or claimed effects of 1-20 μN [16]. The driving voltage was 180 V in amplitude, which resulted in a significant increase in temperature, as seen in the graphs. However, the use of the copper block seems to have removed the presence of the drift seen in earlier experiments.

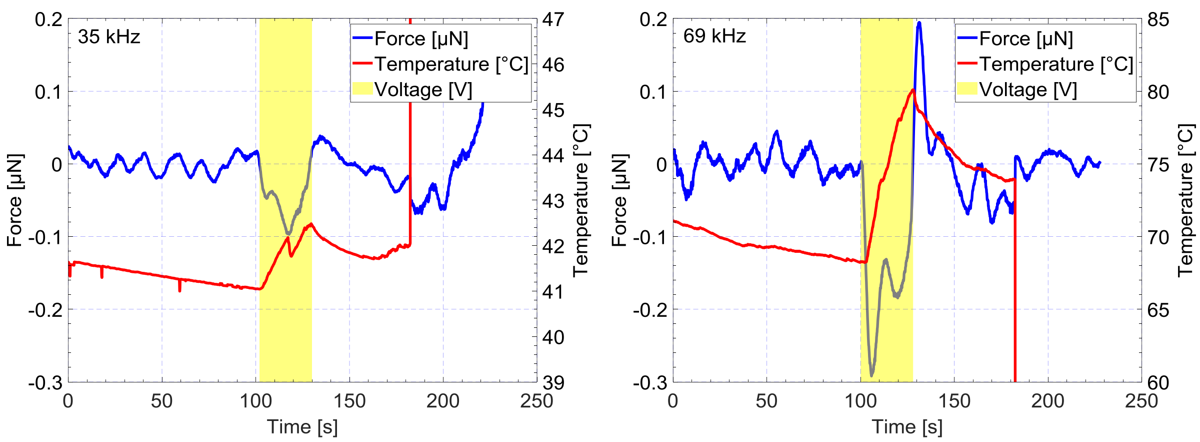

Fig. 87 – TB1 MET04 180° Bridge-Mode Tests

left: 35 kHz driving frequency | right: 69 kHz driving frequency

4.1.5 Discussion

In this section, the TB1 test results are summarized and discussed. When compared to TB2, the former is a bigger balance that has a longer reaction period and can support heavier experiments like the magnetostrictor. The earlier TB version was also used to build up experience, later leading to improvements. A few mistakes were made during the first tests; the DUT was not placed in the middle of the experiment box, resonance tracking led to excessive heat and EMI shielding was insufficient. However, these mistakes led to different lessons learned. Here are the main observations:

- At first, the ambient noise was close to 0.1 µN in amplitude after averaging. This was improved to 0.05 µN by adjusting the damping and averaging more test runs.
- There is visible drift in the force response when applying alternating voltage to any device on the balance. The drift can have a nonlinear behavior, especially after turn-off, and the force trace does not go back to the baseline. The direction of the drift was always the same, independent from the device or box orientation.
- Applying TC on the force responses can reveal impulse-like artifacts that reach over 0.2 µN in amplitude. These nonlinear effects were seen with CU18A, MET03, and MET04, and depend on the orientation of the experiment box. A small impulse was also seen in the DC resistor test.
- The transformer, magnetostrictor, and mixed driving did not change the behavior of the force response, and did not yield the effects predicted by the theory.

First, the origin of the drift will be examined. Since the force's baseline moves to a new equilibrium, or returns very slowly back to the original position, spontaneous outgassing of some component, thrust or electromagnetic forces can be ruled out as an explanation. The experiments rather suggest a preferred path for the heat transfer to the experiment box, and a corresponding imbalance of the buoyancy force, which can account for the small drift observed at the specified vacuum pressure. Hence, it is important to look at the effects of heating. The temperature curves show that the temperature increases during a single pulse were at most 0.4 degrees, for the AC resistor experiment and the magnetostrictor, which resulted in similar drifts. The drift also increased with the use of a transformer with MET03, which was also linked with a higher temperature increase (2 °C). Moreover, heating occurs as soon as the power is switched on, and the temperature profile looks very similar to the balance drift. The force could be due to thermal expansion in one part of the device. However, the resistors do not have a preferred direction of expansion and are built symmetrically, unlike the MET devices. Furthermore, the direction of the drift seems to be independent of the thruster's orientation, thus, opposing the idea of a center-of-mass shift due to thermal expansion that would depend on the device's orientation. The drift could also be caused by the shifting of a balance component due to stick-slip vibration.

Secondly, comparing the balance results before and after TC leads to two interesting points. On one hand, TC can reveal a force that is hidden in the balance drift. On the other hand, since the TC method uses a linear approximation to the drift, any nonlinearity in the drift can lead to fake forces. The temperature profile of the experiments is another good example of a nonlinear process. It is not surprising that the larger forces observed from the magnetostrictor and transformer tests were also linked with larger drifts of the force response. However, MET03 tests showed that the sign of the remaining force after TC was related to the orientation of the box rather than the orientation of the thruster. These observations hint again at the preferred heat transfer path on the balance and a resulting imbalance of buoyancy forces. The heat transfer path would rather depend on the orientation of the box and mount, which is a larger structure than the thruster. However, this argument does not exclude the possibility of stick-slip vibration and the shifting of a component in the experiment box.

Lastly, sources of EMI between the balance and its surroundings or between internal components on the balance could lead to some impulses. The dummy DC tests revealed a small force in sector 3 that disappeared after disabling the electric field. This effect could arise from the interaction between the Earth's magnetic field and the power cables. An interaction between the feedthrough cables and the magnets from the voice coil and damping can be excluded, since they are also placed on the same balance beam. The effect could be a result of cables straightening due to electrostatic repulsion and resulting in a new null position of the balance arm. This test sets the limit of what can be considered an experimental artifact from EMI sources and amounts to around 0.2 µN for a current of 1.5 A. Better electromagnetic shielding is necessary to measure lower levels of thrust. Fortunately, DC currents do not occur during MET tests, which are driven with AC voltage.

At this stage, whether the drift comes from vibration, thermal or electromagnetic sources remains to be elucidated, and the possible Mach-effect thrust or signals observed by Woodward remain hidden in experimental artifacts and below the predictions. These conclusions are summarized in Table 21.

Test Setup	**Dummy**	**CU18A**	**MET03/04**
Variations	Resistor (AC/DC)	Single/Mixed, 0/52g	Frequency, voltage, configuration, flip
Max. Measured [µN]	0.3	0.6	2.5
Predicted [µN]	0	> 1	> 1
Observations	• Drift = 2.5 µN/min • Thermal, EM interactions, or a combination	• Drift = 2.4 µN/min • Switching transients • Effect shows the same direction regardless of the configuration	• Drift = 1-10 µN/min • Beam signal does not revert to zero. • Effect present in all configurations. • Effect depends on the orientation of the box.

Table 21 – TB1 Test Results Summary

4.2 Torsion Balance II Test Results

4.2.1 Dummy Tests

The test campaign with TB2 started with dummy tests used to identify experimental artifacts and to compare its behavior to TB1. This time, the dummy tests also included a capacitor. The resistor test setup is shown in Fig. 88, and the capacitor test setup is in Fig. 89. During the tests, the Faraday-cage made up of bent mu-metal sheets is closed and grounded. Temperature is measured with a K-type thermocouple fixed on the copper plate. The tests and their parameters are summarized in Table 22, showing different combinations and the amplifier electronics. The whole balance arm, through which the power cables are fed, is covered in thin mu-metal plates and grounded to reduce EMI even further. No magnetostrictor tests were performed, and the resonance tracker was not used.

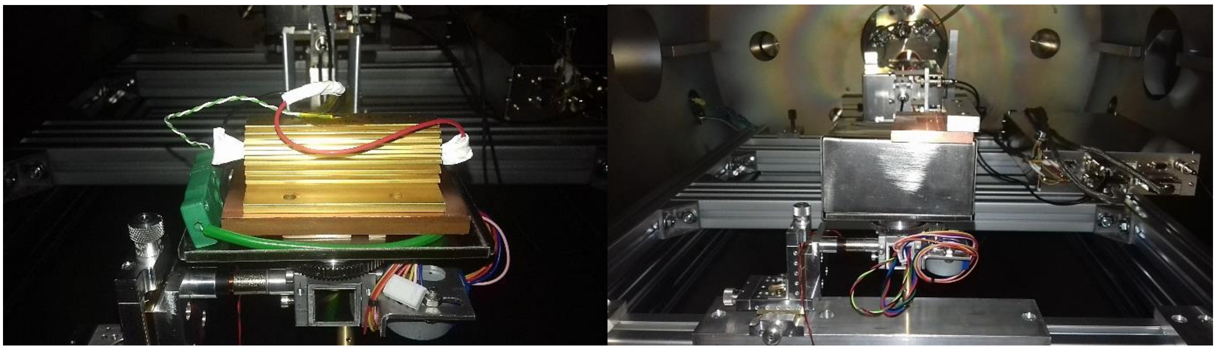

Fig. 88 – TB2 Resistor Dummy Test Setup

left: resistor setup without mu-metal cage | right: with mu-metal cage

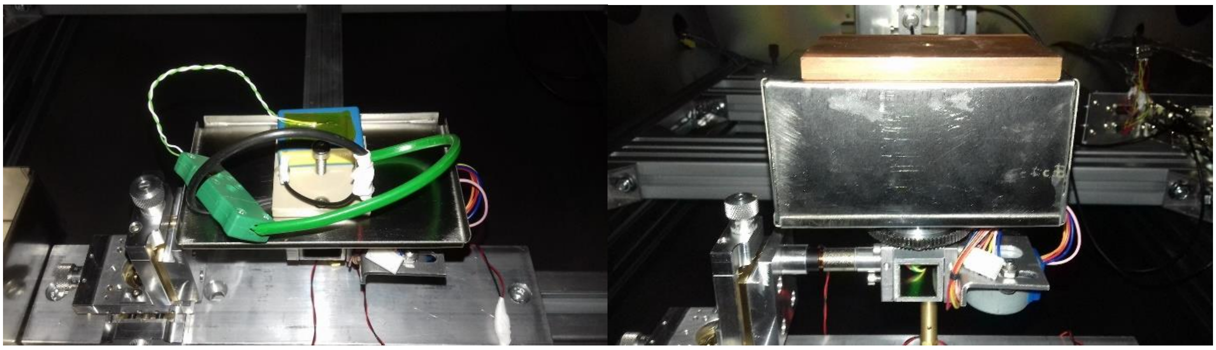

Fig. 89 – TB2 Capacitor Dummy Test Setup

left: capacitor setup without mu-metal cage | right: with mu-metal cage

No. Tests	Device	No. Profiles	Voltage [V]	Pulse Time [s]	Signal Type	Electronics
25	470 Ω	10	180	20-30	DC/AC	PA04(2)/CARVIN
1	32 Ω	160	180	25	AC	CARVIN
4	18 Ω	10	180	20	DC	PS
4	22 nF	10	200	20	AC/DC	CARVIN/PS

Table 22 – TB2 Dummy Test Series

In the first series of tests, a DC signal is applied to the 18 Ω resistor. The temperature increase is linked to a small thermal drift on the balance of 20 nN, but no impulsive forces. The force response curves stabilize once the temperature is also stabilized. The thermal drift cannot be avoided in this new setup as well, however, the EMI with the DC current is not present as can be seen from the absence of a pulse. Furthermore, removing the thermal drift results in a very low distortion after averaging 160 profiles. The noise can be seen in Fig. 90 with an amplitude under 5 nN, which is an order of magnitude better than with TB1.

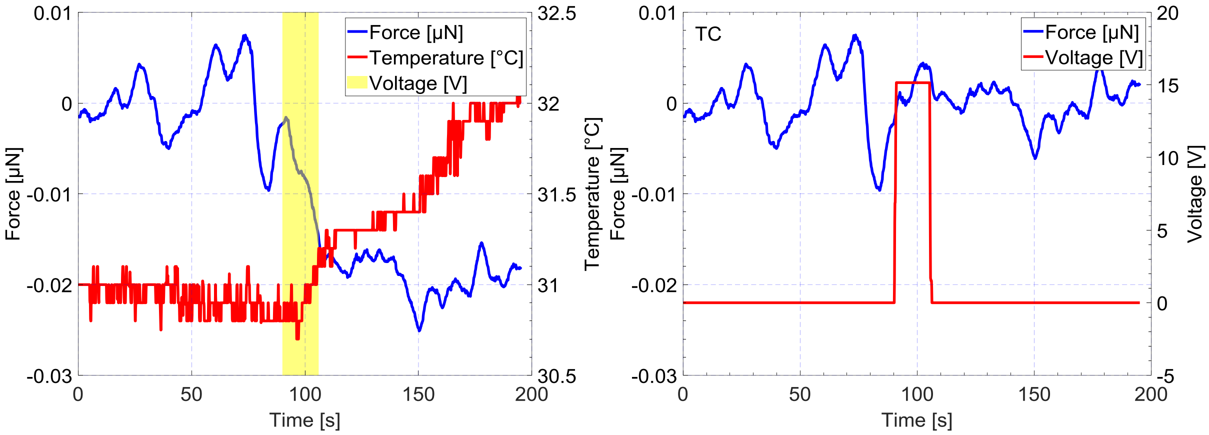

Fig. 90 – TB2 Resistor DC Test

left: no thermal correction | right: with thermal correction

The next tests consist of AC voltage tests with a frequency of 33 kHz and a current of around 0.6 A. Fig. 91 shows no significant switching transients or impulses that would come from EMI, except a slow drift until 0.13 μN. This shows that the balance is well protected against cross-talk or EMI, even for a reasonable current and voltage, which is another improvement compared to the previous balance.

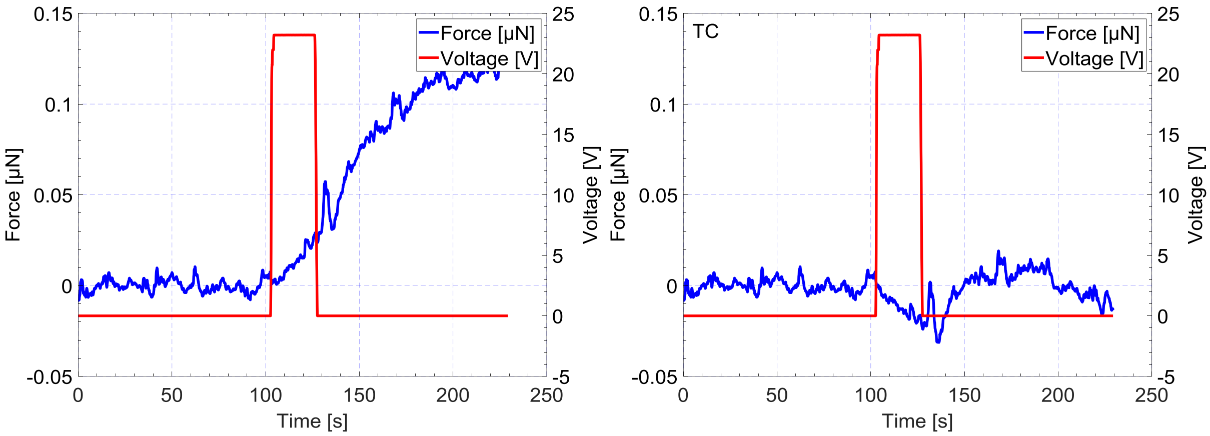

Fig. 91 – TB2 Resistor AC Test

left: no thermal correction | right: with thermal correction

Furthermore, a DC test with a capacitor of 22 nF showed different behaviors depending on the grounding of the balance. The diagram on the left in Fig. 92 shows the result of the test where the balance isn't grounded. There is an EMI between the surroundings and the loaded capacitor amounting to a force of 100 nN. Grounding the balance had the consequence of eliminating the effect. These tests were very useful in determining the effect of improper grounding.

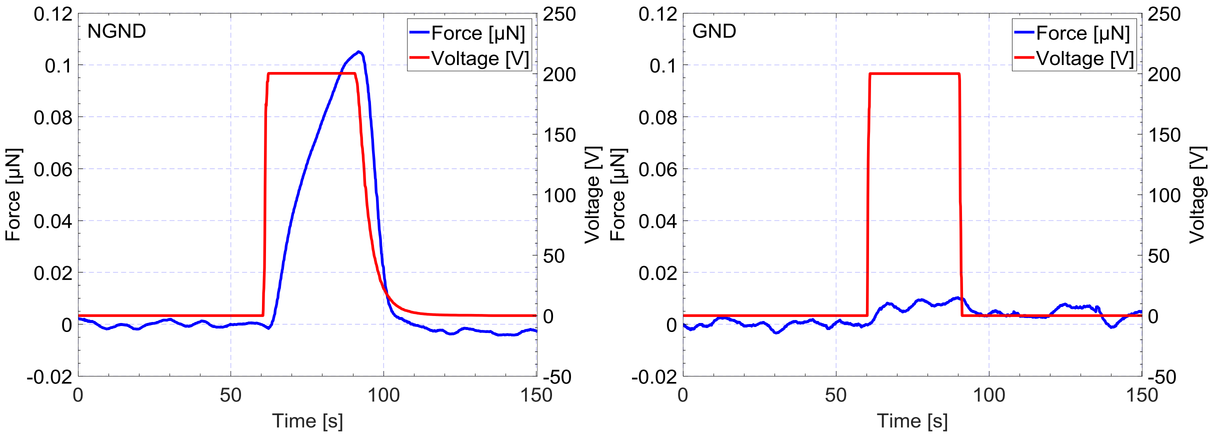

Fig. 92 – TB2 Capacitor DC Test

left: balance beam not grounded | right: grounded balance beam

Then, the capacitor test performed with CSUF electronics at 34 kHz produced the results shown in Fig. 93. These tests only show the balance noise and minimal drift. Thus, the problem connected with balance grounding did not occur with these amplifier electronics. Due to the lower number of profiles, the noise is averaged to an amplitude of 7.5 nN at the sampling frequency of 10 Hz. Thus, the dummy tests reveal that TB2 is well shielded and more resistant to thermal drift and electromagnetic interactions with the environment, if grounded properly.

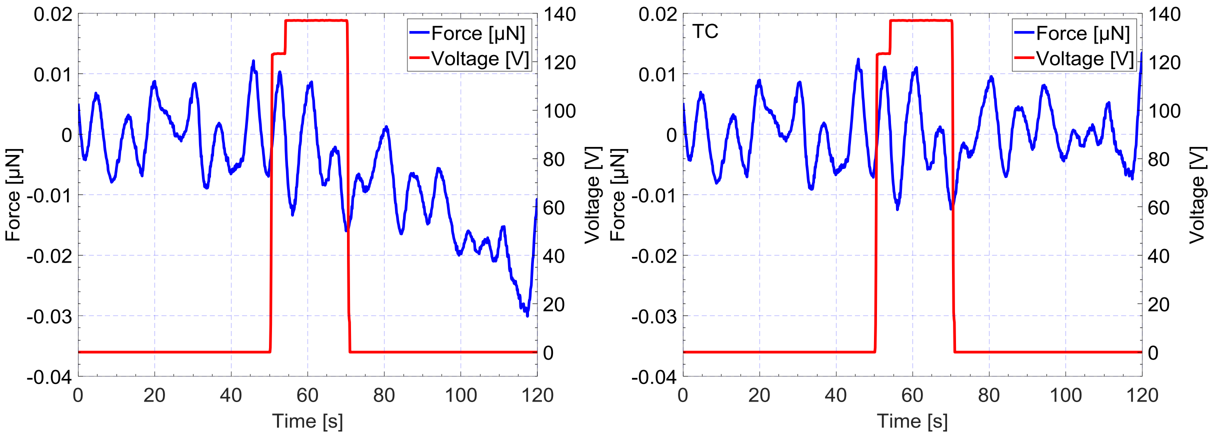

Fig. 93 – TB2 Capacitor AC Test

left: no thermal correction | right: with thermal correction

4.2.2 MET05

Although several tests were performed with MET03, MET04, and MET06, the campaign with MET05 was the most productive and regroups most key results. Multiple parameters were varied during the tests, as shown in Table 23. Pictures of the different setups including copper block, closed box, yoke, and two different device orientations are included in Fig. 94 and Fig. 95.

The yoke shown in Fig. 95 and Fig. 96 was also provided by Woodward. The pieces are cut from acrylic plates with a 6 mm thickness. O-rings are used between the washers and the screws to provide vibration damping. Although these rubber rings might reduce low-frequency damping, the screw connections also enabled more twisting of the experiment box. The 0° and 90° configurations are shown in the pictures below. The 90° orientation with the mounting yoke is a vertical configuration unlike with other mounts. The resonances of MET05 are at 34, 46, and 70 kHz according to its electromechanical characterization.

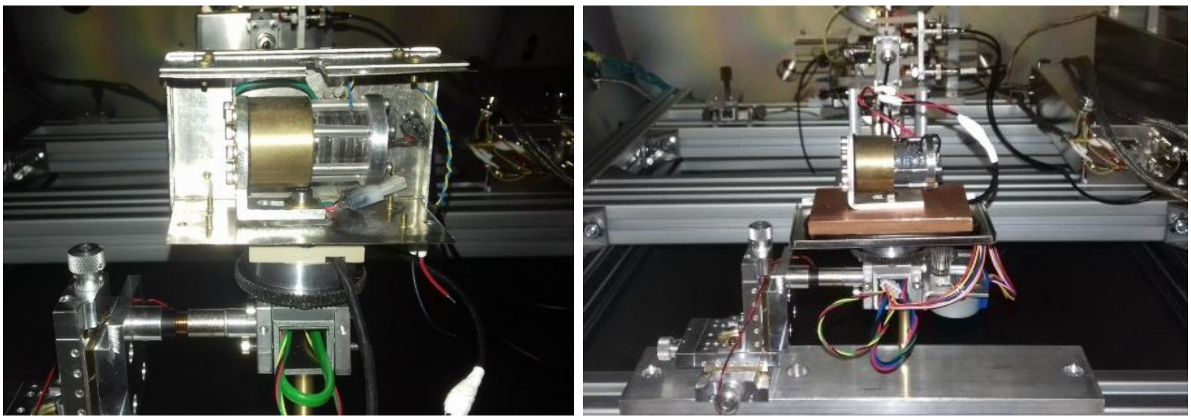

Fig. 94 – TB2 MET05 Solid Mount Setup

left: 0° configuration without copper block | right: 0° configuration with copper block

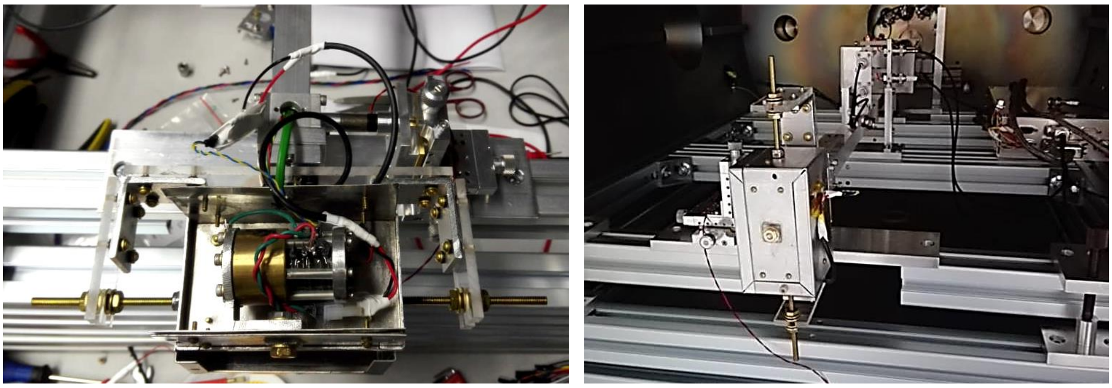

Fig. 95 – TB2 MET05 Yoke Configurations
left: 0° yoke configuration | right: 90° yoke configuration

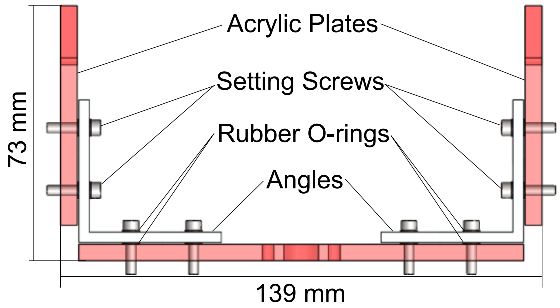

Fig. 96 – MET Mounting Yoke CAD [14]

No. Tests	Orientations [°]	No. Profiles	Voltage [V]	Time [s]	Signal Type	Setup	Electronics
10	0	2	220	8, 12, 16	Single	20 mbar, 50 µbar, 1 nbar	CSUF
31	0/90/180	5	200	16	Single	Copper/ No Copper	CSUF
6	-90/180	5	200	24, 50	Single/ Sweeps	Yoke	CSUF-Trafo(1:2)
40	0/90/ -90/180	2-5	180	8, 16	Single/ Sweeps/ Mixed	Copper/ No Copper	PA04(2)
4	180/-90	5	180	16	Single	Yoke	PA04(2)
6	0	3	180	16	Single	No Rubber	PA04(2)
6	0/180	5	180	16	Single	Copper	PA04(2)-Trafo

Table 23 – TB2 MET05 Test Series

The graphs of Fig. 98 show some key results with MET05. The results of the tests with CSUF electronics are shown first. This time, the resonance tracker has not been used and a fixed frequency corresponding to the resonance frequency, or its neighborhood, was maintained with a constant voltage. The driving frequency represents the longitudinal resonance at 36.3 kHz. The first series of diagrams do not involve TC, except for the balance drift in Sector 1.

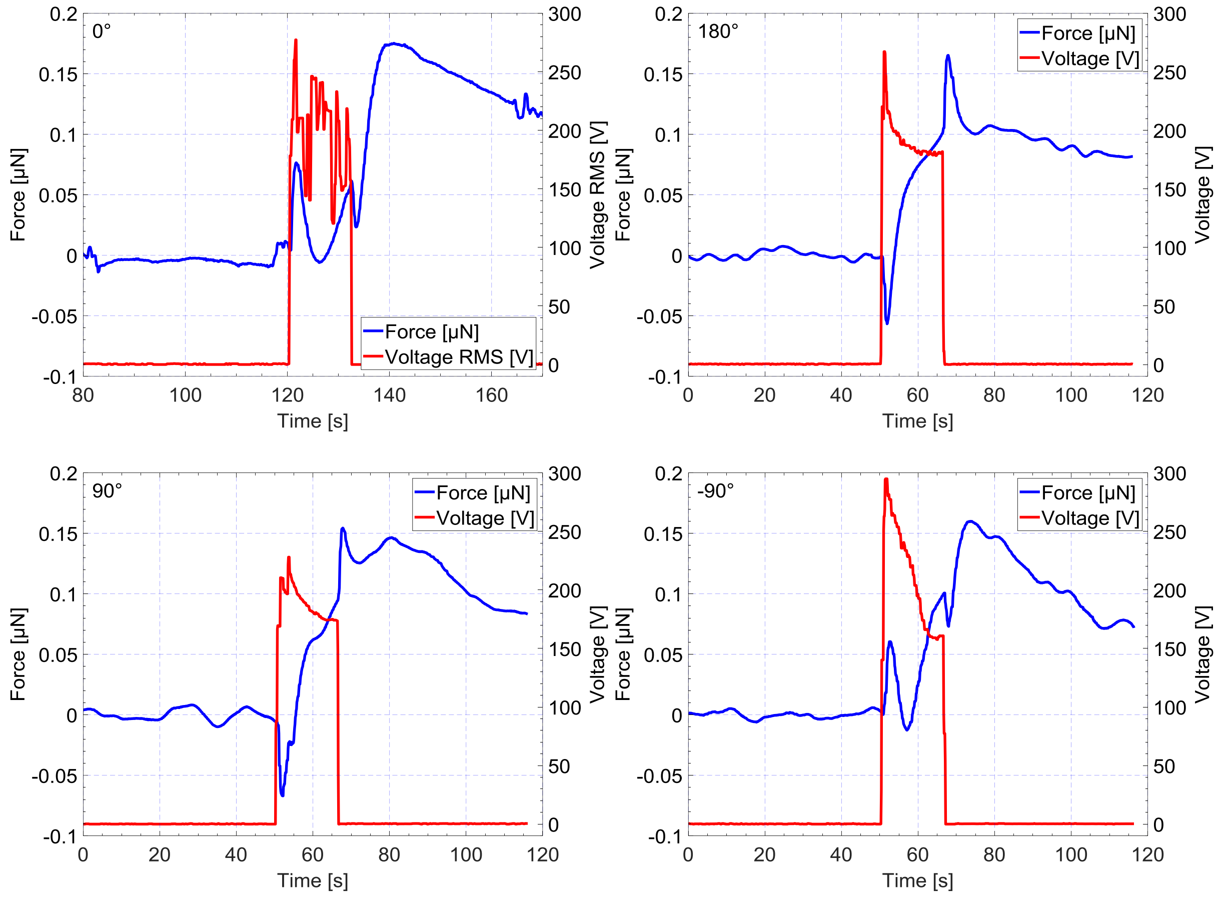

Fig. 97 – TB2 MET05 CSUF Fixed Frequency Tests

top left: 0° configuration | top right: 180° configuration

bottom left: 90° configuration | bottom right: -90° configuration

The results show sharp peaks that are dependent on the device orientation, as observed by Woodward. The switching transients are exactly opposite when looking at the 0° and 180° configurations. The graphs also clearly show a drift in the beam position of up to 0.1 µN after the pulse, after which the balance beam then starts to slowly come back to the zero line, but not promptly after switch-off. The drift is always in the same direction, irrespective of the MET orientation. Furthermore, the effect is also present in the 90° and -90° directions with switching transients of the same magnitude as for 0° and 180°. Finally, although the voltage and current behaviors are not identical, the force observed is roughly the same order of magnitude for all orientations. The variations in voltage and current are due to the small changes in impedance occurring after test cycles or the slight change of boundary conditions, although the driving frequency is kept constant. In Fig. 98, the diagrams show the result of linear TC on the same force traces.

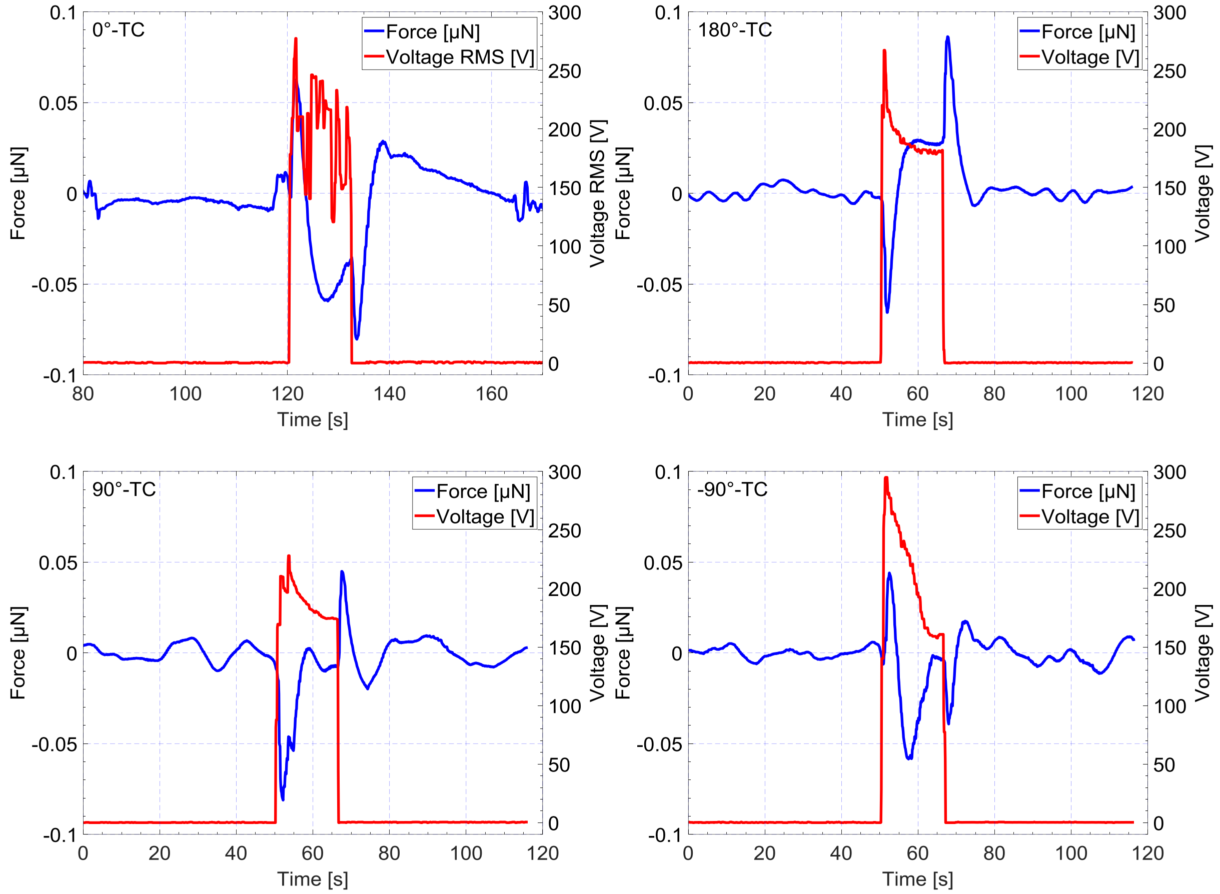

Fig. 98 – TB2 MET05 CSUF Fixed Frequency Tests (TC)
top left: 0° configuration with TC | top right: 180° configuration with TC
bottom left: 90° configuration with TC | bottom right: -90° configuration with TC

Without the drift, Fig. 98 shows the same effect as observed by Woodward [16], and seen in Fig. 12. Furthermore, it was reproduced with the same electronics and device as at CSUF. There are switching transients of about 0.06 μN, an order of magnitude or two below the effects reported by Woodward. The switching transients also depend on the orientation of the device. Where the thermal drift of Sector 3 has been removed, there is a small steady-state component representing half the amplitude of the switching transients. This steady-state component seems to vanish for the 90° and -90° orientations, although the switching transients are still present.

The next graphs show the influence of the copper block mount in Fig. 99. Both tests used CSUF electronics in the 0° and 180° orientations and a driving frequency of 36 kHz. The results involve no TC. These show a lower force, compared to Fig. 97. However, the lower voltage also indicates that the same driving conditions were not obtained despite the same target frequency. These tests proved that the switching transients are present despite different driving conditions. The copper block can have slightly shifted the resonance spectrum, but it also seems to remove the drift, as was observed in experiments with TB1. Interestingly, the balance drift seen in Fig. 97 is not observed here, despite the large temperature increase observed.

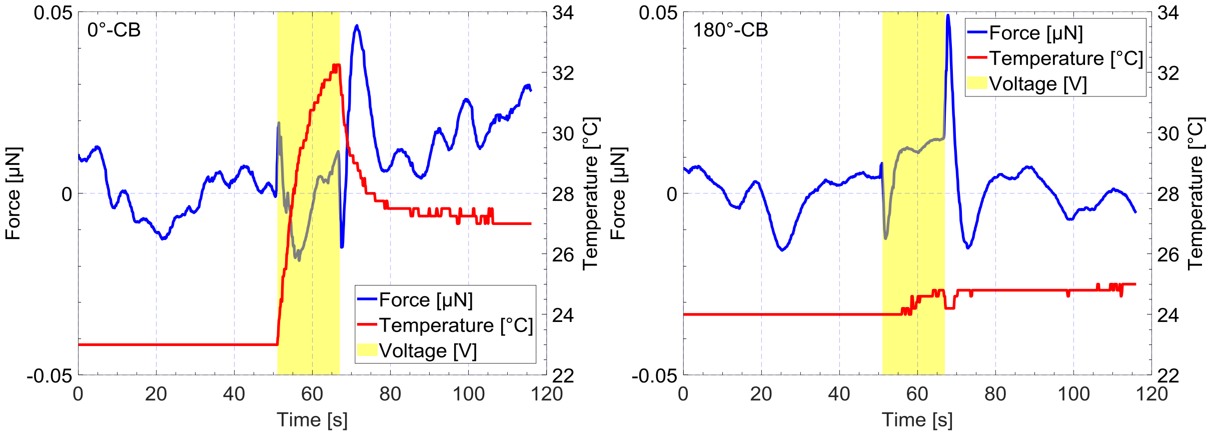

Fig. 99 – TB2 MET05 CSUF Copper Block

left: 0° configuration | right: 180° configuration

In the next tests, the effect of the ambient pressure is investigated using the same driving voltage and frequency. The electronics are the CSUF electronics and the mount is the solid mount without a copper block. Fig. 100 shows the same amount of drift for both chamber pressures, as well as the same behavior and order of magnitude of the transient effect. Hence, the chamber pressure does not influence the force response in this low-pressure regime. To avoid a dielectric breakdown in the air gaps between electrodes, however, most tests were performed under a low atmosphere. The commanded frequency was 36.3 kHz.

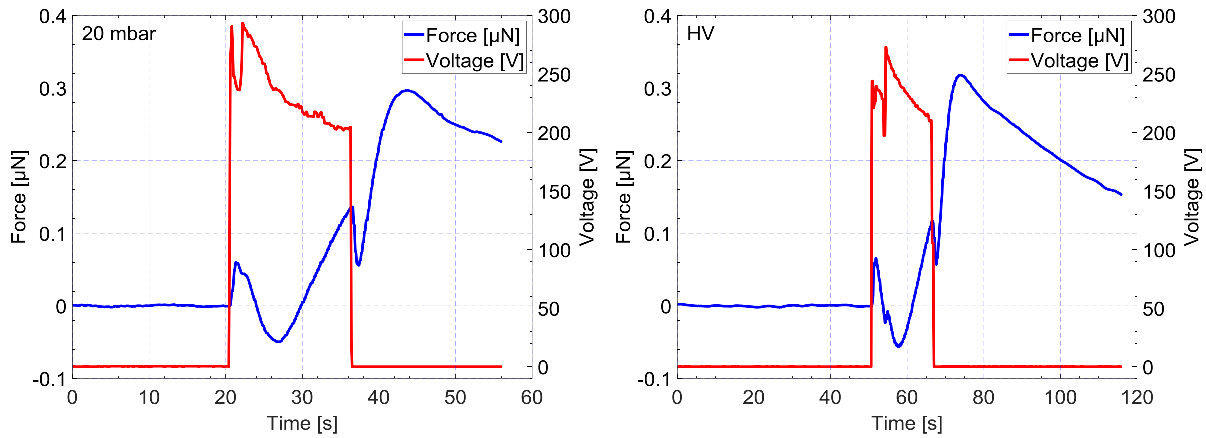

Fig. 100 – TB2 MET05 CSUF Variation with Pressure

left: 20 mbar | right: high-vacuum (10E-6 mbar)

Fig. 101 shows the results using the same configuration (0°) but for different driving frequencies and with CSUF electronics and copper block. The effect is always around the same order of magnitude, even if the frequency should have a great influence on the thrust according to the theory and the electromechanical characterization performed in Chapter 3. All the graphs below are plotted without TC. Interestingly, the temperature increase of the 36 kHz run is double the increase of the 34 kHz run, but the effect is similar in magnitude. The temperature does not seem to influence the drift.

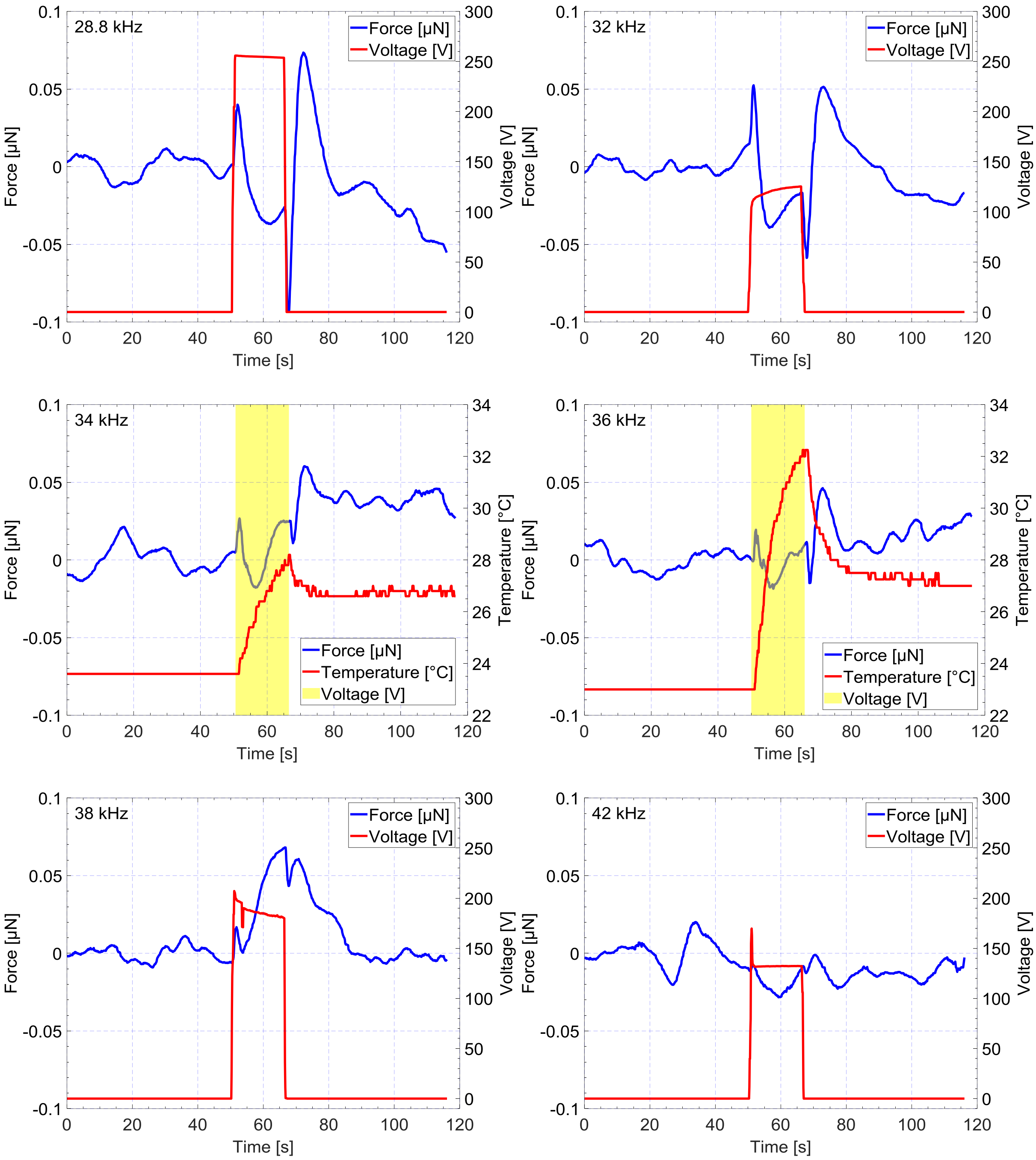

Fig. 101 – TB2 MET05 CSUF Various Frequency Tests

The tests have also been performed with a different mounting, using the isolating yoke provided by Woodward. Also, a different transformer, with a ratio of 1:2, was tested together with the CSUF electronics, instead of the 1:4 transformer usually used. The effect seen in Fig. 102 includes switching transients and a small drift. The force peaks and drift can be seen in different directions for the 180° and -90° orientations. However, the transformer and the yoke do not seem to have a great influence on the magnitude or behavior of the effect, when compared to previous experiments.

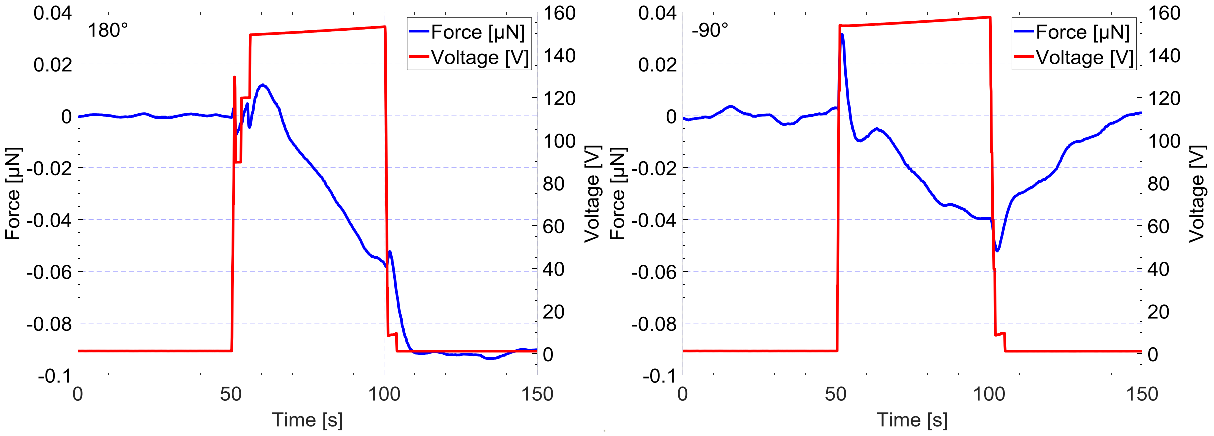

Fig. 102 – TB2 MET05 CSUF Tests with Transformer (1:2) and Yoke

left: 180° configuration | right: -90° configuration

The driving frequencies in the fixed frequency tests were selected using different criteria. Most tests were conducted using the resonance frequency, which was identified by the maximum current when sweeping a small frequency range. Some other tests were conducted at the driving frequency specified by Woodward in private communications. Lastly, some tests were conducted at a frequency with significant nonlinearity in current and strain gauge waveform signals. The resonance tracker allowed to follow the peak of maximum current during the experiment.

Driving frequency sweeps were also performed, comparing the CSUF electronics with the TUD electronics using the bridge-mode amplifier PA04(2) without a transformer. The advantage of performing sweeps consists in allowing to test all possible vibration modes, as well as pin-point, albeit short, driving at the required conditions for maximal thrust. The driving frequency was varied from 48 to 24 kHz in a backward sweep. The results from Fig. 103 clearly show the impulsive deflection of the beam at certain frequencies, around 32 kHz and 36 kHz. These impulses occur for a thrust-producing orientation of 0° as well as for the no-thrust-producing 90° orientation. The temperature is also shown to increase in the neighborhood of the resonance and the force response peaks.

The sweeps conducted using CSUF electronics show similar behavior: an impulsive deflection of the beam at a certain frequency, but these are always followed by a reaction force of the same magnitude in the other direction. The behavior is not fully repeatable and only a few profiles were executed, hence, individual test results are shown in Fig. 103. The peaks are seen in both the 0° and -90° configurations. More individual test results can be seen in Appendix B, as well as other fixed frequency tests using TUD electronics.

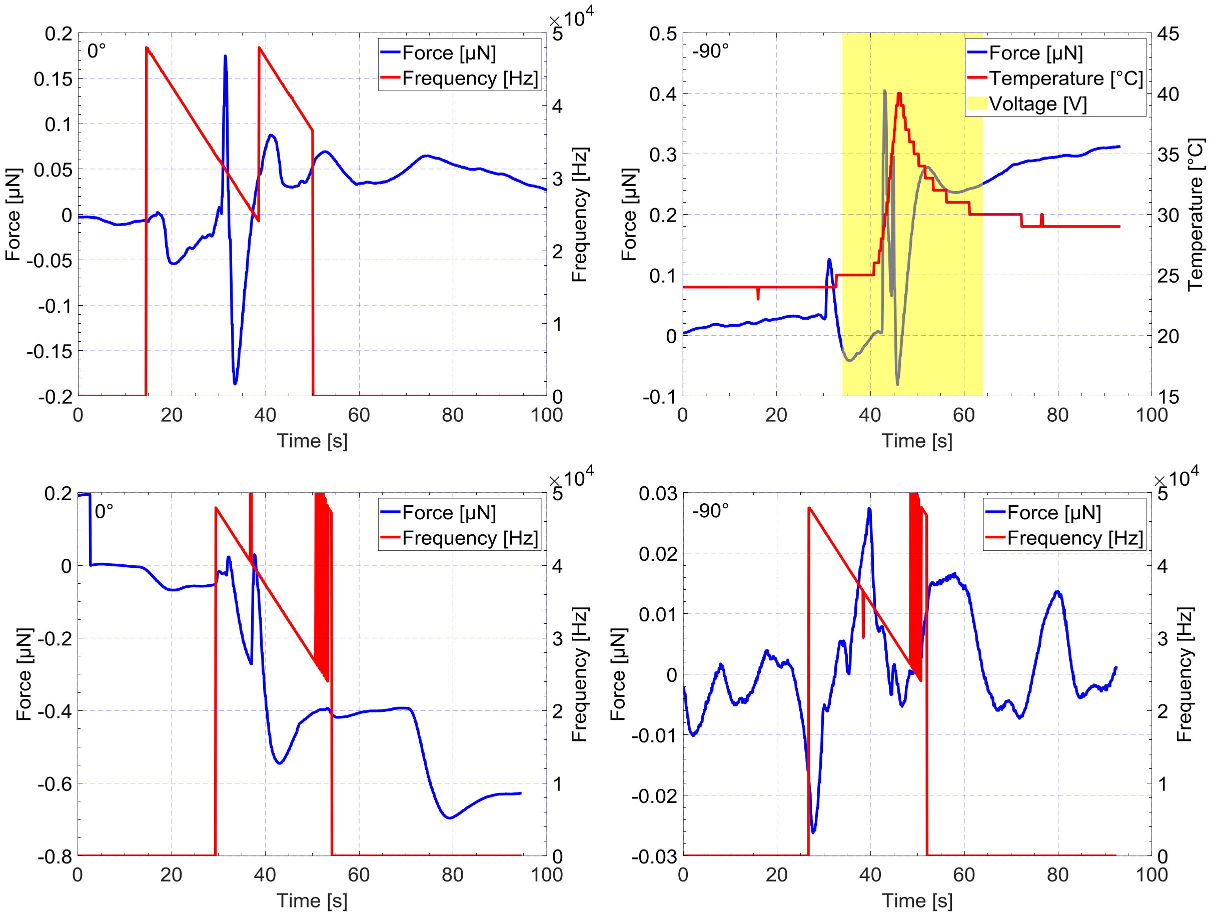

Fig. 103 – TB2 MET05 Sweeps with Copper Block

top left: TUD electronics, 0° configuration | top right: TUD electronics, -90° configuration
bottom left: CSUF electronics, 0° configuration | bottom right: CSUF electronics, -90° configuration

4.2.3 Beam Vibration

The method described in Section 3.1.6 for the thruster's vibrometry analysis was also used to examine the displacement of the TB2 beam during a driving frequency sweep with MET06 mounted on the yoke in the 0° configuration using TUD electronics and a fixed 50 V amplitude. The high sampling frequency of the interferometer's analog output allowed the full resolution of high-frequency components in the balance's response. The results are summarized below. Fig. 104 is a DFT of the current and vibration signals at a driving frequency close to resonance and represents a 0.6 ms-long snapshot within the frequency sweep. The graph shows the unique current peak around 36 kHz, and several small peaks in the vibration signal. The balance beam movements mostly occur below 20 Hz due to low-frequency vibrations in the building related to people walking and cars driving on the streets. This low frequency noise has also been observed in previous force diagrams (Fig. 92, Fig. 93, Fig. 98). The vibration of the beam at the driving frequency is very low, and is consistent with observations made by Woodward et al. [83]. However, there are two other sharp peaks that are interesting, one at 70 Hz and one at 500 Hz. The higher frequency vibration peak was studied in more detail.

Fig. 105 is a compilation of the main components in the current and vibration signals, obtained during a full driving frequency sweep. The current curve was obtained by extracting the current amplitude at the driving frequency using a DFT for each 0.6 ms interval and a sampling frequency of 100 kHz. The vibration curve was obtained by taking the amplitude of the vibration occurring at 500 Hz in each 0.6 ms snapshot of the sweep. The curve shows an increase in this particular vibration in the neighborhood of the resonance peaks, which can be identified from the peaks in the current curve of the same diagram. Hence, even though beam vibration is very low at the driving frequency itself, vibration from the MET can be coupled to larger lower-frequency vibrations on the balance.

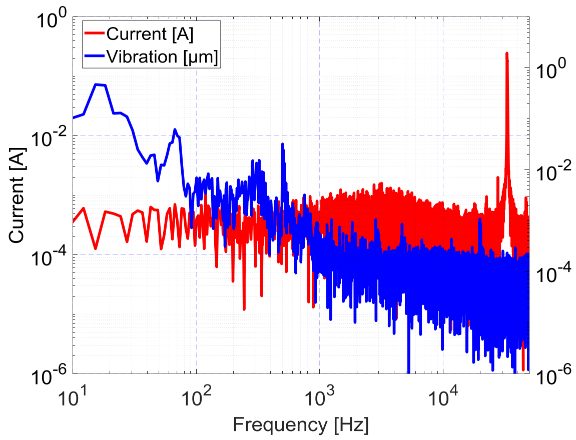

Fig. 104 – TB2 Beam Vibration DFT

Current and vibration DFT with MET06 and TUD

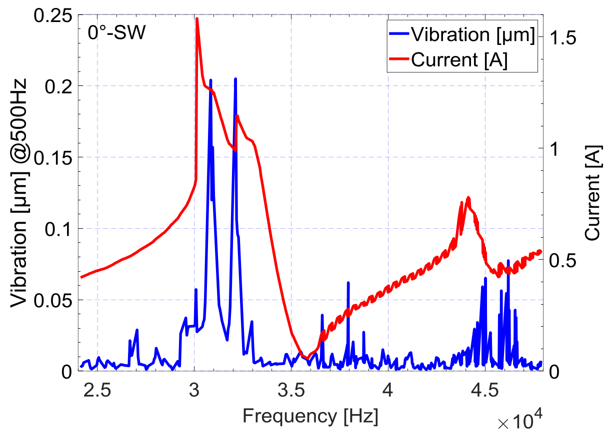

Fig. 105 – TB2 MET06 TUD Beam Vibration

Current and vibration sweep

4.2.4 Discussion

TB2 was adapted for the MET campaigns, and it showed the best resolution and time response so far. Its dynamic behavior is closer to Woodward's balance [16] since it has a quicker reaction time. It has better electromagnetic protection and mu-metal shielding than TB1. Finally, the MET test campaign on TB2 was the most extensive in terms of parameter variations and number of runs. This section is an attempt to unravel many of the remaining mysteries. The main observations are listed here:

- Dummy tests with resistor and capacitor reveal that impulses due to EMI are reduced by one order of magnitude in comparison to balance TB1, when the balance is well grounded.
- Drift is still present in the dummy resistor tests with AC voltage. The drift as well is reduced by one order of magnitude when compared to TB1.
- Without proper grounding, dummy tests with a capacitor and MET04 have revealed a positive force response of about 0.5 µN due to the floating potential and interaction with the surroundings, despite AC voltage. Grounding the balance eliminates the signals.
- Fixed-frequency tests show the switching transients observed by Woodward, albeit in every orientation, including 90°. In all tests performed with four METs, with Woodward's yoke or copper block, with different electronics, voltage, and frequencies, the force peaks never exceeded 0.2 µN.

- Sweep tests reveal impulses at driving frequencies near resonances for MET devices, occurring for every orientation, including 90°. The force reached up to 0.6 μN in some cases. The behavior was not 100% repeatable.

The first point to be discussed is the grounding of the balance. The dummy resistor tests showed that there would be minimal EMIs on TB2, whether from the DC or AC signals, when the balance was grounded. This eliminates the possibility of an experimental artifact due to interactions with the Earth's magnetic field or cable movement caused by electromagnetic fields. However, an effect arose when the balance was not grounded. This was observed when performing capacitor, MET04 and MET05 tests using TUD electronics with the PA04(2) amplifier in bridge-mode. When the balance beam was not grounded, the amplifier electronics charged the conductive beam and experiment box to a floating potential that led to electrostatic attraction between the mobile and fixed parts of the balance. The effect disappeared once the beam was grounded and didn't occur with the CSUF electronics. In all subsequent tests and MET results shown in this section, the balance was grounded and this effect was prevented.

Furthermore, the balance showed evidence of thermal drift during the dummy resistor tests with AC voltage, although the drift is an order of magnitude lower than with TB1. In tests with MET05, the force spikes in the driving frequency sweeps coincided with a strong temperature increase (Fig. 103). However, the fixed frequency tests showing larger temperature gradients did not directly translate into an increase in the drift (Fig. 101). Next, MET tests using different chamber pressures confirmed that the effect is not influenced by the vacuum level in the chamber. Thus, the effects observed do not originate from convection, buoyancy, or outgassing at a pressure of 0.03 mbar. The tests were not performed at ambient pressure, due to the difficulty to calibrate the balance and the increased disturbances. The predicted thrust from the Mach-effect theory cannot account for the drift observed, since it is not an impulse and did not depend on the thruster's orientation on the balance. Moreover, thermal effects cannot account for the rapid switching transients occurring in the MET tests.

The switching transients that were observed on TB2 correspond to the effects observed by Woodward et al. [16]. However, these transients did not increase with the use of different frequencies and amplifier electronics. Larger force peaks of up to 0.4 μN were detected during frequency sweeps, due to the finer tuning of the resonance frequency. However, the same transients were also observed in the 90° orientation of the thruster, despite the fact that transverse forces should have minimal effect on the balance, as shown in Section 3.3.2. Thus, the concept of thrust along the longitudinal axis of the MET can be rejected. The drift and the transient forces observed must come from a different source.

The findings are summarized once more in Table 24 and include the results of the vibrometry analysis.

Test	**Dummy**	**MET05**	**Vibrometry**
Variations	Resistor (AC/DC) Capacitor (AC)	Electronics, mounting, chamber pressure, frequency, sweeps, pulse length	Balance beam
Max. Measured [μN]	0.03	0.15	$\mathrm{N/A}$
Predicted [μN]	0	> 1	$\mathrm{N/A}$
Observations	• Drift = 50 nN/min • AC signals have an effect when the balance is not GND	• Drift = 0.6 μN/min • Switching transients are present and reverse • Force trace does not go back to zero • Effect present in all orientations • Effect cannot be increased	• Vibration peaks (70 Hz, 500 Hz) • Vibration increased around resonances

Table 24 – TB2 Test Results Summary

The observation of low-frequency beam vibration and vibration increase during resonant driving of MET on the balance led to an investigation of vibrational artifacts. The following analysis studies the influence of vibration on the balance using a single DOF model of the torsion balance as described in Section 3.3.3. Different forcing functions have been tested to examine the reaction of the balance to different stimuli. These tests can be compared with actual tests performed with the sinusoidal excitation of the VC in Section 3.3.2. Evidence of stick-slip includes loosening of the screws, the brass powder inside the experimental setup, and offsets in the force response curve that do not revert to zero after disabling the electric field. Fig. 106 shows the responses to a forcing function with different frequencies. If the driving frequency is low enough (1 Hz), the frequency signature can be seen in the balance response as well, as shown on the left. The switching transients, however, are significantly larger in amplitude. Then, if the forcing frequency reaches a higher value, the frequency signature cannot be observed in the balance response anymore. However, the switching transients are still visible, as shown on the right for a forcing frequency of 100 Hz. The amplitude of the switching transients also gets reduced. This is an important observation that could well apply to the behavior observed during the TB tests with the MET.

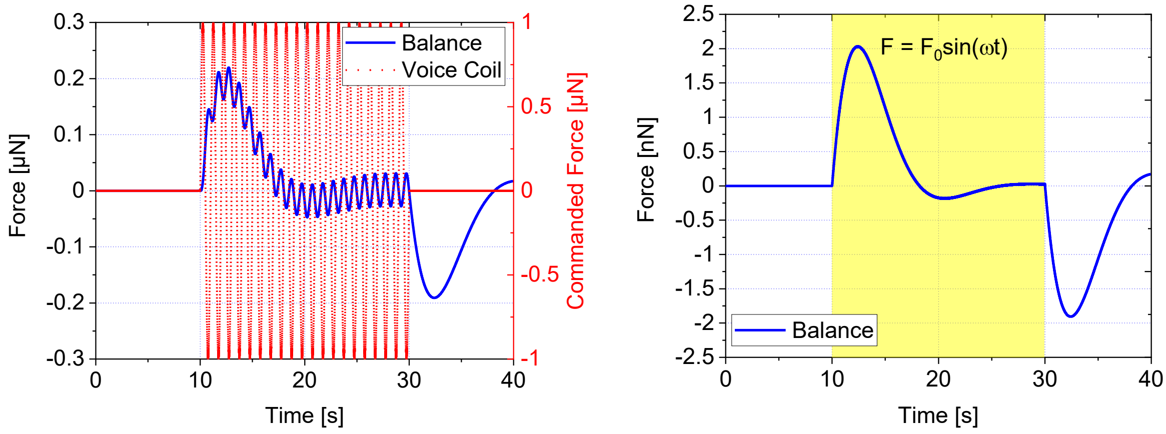

Fig. 106 – TB2 Pulse Response Simulation

left: 1 µN, 1 Hz pulses | *right: 1µN, 100 Hz pulses*

Another important observation is the simulation of a discontinuity in the vibration operation. In the event of a longer interruption, the balance response might be subjected to jumps of the switching transients. This behavior could be explained by the intermittence of the vibrations as the resonances get activated during the sweeps. A discontinuity was included in the forcing function and the simulated response was plotted in Fig. 107.

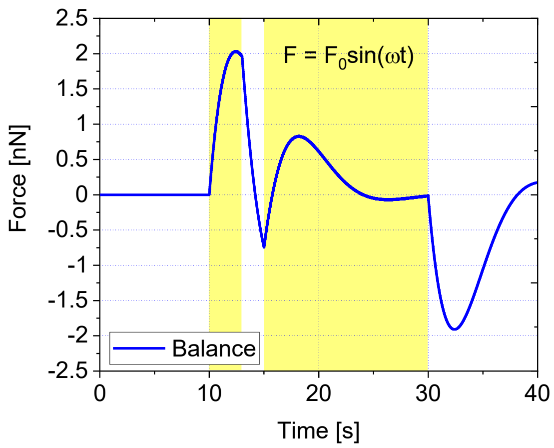

Fig. 107 – TB2 Discontinuous Pulses Simulation

1 µN, 100 Hz pulses with discontinuity

Finally, nonlinearity was added to the forcing function and equation of motion in the simulation. In the event of a second harmonic signal superposed to the driving frequency, as would be the case for the nonlinear responses of piezoelectric materials described in Section 3.1.9, no significant behavior deviation can be seen in the balance response shown on the left, in Fig. 108. However, if a significant nonlinearity is added to the equation of motion, such as the sudden change in the spring constant of the balance is added, a significant deviation can occur, as seen on the right.

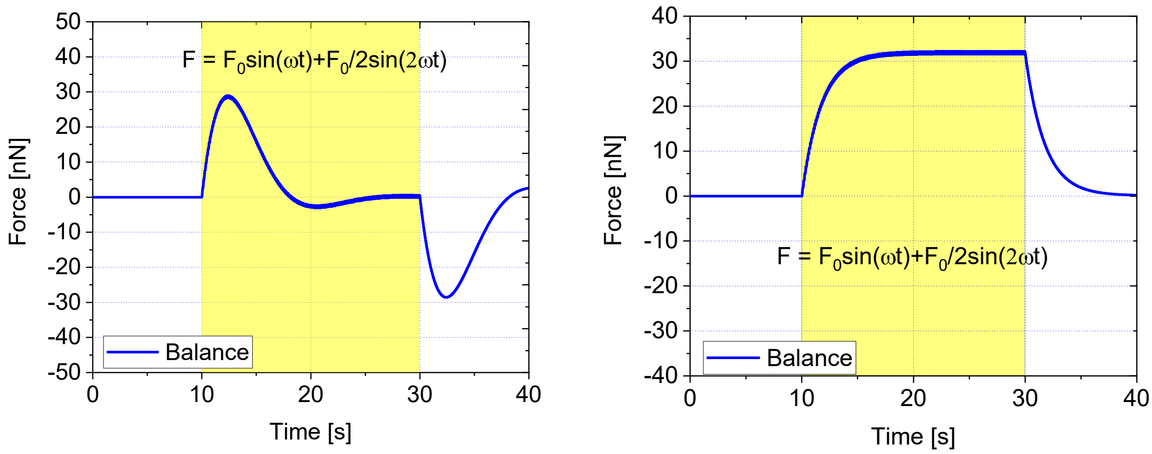

Fig. 108 – TB2 Non-linear Pulse Simulation

left: 1 µN, 10 Hz, sine function with second harmonic content, right: 1 µN, 10 Hz and change in spring constant

Thus, the single DOF simulation of the torsion balance and the addition of a high-frequency vibration stimulus can reproduce the same transient behavior as observed by previous researchers [16,81] in MET experiments mentioned in Section 2.4 and observed in this section. Furthermore, the vibration of the balance beam at the driving frequency is extremely reduced, despite the presence of slower transients, which is consistent with previous observations from Woodward [82].

The reason behind the absence of switching transients in the MET experiments with TB1 are two-fold. First, the larger electromagnetic and thermal effects in comparison with TB2 experiments exceeded 0.4 µN in magnitude, whereas the transients measured on TB2 only had an amplitude of 0.1 µN. Secondly, the slower pulse response of TB1 observed in its characterization tests are a result of the larger rotational inertia of the balance beam. This implies that the balance's reaction to a high-frequency vibration stimulus will be reduced when compared to TB2, effectively reducing the amplitude of the force transients. Finally, the faster dynamic response of Woodward's balance can also be an explanation for the larger force peaks measured by Woodward et al. [78], using the same argument.

The origin of the drift observed on TB2 remains unexplained, since it does not seem to vary greatly with different temperature increases or with the chamber pressure, and since electromagnetic effects have been eliminated. Nevertheless, an observation of different drift magnitudes depending on the mounting of the MET, including the yoke and the copper block, also suggests the presence of a vibrational artifact related to the device's mechanical connection on the balance. Indeed, the shift of the balance beam's position is visible long after removing the driving voltage cannot be due to a thrust force. Instead, this drift can be explained by stick-slip vibrations that are infamous for being behind the oscillation thrusters, also called "Dean drives" as carefully explained in Chapter 6 of Frontiers of Propulsion Science [13].

4.3 Double-pendulum Balance Test Results

4.3.1 Dummy Tests

Dummy tests were performed with a 15 Ω resistor to examine the EMI on the double-pendulum balance described in Section 3.4.1. The AC signal tests are missing from this campaign. However, the balance was always grounded when using the bridge-mode amplifier after having learned the lesson with TB2, meaning that EMI was kept to a minimum. The device setup and uppermost plane of the balance are shown in Fig. 109. The resistor was simply placed on the platform, without a screwed connection. The test parameters are summarized in Table 25 and were performed at both ambient pressure and medium vacuum (0.03 mbar).

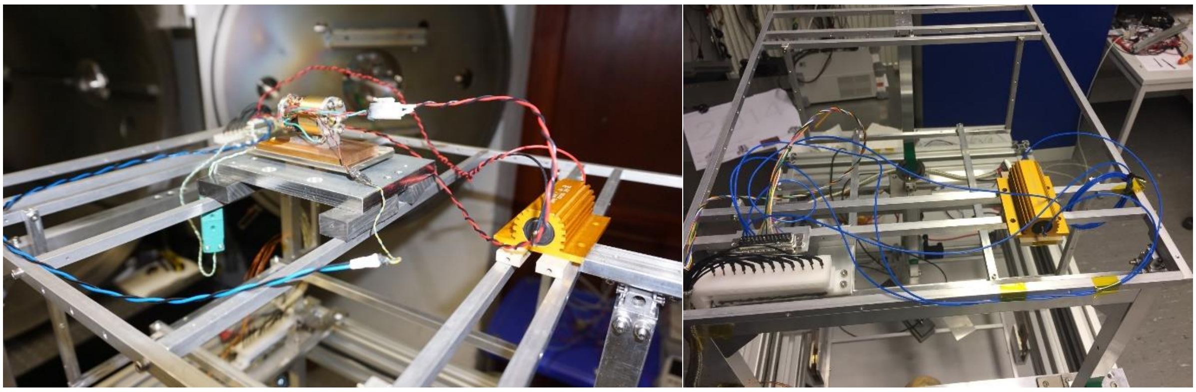

Fig. 109 – DP1 Resistor Test Setup

No. Tests	Orientation [°]	No. Profiles	Voltage [V]	Time [s]	Signal Type	Particularity	Electronics
1	0	15	180	30	DC	Pin-contacts	PA04(2)

Table 25 – DP1 Dummy Test Series

The test results featured in Fig. 110 show a strong reaction to DC current and heating. Tests at medium vacuum and ambient pressure with the same driving parameters show a difference of a factor of 2 in magnitude. The graphs show the presence of a negative drift, noted from the difference between the traces before and after the test profile, but also an impulse effect that can be seen from the sharper response at turn-on and turn-off.

This impulse can be attributed to electromagnetic effects that do not vary significantly with the atmospheric pressure. However, thermal effects can be superposed on the electromagnetic effects. It was found later in a test campaign with the EmDrive, that the main culprits for the forces observed were the liquid-metal-pin connections of the balance for the amplifier supply [25]. A DC current passing through the off-centered liquid-metal-pin connection could bring about a deviation of the balance's platform. However, since the amplifier used in MET tests is not on the balance but outside the vacuum chamber, artifacts caused by DC currents as shown in this test should not occur. Nevertheless, effects related to heat transfer cannot be excluded from the MET tests.

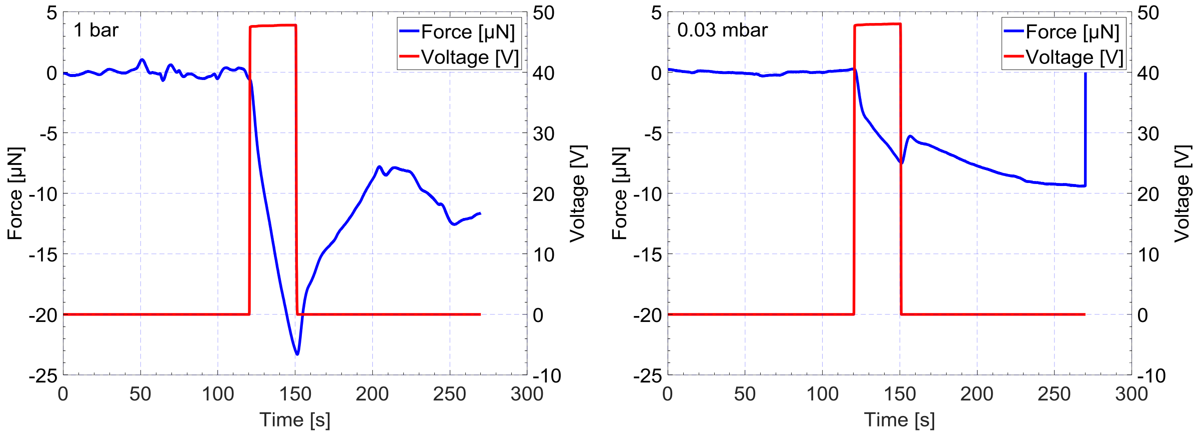

Fig. 110 – DP1 Resistor DC Test

left: ambient pressure (1 bar) | right: vacuum pressure (10E-2 mbar)

4.3.2 MET03

Having already sent loaned devices MET05 and MET06 back to California in 2020, DP1 tests were performed with MET03 after it had undergone a transformation or possible partial depolarization due to heat and stress in previous experiments. The new resonance frequency was around 21 kHz, as shown in Section 3.1.7. The device was placed on a copper plate to dissipate the heat coming from resonant vibration, and the whole assembly was simply placed on Sorbothane® pads to reduce the transmission of vibration. The device was encased in a mu-metal box to shield the balance from the magnetic fields, however, that cage was not grounded. In a few tests, the assembly was taped to the structure using Kapton® tape to make it a more rigid connection. All tests were conducted with the same device, setup, and electronics, using the dedicated APEX amplifier in bridge-mode from the TUD electronics. The setup for the 0° configuration is shown in Fig. 111, and the test parameters are summarized in Table 26. A positive thrust corresponds to a movement of the device towards the brass mass.

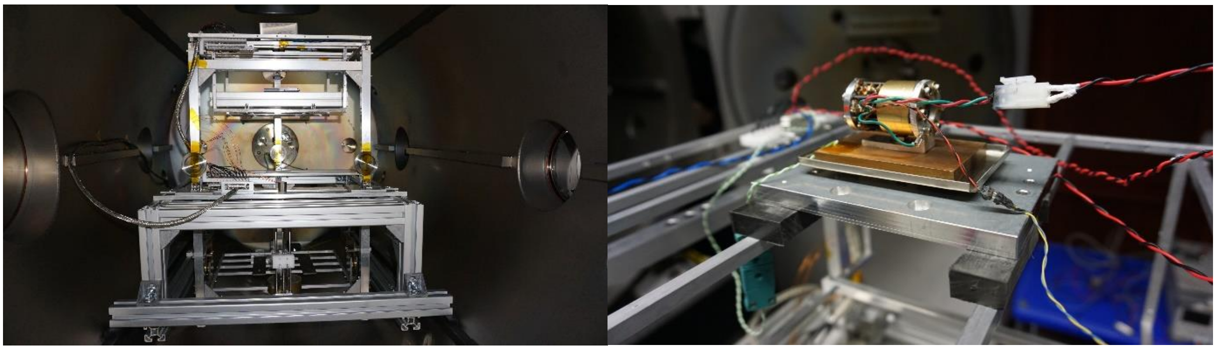

Fig. 111 – DP1 MET03 0° Test Setup

No. Tests	Orientation [°]	No. Profiles	Voltage [V]	Time [s]	Signal Type	Particularity	Electronics
6	0	20	180	20	Single/Sweeps	Sorbothane/ Kapton	PA04(2)
2	90	5	180	20	Single/Sweeps	Sorbothane/ Kapton	PA04(2)

Table 26 – DP1 MET03 Test Series

The fixed frequency tests were performed with a driving frequency of 21.8 kHz for the 0° configuration and 24 kHz for the 90° configuration, the results of which are shown in Fig. 112. The frequencies were chosen to maximize the effect observed, after having performed frequency sweeps to identify the resonances. The 24 kHz resonance frequency appeared during high voltage sweeps only, and was not seen in the electromechanical analysis of Section 3.1.7.

The results show the typical Woodward [16] trace with the switching transients in the 0° orientation. These transients are much smaller in the 90° orientation. The results without thermal correction additionally show the drift of the balance's baseline. The force peaks observed are around 100 nN after TC, and the drift was about 150 nN and in the same direction in both 0° and 90° orientations. The force responses shown in Fig. 112 drift in the same direction except for a rare few individual runs of the 0° configuration shown in Appendix B. The magnitude of the drift and the switching transients is very similar to the results obtained on TB2.

Driving-frequency sweeps from 20 to 48 kHz were also performed in two perpendicular orientations (0° and 90°) and the force responses are shown in Fig. 113. The force curve looks very similar when comparing both tests. The sudden jerk of the balance beam occurs with the same magnitude and direction but at a slightly different driving frequency. The resonances obtained from the current spectrum of MET03 are around 21, 24 and 48 kHz and correspond to the beginning and end of the sweep. The balance response further drifts downward after the voltage is switched off, and reaches well below the original position.

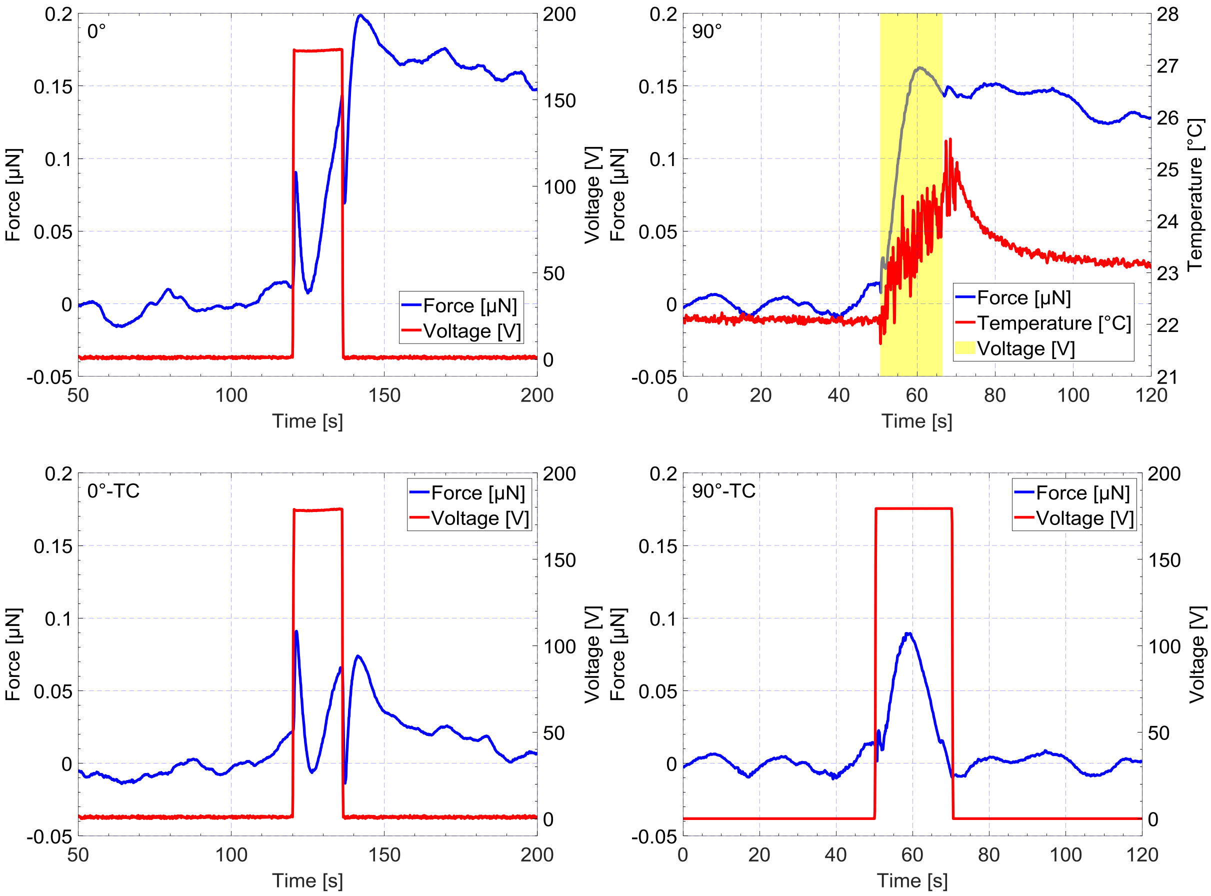

Fig. 112 – DP1 MET03 CSUF Fixed Frequency Tests

top left: 0° configuration | top right: 90° configuration

bottom left: 0° configuration with TC | right: 90° configuration with TC

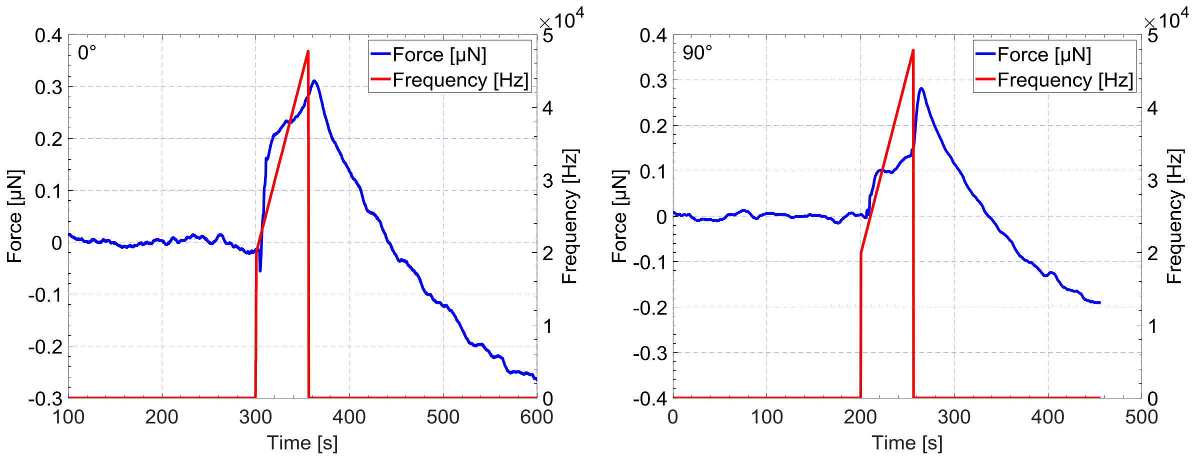

Fig. 113 – DP1 MET03 CSUF Sweeps

left: 0° configuration | right 90° configuration

Lastly, vibrometry was used to examine higher and lower-order vibration components of the balance platform. Driving frequency sweeps were performed from 20 to 30 kHz at a constant voltage with MET03 in the 90° configuration. As in the vibration analysis for TB2, a snapshot of the current and beam vibration is provided for a single driving frequency. Fig. 115 represents a DFT of the signals in a 0.6 ms snapshot within the 30 s sweep, where the driving frequency is around 24 kHz. The diagram shows a small peak at 20 Hz, corresponding to some oscillation from the environment also seen with the TB. Another isolated vibration peak can be seen at 900 Hz when driving the piezoelectric devices. There is minimal vibration at the driving frequency of 24 kHz.

The amplitude of the 900 Hz vibration component of every 0.6 ms interval was plotted over the entire driving frequency sweep, next to the current curve that was obtained by compiling the current amplitude at the driving frequency, in Fig. 114. Similar to the behavior observed with TB1, the high-frequency vibration component increased at the same frequency as the current peaks that indicate the resonance state. Hence, more beam vibration can be associated with resonance driving, and the high-frequency vibration of the MET is coupled to lower-frequency vibration even in the 90° configuration on the DP1.

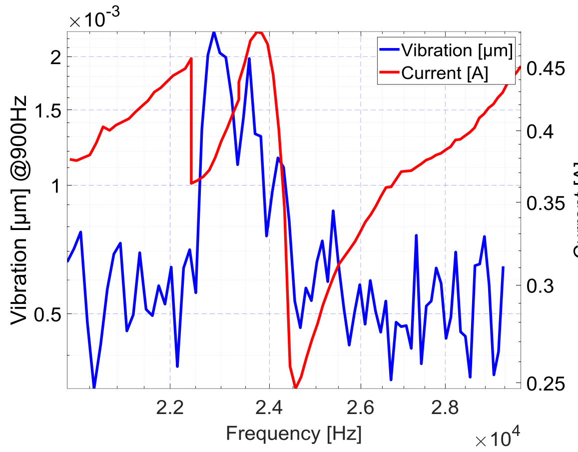

Fig. 114 – DP1 MET03 Beam Vibration

current and 900 Hz-vibration curves

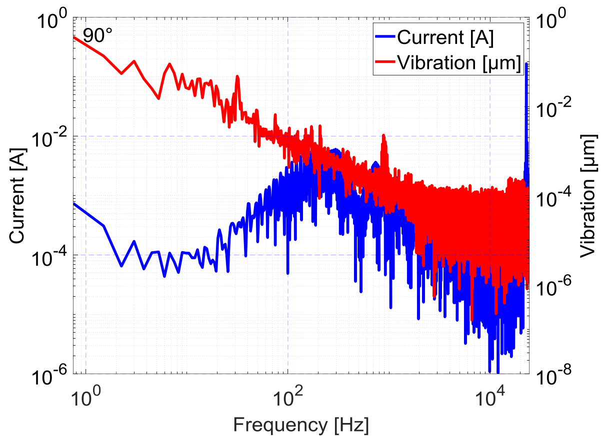

Fig. 115 – DP1 MET03 Beam Vibration DFT

current and vibration DFT

4.3.3 Discussion

The tests performed with DP1 are summarized and discussed. This new balance has a good resolution and reaction time comparable to TB2 [25,76]. The test campaign with DP1 was limited, since it was mainly used for other thruster test campaigns. The first difference to the TB is its more complex structure involving more parts and torsional pivots, but it is also more stable and resistant to thermal shifts occurring in one plane, and against torsional moments that tend to displace the balance beam. Furthermore, the metal liquid contacts that ensure friction-free power transmission are placed on the side of the balance, rather than within the balance's pivot axis. This new configuration could introduce new experimental artifacts. Here are the main lessons learned:

- Dummy tests with DC current reveal the presence of EMI with the off-centered liquid contacts of the balance for power transfer.
- Dummy tests also show the presence of thermal effects, as seen from the impact of the chamber pressure on the balance response to DC current.
- MET tests confirm what has been seen on the TBs: switching transients of up to 100 nN are seen at resonance in 0° and 90° configurations.
- A drift of at most 300 nN can also be seen when looking at force responses during the sweeps without thermal correction. The offset does not seem to depend on the device orientation.
- Small amplitude beam vibration has been detected at multiple frequencies and increased close to resonances.

The order of magnitude of the drift or offset in the force baseline of MET experiments is similar to the TB tests. The drift or offset was seen for both 0° and 90° orientations, thus it cannot be due to thrust along the longitudinal axis of the thruster. The Faraday cage of the thruster was not grounded, which could imply some interaction between the balance platform and the box. However, since the balance's support structure is larger and more rigid than the TB beam, that interaction should be very small. Furthermore, the DC interaction observed in the dummy tests is excluded when using oscillatory signals.

The switch-on and switch-off transients in fixed frequency tests and the sudden jerks during frequency sweeps represent more spontaneous events. Thermal drift is excluded from the cause of these spontaneous deflections, since the movement is more rapid than the propagation of heat as shown by the temperature curve.

Another point to be considered is that the device box was not fixed on the balance platform but placed on sticky Sorbothane ® pads. Thus, the possibility of stick-slip cannot be excluded. Furthermore, as can be seen from the beam vibration analysis, the platform was seen to vibrate around 900 Hz and this can lead to the same phenomenon analyzed in the previous section.

Moreover, the effect observed in fixed-frequency tests has the same order of magnitude and behavior as in the TB tests, despite the added rigidity and structural support of the double-pendulum balance. This is not surprising if the effect is caused by vibration as explained in Section 4.2.4, since DP1 has a similar reaction time and stiffness as TB2. The observations are summarized in Table 27.

The observations made with TB1, TB2 and DP1 lead to the conclusion that the forces seen are linked with a vibrating object on the balances, as examined in the simulation and discussion after the TB2 tests. Moreover, the drift observed in both TB2 and DP1 is not a consequence of thrust, and could be explained by the stick-slip vibration of some part of the test device or balance. The transient forces can be explained by the oscillation of the piezoelectric actuator.

Finally, the sensitive thrust balance experiments resulted in a measurement resolution of 10 nN, despite the presence of significant vibration, and reject the claims made by the Mach-effect theory and the thrust predictions made by Woodward [16].

Test	**Dummy**	**MET05**	**Vibrometry**
Variations	Resistor (AC/DC) Capacitor (AC)	Electronics, mounting, chamber pressure, frequency, sweeps, pulse length	Balance beam
Max. Measured [μN]	7.5	0.3	$\mathrm{N/A}$
Predicted [μN]	0.0	> 1	$\mathrm{N/A}$
Observations	• Drift = 15 μN/min • Off-center electric contacts introduce a force during DC voltage	• Drift = 0.6 μN/min • Switching transients • Effect observed in both 0° and 90° configurations	• Vibration peaks (30 Hz, 900 Hz) with a few nm in amplitude • Vibration increase at resonance

Table 27 – DP1 Test Results Summary

5. Centrifugal Balance Experiments

5.1 Centrifugal Balance

As thrust was not detected using the MET experiments on double-pendulum and torsion balances in vacuum, the next logical step to detect mass fluctuations was to pursue direct centrifugal measurements of the transient mass, in an attempt to increase the measurement resolution even further and remove the artifacts associated with vibration. By rotating a device at high speed, its mass or any fluctuation in mass can be converted to a force and measured using a piezoelectric transducer. The relation between mass and centrifugal forces is demonstrated by Equation (95), where ω is the rotation frequency, r the moment arm, and $m(t)$ the mass fluctuation. Then, the relation between the transducer signal and the mass fluctuation is in the next equation, where $V(t)$ is the measured signal and K the transducer's conversion constant:

$$\boldsymbol{F(t) = m(t)\omega^2 r} \quad , \tag{95}$$

$$m(t) = \frac{V(t)}{K\omega^2 r} \quad . \tag{96}$$

Woodward was the first with the idea to use centrifuges to investigate mass fluctuations with the centrifugal force as an amplification factor for weight measurements [96]. The measurement of transient mass at the frequency required to drive a significant energy fluctuation requires a linear transducer in the high-frequency range, as well as a good calibration. This chapter presents a summary, analysis, and discussion of the tests performed with the centrifugal balance (CB1) and rotating Mach-effect devices. The chapter is divided into sections describing the experimental setup, the calibration process, the test results, and the sources of error. The test results show the piezoelectric transducer signal V_{SG} for different voltages applied to the test device V_{OUT} and balance rotation frequencies.

5.1.1 Description

A rotating system was designed and built by colleague Willy Stark to analyze mass fluctuations with a piezoelectric force transducer, inspired by Woodward's rotating experiment [96]. With the apparatus, a test device of up to 200 g could be rotated to a maximum of 3600 rpm (60 Hz) with a rotation radius of 9 cm. With these parameters, the maximal centrifugal acceleration reached around 1300 g_0. The apparatus consists of a stainless-steel frame including two support bearings for the 17 mm diameter rotating shaft. Rotation is imparted by a DC brush motor, HCP-1077 from Johnson Electrics. The motor operates with a torque of 1.2 Nm and has a free rotation rate of 22000 rpm. During rotation, 170 W is supplied by a DC power supply. Mechanical rotation is transmitted with a 20:12 gear ratio using a toothed belt. To reduce the noise coming from the DC motor 100 µF capacitors were connected between the terminals. No significant noise was detected apart from EM noise from the motor supply when turning the motor on. The rotating shaft is balanced using appropriate counterweights to avoid rotation eccentricity, which would increase signal noise as well as the required torque. The rotation rate is calculated employing a photoelectric barrier that faces a set of regularly spaced openings in a rotating disk affixed to the shaft. Power and signal transmission to the device is achieved using a slip-ring, SNG012-12 from Senring, that can be rotated up to 5000 rpm and through which 200 VDC can be transmitted. The slip-ring's axis was re-machined to ensure low eccentricity rotation. To protect the user, and eliminate electric fields in the cage, a 3.5-mm thick aluminum cage was built around the apparatus. Access to the device is controlled by a 10-mm thick acrylic plastic door, which is covered by a metal grid. The grounded metal grid was found necessary to reduce EMIs between the acrylic door and the data cables, by dissipating the charges generated in the dielectric material. The CAD rendering and principle of the experimental setup are shown in Fig. 116.

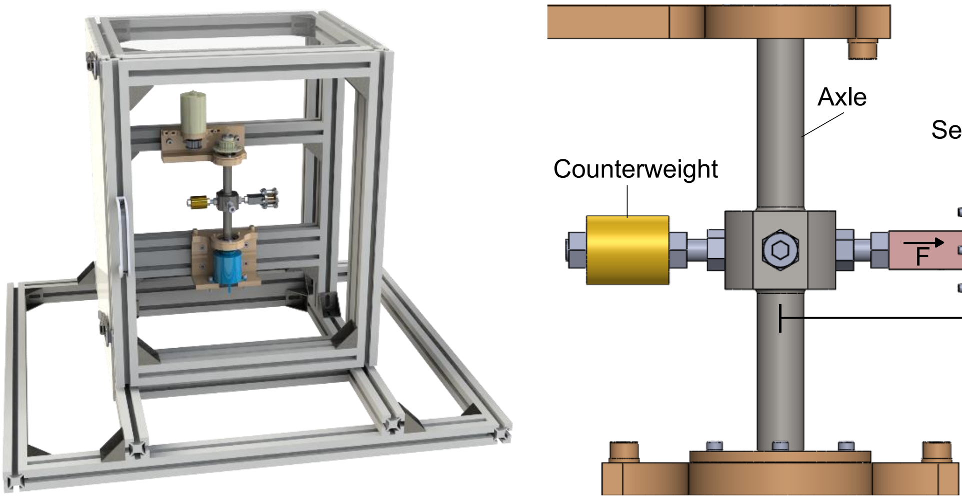

Fig. 116 – CB1 CAD

left: isometric view | right: front view

In Fig. 117, the picture of the centrifugal balance shows the aluminum panels installed, not shown is the 10 mm thick acrylic front panel covered by a metal mesh to protect the user. The electronics in the right-hand diagram show the presence of the slip-ring and the DC motor to power the rotation of the shaft. The rotating shaft and surrounding structure all need to be grounded using the star formation to avoid electrostatic effects and EMI. It was discovered that the ball bearings from the slip-ring do not reliably conduct electricity during rotation, and thus the structure needed to be grounded through the slip-ring as well. The piezoelectric transducer is isolated from the rest, ideally using an instrument amplifier to reduce its impedance and make it less susceptible to noise. The electronic components used are the same as in the TUD electronics for the thrust balance experiments in Chapter 4 and described in Chapter 3. The amplifier is the bridge-mode amplifier from APEX and the oscilloscope and frequency generator is the Picoscope for the CD01 tests. The Picoscope was replaced by the MFLI Lock-in amplifier, in the same configuration as shown in the block diagram, for the tests performed with CD02 and further devices. Different filters were used in combination with the strain gauge or sensor signal V_{SG}, for instance F01 with CD01, and these will be described in the individual test sections.

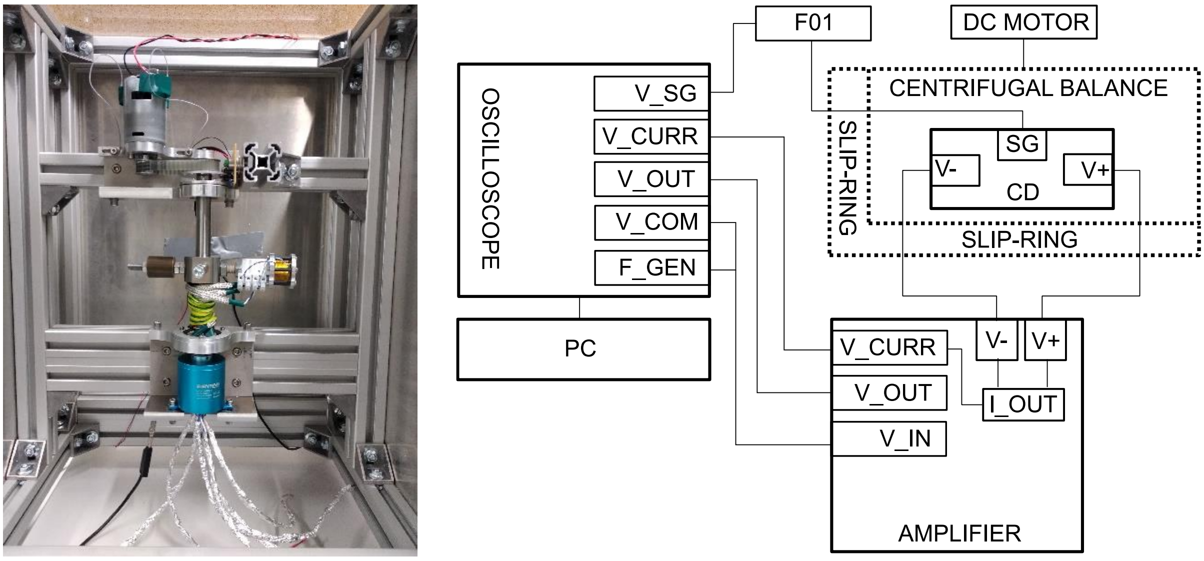

Fig. 117 – CB1 Picture and Electronics

left: CB setup picture | right: block diagram of electronics

5.1.2 Centrifugal Devices

The devices and tests performed on the centrifugal balance are summarized in Table 28.

Device Model	Type	Maker	Year of Issue	No. Tests	No. Runs	Resonances
CD01	Piezoelectric	Woodward	<2018	10	219	32, 39, 55, 65
CD02	Capacitive	Monette	2019	5	55	–
CD03	Capacitive	Monette	2021	7	289	–
CD04	Inductive	Monette	2021	6	372	97
CD05	Piezoelectric	PI Ceramic	2020	20	360	65, 111

Table 28 – Overview of CD

Below are descriptions and pictures of the Centrifugal Devices (CD) tested on the rotating apparatus. As can be seen from Fig. 118 and Fig. 119, the devices CD01 and CD02 are sandwiched between two aluminum plates using screws. This configuration makes the calculation of the transducer's coefficient a bit more complicated. The concept was changed from CD03 onwards, as seen in Fig. 120 and Fig. 121, where there is no parallel spring connected to the transducer, except the electric cables connected to the device, which are very compliant. The later designs make the conversion factor easier to calculate and the quasi-static calibration less liable to deviations. CD05 is a piezoelectric stack actuator that was designed and manufactured in collaboration with PI Ceramic GmbH, shown in Fig. 122.

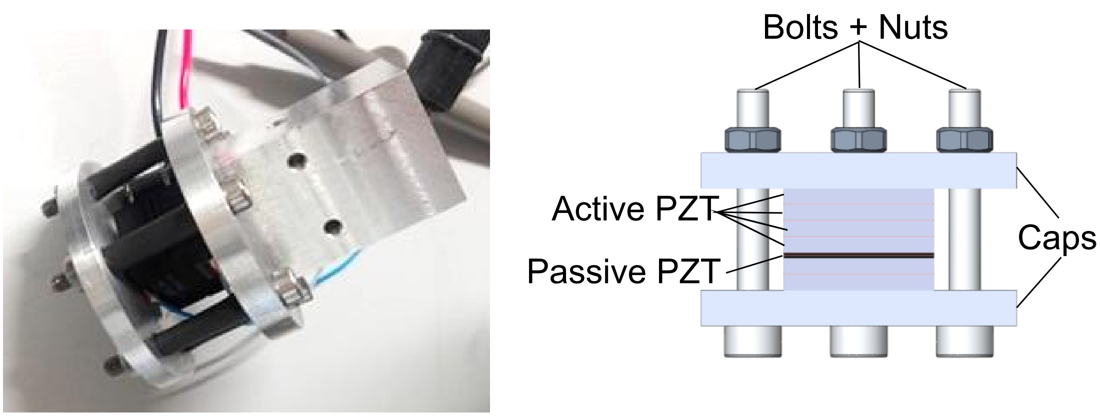

Fig. 118 – CD01 Construction
left: CD01 picture | right: CD01 sketch

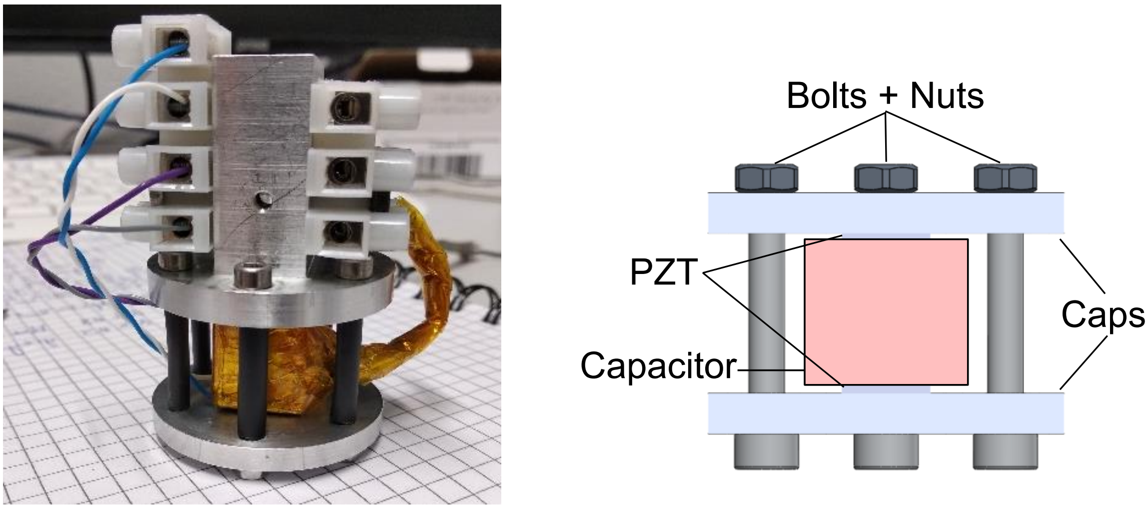

Fig. 119 – CD02 Construction
left: CD02 picture | right: CD02 sketch

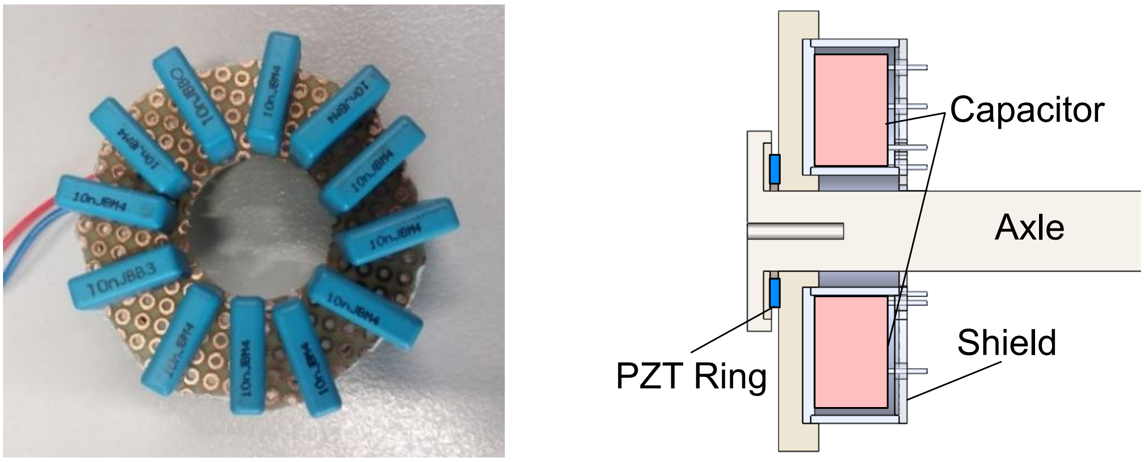

Fig. 120 – CD03 Construction
left: CD03 picture | right: CD03 sketch

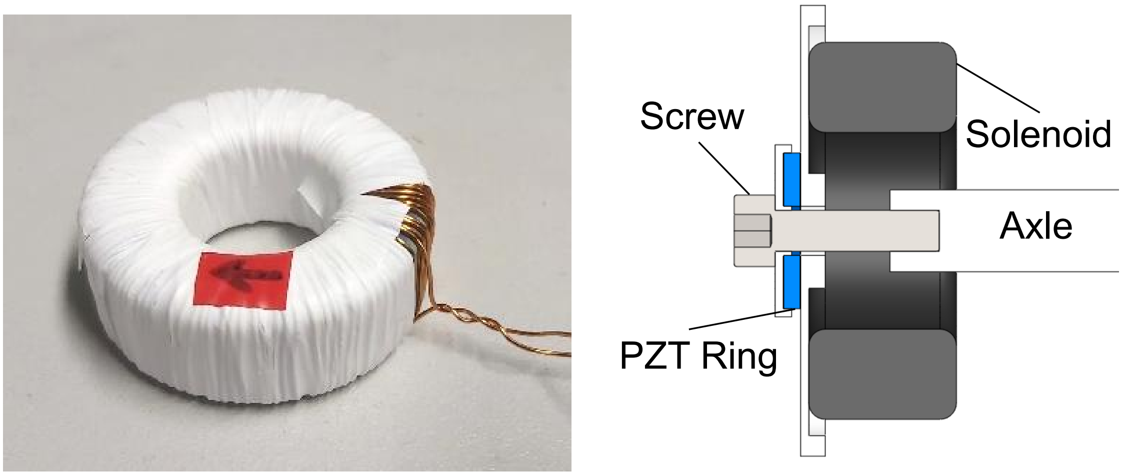

Fig. 121 – CD04 Construction
left: CD04 picture | right: CD04 sketch

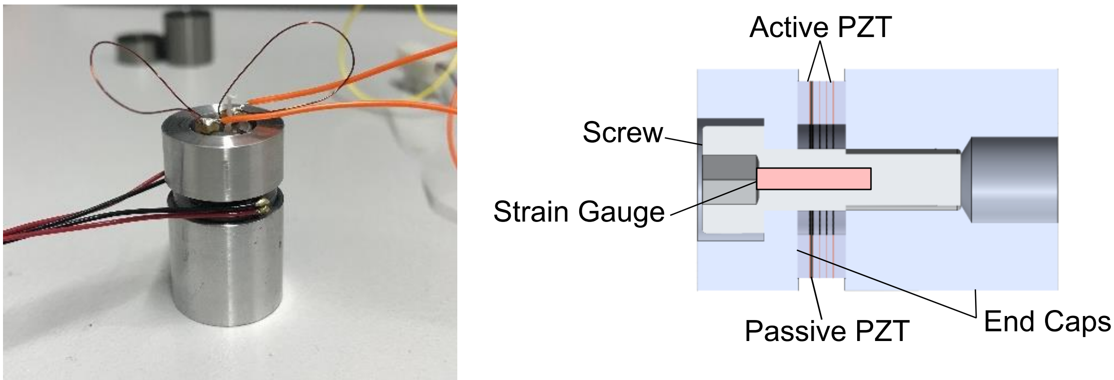

Fig. 122 – CD05 Construction
left: CD05 picture | right: CD05 sketch

5.1.3 Predictions

According to the calculations and formulas based on Woodward's theory [16] described previously in Section 2.3.1, the predictions for the experiments as well as the main relevant parameters are summarized in Table 29. The maximum power and mass fluctuations are calculated at the resonance of piezoelectric devices, at the highest driving frequency for the capacitive devices, and the lowest driving frequency for the inductive device. The best measurement resolution is obtained at 60 Hz rotation, and the relation between the measurement resolution and the rotation rate is quadratic. The measurement resolution was obtained from the experiments. The values of the mass fluctuation and measurement resolution were determined for the second harmonic frequency (twice the driving frequency). Despite the presence of noise and a calculated uncertainty of 54% in the prediction as per Section 3.1.9 for piezoelectric devices, the effect's upper limit reached a few orders of magnitude below the predicted mass fluctuations. The results show that the mass fluctuations were not detected by the apparatus. The uncertainty in the centrifugal experiments will be estimated in the following sections.

Device Model	Device Type	Driving Frequency [kHz]	Maximum Power [W]	Predicted Mass Fluctuation [g]	Experiment Upper Limit [g]
CD01	Piezoelectric	$15 - 40$	90.0	0.7	$1.2 \cdot 10^{-2}$
CD02	Capacitive	$30, 60$	73.3	1.0	$4.0 \cdot 10^{-3}$
CD03	Capacitive	$15 - 25$	152.0	0.6	$4.3 \cdot 10^{-5}$
CD04	Inductive	$15 - 100$	18.4	$6.3 \cdot 10^{-3}$	$4.2 \cdot 10^{-5}$
CD05	Piezoelectric	$50 - 70$	90.0	2.6	$4.7 \cdot 10^{-1}$

Table 29 – CD Mass Fluctuation Predictions

5.2 Transducer Calibration

This section describes the different methods for calibrating the force transducer. The operation of force transducers in the high-frequency range is prone to error due to resonances and the lack of non-intrusive calibration. Although the balance presents difficulties of calibration and spurious signals, it is possible to apply any desired gain, allowing to simulate testing conditions of microgravity (under 1G) to hypergravity (above 1G), in the direction perpendicular to the rotation, depending on the rotation rate. To detect the mass change using such a setup, strain gauges or piezoelectric load cells can be used. Strain gauges are superior in accuracy, with a linearity of 0.01%, and are perfectly adapted for static forces [87,97]. Both types have a ringing or resonant frequency that limits the application bandwidth, however, piezo-gauges can have a rather high resonant frequency because of their stiffness [98]. Thus, this balance can use a combination of both types of sensors to provide both advantages and offer a higher resolution and a larger measurement bandwidth.

The calibration of the piezoelectric force transducer is a complex process that requires different methods depending on the type of application. Current leakage in the piezoelectric material limits the sensor’s static measurement capability and the appropriate conditioning electronics only allow quasi-static measurement with an associated direct time constant [123]. The calibration method that allows the sensor characterization in the quasi-static domain, at frequencies below 1 kHz, implies step and continuous loading with a mechanical press or deposited weights method [98,124]. The quasi-static calibration results in lower accuracy in the higher frequency domain. Therefore, an additional, dynamic calibration is required. Higher frequency calibration methods include the impact hammer, impedance analysis, and vibrometry [125,126]. The selected calibration methods use the piezoelectric force transducer and an electromechanical press for the quasi-static calibration, and the dynamic calibration uses a strain gauge in the central bolt of the piezoelectric devices. The strain gauge signal is compared to the response signal of an embedded passive piezoelectric disk. Furthermore, the resonance spectrum is examined regularly to observe the effect of rotation and pre-load on the gauge response. Another possibility would be to use vibrometry analysis using a laser interferometer, however, this method was not implemented. The results of the calibration as well as the sensor parameters are summarized in Table 30.

Device	Sensor Disk Area [mm^2]	Sensor Disk Thickness [mm]	Conversion Constant [mV/N]	Piezo-material	Mass [g]
CD01	284	0.2	33.4	SM211	121.8
CD02	79	1.0	21.4	PIC181	47.8
CD03	286	2.0	195.9	PIC181	53.4
CD04	286	2.0	195.9	PIC181	96.3
CD05	137	0.2	33.2	PIC155	38.2

Table 30 – CD Properties

5.2.1 Quasi-Static Calibration I

The conversion constants in Table 30 were obtained using the ElectroPuls E3000 electrodynamic testing machine from Instron. This method is called quasi-static because the dynamic loading is performed at ultra-low frequencies up to 100 Hz. The devices were put under load, the embedded piezo-sensor was connected to an oscilloscope. The Dynacell load cell used, had a dynamic capacity of 5 kN, a linearity of 0.25% of reading, and a repeatability of 0.25%, whereas the machine could be used up to 100 Hz with a dynamic load capacity of 3 kN. The stacks were tested under preload levels ranging from 100 to 500 N, the dynamic force amplitude F_d was also varied between 100 and 200 N, and the forcing frequency was varied from 10 to 100 Hz. The setup is shown in Fig. 123, with CD02 in the machine clamps.

The results for devices CD01 and CD02 are summarized in Fig. 124 for a forcing function with an amplitude of 100 N. The conversion factor is calculated as the ratio of the transducer or strain gauge signal V_{SG} over the input force F_d. Due to the current leaking of the piezoelectric transducers, the conversion factor was under its nominal value for low forcing frequencies. As the forcing frequency was increased, the measured piezo-sensitivity reached an asymptotic value that was close to the calculated prediction for both devices. The error was estimated using the last three data points, resulting in an averaged error of 3.8% for CD01 and 2.0% for CD02. This quasi-static calibration method was deemed conclusive for the low-frequency range. The calibration method was not repeated for CD03, CD04, and CD05 and the conversion constants were obtained from Equation (97), where t is the thickness of the sensor, A the cross-section area and g_{33} the piezoelectric voltage constant in the thickness direction:

$$K = \frac{g_{33} t}{A} \quad . \tag{97}$$

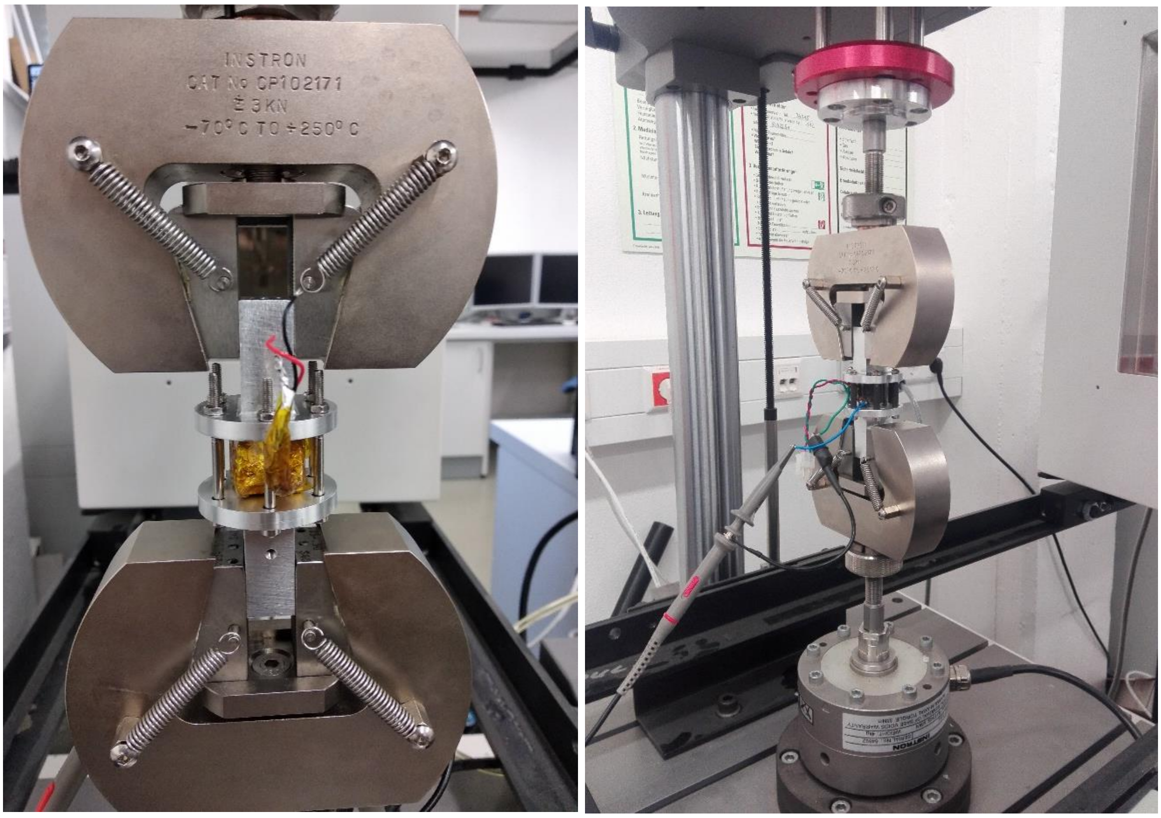

Fig. 123 – Quasi-Static Calibration I Setup

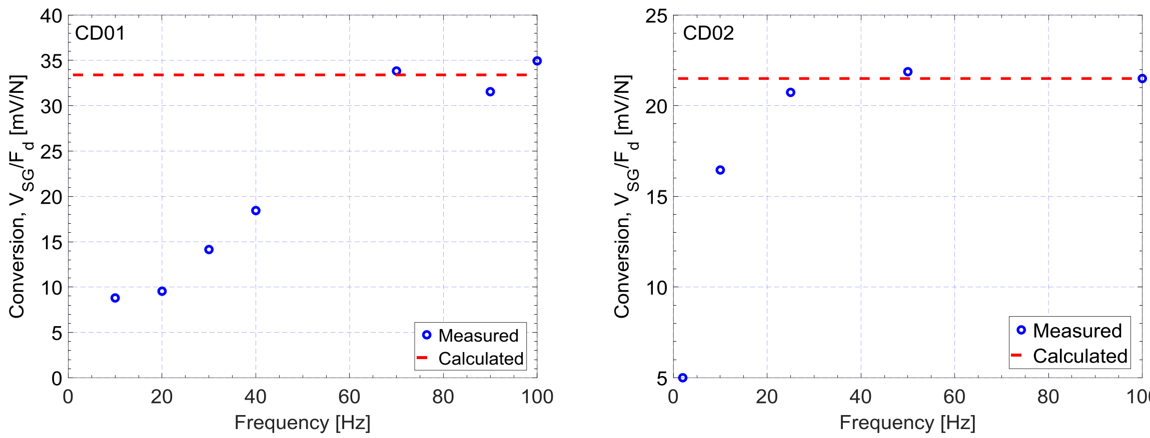

Fig. 124 – Quasi-static Calibration Results for CD01 & CD02

left: CD01 plot | right: CD02 plot

5.2.2 Quasi-Static Calibration II

The second calibration method uses an embedded strain gauge in the central screw of the piezoelectric stack CD05. The cylindrical screw strain gauges LB11 were graciously provided by Hottinger Bruel & Kjaer along with experimental epoxy EP70 to fix them in the screw without the appearance of bubbles during the curing process. To ensure proper installation, thermal tests were conducted using the system shown in Fig. 125. The gauge was implemented in a four-element Wheatstone bridge and the voltage was measured by a sensitive voltmeter (2405A Keithley). The resistors used had a resistance of 120 Ω. The screws and implementation with CD05 can be seen in Fig. 126. The gauge was calibrated by the manufacturer and the specified sensitivity of 2.04 mV/μm was used for all experiments.

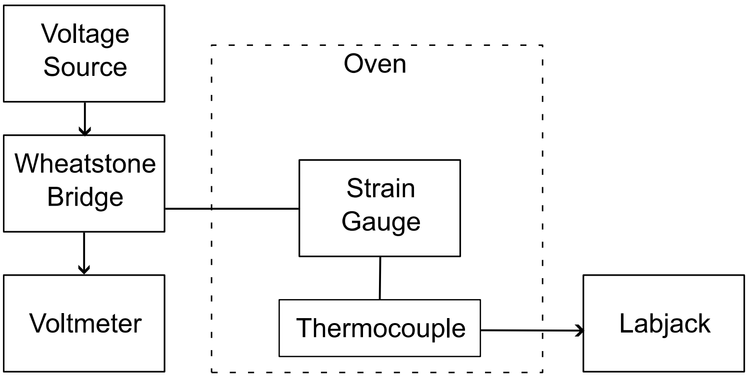

Fig. 125 – Strain Gauge Thermal Experiment Setup

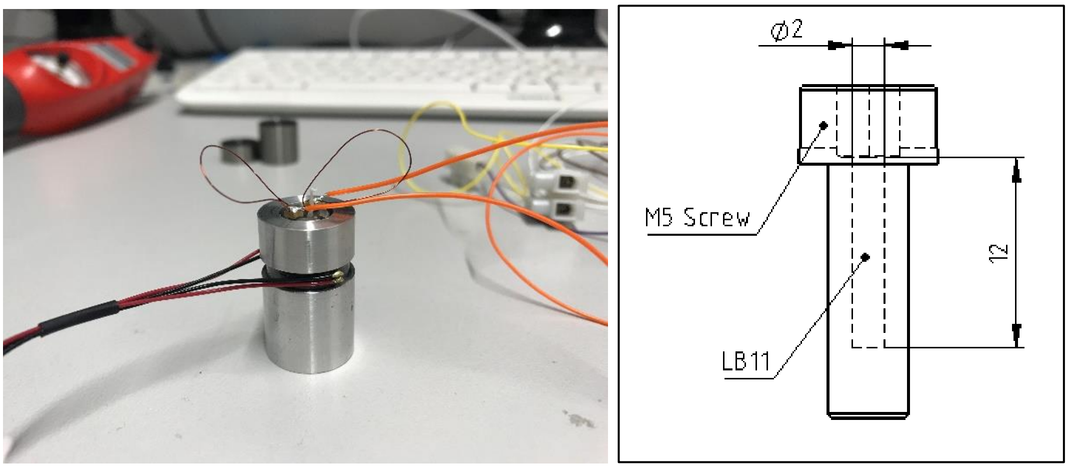

Fig. 126 – CD05 and Cylindrical Strain Gauge for Central Screw

The screws were heated from room temperature to 70 °C at a rate of 5°C/min and then cooled down to room temperature. The input voltage was 7 V and the strain S was calculated from the measured output voltage V_o, where K is the strain gauge constant, and V_i the input voltage:

$$S = \frac{4V_o}{V_i K} \quad . \tag{98}$$

The results are summarized in Fig. 127, where the screw strain is plotted against the temperature and the supplier's data. The graphs show high hysteresis in the case of the gauges in the stainless-steel screw and there is a large discrepancy between the gauges in screws 1 and 2. These results indicate the effect of thermal expansion on the strain gauge. It is to be concluded that the strain gauge in one of the stainless-steel screws was not properly installed. Furthermore, the thermal expansion behavior is not linear due to the presence of hysteresis. Fortunately, the temperature is not expected to vary as significantly during the experiments and is far from the same time scale as the vibration or energy fluctuation happening at 50 kHz.

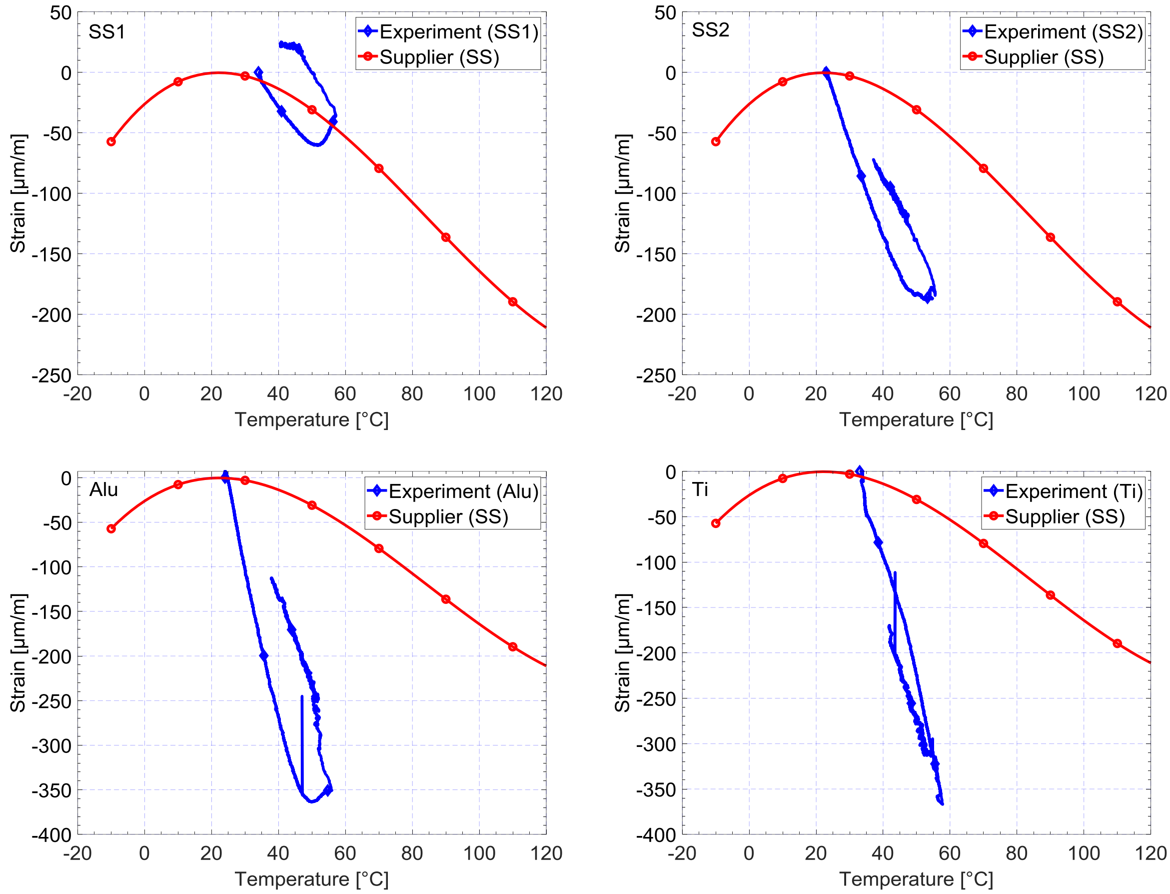

Fig. 127 – Thermal Test Results

top: stainless steel screw comparison with supplier data (2 samples)
bottom left: aluminum screw data | bottom right: titanium screw data

Subsequently, a torque was imparted to the screws to examine the response to preloading. Calculating the stress T in the screw from the cross-section area A_t, the nominal screw diameter D_n, the torque Ψ and an estimated torque coefficient K_t of 0.2 for stainless steel:

$$T = \frac{\Psi}{K_t D_n A_t} \quad . \tag{99}$$

Calculating the strain S from the calculated stress U and the estimated Young's Modulus:

$$S = \frac{T}{Y} \quad . \tag{100}$$

In Fig. 128, the strain is plotted against the imparted torque. The curves obtained have high linearity. The different slopes between the measured and calculated curves for the titanium screw may be explained by a discrepancy in the estimated torque coefficient. Indeed, titanium alloys have been found to exhibit a coefficient of friction of 0.25 to 0.3 in comparison to the 0.5 to 0.6 of stainless-steel [127]. Thus, looking back at Equation (99), the coefficient of friction has a direct impact on the slope of the strain-torque slope. However, aluminum on aluminum has a frictional coefficient of 1.05-1.35, whereas lubricated aluminum has a coefficient of 0.3. It seems, in this case, that aluminum had a lower coefficient of friction than titanium. This method was used to characterize the piezoelectric stack according to the pre-load, as examined with resonance spectra in Section 3.1.7.

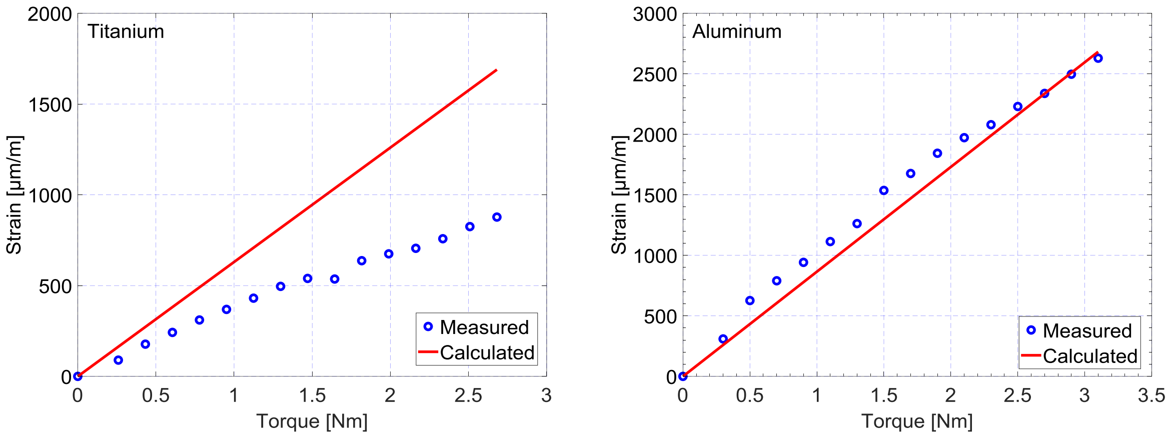

Fig. 128 – Preloading Measurements vs Calculation

left: titanium screw comparison | right: aluminum screw comparison

Thus, the strain gauge could finally be used as a quasi-static calibration at low frequencies if the driving frequency is under the resonance of the gauge. Another advantage of this calibration is that it can be performed for different loading conditions, during rotation for example. The results of the calibration are shown in Fig. 129 for different voltages without rotation using CD05, and the strain measured by the passive disk in the stack is converted to the screw strain and compared to the screw strain measured by LB11 in the screw. The stack's transducer measurement was converted to strain in the screw using the fact that an internal force will place the piezoelectric disks and the screw as springs in series instead of parallel, and thus, the measured force in the stack is the same one acting on the screw. Both diagrams show measurements of the screw strain with the applied voltage in the legend. For a driving voltage of 20 V, the strain measured by the passive piezo-disk is comparable to the strain measured by the screw in behavior, as the stack resonance can be seen in both measurements around 55 kHz. Fig. 129 also shows that the resonance shifts to lower frequencies with increasing driving voltage, as discussed by Uchino [101] in high-power applications. The resonance that does not seem to shift with the level of stress at 65 kHz in the strain gauge measurement is probably a resonance of the strain gauge in the screw. This method also has limited accuracy at higher frequencies, due to strain gauge resonances, but it can be used above 100 Hz and far from the screw gauge's resonance, at most until 55 kHz. The resulting deviation ranges from 500% away from the resonance to 12% closer to the stack resonance. Apart from the strain gauge's resonance, the larger discrepancy over the frequency range can be due to the very small μV signal amplitudes measured in the Wheatstone bridge configuration as a result of the small dynamic strain occurring in the stack.

Finally, these measurements show the accuracy limits of the quasi-static calibration and force measurement methods using piezoelectric and strain gauges at higher frequencies.

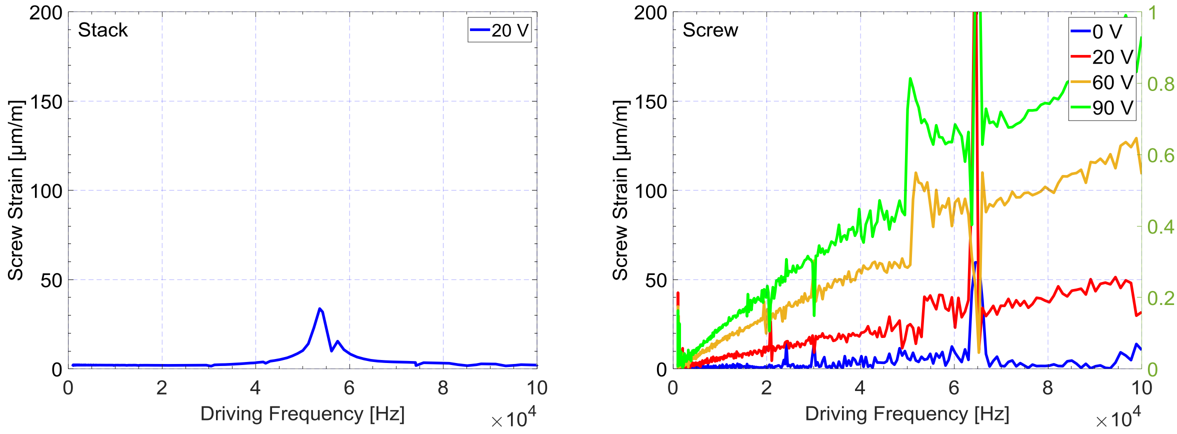

Fig. 129 – CD05 Strain vs Voltage Sweep

left: screw strain measured from the stack transducer with 20 V in driving voltage | right: screw strain measured from the screw gauge with different driving voltages

5.2.3 Dynamic Calibration

The dynamic calibration uses the method introduced in Chapter 3 and indicates the presence of resonance and anti-resonance frequencies, but it only provides a relative measurement. The transducer's resonance spectra are shown below, where the vertical axis stands for the ratio of the transducer signal to the commanded voltage. The results show multiple peaks, anti-resonances, and some flat regions at lower frequencies. The resonances are summarized in Table 28, indicating maximum energy transmission for piezoelectric devices, but also, the regions of greatest distortion of the gauge calibration. Also important are the stable frequency ranges, far from resonances or anti-resonances. Fig. 130 shows the unloaded frequency spectra for devices CD01 and CD02, Fig. 131 for CD03 and CD04, and Fig. 132 for CD05, without balance rotation and at very low voltage. The spectroscopy is also useful to demonstrate the effect of rotation on the location of the resonances. The sensitivity could be increased in the neighborhood of the resonances, however, since the relationship between the sensor sensitivity and the voltage ratio is not exactly known, the quasi-static conversion obtained through calculation and measurement in Section 5.2.1 is assumed constant for the whole frequency range. The limits of this assumption have already been examined in Section 5.2.2.

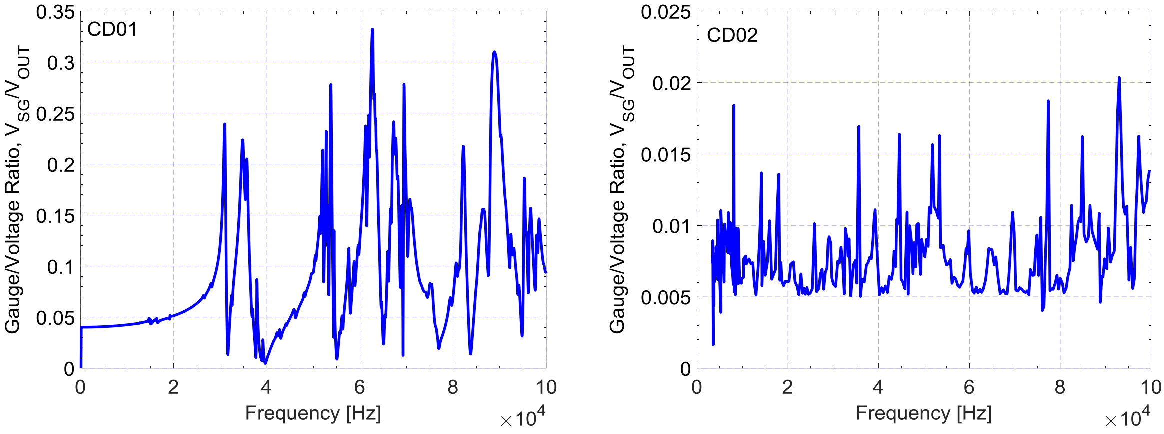

Fig. 130 – CD01 & CD02 Unloaded Resonance Spectrum

left: CD01 spectrum | right: CD02 spectrum

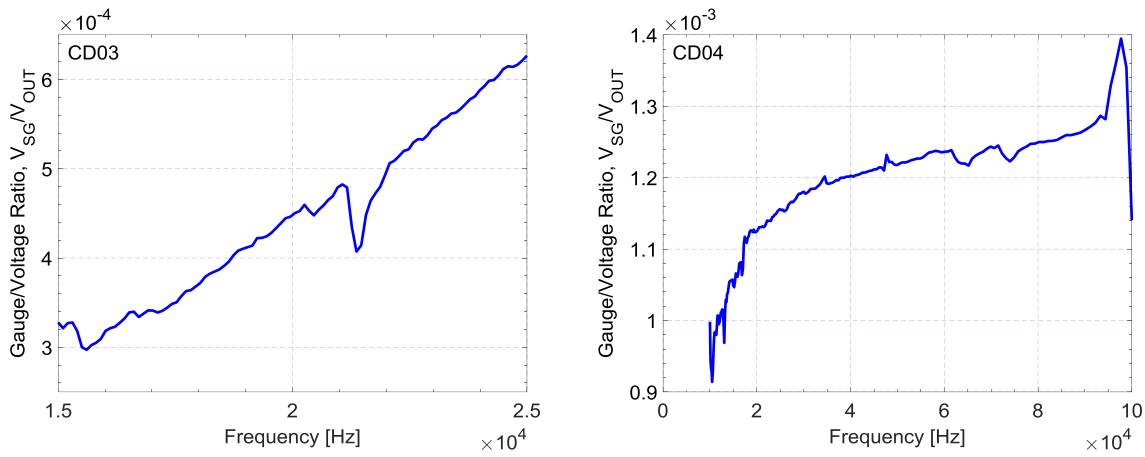

Fig. 131 – CD03 & CD04 Unloaded Resonance Spectrum

left: CD03 spectrum | right: CD04 spectrum

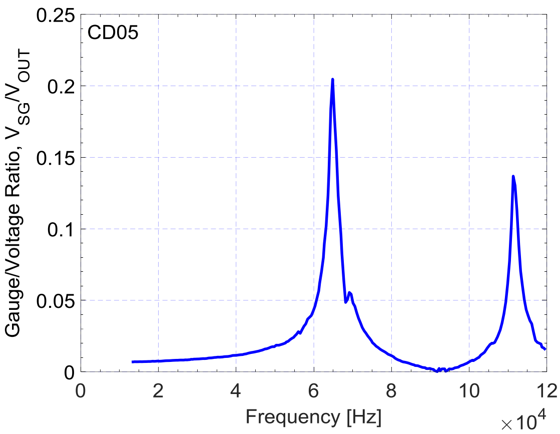

Fig. 132 – CD05 Unloaded Resonance Spectrum

5.3 Centrifugal Balance Test Results

5.3.1 Characterization

Standard tests were conceived to characterize the centrifugal balance, and the transducer's signal V_{SG} was examined. In the first series of tests, a simple mass was equipped with a piezoelectric force transducer and rotated at a given frequency. The centrifugal acceleration was measured using the photoelectric sensor and the signals of the piezoelectric transducer were also examined. The histogram in Fig. 134 shows the angular frequency measurement from the photoelectric sensor at 60 Hz, showing a normal distribution with a standard deviation of 0.3 Hz. The right-hand diagram shows the transducer signal V_{SG} without any applied voltage V_{OUT}, to analyze the noise in the setup. The effect of rotation on the sensor response was examined at different angular frequencies. A lock-in frequency sweep was performed without applying any power to the test device.

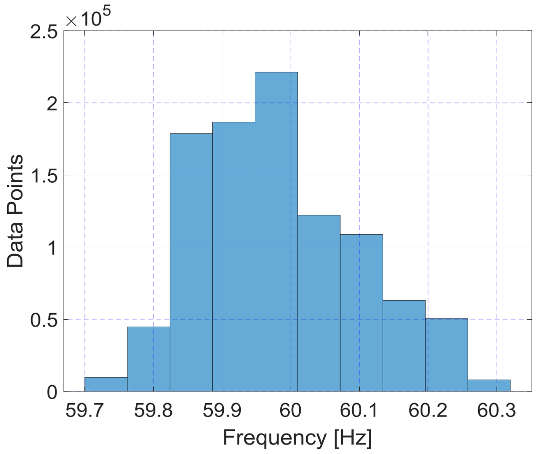

Fig. 134 – 60 Hz Rotation Measurement

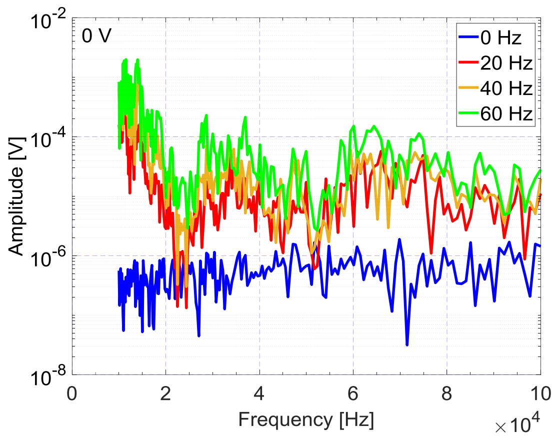

Fig. 133 – Noise Characterization at 0 V

Fig. 133 shows the presence of eccentricity and other distortions towards the lower end of the spectrum. Moreover, the increase in frequency entails an increase in the measured background noise level across the whole spectrum. Cross-talk measurements without rotation indicate the influence of EMI between the driving signal and the transducer signal. However, this behavior is unique for each individual device and must be analyzed for each one.

5.3.2 CD01

The test results for CD01, a piezoelectric device, show the transducer signal for different applied voltages and rotation rates in Fig. 135. The measurement on the left, shows the linear response to the driving voltage (1ω), and the diagram on the right shows the second harmonic response (2ω) for the corresponding driving frequency. In the following diagrams, the y-axis is always the transducer signal amplitude V_{SG} and the x-axis is the driving frequency. The measurement presented a few challenges, one being the piezoelectric vibration in the longitudinal axis, the same axis where the transient mass is measured. Since the expected transient mass signals should occur at twice the driving frequency, the effect is hardly distinguishable from nonlinear vibrations occurring as the second harmonic effect discussed in Section 3.1.1. The tests have yielded interesting nonlinear signals and other spurious effects at subharmonic frequencies of the sensor's resonances, as can be seen in the left-hand diagram of Fig. 135. The results show a force measurement dispersion equivalent to a few milligrams around the resonances, with a nonlinear dependence on the rotation. The tests also show the presence of a few parasitic modes of vibration that limit the sensor's precision. These tests used a filter, 7th-order Chebyshev band pass filter with a center frequency of 40 kHz, to amplify the second harmonic of the measured transducer signal. The filter's Bode plot can be found in Fig. 136. The results show the resonance frequencies and the nonlinearity of the device. The nonlinearity comes from the poor construction using several bolts and asymmetric loading, as well as the high-voltage driving of the device. The amplitude of the second harmonic transducer signal varied by around 10 mV at the resonances of the device, which resulted in a measured mass fluctuation of 12 mg, more than an order of magnitude below the prediction of 700 mg. To obtain this result, the sensor's sensitivity at low frequencies was used in the flat region at the lower end of the device's frequency spectrum.

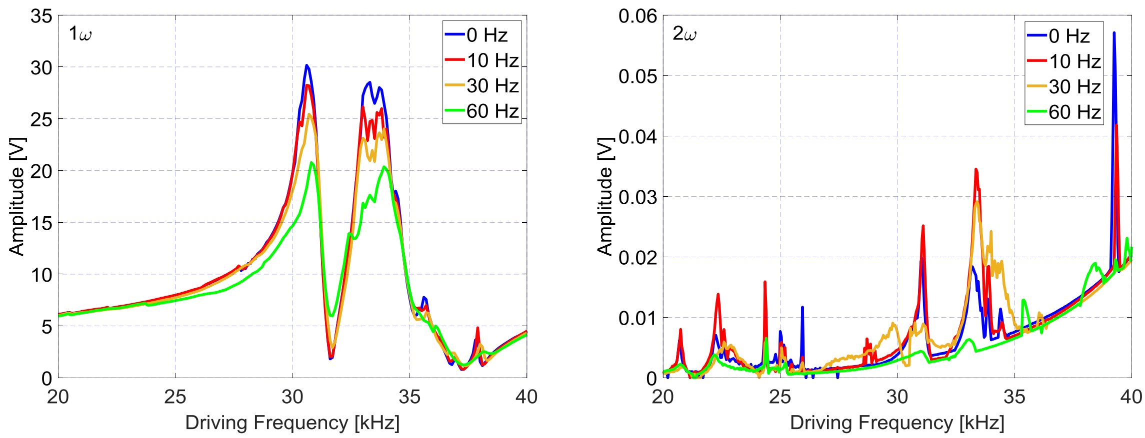

Fig. 135 – CD01 First and Second Harmonic Spectra

left: first harmonic content | right: second harmonic content

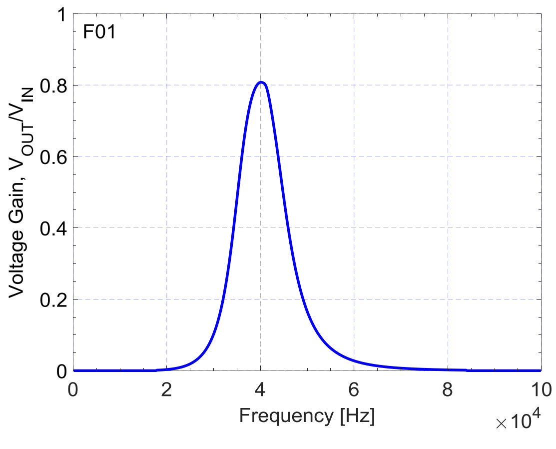

Fig. 136 – F01 Bode Plot

5.3.3 CD02

CD02 is a capacitive device that is sandwiched between aluminum plates. The pre-stressed configuration of this device made the conversion factor more difficult to calculate, but the device was also calibrated using the electrodynamic test machine to obtain an accurate sensitivity at low frequencies. Furthermore, this device's resonance spectrum did not contain huge resonances to distort the signal over the frequency range of interest. The plots in Fig. 137 show the results in the form of a Fourier transform of the transducer signal V_{SG} when driving the capacitor with a fixed frequency of 60 kHz and a voltage of 180 V. Both plots show the same waveform, but different portions of the frequency spectrum. The discrepancy between the signals at 0 and 60 Hz can be explained by distortion through the rotation at low frequencies, whereas the high-frequency discrepancies are minimal and represent the transient mass measurement resolution. At 120 kHz, the discrepancy is about 330 μV and this resolution is more than three orders of magnitude below the predicted effect. Here as well, higher-order components can be seen to represent the nonlinearity present in the electrical system. This experiment can be improved by using more accurate instruments.

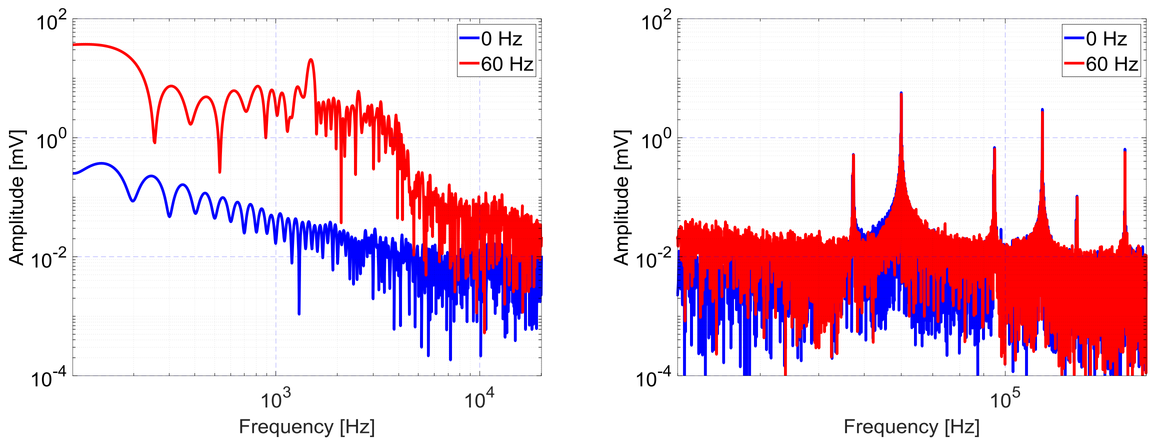

Fig. 137 – CD02 DFT Gauge Signal Comparison with Rotation
left: broader frequency range | right: narrower frequency range

5.3.4 CD03

Fig. 138 shows the test results using CD03, the next generation of capacitive devices. In this case, the calibration is easier to calculate since there are no springs connected in parallel to the sensor, and a lock-in amplifier (MFLI, Zürich Instrumente) was used to examine the transducer signal. The diagrams show the sweeps performed with the lock-in frequency being the same as the driving frequency (1ω) on the left, and the lock-in frequency being double the driving frequency on the right (2ω). The graphs show the increase in transducer response with increasing rotation frequency, and also the presence of peaks at device resonances. The transient mass measurement resolution, in this case, is 0.1 mg, three orders of magnitude below the 0.6 g prediction. The cross-talk measurements are performed when driving a maximum voltage amplitude of 180 V to the capacitor without rotating the apparatus. The noise was already shown for different angular frequencies in the previous sub-section. Reducing the cross-talk implies using an instrumentation amplifier to reduce the impedance of the transducer.

The left-hand figure shows the transducer signal at the driving frequency, and the right-hand figure shows the transducer signal at the second harmonic frequency, with the driving frequency as the x-axis in both cases. The experiments were repeated using differential measurements, and better grounding, to improve the resolution by one order of magnitude. The experiments were also repeated using a 1:1 buffer amplifier based on INA217 to reduce the output impedance between the transducer and the slip-ring before going to the oscilloscope; however, the resolution could not be improved further.

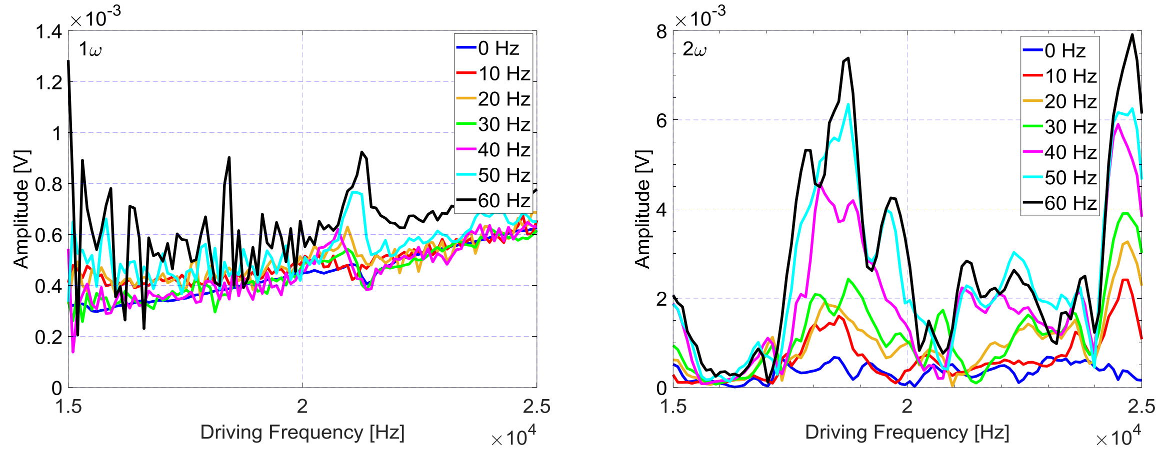

Fig. 138 – CD03 Frequency Sweep vs Rotation Rate

left: first harmonic content | right: second harmonic content

The next results were obtained to examine the level of EMI or cross-talk between transducer and DUT. The diagram on the left of Fig. 139 represents the DFT of the cross-talk for different driving voltages at a fixed driving frequency of 20 kHz and without rotation, and on the right, the DFT of the cross-talk at maximum rotation.

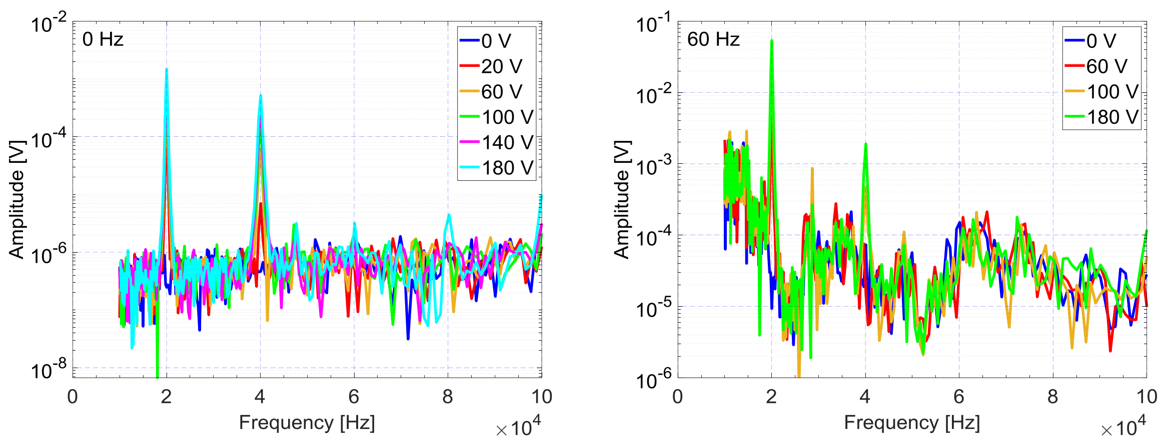

Fig. 139 – CD03 Fixed Frequency Cross-Talk Tests vs Voltage

left: 0 Hz rotation | right: 60 Hz rotation

Fig. 139 shows the presence of significant EM between the cables conducted through the slip-ring, even without rotation, but also the increase in noise while rotating the apparatus. The cross-talk between cables in the slip-ring cannot be circumvented by better instruments. Furthermore, the increase in noise resulting from high-rate rotation can be seen even without the application of voltage. The legends in the diagrams show the driving voltage of the DUT.

In Fig. 140, the figure on the left shows the cross-talk DFT at maximum driving voltage for different rotation frequencies for a fixed capacitor driving frequency of 20 kHz. The figure on the right is for examining the repeatability of the measurements. On the right, the discrepancy in signals of different runs performed with the same driving conditions is on the order of 1 mV at lower frequencies, and 0.1 mV at higher frequencies. These results show that the experiments are repeatable and the given measurement resolution is very stable.

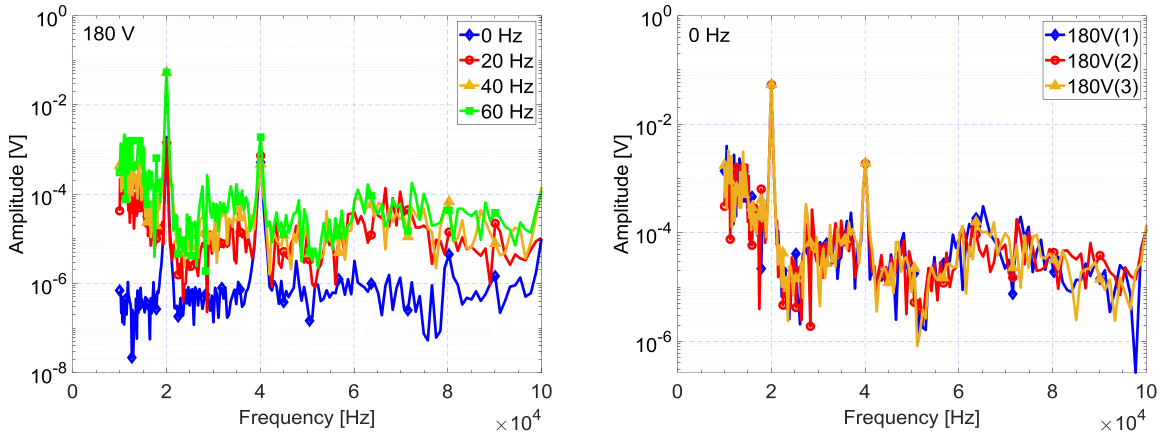

Fig. 140 – CD03 Fixed Frequency Tests with Rotation Rate

left: 180 V driving voltage at various rotation rates | right: 180 V driving voltage, repeatability tests at 0 Hz rotation

5.3.5 CD04

The test results for experiments performed with CD04, the first inductive device consisting of copper wire wrapped around a toroidal core, are shown in Fig. 141. Two different cores were tested: the first set of results was obtained with the iron core with a higher magnetic permeability and inductance, and the second set with the Teflon core with a relative permeability of about 1. The first tests only reached an angular frequency of 30 Hz, due to the weight and high stress on the piezoelectric transducer that resulted in a mechanical failure, whereas the tests were repeated using a Teflon core, reaching a maximal angular frequency of 50 Hz. The results at 30 Hz rotation were affected by the cracking of the piezo-ceramic during rotation, as can be seen from the increased noise amplitude. The tension and shear loads at high rotation were too large for the construction. In the next diagrams, the x-axis shows the driving frequency and the y-axis shows the amplitude of the first-harmonic (1ω) and second-harmonic (2ω) transducer signal amplitude, V_{SG}.

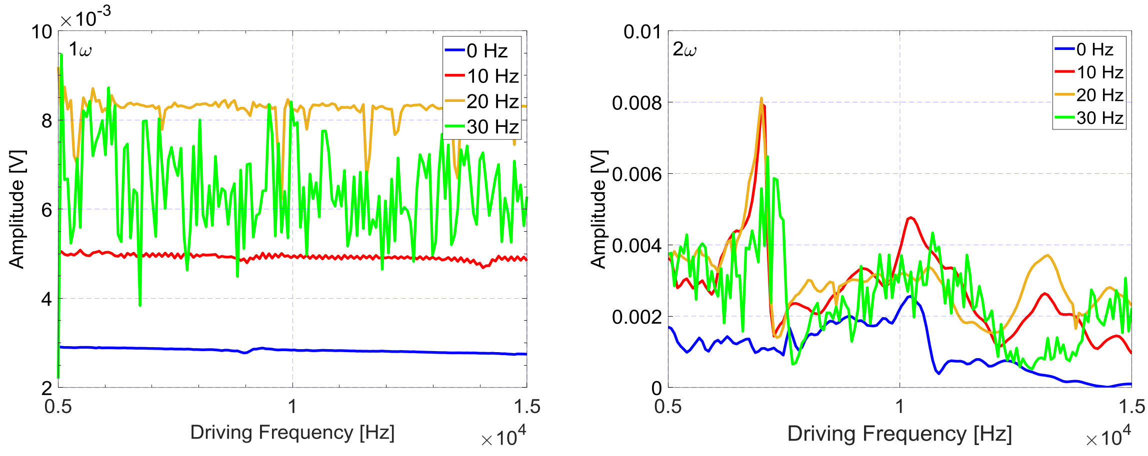

Fig. 141 – CD04(Fe) Sweep vs Rotation Rate

left: first harmonic content | right: second harmonic content

With the Teflon core, the experiment just weighed 96.3 g, had an inductance of 2.9 μH, and increased the prediction to 6 mg. Fig. 142 shows the first harmonic transducer signal on the left and the second harmonic transducer signal on the right. The figure on the right demonstrates a measurement resolution below 100 μV when comparing 0 and 50 Hz signals.

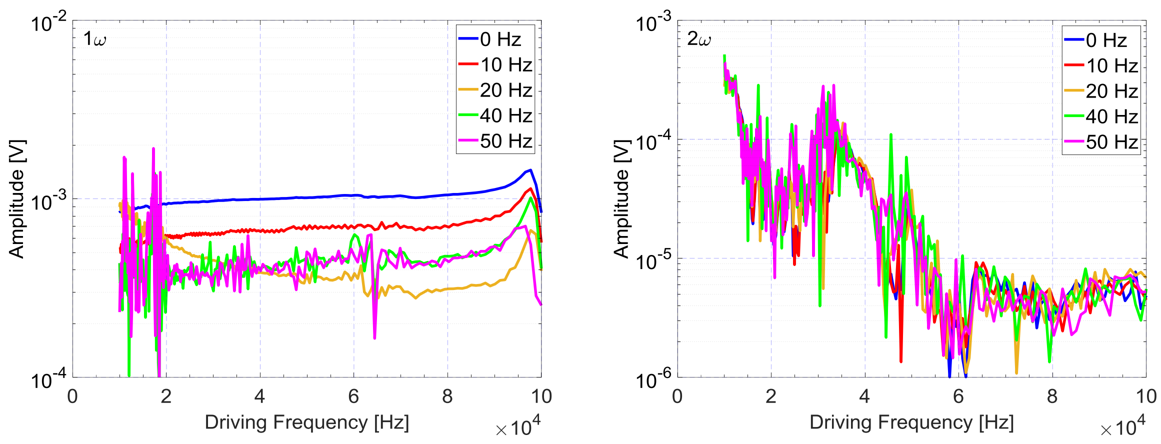

Fig. 142 – CD04(T) Sweep vs Rotation Rate

left: first harmonic content | right: second harmonic content

In the new test series with the Teflon core, the setup was also modified with the 1:1 buffer amplifier based on IC INA217 to reduce the transducer's output impedance and limit signal distortion due to external effects, for example, due to rotation at different rates. The lower level of noise and increased resolution can be observed in Fig. 143. The buffer amplifier seems to have affected the first harmonic frequency results, but also to have led to an increase in noise at the higher end of the spectrum when analyzing the second harmonic signal illustrated on the right. The measurement resolution was not improved with this method.

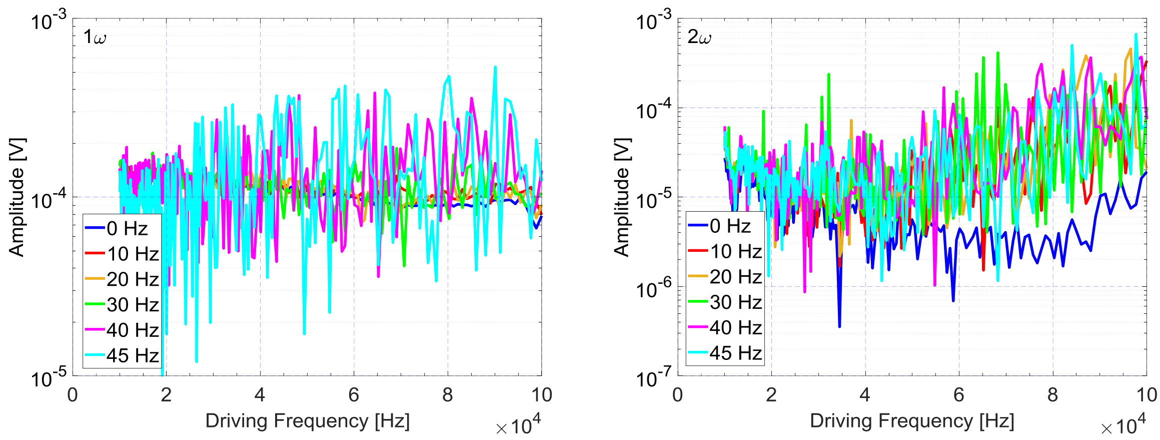

Fig. 143 – CD04(T) Sweep vs Rotation Rate with Buffer Amplifier

left: first harmonic content | right: second harmonic content

5.3.6 CD05

The tests performed with piezoelectric CD05 are summarized in Fig. 144. The titanium end pieces and titanium screw were used and the 3.8 MPa pre-load of the central screw was controlled using a torque wrench calibrated using the strain gauge. A difference of about 200 mV in the second harmonic content can be seen at the resonance peak around 59 kHz when comparing maximum rotation (60 Hz) to no rotation. This result represents a measurement of 0.4 g, an order of magnitude below the prediction, assuming that the sensor sensitivity is invariant over the frequency range. Of course, if the sensitivity of the sensor is increased in the neighborhood of the resonance, then the measurement resolution can only improve.

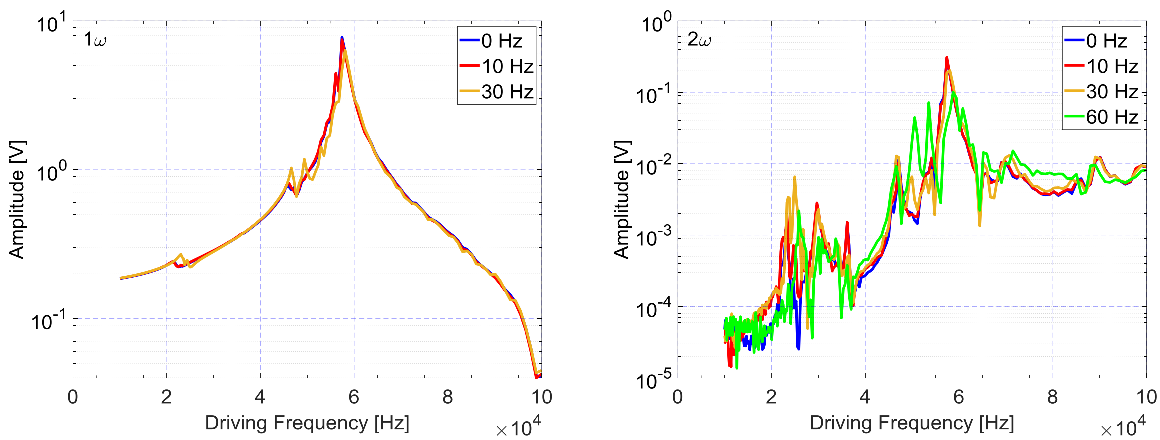

Fig. 144 – CD05 Frequency Sweep vs Rotation Rate

left: first harmonic content | right: second harmonic content

5.4 Discussion & Error Analysis

Different experimental artifacts can explain the measurements obtained above. For piezoelectric devices CD01 and CD05:

- The longitudinal vibrations and nonlinearity are most likely causing the first and second harmonic components that can be seen in the analysis of piezoelectric devices.

As already discussed, nonlinearity in piezoelectric devices includes electrostriction, piezoelectric, dielectric, and mechanical nonlinearity [102]. The nonlinearity can be observed by examining the second harmonic gauge signal at higher voltage levels without rotation. The high centrifugal acceleration has a significant impact on both first and second harmonic piezoelectric responses, since these depend on the material properties and stress conditions that inevitably vary during rotation. Unfortunately, the piezoelectric nonlinearity could not be reduced with the central bolt design and the DC bias driving of CD05 when compared to CD01.

- Faster rotation brings in additional noise and distortions over the entire frequency spectrum.

This has been observed for all the different devices. At higher rotation rates, large noise peaks appear below 1 kHz. These could be due to faulty contacts from the brushes in the slip-ring occurring at multiples of the rotation frequency and linked to increased resistance and heat generation. The background level of noise also increased over the whole spectrum with the rotation and can be related to a decrease in the slip-ring conduction at higher rotation frequency and increased temperature according to Ohm’s law.

- Grounding helps to reduce the noise, but only for certain frequency components.

Grounding the device didn’t change the value of the measured second harmonic cross-talk, however, it affected the measurement of the first harmonic cross-talk. The reasoning behind this can be attributed to the nature of the observed effects, since cross-talk between the power signal and the gauge signal should be affected by grounding, but the nonlinear mechanical or piezoelectric response might not. This indicates that the first harmonic signal is largely influenced by cross-talk.

- Differential measurement helps to reduce noise, but only for certain frequency components.

The differential measurement didn’t change the value of the measured second harmonic cross-talk, however, it did affect the measurement of the first harmonic cross-talk. The same reasoning should apply here since the second harmonic component is dominated by nonlinear effects that are separate from the EMI of the power signal.

- Adding a buffer amplifier reduced the noise level in a certain frequency range.

The buffer amplifier reduces the output impedance of the piezo-transducer to limit the EMI between the cables. However, the buffer amplifier also added sharp peaks and white noise at higher frequencies. The influence of the lower output impedance at higher frequencies should be examined separately.

- The calibration still lacks accuracy for high rotational velocity and at high frequencies.

Quasi-static calibration method #1 with the electrodynamic test machine first provided accurate measurements in agreement with the calculations at low frequencies. Quasi-static calibration #2, however, already showed the limitations in the range from 20 to 50 kHz in the measurement deviation of 500% when comparing the screw and stack gauge measurements of the strain. In these measurements, an additional problem arose due to the existence of the screw gauge's resonance. Indeed, the resonances of the elements connected to any sensor in the stack can affect its mechanical properties and the calibration factor as well. Furthermore, the resonance shifts due to hysteresis, heat generation, and the changing stress conditions due to rotation during experiments made it harder to obtain an accurate calibration in the neighborhood of the resonances. These resonance shifts were observed in the analysis of the stack gauge's measurements for different rotation frequencies and driving voltages over the whole frequency spectrum. However, the embedded gauge signal only provided a relative measurement and no absolute measurement of the strain. Despite the observed gauge signal fluctuations, the strong dependence on the rotation frequency as predicted by the Mach-effect theory was not observed.

Finally, even if the upper limit of the measured effects falls below the predictions by one to four orders of magnitude, depending on the device type, a higher resolution with better stability and accuracy in the measurements is desirable. A new centrifugal balance design will have to rely on a calibration that is separate from the mechanical structure and can take into account the changing load conditions due to rotation, such as a laser interferometer.

6 Conclusions

6.1 Research Summary

This thesis represents the results of an experimental team effort to discover breakthrough propulsion for interstellar travel; propellantless propulsion with a significant thrust-to-power ratio to markedly reduce the demands of interstellar space voyages. More specifically, the objective was to detect the presence of mass fluctuations predicted by the Mach-effect as derived by Woodward, either indirectly through thrust balance measurements or directly using centrifugal mass measurements. The work required mechanical and electrical engineering solutions to increase the resolution and reduce experimental artifacts in the measurement of these forces. It also required a good understanding of piezoelectric systems that are the basis of the MET and sensing devices to ensure the right conditions for resonant driving.

Chapter 1 first listed the shortcomings of conventional propulsion and set an order of magnitude on the requirements for interstellar travel. Then, it addressed known problems in physics to set the path toward breakthrough propulsion using mass fluctuations. Chapter 2 critically examined Woodward's Mach-effect theory [16], the mass-fluctuation propulsion concept, experiments conducted by different groups [24,80], and the thruster design in detail. The analysis identified some critical points that pointed towards possible improvements for the experiments and later led to the design of a piezo-actuator with a unique resonance frequency and fewer parasitic resonances. The potential and limitations of transient mass and force measuring instruments and sensing technologies were also assessed.

On the experimental side, the electromechanical characterization was first important to describe the piezoelectric test devices and understand their behavior in different driving conditions. The descriptions in Chapter 3 led to simulations and predictions of the thrust to be observed on the balances, which included a strong correlation of the predicted force with voltage, driving frequency, and actuation nonlinearity. Impedance spectroscopy and circuit modeling showed that the quality and location of the electromechanical resonances depended on a lot of factors to be considered in the experiments: the amplifier electronics, the stack pre-stress, the voltage level, the temperature, and the mounting. The characterization of the torsion balances (TB1, TB2) and the double-pendulum balance (DP1) was also necessary to understand their performance and response to the presence of pulsed forces, vibration, heating, and electromagnetic interaction (EMI). In Chapter 4, the thrust balance tests regrouped all MET tests performed on TB1, TB2, and DP1 in vacuum to reduce artifacts linked with the interaction with the residual atmosphere in the chamber. The tests with TB1, which included MET03, MET04, a magnetostrictor, resonance tracking, and mixed-mode driving, showed that the force measurements remained under 1 µN, despite predictions of a few mN and claims of up to 200 µN of thrust. The observation of experimental artifacts linked with EMI in the dummy resistor and MET tests led to the need for an improved balance with better electromagnetic shielding and resolution.

The results from MET tests on TB2 and DP1 showed the presence of short force peaks at switch-on and switch-off of the power to the MET, also observed by Woodward; the pulses were exact opposites of each other in direction. These switching transients, however, were observed in all thruster orientations with the same order of magnitude, between 0.1 and 0.3 µN, regardless of the mounting with yoke or copper block, amplifier electronics with transformer or without, single or mixed sinusoidal driving signals, and they were observed for different driving frequencies. The experiments also showed the presence of a drift in the balance response, with the drift direction being independent of the thruster orientation on the balance. Extensive dummy tests on TB2 excluded the effect of EMI or heating as an explanation for that drift. Observing the loosening of the screws in the MET devices after experiment runs, brass powder in the experiment box and increased balance beam vibration around the resonances hinted at significant vibration being transmitted from the piezo-actuator to the balance. The connection between the high-frequency device vibration and the low-frequency effects observed was explained using a simple spring-mass model of the balance and appropriate forcing function. These observations led to the conclusion that the typical thrust trace observed in Woodward's MET experiments [16] is a result of vibration on the torsion-spring balance.

Chapter 5 was an attempt at a direct mass fluctuation measurement using a unique type of balance relying on centrifugal acceleration. This measurement method had the advantage of circumventing the need of synchronizing mass fluctuations with an oscillating acceleration and excluding the low-frequency vibrational artifacts present in the thrust balance experiments. The direct measurement of mass transients was made, in principle, using the conversion of a mass to a force through centrifugal acceleration and detecting high-frequency variations of this force with an embedded piezoelectric sensor. The devices included capacitive (CD02, CD03), inductive (CD04), and piezoelectric devices (CD01, CD05) and were subjected to sinusoidal voltages in the frequency range between 20 and 100 kHz to generate energy fluctuations. During the application of voltage, the test devices were rotated with an angular frequency of up to 3600 rpm, which represented an amplification of the force measurement by a factor of up to 1300 times the gravitational acceleration on Earth.

The calibration of the piezoelectric transducer was done using an electrodynamic press, a screw strain gauge, and resonance spectroscopy. The quasi-static calibration methods were accurate at low frequencies but presented some limitations at higher frequencies, as demonstrated by the strain gauge experiments. Nonetheless, even considering a discrepancy of up to 500 % in the driving frequency range, the measurement resolution was increased to exceed the predicted value for the mass fluctuations by one to four orders of magnitude, depending on the device type. The measurement of forces in the neighborhood of the device resonances has even been shown to increase the sensitivity of the force transducers, and the quadratic dependence of the force to the rotation frequency was not observed in any of the experiments. Hence, these observations rule out mass fluctuations as predicted by Woodward's Mach-effect derivation [62].

The main points of the thesis are summarized below:

- Developing space propulsion to escape the rocket equation is vital to the successful venture of humans to the stars. Woodward's claims and Mach-effect theory suggest the existence of groundbreaking physics useful for interstellar space propulsion.
- Thrust balance experiments with the MET show the presence of spurious effects in the form of convective, thermal, vibration, and electromagnetic artifacts. Improvement in the double-pendulum and torsion balance experiments led to the elimination of convective, thermal, and electromagnetic artifacts. Vibrational artefacts could not be eliminated and thrust according to the theory derived by Woodward was not observed.

- Experimental efforts with a centrifugal balance to measure mass fluctuations presented mitigated results. Despite an accurate calibration of the piezo-electric sensor in the quasi-static regime, larger discrepancies were observed in the frequency regime of interest. Nevertheless, the results show experimental artifacts a few orders of magnitudes lower than predictions using the Mach-effect theory and the quadratic dependence of the effects on rotation is absent.

Thus, the experiments described in Chapters 4 and 5 did not lead to the observation of Mach-effect thrust or mass fluctuations in the order of magnitude and behavior predicted from Woodward's derivation and experimental claims. Instead, the typical force signals obtained in Woodward's experiments can be explained by experimental artifacts.

6.2 Further Research

Mass fluctuations can be very promising for space propulsion and increasing the measurement resolution and reducing experimental artefacts even further is the proper way to their detection. However, their usefulness becomes questionable if the propulsion method is equal or worse than classical photon thrusters in terms of thrust-to-power ratio. Increasing the accuracy of torsion balances can be reached using springs with even lower torsional stiffness. The accuracy of the centrifugal balance can be improved by increasing the rotation speed or arm length, reducing the rotation eccentricity and friction, and improving the sensitivity of the piezoelectric transducer or strain gauge. However, increasing the resolution alone is not sufficient, due to the presence of experimental artifacts. Increasing the chance of detecting mass fluctuations also relies on reducing noise, for example by decoupling the transducer signal from the power signal on the centrifugal balance or moving to laser interferometry for force detection. Proper vibration damping on the balances could also help reducing vibrational artifacts. However, damping the acoustic waves coming from piezoelectric actuators represents a difficulty because of the high frequency at which they occur and the constant change of the impedance and dynamic test conditions. Electromagnetic shielding can also always be improved to reduce cross-talk noise between test device and transducer. Lastly, another way to increase the chance of detection would be to increase the mass fluctuation effect. An obvious way of doing so is to increase the transmitted energy and dimension of the actuator, which is only realizable with greater financial means. The author used the maximum output power of the amplifiers available within the SpaceDrive project. One could also vary the nature of the energy fluctuation and examine its dependence on power and wavelength. The next step would be to increase the driving frequency to above 100 kHz, however, this would require completely new equipment and sensors, significant financial means, and a new set of characterization methods. In the end, the quest for breakthrough propulsion must simultaneously rely on a continuous effort to explore the limits of measurement resolution and the evolution of our theoretical understanding of physics.

Appendix A

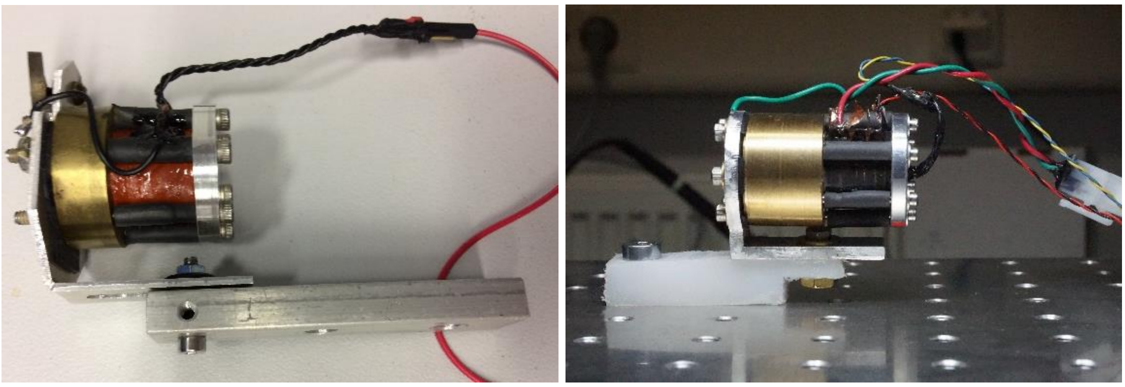

Fig. 145 – Pictures of MET01 & MET02
left: MET01 | right: MET02

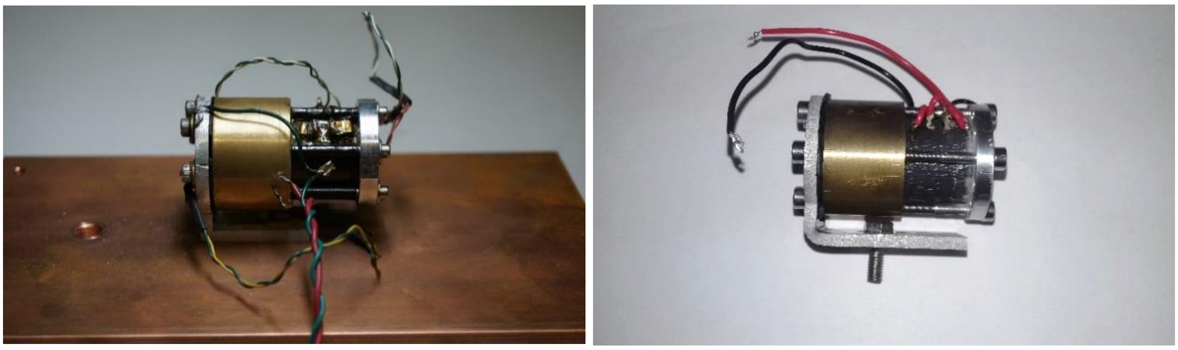

Fig. 146 – Pictures of MET03 & MET04
left: MET03 | right: MET04

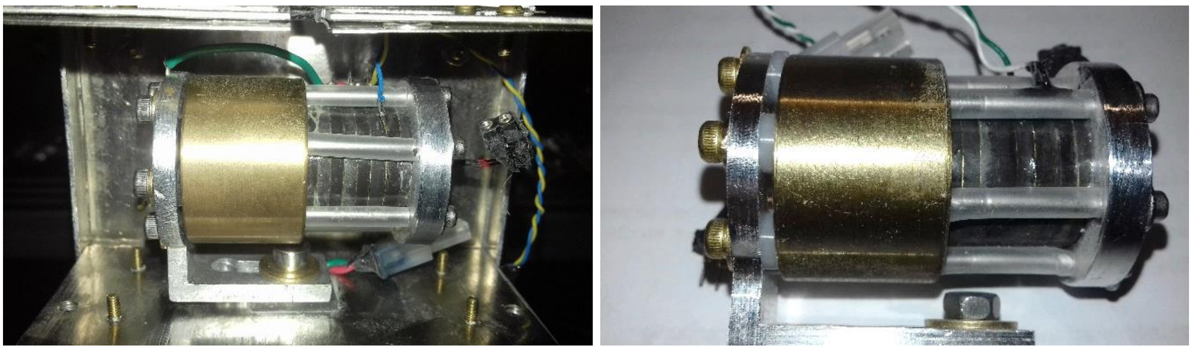

Fig. 147 – Pictures of MET05 & MET06
left: MET05 | right: MET06

Appendix B

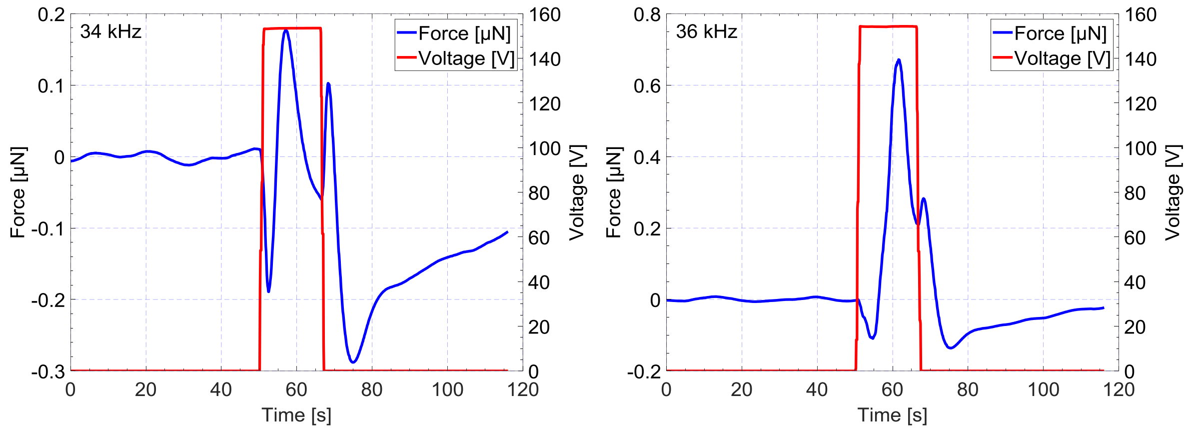

Fig. 148 – TB2 MET06 TUD Fixed Frequency Tests with Yoke

left: 0° configuration, 34 kHz | right: 0° configuration, 36 kHz

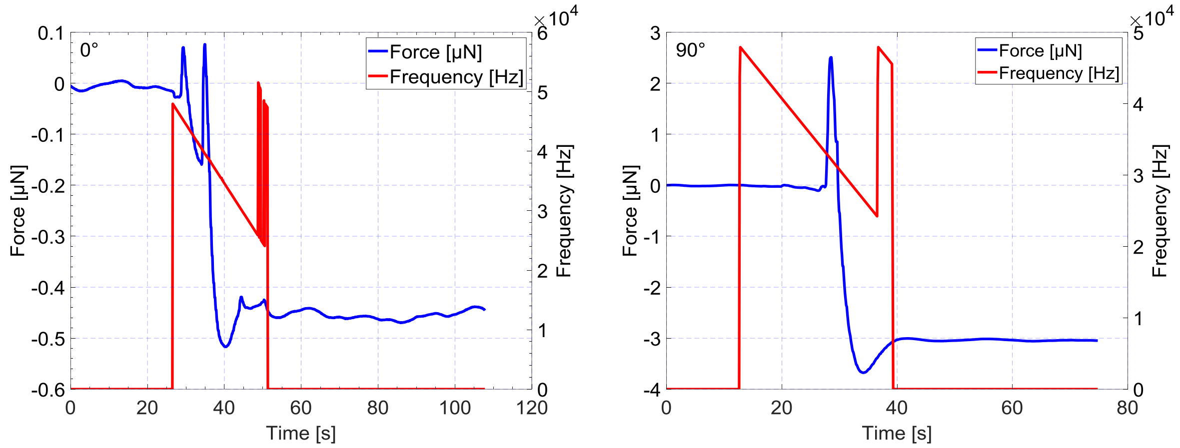

Fig. 149 – TB2 MET05 CSUF Frequency Sweeps with Copper Block

left: 0° configuration | right: 90° configuration

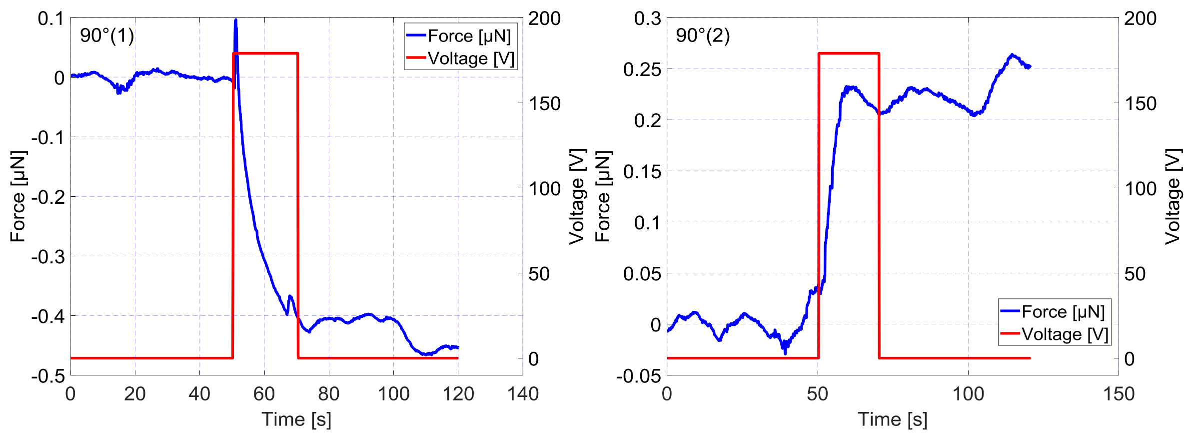

Fig. 150 – DP1 MET03 TUD Fixed Frequency Test Runs

left: individual run #1, 90° configuration | right: individual run #2, 90° configuration

Bibliography

[1] R.H. Frisbee, S.D. Leifer, Evaluation of Propulsion Options for Interstellar Missions, in: 34th AIAA/ASME/SAE/ASEE Joint Propulsion Conference and Exhibit, 1998: pp. 1–23. https://doi.org/10.2514/6.1998-3403.

[2] K.E. Tsiolkovkiy, Collected Works of K.E. Tsiolkovskiy - Volume II - Reactive Flying Machines, NASA, 1954.

[3] J.B. Marion, S.T. Thornton, Classical Dynamics of Particles and Systems, 4th Ed., Saunders College Pub., Fort Worth, 1995.

[4] G.P. Sutton, O. Biblarz, Elements of Rocket Propulsion, 7th ed., John Wiley & Sons, 2001.

[5] M. Tajmar, Advanced Space Propulsion Systems, Springer-Verlag Wien GmbH, Seibersdorf, 2003.

[6] R.H. Frisbee, Impact of Interstellar Vehicle Acceleration and Cruise Velocity on Total Mission Mass and Trip Time, Collection of Technical Papers - AIAA/ASME/SAE/ASEE 42nd Joint Propulsion Conference. 11 (2006) 8631–8648. https://doi.org/10.2514/6.2006-5224.

[7] R.L. Forward, Roundtrip interstellar travel using laser-pushed lightsails, J Spacecr Rockets. 21 (1984) 187–195. https://doi.org/10.2514/3.8632.

[8] S.P. Worden, W.A. Green, J. Schalkwyk, K. Parkin, R.Q. Fugate, Progress on the Starshot Laser Propulsion System, Appl Opt. 60 (2021) H20–H23. https://doi.org/10.1364/ao.435858.

[9] M. Alcubierre, The Warp Drive: Hyper-fast Travel within General Relativity, Class Quantum Gravity. 11 (1994). https://doi.org/10.1088/0264-9381/11/5/001.

[10] R.L. Forward, Negative Matter Propulsion, J Propuls Power. 6 (1990) 28–37. https://doi.org/10.2514/3.23219.

[11] H. White, J. Lawrence, P. March, J. Vera, P. Sylvester, P. Bailey, Measurement of Impulsive Thrust from a Closed Radio-Frequency Cavity in Vacuum, J Propuls Power. 33 (2016) 1–12. https://doi.org/10.2514/1.B36120.

[12] R. Evans, Greenglow and the Search for Gravity Control, Troubador Publishing Ltd, Cornwall, 2015.

[13] M. Millis, Frontiers of Propulsion Science, 2009. https://doi.org/10.2514/4.479953.

[14] R. Shawyer, Second Generation EmDrive Propulsion Applied to SSTO Launcher and Interstellar Probe, Acta Astronaut. 116 (2015) 166–174. https://doi.org/10.1016/j.actaastro.2015.07.002.

[15] D. Rabounski, L. Borissova, A Theory of the Podkletnov Effect based on General Relativity : Anti-Gravity Force due to the Perturbed Non-Holonomic Background of Space, Progress in Physics. 3 (2007) 57–80.

[16] J.F. Woodward, Making Starships and Stargates: The Science of Interstellar Transport and Absurdly Benign Wormholes, Springer, New York, 2013. https://doi.org/10.1007/978-1-4614-5623-0.

[17] M. Tajmar, M. Kößling, M. Weikert, M. Monette, The SpaceDrive Project - Developing Revolutionary Propulsion at TU Dresden, in: 68th International Astronautical Congress (IAC), Adelaide, 2017.

[18] J. Hansson, The 10 Biggest Unsolved Problems in Physics, International Journal of Modern Physics and Applications. 1 (2015) 12–16. http://www.publicscienceframework.org/journal/ijmpa.

[19] H. Fearn, J. Woodward, Recent Results of an Investigation of Mach Effect Thrusters, in: 48th AIAA/ASME/SAE/ASEE Joint Propulsion Conference & Exhibit, Atlanta, 2012: pp. 1–15. https://doi.org/10.2514/6.2012-3861.

[20] D.W. Sciama, On the Origin of Inertia, Cambridge, 1953.

[21] M. Monette, M. Kößling, M. Tajmar, The SpaceDrive Project - Progress in the Investigation of the Mach-Effect-Thruster Experiment, in: 36th International Electric Propulsion Conference, 2019: pp. 15–20.

[22] M. Tajmar, M. Kößling, M. Weikert, M. Monette, The SpaceDrive Project - First Results on EMDrive and Mach-Effect Thrusters, in: Space Propulsion Conference, Sevilla, 2018: pp. 1–10.

[23] M. Kößling, M. Monette, M. Weikert, M. Tajmar, The SpaceDrive project - Thrust balance development and new measurements of the Mach-Effect and EMDrive Thrusters, Acta Astronaut. 161 (2019) 139–152. https://doi.org/10.1016/j.actaastro.2019.05.020.

[24] M. Monette, M. Kößling, M. Tajmar, Experimental investigation of Mach-Effect thrusters on torsion balances, Acta Astronaut. 182 (2021) 531–546. https://doi.org/10.1016/j.actaastro.2021.02.037.

[25] M. Tajmar, O. Neunzig, M. Weikert, High-accuracy Thrust Measurements of the EMDrive and Elimination of False-positive Effects, CEAS Space Journal. 14 (2022) 31–44. https://doi.org/10.1007/s12567-021-00385-1.

[26] O. Neunzig, M. Weikert, M. Tajmar, Thrust Measurements and Evaluation of Asymmetric Infrared Laser Resonators for Space Propulsion, CEAS Space Journal. 14 (2022) 45–62. https://doi.org/10.1007/s12567-021-00366-4.

[27] O. Neunzig, M. Tajmar, Development of a Superconducting Levitation Thrust Balance for Propellantless Propulsion, in: 69th International Astronautical Congress, Bremen, 2018: pp. 1–5.

[28] M. Monette, O. Neunzig, M. Tajmar, The SpaceDrive Project – Mach-Effect Thruster Experiments on High- Precision Balances in Vacuum, in: Space Propulsion 2020+1, Estoril, 2021.

[29] M. Monette, W. Stark, M. Tajmar, Centrifugal balance for the detection of mass fluctuations in advanced propulsion concepts, Acta Astronaut. 212 (2023) 270–283. https://doi.org/10.1016/j.actaastro.2023.07.046.

[30] Space Studies Institute, 2017 Advanced Propulsion Workshop, (2017). https://ssi.org/the-2017-advanced-propulsion-workshop/ (accessed March 16, 2023).

[31] Space Studies Institute, 2018 Advanced Propulsion Workshop, (2018). https://www.youtube.com/playlist?list=PL_YvUODKu7CsdWPGxPm4uVxGdSv_m7gwb (accessed March 16, 2023).

[32] J.C. McDowell, The edge of space: Revisiting the Karman Line, Acta Astronaut. 151 (2018) 668–677. https://doi.org/10.1016/j.actaastro.2018.07.003.

[33] K.M. Ferrière, The Interstellar Environment of our Galaxy, Rev Mod Phys. 73 (2001) 1031–1066. https://doi.org/10.1103/RevModPhys.73.1031.

[34] R.W. Bussard, Galactic Matter and Interstellar Flight, Astronautica Acta. 6 (1960) 179–194.

[35] D. Besson, D. Cowen, M. Selen, C. Wiebusch, Neutrinos, in: Proc Natl Acad Sci U S A, 1999: pp. 14201–14202. https://doi.org/10.1073/pnas.96.25.14201.

[36] C. Yanagisawa, Looking for Cosmic Neutrino Background, Front Phys. 2 (2014) 1–6. https://doi.org/10.3389/fphy.2014.00030.

[37] P.A. Zyla, Particle Data Group, Cosmic Microwave Background, Progress of Theoretical and Experimental Physics. 083C01 (2020) 1–23.

[38] W. Seboldt, Ignition! - Missionskonzepte, fiktive Raketen und Antriebssysteme - "Mission concepts, fictitious rockets and propulsion systems," in: H. Zaun (Ed.), Expedition Ins Sternenmeer, Perspektiven, Chancen Und Risiken Einer Interstellaren Raumfahrt - "Expedition in the Sea of Stars, Chances and Risks in Interstellar Missions," Springer-Verlag GmbH Deutschland, 2022: pp. 139–153.

[39] J. Benford, G. Benford, Near-Term Beamed Sail Propulsion Missions: Cosmos-1 and Sun-Diver, in: AIP Conf Proc, 2003: pp. 358–368. https://doi.org/10.1063/1.1582124.

[40] Y.K. Bae, Prospective of Photon Propulsion for Interstellar Flight, Phys Procedia. 38 (2012) 253–279. https://doi.org/10.1016/j.phpro.2012.08.026.

[41] K. Mori, Beamed Launch Propulsion, in: Propulsion Systems, IntechOpen, 2018: pp. 1–18. https://doi.org/http://dx.doi.org/10.5772/intechopen.82236.

[42] M.S. Morris, K.S. Thorne, U. Yurtsever, Wormholes, Time Machines, and the Weak Energy Condition, Phys Rev Lett. 61 (1988) 1446–1449.

[43] J.S. Farnes, A unifying theory of dark energy and dark matter : Negative masses and matter creation within a modified ΛCDM framework, Astron Astrophys. 620 (2018) 1–20.

[44] K.H. Wanser, Center of Mass Acceleration of an Isolated System of Two Particles with Time Variable Masses Interacting with Each Other via Newton's Third Law Internal Forces: Mach Effect Thrust 1, Journal of Space Exploration. 2 (2013) 121–130.

[45] A.J. Higgins, Reconciling a Reactionless Propulsive Drive with the First Law of Thermodynamics, (2015) 1–7. http://arxiv.org/abs/1506.00494.

[46] R. Sedwick, H. White, Spacedrives and conservation laws, J Spacecr Rockets. 55 (2018) 1033–1038. https://doi.org/10.2514/1.A34116.

[47] A.R. Plastino, J.C. Muzzio, On the Use and Abuse of Newton's Second Law for Variable Mass Problems, Celest Mech Dyn Astron. 53 (1992) 227–232. https://doi.org/10.1007/BF00052611.

[48] S. Weinberg, Gravitation and Cosmology: Principles and Applications of the General Theory of Relativity, John Wiley & Sons, Inc., Boston, 1972.

[49] A. Pais, Subtle Is the Lord: The Science and the Life of Albert Einstein, Sci Soc. 50 (1986).

[50] S.W. Hawking, G.F.R. Ellis, The Large Scale Structure of Space-Time, Cambridge University Press, Cambridge, 1975.

[51] A. Einstein, Is There a Gravitational Effect Which Is Analogous to Electrodynamic Induction?, 44 (1912) 37–40. http://mc1soft.com/papers/1912-Einstein_Inertia.pdf.

[52] C.W.F. Everitt, D.B. Debra, B.W. Parkinson, J.P. Turneaure, J.W. Conklin, M.I. Heifetz, G.M. Keiser, A.S. Silbergleit, T. Holmes, J. Kolodziejczak, M. Al-Meshari, J.C. Mester, B. Muhlfelder, V.G. Solomonik, K. Stahl, P.W. Worden, W. Bencze, S. Buchman, B. Clarke, A. Al-Jadaan, H. Al-Jibreen, J. Li, J.A. Lipa, J.M. Lockhart, B. Al-Suwaidan, M. Taber, S. Wang, Gravity probe B: Final results of a space experiment to test general relativity, Phys Rev Lett. 106 (2011) 1–5. https://doi.org/10.1103/PhysRevLett.106.221101.

[53] H. Bondi, J. Samuel, The Lense-Thirring Effect and Mach's Principle, Physics Letters, Section A: General, Atomic and Solid State Physics. 228 (1997) 121–126. https://doi.org/10.1016/S0375-9601(97)00117-5.

[54] D.W. Sciama, P.C. Waylen, R.C. Gilman, Generally covariant integral formulation of Einstein's field equations, Physical Review. 187 (1969) 1762–1766. https://doi.org/10.1103/PhysRev.187.1762.

[55] C.H. Brans, Mach's Principle and the Locally Measured Gravitational Constant in General Relativity, Physical Review. 125 (1962) 388–396.

[56] F. Hoyle, J. V. Narlikar, A new theory of gravitation, Proc R Soc Lond A Math Phys Sci. 282 (1964) 191–207. https://doi.org/10.1098/rspa.1964.0227.

[57] H. Lichtenegger, B. Mashhoon, Mach's Principle, 2008. https://doi.org/10.1007/s12045-011-0037-9.

[58] K. Nordtvedt, Existence of the Gravitomagnetic Interaction, International Journal of Theoretical Physics. 27 (1988) 1395–1404. https://doi.org/10.1007/BF00671317.

[59] H. Fearn, A. Zachar, K. Wanser, J. Woodward, Theory of a Mach Effect Thruster I, Journal of Modern Physics. 6 (2015) 1510–1525.

[60] J.J.A. Rodal, A Machian wave effect in conformal , scalar – tensor gravitational theory, Gen Relativ Gravit. 51 (2019) 1–23. https://doi.org/10.1007/s10714-019-2547-9.

[61] J.B. Barbour, H. Pfister, Mach's Principle: From Newton's Bucket to Quantum Gravity, Birkhäuser, Dordrecht, 1995. https://doi.org/10.1007/978-94-017-3327-4_27.

[62] J.F. Woodward, Flux Capacitors and the Origin of Inertia, Found Phys. 34 (2004) 1475–1514.

[63] J. Rodal, A Machian wave effect in conformal, scalar–tensor gravitational theory, Gen Relativ Gravit. (2019). https://doi.org/10.1007/s10714-019-2547-9.

[64] J.P. Mbelek, Temporal Variation of Earth-Based Gravitational Constant Measurements, Gravitation and Cosmology. 25 (2019) 250–258. https://doi.org/10.1134/S0202289319030083.

[65] L.L. Williams, N. Inan, Maxwellian Mirages in General Relativity, 2020. http://arxiv.org/abs/2012.08077.

[66] C.L. Bennett, D. Larson, J.L. Weiland, N. Jarosik, G. Hinshaw, N. Odegard, K.M. Smith, R.S. Hill, B. Gold, M. Halpern, E. Komatsu, M.R. Nolta, L. Page, D.N. Spergel, E. Wollack, J. Dunkley, A. Kogut, M. Limon, S.S. Meyer, G.S. Tucker, E.L. Wright, Nine-year Wilkinson Microwave Anisotropy Probe (WMAP) Observations: Final Maps and Results, Astrophysical Journal, Supplement Series. 208 (2013) 1–177. https://doi.org/10.1088/0067-0049/208/2/20.

[67] J.F. Woodward, Inertia and Propulsion in General Relativity : a Reply to Rodal, Gen Relativ Gravit. (2020) 1–12. https://doi.org/10.1007/s10714-019-2654-7.

[68] C.H. Brans, Absence of Inertial Induction in General Relativity, Phys Rev Lett. 39 (1977) 856–857. https://doi.org/10.1103/PhysRevLett.39.856.

[69] Y.A. Çengel, Thermodynamics : an engineering approach, Sixth Edit, McGraw-Hill Higher Education, Boston, 2008. https://search.library.wisc.edu/catalog/9910062108002121.

[70] M. Tajmar, Mach-Effect thruster model, Acta Astronaut. 141 (2017) 8–16. https://doi.org/10.1016/j.actaastro.2017.09.021.

[71] PI Ceramics, Piezoelectric Actuators: Components, Technologies, Operation, 2012.

[72] J.F. Woodward, A New Experimental Approach to Mach's Principle and Relativistic Gravitation, Foundations of Physics Letters. 3 (1990) 497–506.

[73] J.F. Woodward, A Stationary Apparent Weight Shift from a Transient Machian Mass Fluctuation, Foundations of Physics Letters. 5 (1992) 425–442. https://doi.org/10.1007/BF00690424.

[74] J.F. Woodward, Method for Transiently Altering the Mass of Objects to Facilitate their Transport or Change their Stationary Apparent Weights, 5,280,864, 1992.

[75] J.F. Woodward, A Laboratory Test of Mach's Principle and Strong-field Relativistic Gravity, Foundations of Physics Letters. 9 (1996).

[76] M. Kößling, M. Tajmar, Design and performance of a nano-Newton torsion balance, Review of Scientific Instruments. 93 (2022) 1–8. https://doi.org/10.1063/5.0086975.

[77] C-Flex Bearing Co. Inc., Flex Pivot - Frictionless Bearings, (2015). https://c-flex.com/ (accessed March 16, 2023).

[78] H. Fearn, J.F. Woodward, New Experimental Results of the Mach Effect Gravitational Assist (MEGA) Drive, in: AIAA Propulsion and Energy Forum NNF, Indianapolis, 2019: pp. 1–12. https://doi.org/10.2514/6.2019-4285.

[79] H. Fearn, N. van Rossum, K. Wanser, J.F. Woodward, Theory of a Mach Effect Thruster II, Journal of Modern Physics. 06 (2015) 1868–1880. https://doi.org/10.4236/jmp.2015.613192.

[80] N. Buldrini, M. Tajmar, K. Marhold, B. Seifert, Experimental Results of the Woodward Effect on a uN Thrust Balance, in: AIAA/ASME/SAE/ASEE Joint Propulsion Conference & Exhibit, 2006: pp. 1–12. https://doi.org/10.2514/6.2006-4911.

[81] N. Buldrini, Verification of the Thrust Signature of a Mach Effect Device, Wiener Neustadt, 2014.

[82] J. F. Woodward, Gravity and Inertia in General Relativity, in: K.S. Essa (Ed.), Gravitational Field - Concepts and Applications, IntechOpen Limited, 2021: pp. 1–29. https://doi.org/10.5772/intechopen.99760.

[83] Z.J. Jabbour, S.L. Yaniv, The Kilogram and Measurements of Mass and Force, J. Research Natl. Inst. Standards Tech. 106 (2001) 25–46.

[84] A. Hajjam, J.C. Wilson, S. Pourkamali, Individual Air-borne Particle Mass Measurement using High-Frequency Micromechanical Resonators, IEEE Sens J. 11 (2011) 2883–2890. https://doi.org/10.1109/JSEN.2011.2147301.

[85] V. Zarko, V. Perov, A. Kiskin, D. Nalivaichenko, Microwave Resonator Method for Measuring Transient Mass Gasification Rate of Condensed Systems, in: 7th EUCASS, 2017: pp. 1–6. https://doi.org/10.13009/EUCASS2017-98 7TH.

[86] Sartorius Lab Instruments GmbH & Co. KG., Cubis II Catalogue, (2020) 1–12. https://www.sartorius.com/en/products/weighing/laboratory-balances/premium-level-balances/cubis-ii-de.

[87] Piezotronics PCB, PCB Load Cells Catalogue, (2014) 1–4. https://www.pcb.com/sensors-for-test-measurement/load-cells.

[88] R. Kumme, O.Mack, B.Bill, Ch.Gossweiler, H.R.Haab, The Dynamic Calibration of Piezoelectric Force Measuring Devices, 2001.

[89] Q. Xing, J. Zhang, M. Qian, Z.Y. Jia, B.Y. Sun, Thrust Stand for Low-thrust Liquid Pulsed Rocket Engines, Review of Scientific Instruments. 81 (2010). https://doi.org/10.1063/1.3481788.

[90] C. Spells, A. Craig, A. Ketsdever, Development of a Transient Thrust Stand with Sub-millisecond Resolution, Review of Scientific Instruments. 90 (2019) 1–12. https://doi.org/10.1063/1.5098009.

[91] B. D’Souza, A.D. Ketsdever, Investigation of Laser-surface Interactions using a Nano-impulse Balance, in: 35th AIAA Plasmadynamics and Lasers Conference, 2004: pp. 1–16. https://doi.org/10.2514/6.2004-2664.

[92] J. Twiefel, A. Glukhovkoy, S. de Wall, M.C. Wurz, M. Sehlmeyer, M. Hitzemann, S. Zimmermann, Towards a Highly Sensitive Piezoelectric Nano-mass Detection—a Model-based Concept Study, Sensors. 21 (2021). https://doi.org/10.3390/s21072533.

[93] F. Mier-Hicks, Thrust Measurements of Ion Electrospray Thrusters using a CubeSat Compatible Magnetically Levitated Thrust Balance, in: Joint Conference of 30th International Symposium on Space Technology and Science 34th International Electric Propulsion Conference and 6th Nano-Satellite Symposium, Kobe, 2015.

[94] A. Connelly, The laboratory balance: a practical guide, (n.d.). https://andyjconnelly.wordpress.com/2017/02/12/the-laboratory-balance-a-practical-guide/.

[95] Kistler Group, Force Sensors Catalogue, (2023) 1–42. https://doi.org/10.1016/b978-1-85617-695-8.00032-4.

[96] J.F. Woodward, A Test for the Existence of Mach Effects With a Rotary Device, in: AIP Conference Proceedings 1208, 2010: pp. 227–236.

[97] Hottinger Baldwin Messtechnik GmbH, Strain Gauge Catalogue, (2023). https://www.hbm.com/en/9803/strain-gauges-for-experimental-stress-analysis/#c421832.

[98] M. Li, W. Cheng, J. Chen, R. Xie, X. Li, A High Performance Piezoelectric Sensor for Dynamic Force Monitoring of Landslide, Sensors. 17 (2017). https://doi.org/10.3390/s17020394.

[99] K. Uchino, Introduction to Piezoelectric Actuators and Transducers, University Park, 2003.

[100] K. Uchino, Advanced Piezoelectric Materials, Woodhead Publishing Limited, Cornwall, 2010. https://doi.org/10.1533/9781845699758.frontmatter.

[101] K. Uchino, J. Zheng, A. Joshi, Y. Chen, S. Yoshikaw, S. Hirose, High Power Characterization of Piezoelectric Materials, (1998) 33–40.

[102] D. Guyomar, N. Aurelle, L. Eyraud, Piezoelectric Ceramics Nonlinear Behavior. Application to Langevin Transducer, Journal de Physique III. 7 (1997) 1197–1208. https://doi.org/10.1051/jp3:1997183.

[103] M.J. Haun, Z.Q. Zhuang, E. Furman, S. -J Jang, L.E. Cross, Electrostrictive Properties of the Lead Zirconate Titanate Solid-Solution System, Journal of the American Ceramic Society. 72 (1989) 1140–1144. https://doi.org/10.1111/j.1151-2916.1989.tb09697.x.

[104] F. Li, L. Jin, Z. Xu, S. Zhang, Electrostrictive effect in ferroelectrics : An alternative approach to improve piezoelectricity, Appl Phys Rev. 1 (2014). https://doi.org/10.1063/1.4861260.

[105] W. Jiang, W. Cao, Nonlinear Properties of Lead Zirconate–Titanate Piezoceramics, J Appl Phys. 88 (2000) 6684–6690. https://doi.org/10.1063/1.1325384.

[106] PI Ceramic GmbH, Material Data, (n.d.). https://www.piceramic.com/en/products/piezoelectric-materials/#c15193.

[107] Steiner & Martins Inc., PZT Materials, (2023). https://www.steminc.com/PZT/en/ (accessed March 16, 2023).

[108] A. Abdullah, M. Shahini, A. Pak, An Approach to Design a High Power Piezoelectric Ultrasonic Transducer, J Electroceram. 22 (2009) 369–382. https://doi.org/10.1007/s10832-007-9408-8.

[109] A. Wolff, D. Cramer, H. Heliebrand, C. Schuh, T. Steinkopff, K. Lubitz, Energy Considerations of PZT Multilayer Actuators under Dynamic Driving Conditions, in: IEEE 1996, 1996: pp. 317–320. https://doi.org/10.1109/ISAF.1996.602758.

[110] D.A. DeAngelis, G.W. Schulze, K.S. Wong, Optimizing Piezoelectric Stack Preload Bolts in Ultrasonic Transducers, in: 43rd Annual Symposium of the Ultrasonic Industry Association, 2015: pp. 11–20. https://doi.org/10.1016/j.phpro.2015.03.003.

[111] Etrema Products Inc., Detailed Manual: Ultrasonic Transducer CU18A, (2012) 1–16.

[112] A.G. Olabi, A. Grunwald, Design and Application of Magnetostrictive Materials, Mater Des. 29 (2008) 469–483. https://doi.org/10.1016/j.matdes.2006.12.016.

[113] R. Bhamore, P.K. Sahu, Review Paper on Belleville Spring Through Numerical and Simulation Approach, International Research Journal of Engineering and Technology. 6 (2019) 1834–1836.

[114] A. Behera, Advanced Materials: An Introduction to Modern Materials Science, in: A. Behera (Ed.), Magnetostrictive Materials, Springer International Publishing, Cham, 2022: pp. 127–156. https://doi.org/10.1007/978-3-030-80359-9_4.

[115] S. Karunanidhi, M. Singaperumal, Design, Analysis and Simulation of Magnetostrictive Actuator and its Application to High-dynamic Servo-valve, Sens Actuators A Phys. 157 (2010) 185–197. https://doi.org/10.1016/j.sna.2009.11.014.

[116] eFunda Inc., Lead Zirconate Titanate (PZT-4), (2023). https://www.efunda.com/materials/piezo/material_data/.

[117] J. Kim, B.L. Grisso, J.K. Kim, J. Kim, D.S. Ha, D.J. Inman, Electrical Modeling of Piezoelectric Ceramics for Analysis and Evaluation of Sensory Systems, in: IEEE Sensors Applications Symposium, Atlanta, 2008: pp. 122–127. http://ieeexplore.ieee.org/xpls/abs_all.jsp?arnumber=4472956.

[118] S. Sherrit, H.D. Wiederick, B.K. Mukherjee, M. Sayer, An Accurate Equivalent Circuit for the Unloaded Piezoelectric Vibrator in the Thickness Mode, J Phys D Appl Phys. 30 (1997) 2354–2363. https://doi.org/10.1088/0022-3727/30/16/014.

[119] Carvin, Carvin Engineering Data: Operating Manual DCM1000, n.d.

[120] B. Seifert, A. Reissner, N. Buldrini, F. Plesescu, C. Scharlemann, Development and Verification of a µN Thrust Balance for High Voltage Electric Propulsion Systems, in: 33rd International Electric Propulsion Conference, 2013: pp. 1–11.

[121] T. Liu, P. Sen, C.J. Kim, Characterization of Nontoxic Liquid-Metal Alloy Galinstan for Applications in Microdevices, Journal of Microelectromechanical Systems. 21 (2012) 443–450. https://doi.org/10.1109/JMEMS.2011.2174421.

[122] J.E. Polk, A. Pancotti, T. Haag, S. King, M. Walker, J. Blakely, J. Ziemer, Recommended Practice for Thrust Measurement in Electric Propulsion Testing, J Propuls Power. 33 (2017). https://doi.org/10.2514/1.B35564.

[123] B.E. Lee, Dynamic Force Measurement with Strain Gauges, Am J Phys. 42 (1974) 108–110. https://doi.org/10.1119/1.1987625.

[124] R. Kumme, O. Mack, B. Bill, H.R. Haab, C. Gossweiler, Investigation of Piezoelectric Force Measuring Devices in Force Calibration and Force Standard Machines, in: 17th International Conference on Force, Mass, Torque and Pressure Measurements, Istanbul, 2001: pp. 17–21.

[125] M. Kobusch, Characterization of Force Transducers for Dynamic Measurements, 2015.

[126] S. Safour, Y. Bernard, Static Force Transducer Based on Resonant Piezoelectric Structure: Root Cause Investigation, Smart Mater Struct. 26 (2017) 1–11. https://doi.org/10.1088/1361-665X/aa63da.

[127] R. Saideepak, Inspection of Cp Titanium Material and its Coefficient of Friction, International Research Journal of Engineering and Technology. 8 (2021) 318–326. www.irjet.net.